Tailoring of Material Properties in Perovskites for Solar Thermochemical Applications

Anpassung der Materialeigenschaften von Perowskiten für solarthermochemische Anwendung

Von der Fakultät für Maschinenwesen der Rheinisch-Westfälischen Technischen Hochschule Aachen zur Erlangung des akademischen Grades einer Doktorin der Naturwissenschaften genehmigte Dissertation

vorgelegt von

Lena Friederike Klaas

Berichter:	Univ.-Prof. Dr. rer. nat. Christian Sattler
	apl. Prof. Dr. rer. nat. habil. Martin Schmücker
Tag der mündlichen Prüfung:	17. Januar 2024

Abstract

In light of the negative impact of CO_2 emissions on the climate, the industry needs to transition to a fossil-free one. Due to the fluctuating nature of renewable energies, such as wind and solar, energy storage gains in importance. Thermochemical energy storage serves as an excellent long-term and seasonal storage. Here, one important and already well-established chemical commodity is ammonia. To produce fossil-free ammonia, green nitrogen is required. Green nitrogen can be produced sustainably using solar thermochemical cycles. The selected redox material is crucial for efficiency and operating conditions, such as temperatures. Perovskites have emerged as a suitable material class for this purpose. Perovskites have the advantage that they can be composed of many different elements. Thus, understanding the impact of partial elemental substitution in perovskites is essential to tailor the material properties. The impact of partial substitution on the crystal structure is analyzed by X-ray diffraction (XRD) applying the Rietveld refinement, high-temperature XRD, and complemented with the analysis of molecular vibrations by Raman spectroscopy. Thermodynamical changes are analyzed by thermogravimetric analysis (TGA) applying the *van't Hoff* approach. The results reveal that the changes in the crystal structure impact the thermodynamic properties. The reduction and oxidation kinetics are as well analyzed by TGA. This work shows that oxidation kinetics can be affected by both element substitution and microstructural changes. Finally, the impact of the material composition on the energetic requirements for an air separation process is analyzed by thermodynamic-based energy calculations. Small-scale packed-bed reactor experiments validate them. All in all, this work highlights the effects of partial element substitution and microstructure on the perovskite properties in terms of efficiency and operating conditions. Understanding these effects enables tailoring of material properties for solar thermochemical applications to get the right feature.

Zusammenfassung

In Anbetracht der negativen Auswirkungen von CO_2-Emissionen auf das Weltklima muss die Industrie fossilfrei werden. Aufgrund der Variabilität der erneuerbaren Energien, wie Wind und Sonne, gewinnt die Energiespeicherung an Bedeutung. Thermochemische Energiespeicher dienen als gute Langzeit- und Saisonspeicher. Ein dabei wichtiger und bereits etablierter Rohstoff ist Ammoniak. Um Ammoniak fossilfrei zu produzieren, wird grüner Stickstoff benötigt. Grüner Stickstoff kann mit solarthermochemischen Kreisläufen nachhaltig produziert werden. Für die Effizienz und die Betriebsbedingungen, wie z. B. die Temperatur, ist das verwendete Redoxmaterial entscheidend. Perowskite haben sich als eine gute Materialklasse für diesen Zweck herausgestellt. Sie haben den Vorteil, dass sie aus vielen verschiedenen Elementen zusammengesetzt werden können. Daher ist wichtig, die Auswirkungen der teilweisen Substitution von Elementen in Perowskiten zu verstehen, um die Materialeigenschaften anzupassen. Die Auswirkungen der partiellen Substitution auf die Kristallstruktur werden mit Hilfe der Röntgenbeugung unter Anwendung der Rietveld-Verfeinerung und der Hochtemperatur-Röntgenbeugung analysiert und durch die Analyse der Molekülschwingungen mittels Raman-Spektroskopie ergänzt. Thermodynamische Veränderungen werden mittels thermogravimetrischer Analyse (TGA) unter Anwendung des *van't Hoff* Ansatzes analysiert. Die Ergebnisse zeigen, dass sich die Veränderungen der Kristallstruktur auf die thermodynamischen Eigenschaften auswirken. Die Reduktions- und Oxidationskinetik wird ebenfalls mittels TGA analysiert. Diese Arbeit zeigt, dass die Oxidationskinetik sowohl durch die Substitution von Elementen als auch durch mikrostrukturelle Veränderungen beeinflusst werden kann. Schließlich wird der Einfluss der Materialzusammensetzung auf den Energiebedarf für einen Luftzerlegungsprozess durch thermodynamisch basierte Energieberechnungen analysiert. Diese Berechnungen werden durch Experimente in einem Festbettreaktor im kleinen Maßstab validiert. Insgesamt zeigt diese Arbeit die Auswirkungen der partiellen Elementsubstitution und der Mikrostruktur auf die Eigenschaften des Perowskits in Bezug auf die Effizienz und den Betriebsbedingungen. Das Verständnis dieser Effekte ermöglicht, die Materialeigenschaften für solarthermochemische Anwendungen so anzupassen, dass die richtigen Eigenschaften erzielt werden.

Contents

Nomenclature

Chemical Elements and Molecules

Ar	Argon
Ca	Calcium
CO_2	Carbon dioxide
C	Carbon
Fe	Iron
H_2O	water
H_2	Hydrogen molecule
Hg	Mercury
Mn	Manganese
N_2	Nitrogen molecule
NH_3	Ammonia
O	Oxygen
Sr	Strontium

Abbreviations

A	A-site ion in perovskite structure
ABO_3	Perovskite structure
B	B-site ion in perovskite structure
CMO	$CaMnO_3$
CN	Coordination number

CS10MO	$Ca_{0.9}Sr_{0.1}MnO_3$
CS20MO	$Ca_{0.8}Sr_{0.2}MnO_3$
CS30MO	$Ca_{0.7}Sr_{0.3}MnO_3$
CS40MO	$Ca_{0.6}Sr_{0.4}MnO_3$
DFT	Density functional theory
DSC	Differential scanning calorimetry
EDS	Energy dispersive X-ray spectroscopy
$Foam_{BM}$	Foam whose suspension was ball-milled
$Foam_{MS}$	Foam whose suspension was magnetic stirred
HT-XRD	In-situ high-temperature X-ray Diffraction
ICCD	International Center for Diffraction Data
ICSD	Inorganic Crystal Structure Database
MFC	Mass flow controller
P_{2BM}	Ball-milled powder whose slurry is ball-milled
$P_{BM,MS}$	Ball-milled powder whose slurry is magnetically stirred
P_{BM}	Ball-milled powder
P_M	Manually grounded powder
$Pellet_{BM}$	Pellet whose powder was ball-milled
$Pellet_M$	Pellet whose powder was ground manually
PID	*PID Eng&Tech MicroEffi system*
PSA	Pressure swing adsorption
PSD	Particle size distribution
PU	Polyurethane
SEM	Scanning electron microscopy

SFO	$SrFeO_3$	
XRD	X-ray Diffraction	

Variables

α	Polarizability	Cm^2/V
$\bar{x}_{O_2}$	Mean oxygen molar fraction	-
β	Reaction order	-
Δg_δ	Partial molar change in Gibbs free energy	J
Δg_δ°	Partial molar change in Gibbs free energy at standard pressure	J
Δh_δ°	Partial molar change in enthalpy at standard pressure	kJ/mol
Δs°	Change in entropy at standard pressure	J/K
Δs_δ	Partial molar change in entropy	J/molK
Δs_δ°	Partial molar change in entropy at standard pressure	J/molK
Δs_{conf}	Configuration entropy	J/K
$\Delta s_{\text{th}}^\circ$	Thermal entropy at standard pressure	J/molK
δ	Oxygen non-stoichiometry	-
δ_0	Oxygen non-stoichiometry at $t = 0$	-
δ_∞	Equilibrium oxygen non-stoichiometry	-
δ_{ox}	Oxygen non-stoichiometry of oxidized state	-
δ_{red}	Oxygen non-stoichiometry of reduced state	-
$\dot{n}_{O_2}$	Molar feed rate of oxygen	mol/s
$\dot{V}_{O_2}$	Flow of absorbed oxygen	Nm^3
$\dot{V}_{\text{ox}}$	Inlet flow rate during oxidation	Nm^3/s
η_{gas}	Gas heat exchange efficiency	-
$\eta_{\text{PSA}-\text{recov}}$	Nitrogen recovery fraction	-

γ	Dimensionless parameter determining the number of moles mixed	
$\Delta a_{\mathrm{cubic}}$	Slope of the evolution of cubic lattice parameter	%/K
$\Delta a_{\mathrm{ortho}}$	Slope of the evolution of orthorhombic lattice parameter	%/K
ΔL	Length of packed-bed	mm
ν	Fluid velocity of empty pipe	m/s
ψ	Porosity of filling	-
θ	Bragg's angle	°
$\vec{E}$	Electric field vector	V/m
$\vec{p}$	Electric dipol vector	C· m
a	Lattice parameter	Å
a_0	Lattice parameter at 303 K	Å
$a_{\mathrm{pseudo-cubic}}$	Converted lattice parameter a	Å
a_{sl}	Slope of the evolution of the modes wavenumber	cm^{-1}/%Sr
b	Lattice parameter	Å
$b_{\mathrm{pseudo-cubic}}$	Converted lattice parameter b	Å
c	Lattice parameter	Å
$c_{\mathrm{O_2}}$	Oxygen concentration	$\mathrm{mol\ m}^{-3}$
$c_{\mathrm{pseudo-cubic}}$	Converted lattice parameter c	Å
c_p	Heat capacity	J/molK
D	Crystallite size	nm
d	Diameter	mm
D_{JT}	Distortion of perovskite structure	-
$D_{[010]}$	Distortion of perovskite structure	-
$D_{[101]}$	Distortion of perovskite structure	-

$D_{A-\text{shift}}$	Distortion of perovskite structure	-
E_A	Activation energy	J/mol
$f(X)$	Reaction model	-
h,k,l	Miller index	-
$h(c_{\text{O}_2})$	Oxygen concentration dependence	$(\text{mol m}^{-3})^n$
$I_{\text{calc},i}$	Calculated intensity of the ith reflection of N total reflections	-
$I_{\text{obs},i}$	Observed intensity of the ith reflection of N total reflections	-
k	Rate constant	$\text{s}^{-1}(\text{mol m}^{-3})^{-n}$
k_0	Pre-exponential factor	$\text{s}^{-1}(\text{mol m}^{-3})^{-n}$
m	Sample mass	mg
m_{redox}	Mass of redox material	kg
n	Order of oxygen concentration dependence	-
$n_{\text{in,red/ox}}$	Inlet molar amount of gas	mol
n_{O_2}	Molar amount of oxygen adsorbed	-
$n_{\text{out,red/ox}}$	Outlet molar amount of gas	mol
n_{redox}	Molar amount of redox material	-
P	Pressure	bar
p°	Standard pressure	bar
$p_{\text{O}_2,\text{inlet}}$	Inlet oxygen partial pressure	bar
$p_{\text{O}_2,\text{product}}$	Product oxygen partial pressure	bar
$p_{\text{O}_2,\text{ox}}$	Oxidation oxygen partial pressure	bar
$p_{\text{O}_2,\text{red}}$	Reduction oxygen partial pressure	bar
p_{O_2}	Oxygen partial pressure	bar
p_{red}	Total pressure during reduction	bar

$p_{\mathrm{tot,ox}}$	Total pressure during oxidation	bar
$Q(T)$	Molar heat	J/mol
Q_{chem}	Chemical energy	J
Q_{gas}	Energy to heat gas	J
Q_{sens}	Sensible heat	J
Q_{tot}	Total energy required for air separation	J
R_{Bragg}	Bragg-R-value	-
r_{ion}	Ionic radii of ion	Å
R_{wp}	Weighted profile factor	-
T	Temperature	K
t	Time	s
t_{cycle}	Time for completion of a redox cycle	h
t_{G}	*Goldschmidt* tolerance factor	-
T_{ox}	Oxidation temperature	K
t_{ox}	Oxidation time	s
T_{PT}	Phase change temperature	K
T_{red}	Reduction temperature	K
$t_{1/2}$	Half life	s
V	Volume	Nm^3
$V_{\mathrm{in,exp}}$	Volume of purified inlet gas	Nm^3
V_{in}	Volume of inlet gas	Nm^3
$V_{\mathrm{O_2,exp}}$	Total volume of absorbed oxygen	Nm^3
$V_{\mathrm{O_2}}$	Volume of oxygen	Nm^3
V_{ProdRate}	Production rate of purified gas	Nm^3

V_{Product}	Volume of product gas	Nm^3
$W_{\text{adiabatic}}$	Adiabatic compression work	$\text{J mol}_{\text{air}}^{-1}$
W_{comp}	Work to compress air	$\text{J mol}_{\text{air}}^{-1}$
W_{PSA}	Work to produce nitrogen using PSA	$\text{J mol}_{\text{N}_2}^{-1}$
$W_{\text{pump,ox}}$	Work to pump gas during oxidation	J
$W_{\text{pump,red}}$	Work to pump gas during reduction	J
W_{pump}	Work to pump gas	J
w_i	Weight of the weighted profile factor	-
X	Conversion extent	-
x	Strontium content	-
$x_{\text{N}_2,\text{air}}$	Nitrogen molar fraction in air	-
$x_{\text{O(2)}}$	Deviation of the coordinate from cubic coordinate	-
$x_{\text{O}_2,\text{inlet}}$	Inlet oxygen molar fraction	-
$x_{\text{O}_2,\text{min}}$	Minimal oxygen molar fraction	-
$x_{\text{O}_2,\text{outlet}}$	Outlet oxygen molar fraction	-
x_{O_2}	Oxygen molar fraction	-
x_A	Deviation of the coordinate from cubic coordinate	-
$y_{\text{O(2)}}$	Deviation of the coordinate from cubic coordinate	-
$y_{\text{calc},i}$	Calculated intensity at point i of N data points	-
$y_{\text{obs},i}$	Observed intensity at point i of N data points	-
$z_{\text{O(1)}}$	Deviation of the coordinate from cubic coordinate	-
$z_{\text{O(2)}}$	Deviation of the coordinate from cubic coordinate	-
FWHM	Full width at half maximum	°
M_{O}	Molar mass of oxygen	g/mol
M_{Sample}	Molar mass of sample	g/mol
R	Ideal gas constant	J/molK

1. Introduction

In 1856, *Eunice Foote*[1] published for the first time a paper in which she mentioned the effects of carbon dioxide concentration in the atmosphere on the temperature of the atmosphere. She stated that:

> An atmosphere of [carbon dioxide] would give to our earth a high temperature; and if as some suppose, at one period of its history the air had mixed with it a larger proportion than at present, an increased temperature [...] must have necessarily resulted.[1]

After identifying the correlation between CO_2 content in the atmosphere and temperature on earth, this subject was out of focus and not of interest to the general public for several centuries. This changed upon the increased CO_2 emissions due to industrialization. *ExxonMobil* investigated and confirmed anthropogenic global warming since the late 1970s in scientific journals and internal documents. In contrast, *ExxonMobil* emphasized the uncertainties of global warming in public and advertising communications.[2–4] In 2015, nearly 190 countries agreed on reducing the greenhouse gas emissions, such as carbon dioxide, to prevent global warming from rising above 1.5 °C in the Paris Agreement.[5] This decision paved the way for the European Union's decision to be greenhouse gas neutral by 2050[6] and the German government's decision to be greenhouse gas neutral by 2045.[7]

To fulfill this decision, all sectors, such as industry and transportation, must be CO_2 emission-free, and renewable energy must replace fossil-based energy sources. The two most important renewable energy sources are wind and solar radiation. Both have the disadvantage that they are not available on demand but depend on environmental conditions. Therefore, energy storage is becoming more and more critical. Chemical energy storage is used for long-term and seasonal storage.

One possibility for storing energy in a chemical compound is hydrogen. Hydrogen is considered a key factor in the energy transition, but storing and transporting hydrogen has its challenges.[8] Since liquid ammonia NH_3 has proven solutions for storage and transportation in bulk or through pipelines at ambient temperature and low-pressures,[9,10] the further processing of hydrogen to ammonia:

$$N_2 + 3H_2 \leftrightarrow 2NH_3 \tag{1.1}$$

is a viable solution. This potential easy-to-handle hydrogen carrier[11,12] is gaining increasing interest as an energy vector, especially for maritime applications.[12]

Ammonia is already a fundamental chemical commodity with a global annual production of 165 Mt in 2021.[13] To date, it is used mainly as a fertilizer. Yet, the production of ammonia itself causes CO_2 emissions of $1.7\,t/tNH_3$.[14] Currently, ammonia is produced by the Haber-Bosch process[15] where nitrogen and hydrogen are converted to ammonia (eq. 1.1). *Klaas et al.*[16] summarize in a Review alternative production routes to make the production sustainable, which require milder conditions and the integration of solar energy. All these processes are still at low Technology Readiness Level (TRL).

The production of the feedstock causes CO_2 emissions. In particular, the production of nitrogen via cryogenic air distillation causes $0.04\,tCO_2/tNH_3$.[16] *MacFarlane et al.*[17] divided the transition to fossil-free ammonia into three steps or 'Generations' in their roadmap. The three successive Generations are:

1. Generation: Carbon capture and storage in current technologies,
2. Generation: Use of fossil-free feedstock (N_2 and H_2),
3. Generation: Sole utilization of green production routes which are sustainable, resilient, adaptable to variable renewable energy conditions and allow diverse production rates from the kW to the GW scale.[17]

This work and the project *SESAM*, which will be presented in Sec. 2.8 on p. 21, focus on the 2. Generation, especially on the supply of highly pure nitrogen with oxygen concentration in the ppm-range. This low residual oxygen concentration is essential since oxygen poisons the catalyst in the Haber-Bosch process, and the alternative routes also require low oxygen concentrations.[16] One solution for producing fossil-free nitrogen is solar-based thermochemical air separation. On the laboratory scale, the process was proven as a potential option to current fossil-based processes.[18,19] Beside feasibility, *Capstick et al.*[20] proved its energetic competitiveness compared to fossil-based standard processes.

The key to applicability, efficiency, and process parameters are the required redox materials. Redox materials are materials that can be reduced and oxidized. During the oxidation process, the oxygen of the air is incorporated into the material, thus reducing the oxygen concentration within the passing gas.

An essential aspect of the material is the crystal structure. Not only does the crystal structure affect various properties of the sample, but the crystal structure itself must be

stable. The crystal structure may decompose as the system always moves towards the most energetically favorable state. Decomposition can lead to a phase with different and, above all, undesirable properties. Moreover, a phase change between different structures can affect the morphology, as a rapid volume change of the material can accompany it. The appearance of phase changes is particularly interesting for long-term stability in cyclic processes with harsh and rapidly changing conditions. For example, monolithic specimens like honeycombs and foams may suffer from fast expansion or contraction, resulting in cracks.

Additionally, redox thermodynamics is important. It influences the process parameters, directly affecting the technical design, and dictates the lowest achievable oxygen concentration in the product gas. Furthermore, kinetics affects process design, such as flow rates, or makes the process infeasible if the kinetics are too slow for the desired application.

All the aspects mentioned above are affected by the composition of the material. To investigate and better understand the effect of the partial substitution of an ion in the redox material, $Ca_{1-x}Sr_xMnO_{3-\delta}$ was selected in this work for a thorough analysis. $Ca_{1-x}Sr_xMnO_{3-\delta}$ has been applied before for the adjustment of oxygen concentration.[21,22]

To accomplish this, Chap. 2 provides the required theoretical background and Chap. 3 describes the used experimental methods. Chap. 4 contains a thorough crystal structure analysis employing X-ray diffraction at room temperature, elevated temperatures, and different atmospheres. It is rounded up by investigating molecular vibrations via Raman spectroscopy. The impact of the substitution on thermodynamics is presented in Chap. 5. It discusses how the crystal structural changes may be the basis for the observed thermodynamic trends. Chap. 6 focuses on the microstructure. Here, the effects of Sr content will be considered, and various macrostructures and production methods will be considered. Since powder is less interesting for the application, but the structured forms are, Chap. 7 highlights the kinetics of the material for different compositions, macrostructures and production methods. To further guide into the application, Chap. 8 analyzes the composition's impact on the process's energetic requirements. In the end, Chap. 9 summarizes the conclusions of each chapter and provides an outlook for further research.

2. Theoretical Background

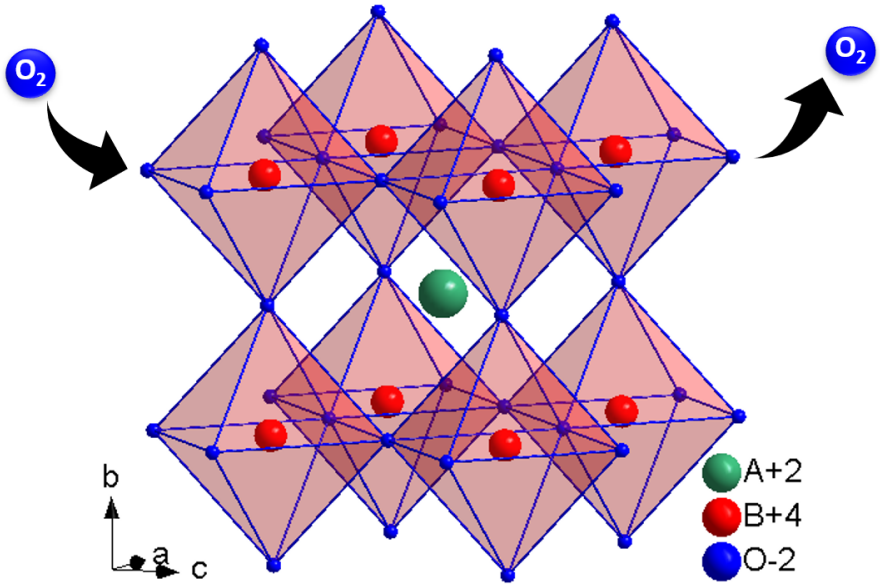

Figure 2.1.: This figure illustrates the crystal structure of a cubic perovskite. Furthermore, it shows that perovskites can be oxidized and reduced.

This chapter is partially based on the following peer-reviewed publications, which are authored by the author of this thesis:

L. Klaas, M. Pein, P. Mechnich, A. Francke, D. Giasafaki, D. Kriechbaumer, Ch. Agrafiotis, M. Roeb, and Ch. Sattler. Controlling thermal expansion and phase transitions in $Ca_{1-x}Sr_xMnO_{3-\delta}$ by Sr content. Physical chemistry chemical physics: PCCP, 24(45):27976-27988, 2022. doi: 10.1039/D2CP04332G.

L. Klaas, B. Bulfin, D. Kriechbaumer, M. Roeb and Ch. Sattler. Impact of the Sr content on the redox thermodynamics and kinetics of $Ca_{1-x}Sr_xMnO_{3-\delta}$ tailored properties. Physical chemistry chemical physics: PCCP, 25(13):9188-9197, 2023. doi: 10.1039/D3CP00267E.

L. Klaas, B. Bulfin, D. Kriechbaumer, N. Neumann, M. Roeb and Ch. Sattler. Energetic optimization of thermochemical air separation for the production of sustainable nitrogen. Reaction Chemistry & Engineering, 8(8):1843-1854, 2023. doi: 10.1039/D3RE00087G.

This chapter summarizes the relevant theoretical background for this thesis. It starts with a general introduction to thermochemical processes and perovskites. The measures for the distortion of perovskite are presented. The concept of molecular vibrations is described, and a model to categorize distortions is discussed. In addition, the material properties of thermodynamics and kinetics are introduced. Additionally, $CaMnO_3$ is introduced as a suitable material for thermochemical cycles, and a project highlighting a possible application is presented. Finally, the chapter concludes with a presentation of the basis for the energy calculations.

2.1. Perovskites in Thermochemical Processes

The chemical formula of an oxide with perovskite structure is ABO_3. Here, A are alkaline or rare earth metals, and B are transition metals.[23] In addition, there are mixed organic-inorganic halide perovskites that are used, for example, in solar cells.[24] Due to their variable nature with a vast number of possible A- and B-site cation combinations, including multi-cation solid solutions, and the associated tunability of their properties, they can be utilized in a variety of applications. Perovskites can be reduced or oxidized non-stoichiometrically.

During the reduction of the perovskite, oxygen is released, and doubly ionized oxygen vacancies are formed. Using the Kröger-Vink notation,[25] this reduction can be written as:

$$\mathrm{O_O^\times} + 2\,\mathrm{B_B^\times} = \mathrm{V_O^{\bullet\bullet}} + 2\,\mathrm{B_B'} + \frac{1}{2}\,\mathrm{O_2}. \tag{2.1}$$

The reduction is accompanied by a chance of the valence of the B-site cation to fulfill charge neutrality. Whereas the A-site cation typically does not change the valence state during the reaction.[23] The reduction of the perovskite is a reversible process. Thus, it can be oxidized again. The reduction-oxidation process is a thermochemical process often abbreviated to the term 'redox process'.

Fig. 2.2 shows the schematic of a redox process. The oxidized perovskite $ABO_{3,\mathrm{ox}}$ is heated and thereby reduced. The reduced perovskite $ABO_{3,\mathrm{red}}$ is then cooled and oxidized by exposure to oxygen. A new redox cycle is started. If the heat required for the reduction of the material is provided by concentrated solar radiation, this is referred to as a solar thermochemical process.

The oxygen can be supplied in different ways; therefore, this redox process can be used for different applications. First, the redox process can be used to store heat.[26–30] Second, the process can as well be used for air separation[31–36] or as an oxygen pump.[18,21,22] Moreover, hydrogen can be produced by splitting water steam.[37–41] Since the oxygen and the hydrogen generation occurs during different steps, the gases can easily be separated and further processed. In addition, CO_2 can be separated into carbon monoxide and oxygen.

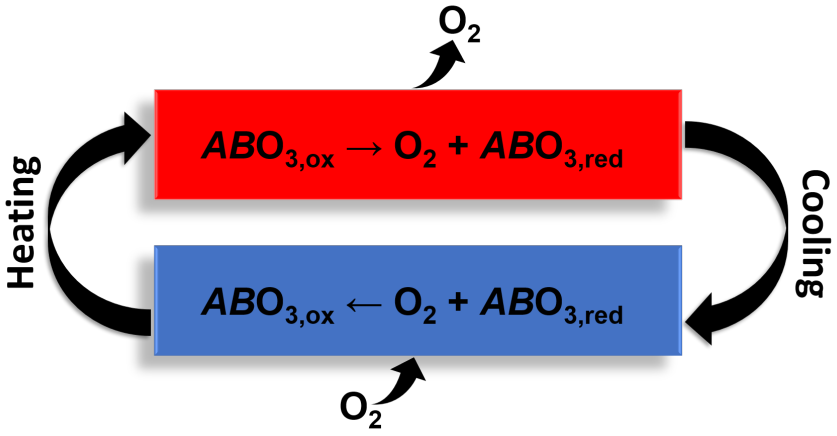

Figure 2.2.: Schematic of a redox process with a perovskite as the redox material. It consists of a high-temperature endothermic reduction step, where oxygen is released, and a lower-temperature exothermic oxidation step. Here, the oxygen atoms can be exposed to the material either as an oxygen molecule or through water steam and CO_2.

The carbon monoxide and the hydrogen serve as a feedstock for the production of synthetic fuels.[37,38,40,42] If the CO_2 used in this process is either supplied by direct air capture or comes as a waste product from other processes, the produced fuel is carbon-neutral. These processes have in common that the heat is stored chemically.

Slightly aside from the classical fields of application, *Eltayeb* and *Klaas et al.*[43] have theoretically investigated the use of thermochemical cycles with perovskites for oxygen production on Mars. The idea is to use the Martian atmosphere, which contains 0.16 % O_2, and to extract the oxygen during the reduction step. Here, heat is supplied by radioactive isotopes since they have been used frequently in space missions.

The ideal perovskite structure is cubic and displayed in Fig. 2.3a. The B-ions are located at the corner, and the A-ion at the cube's center. The A-ion is surrounded by 12 equidistant oxygen ions. The B-ion is placed at the center of an oxygen-octahedron. These BO_6-octahedra are corner-sharing. Therefore, the detailed structural formula, including the coordination number, is: $A^{\mathrm{XII}}B^{\mathrm{VI}}{O_3}^{\mathrm{VI}}$.[44]

Besides, the ideal cubic structure of the perovskites often incorporates distortions. The mismatching ionic radii of the involved ions cause these. One distortion is the orthorhombic distortion, displayed in Fig. 2.3b for $CaMnO_3$. In the orthorhombic structure, the lattice vectors stay orthogonal but no longer have the same length. Instead, all three have different lengths. Moreover, typically two different oxygen ion positions are distinguished. In the displayed example, O1 is the oxygen ion in the Ca-ion plane, and O2 is the oxygen ion in the Mn-ion plane.

The distortion results in an octahedral tilting. The tilting of the octahedra is described by the Glazer-Notation.[46] Here, the rotation of the octahedra about the three Cartesian axes is

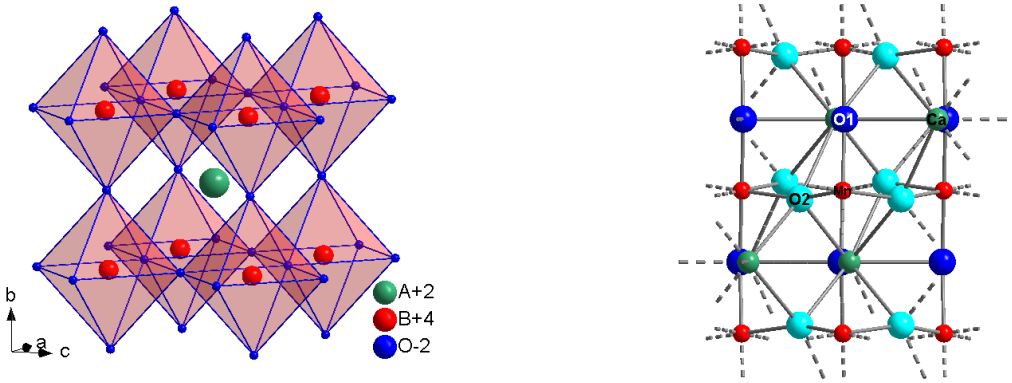

(a) Ideal cubic structure

(b) Orthorhombic distorted structure of $CaMnO_3$

Figure 2.3.: Perovskite structure of an ideal cubic and distorted structure. For clarity, in Fig. 2.3a, the atomic bonds are not displayed, but the octahedra are highlighted. In contrast, Fig. 2.3b shows the atomic bonds but not the octahedra. Reproduced from *Klaas et al.*[45] with permission from the PCCP Owner Societies.

declared. Therefore, the relative magnitude of the rotation and the direction of the rotation for two adjacent layers are specified. For example, $a^+ b^- b^-$ describes that the rotation angle around the x-axis is different than around the y- and z-axis but identical for the latter two. Additionally, it states that the rotation of two neighboring octahedra along the first tilt axis is in the same direction and for the latter two in the opposite direction.

Woodward et al.[47,48] investigated the octahedral tilting. The $a^+ b^- b^-$ tilt structure results in the lowest energy, maximizing the number of short $A-O$ interactions. Contrary, the ideal cubic structure is higher in energy and thus requires stabilizing forces.[47]

Another source of distortion is the Jahn-Teller effect.[49] The Jahn-Teller effect leads to a tetragonal distortion of the octahedra. The electronic state of the material causes this distortion. Here, an energetically degenerated state is compensated by the distortion of the octahedron because this state is energetically lower. As in $CaMnO_3$, no Jahn-Teller distortion occurs for Mn^{4+} since it has a nondegenerate ground state. In contrast, a Jahn-Teller distortion occurs for Mn^{3+} since it has a degenerate ground state.[50]

An advantage of the perovskite structure is that it can be reduced by applying heat or decreasing the oxygen partial pressure (details in Sec. 2.5, p. 15) without primary phase changes.[51] It keeps the perovskite structure up to an oxygen deficiency of $\frac{1}{6}$. Afterward, the defect structure is called brownmillerite with the chemical formula $A_2B_2O_5$.[52] Still, minor phase changes between the different distortions are observed, and these structural changes of the distortions are reversible.

For example, $CaMnO_3$ shows a phase change from orthorhombic to cubic during reduction with a tetragonal intermediate structure.[53,54] The decreasing orthorhombic distortion is based on two effects. One source is the supply of heat,[55] and another is the expansion of

the material due to reduction since the ionic radii are dependent on the oxidation state.[54] *Klarbring et al.*[55] stated that the cubic phase is a dynamical average of the tilted octahedra. Re-oxidizing the material results in an increasing orthorhombic distortion.

2.2. Measures for the Distortion

The *Goldschmidt* tolerance factor is a simplistic measure for the distortion of a perovskite.[56] It is based on the geometric consideration of hard spheres (Fig. 2.4). In a cubic structure, the relation between the straight line and the diagonal equals $\sqrt{2}$. Thus, if the ions are to fill this space as best as possible, the ionic radii must fulfill a specific condition defined as the tolerance factor t_G. It is equal to 1 for a cubic perovskite:

$$\frac{r_A + r_\mathrm{O}}{\sqrt{2}\,(r_B + r_\mathrm{O})} \overset{\text{def}}{=} t_\mathrm{G} = 1\,^{[56]} \tag{2.2}$$

Here, r_A, r_B, and r_O are the ionic radii of the A-site ion, the B-site ion, and the oxygen ion, respectively. Distorted perovskites are formed if the condition $t_\mathrm{G} = 1$ is not met. Moreover, *Goldschmidt* limited his statement in such a way that the ionic radii of the involved ions must not deviate from each other by more than 15 %.[56] Values of the tolerance factor below one are stated to result in an orthorhombic structure, and values of the tolerance factor greater than one are stated to result in a hexagonal structure.[23] The precision of this basic model is limited. Therefore, it has been further developed, e.g., ref.[57–59] Still, it serves as a good initial indicator for the crystal structure and is therefore used in this dissertation.

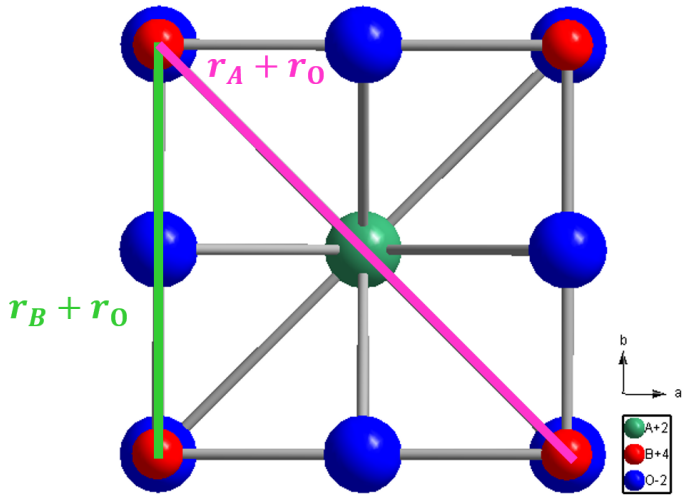

Figure 2.4.: Front view of an ideal cubic perovskite structure ABO_3. This image serves for the explanation of the *Goldschmidt* tolerance factor (eq. 2.2), which is based on geometric considerations. For clarity, the ions are not drawn space-filling.

The ionic radii definition of *Shannon*[60] is used to calculate the tolerance factor. Here, the effective ionic radii depend on the oxidation state and the coordination number (CN). Reflecting the position of the B-ion within the BO_6 octahedron, the B-site ion has a CN of 6. Likewise, oxygen has a CN of 6. In an ideal cubic structure, the CN of the A-site ion is 12. In contrast, empirical studies have demonstrated that mixed coordination between 12 and 10 with a ratio of 80:20 better represents distorted structures.[34] Therefore, this mixed CN is applied throughout this study. The tolerance factors for oxidized $Ca_{1-x}Sr_xMnO_3$ with $x \in [0, 0.4]$ are shown in table 2.1.

Table 2.1.: Calculation of the Goldschmidt tolerance factor t_G of $Ca_{1-x}Sr_xMnO_3$ (eq. 2.2) using the ionic radii of *Shannon*.[60]

x [-]	t_G [-]
0	0.9958
0.05	0.9978
0.1	0.9997
0.11	1.0001
0.15	1.0016
0.2	1.0036
0.25	1.0055
0.3	1.0075
0.40	1.0113

As mentioned previously, the *Goldschmidt* tolerance factor has limited accuracy in predicting the extent of distortion of a perovskite. Thus, a new measure for predicting the degree of orthorhombic distortion is introduced. These measures are the relative magnitudes of the lattice parameters. Throughout this dissertation, the lattice parameter a, c are the base, and b is the height. This convention is exemplified for an ideal cubic structure in Fig. 2.3a. Before comparing the relative magnitudes, they have to be converted into their pseudo-cubic equivalent:

$$a_{\mathrm{pseudo-cubic}} = \frac{a}{\sqrt{2}} \tag{2.3}$$

$$b_{\mathrm{pseudo-cubic}} = \frac{b}{2} \tag{2.4}$$

$$c_{\mathrm{pseudo-cubic}} = \frac{c}{\sqrt{2}}. \tag{2.5}$$

The relation $\frac{c_{\mathrm{pseudo-cubic}}}{a_{\mathrm{pseudo-cubic}}} = \frac{c}{a}$ is a measure of the deviation from the quadratic base.[61] If it equals one, the base is quadratic. The measure $\frac{c_{\mathrm{pseudo-cubic}}}{b_{\mathrm{pseudo-cubic}}} = \frac{\sqrt{2}c}{b}$ relates the base line c to the height b. If it equals one, the plane spanned by these lattice parameters is square.

2.3. Fundamentals of Molecular Vibrations

A complementary approach to crystal structure analysis is the analysis of molecular vibrations. Raman spectroscopy is used to investigate molecular vibrations through the interaction of photons with matter. Therefore, a sample is irradiated with monochromatic electromagnetic radiation. The scattered radiation is collected and analyzed. Here, the scattered light has different contributions (Fig. 2.5). Firstly, the radiation interacts with the molecule and polarizes the cloud of electrons without affecting the nuclear motion. Thus, the molecule is transferred to a short-lived virtual state. A photon with the same wavelength as the incident radiation is quickly re-radiated. This process is called Rayleigh scattering. Secondly, inelastic scattering induces nuclear motion and transfers energy between photons and matter. Therefore, the re-radiated photon has a different wavelength than the incident one. This process is called Raman scattering. Here, the molecule is also transferred to a short-lived virtual state. Only one in 10^6–10^8 photons is Raman scattered.[62]

If the molecule is at the lowest energy level and, therefore, the absorption leads to an excitation of the molecule, the process is called Stokes scattering. If the molecule is at an excited state and the scattering occurs from this excited state to the ground state, the process is called Anti-Stokes scattering. At room temperature, most molecules are at the lowest energy level. That is why the Anti-Stokes lines are less intense than the Stokes line in Raman spectroscopy. Besides, the intensity of the Anti-Stokes lines is affected by the temperature. In this work, only Stokes scattering is investigated.

Using a simplified picture of a ball and spring, where the atoms are the balls and the spring is the bond between the balls, helps to understand the general trend of how frequency is affected by atoms and bonds. The stronger the bond, the higher the frequency, and the heavier the atoms, the lower the frequency.

The intensities as well have a physical meaning. A significant change in the polarizability of the electron cloud leads to vigorous intensity in the Raman scattering. Because of that, modes with symmetric vibrations have higher intensities. Nevertheless, instrument parameters and, e.g., the particle size of the measured sample powder may impact the intensity as well.[62] Therefore, a quantitative analysis of the intensities is possible but needs to be done with caution. An excellent way to do this would be to use internal standards to verify accuracy.

In general, when a molecule is positioned in an electrical field $\vec{E}$, an electrical dipole moment $\vec{p}$ is induced. The induced dipole moment is directly proportional to the electrical field:

$$\vec{p} = \alpha \cdot \vec{E}.^{[63]} \tag{2.6}$$

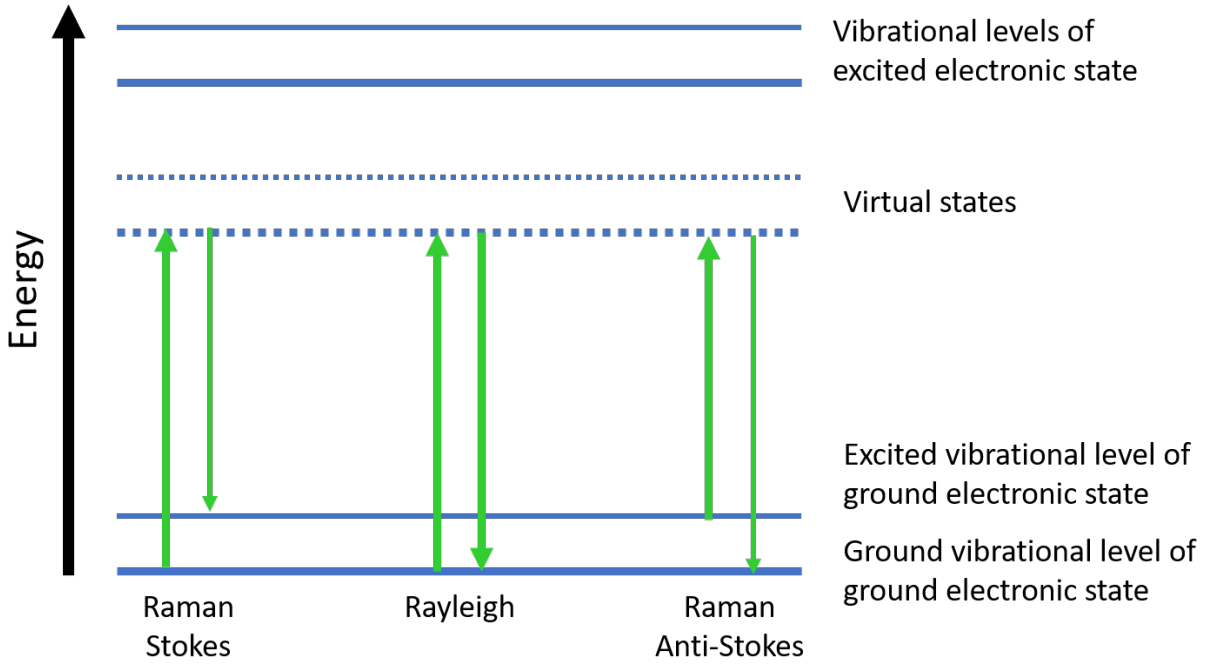

Figure 2.5.: Visualization of the Raman and the Rayleigh scattering. The energy is not for scale. Shown are the ground electronic state with one vibrational state. Clearly, there would be no energy absorption to achieve the higher electronic level. In the Rayleigh scattering, the energy of the scattered radiation (downward arrow) is equal to the incident one (upward arrow). In the Raman scattering, the energy of the scattered light differs from the incident one.

In this process, the molecule's electron cloud is distorted by an amount that depends on the ability of the electrons to polarize, denoted α. Both dipole and electric fields are vectors; thus, the polarizability is a tensor. Therefore, eq. 2.6 can be written as:

$$\begin{pmatrix} p_x \\ p_y \\ p_z \end{pmatrix} = \begin{pmatrix} \alpha_{xx} & \alpha_{xy} & \alpha_{xz} \\ \alpha_{yx} & \alpha_{yy} & \alpha_{yz} \\ \alpha_{zx} & \alpha_{zy} & \alpha_{zz} \end{pmatrix} \cdot \begin{pmatrix} E_x \\ E_y \\ E_z \end{pmatrix}. \tag{2.7}$$

Using the site symmetry of the involved atoms and group theoretical approaches leads to irreducible representations. In the irreducible presentations, the tensors are labeled with letters, e.g., $A_{g/u}$ and $B_{g/u}$. $A_{g/u}$ has a higher symmetry than $B_{g/u}$ and g and u assign if the vibration is even (g) or odd (u). For an orthorhombic perovskite ABO_3 the irreducible representations are:

- A: $2A_g + B_{1g} + 2B_{2g} + B_{3g} + A_u + 2B_{1u} + B_{2u} + 2B_{3u}$
- Mn: $3A_u + 3B_{1u} + 3B_{2u} + 3B_{3u}$
- O1: $2A_g + B_{1g} + 2B_{2g} + B_{3g} + A_u + 2B_{1u} + B_{2u} + 2B_{3u}$

- O2: $3A_g + 3B_{1g} + 3B_{2g} + 3B_{3g} + 3A_u + 3B_{1u} + 3B_{2u} + 3B_{3u}$.[64]

Since only the even modes are Raman active, this results in 24 Raman active modes, namely: $7A_g + 5B_{1g} + 7B_{2g} + 5B_{3g}$.[64] Where the individual tensors are:

$$\mathrm{A}_g = \begin{pmatrix} \alpha_{xx} & & \\ & \alpha_{yy} & \\ & & \alpha_{zz} \end{pmatrix},$$

$$\mathrm{B}_{1g} = \begin{pmatrix} & \alpha_{xy} & \\ \alpha_{yx} & & \\ & & \end{pmatrix},$$

$$\mathrm{B}_{2g} = \begin{pmatrix} & & \alpha_{xz} \\ & & \\ \alpha_{zx} & & \end{pmatrix},$$

$$\mathrm{B}_{3g} = \begin{pmatrix} & & \\ & & \alpha_{yz} \\ & \alpha_{zy} & \end{pmatrix}.$$[64]

2.4. Model of Basic Structural Distortions

Abrashev et al.[65] established a model where the orthorhombic distortion of an ideal cubic perovskite is divided into four basic structural distortions.[1] This approach facilitates the description of the distortion and, therefore, helps to interpret the results of Raman spectroscopy.

The manganese-ions do not participate in the Raman-allowed modes (Sec. 2.3, p. 11). Due to atomic site symmetries, 5 out of 12 atomic coordinates are fixed, reducing the number of degrees of freedom to 7. A new set of variables is introduced. Here, every variable is the difference between the coordinate in the ideal cubic structure and the actual coordinate. These individual distortions are then grouped in order to get the four basic structural distortions. Visualization can be found in Fig. 2.6. In the left column, the real orthorhombic distorted structure is displayed. The space group is *Pnma*. The first basic distortion $D_{[101]}$ is the tilting of the MnO_6 octahedra around the [101] cubic axis. The resulting structure is orthorhombic with space group *Imma*. The second basic distortion $D_{[010]}$ is a rotation around the [010] cubic axis. The resulting structure is tetragonal with space group *P4/mbm*.

[1] This section is based on ref.[65] .

The third basic distortion D_{JT} is a deformation of the MnO_6 octahedra based on the Jahn-Teller deformation. The resulting structure is tetragonal with space group *P4/mbm*. The fourth basic deformation $D_{A-\mathrm{shift}}$ is a shift of the A-ion along the x-direction. The resulting structure is orthorhombic with space group *Cmcm*.

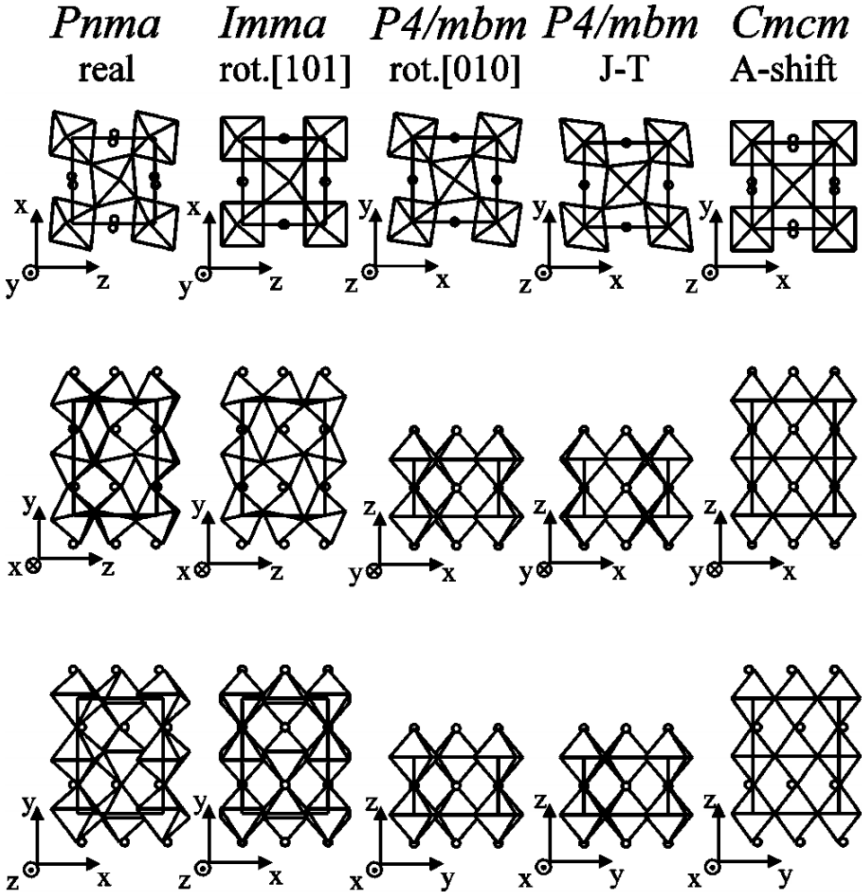

Figure 2.6.: Representation of the basic structural distortion model. Here the *Pnma* is the space group of the actual orthorhombic distorted perovskite. The other space groups represent one basic distortion each. Reprinted figure with permission from ref. [65] Copyright 2023 by the American Physical Society.

The quantification of these distortions can be approximated by measures originating from the newly introduced variables. These measures can be found in Tab. 2.2. $z_{\mathrm{O}(1)}$ is the deviation of the z-coordinate of the $\mathrm{O}_{(1)}$-ion from the cubic coordinate. $x_{\mathrm{O}(2)}/y_{\mathrm{O}(2)}/z_{\mathrm{O}(2)}$ is the deviation of the $x/y/z$-coordinate of the $\mathrm{O}_{(2)}$-ion from the cubic coordinate. x_A is the deviation of the x-coordinate of the A-ion from the cubic coordinate.

Table 2.2.: Measures for the basic distortions.[65] A real orthorhombic distorted perovskite is the superposition of these distortions. The used variables are the deviations of the coordinate from the coordinate of the cubic structure.

Distortion	Measure
$D_{[101]}$	$2\sqrt{2}\left\lvert z_{\mathrm{O}(1)}\right\rvert$ $4\sqrt{2}\left\lvert y_{\mathrm{O}(2)}\right\rvert$
$D_{[010]}$	$2\left\lvert x_{\mathrm{O}(2)} - z_{\mathrm{O}(2)}\right\rvert$
D_{JT}	$2\left\lvert x_{\mathrm{O}(2)} + z_{\mathrm{O}(2)}\right\rvert$
$D_{A-\mathrm{shift}}$	$2\mathrm{x}_A$

2.5. Thermodynamic Principles

For the application in thermochemical cycles, the thermodynamic properties of perovskites are crucial. A huge advantage of the perovskite material class is that it allows varying oxygen vacancy concentrations without major phase transitions. Herein, the vacancy concentration is governed by the temperature T and the oxygen partial pressure p_{O_2}:

$$ABO_3 \overset{T,p_{\mathrm{O}_2}}{\Longleftrightarrow} ABO_{3-\delta} + \frac{\delta}{2}\mathrm{O}_2. \tag{2.8}$$

δ denotes the oxygen non-stoichiometry. Throughout this thesis, oxygen non-stoichiometry and the abbreviation non-stoichiometry are used equally.

Any chemical reaction like the oxygen release occurs spontaneously if the Gibbs free energy is below zero. The Gibbs free energy at standard condition is:

$$\Delta g_\delta^\circ = \Delta h_\delta^\circ - T \cdot \Delta s_\delta^\circ \tag{2.9}$$

Δh_δ° : change in enthalpy

Δs_δ° : change in entropy.

The lowercase indicates that the values are per mole, and $^\circ$ indicates that they are at standard condition. The enthalpy is assumed to be independent of the oxygen partial pressure. Contrary, the entropy is dependent on the oxygen partial pressure because oxygen is a product of the reduction process:

$$\Delta s_\delta = \Delta s_\delta^\circ - \frac{1}{2}\mathrm{R}T \ln\left(\frac{p_{\mathrm{O}_2}}{p^\circ}\right) \tag{2.10}$$

$$\begin{aligned} \mathrm{R} &: \text{ideal gas constant} \\ p_{\mathrm{O}_2} &: \text{oxygen partial pressure} \\ p^\circ &: \text{standard oxygen partial pressure.} \end{aligned}$$

Combining eq. 2.9 and eq. 2.10 results into:

$$\Delta g_\delta = \Delta h_\delta^\circ - T \cdot \Delta s_\delta^\circ + \frac{1}{2}\mathrm{R}T \ln\left(\frac{p_{\mathrm{O}_2}}{p^\circ}\right).^{[66]} \tag{2.11}$$

Throughout this work, the standard oxygen partial pressure is $p^\circ = 1\,\mathrm{bar}$. The fraction $\frac{1}{2}$ arises from the fact that it is common to define Δg_δ, Δh_δ°, and Δs_δ° per mole of oxygen O and not molecular oxygen O_2.

The entropy has two different contributions: The thermal entropy, which is the entropy of the oxygen gas, and the lattice vibrational entropy, and the configuration entropy

$$\Delta s^\circ = \delta \Delta s_{\mathrm{th}}^\circ + \Delta s_{\mathrm{conf}} \tag{2.12}$$

$$\begin{aligned} \Delta s_{\mathrm{th}}^\circ &: \text{thermal entropy} \\ \Delta s_{\mathrm{conf}} &: \text{configuration entropy.} \end{aligned}$$

All configurations are assumed to have the same probability, which is also known as the dilute species assumption.[66,67] Using an analytical expression and this assumption results in a partial molar entropy Δs_δ° which includes both contributions above

$$\Delta s_\delta^\circ = \Delta s_{\mathrm{th}}^\circ + 2\gamma\mathrm{R}\left(\ln\left(0.5 - \delta\right) - \ln\left(\delta\right)\right). \tag{2.13}$$

The dimensionless parameter γ determines the number of moles that are being mixed. The parameter takes into account that defect clusters may form. In particular, if no defect clusters form, one mole of oxygen vacancy defects and two moles of reduced B-ion defects mix and thus, $\gamma = 3$. If all defects form a cluster, one mole is mixed; thus, $\gamma = 1$.[66] Combining equations 2.11, 2.12 and 2.13, gives the equation

$$\begin{aligned} \delta\left(T, p_{\mathrm{O}_2}\right) = &\frac{0.5A^{1/2\gamma}}{1 + A^{1/2\gamma}} \\ &A\left(\frac{p_{\mathrm{O}_2}}{p^\circ}\right)^{-1/2} \exp\left(\frac{\Delta s_{\mathrm{th}}}{\mathrm{R}}\right) \exp\left(\frac{-\Delta h_\delta^\circ}{\mathrm{R}T}\right). \end{aligned} \tag{2.14}$$

This is the equation of state for the non-stoichiometry depending on the temperature and oxygen partial pressure in thermal equilibrium. Here, Δh_δ° might depend not only on the non-stoichiometry but also on the temperature.[66,67] Nevertheless, a temperature dependence has yet to be observed in previous studies of $Ca_{1-x}Sr_xMnO_{3-\delta}$[66] and is therefore neglected in the following.

2.6. Fundamentals for the Kinetic Consideration

In addition to the thermodynamic properties of a material, oxidation and reduction kinetics are essential for the application. Depending on the process, either slow or fast kinetics are of interest. In general, oxidation and reduction reactions should be studied kinetically. In practice, reduction occurs at such high temperatures that it is impossible to analyze the kinetics accurately, as the reduction is completed within a few minutes. In these time scales, the change in mass is also influenced by the changing atmosphere. An oxidation process consists of several individual steps. First, the oxygen is adsorbed at the surface, and the molecule dissociates at this surface. Second, the oxygen reacts with an oxygen vacancy in a layer in proximity to the surface. Lastly, the oxygen diffuses through the bulk.[68]

Two different methods for analyzing the kinetics of a material are presented below. One is independent of a reaction model, and the other depends on a reaction model. The advantage of choosing a reaction model is that more parameters can be extracted from the experimental results. The disadvantage is that a suitable model must be found.

2.6.1. Isoconversional Method

The isoconversional method to analyze kinetics is applied following the *ICTAC Kinetics Committee recommendations for performing kinetic computations on thermal analysis data.*[69] Besides the recommendation, this method was successfully used for similar studies on perovskites.[19,20,70] The underlying assumption is that the process rates can be parametrized by the temperature T, the conversion extent X, and the pressure p:

$$\frac{\mathrm{d}X}{\mathrm{d}t} = k(T)f(X)h(p)\left[\mathrm{s}^{-1}\right]. \tag{2.15}$$

Here, the rate constant $k(T)$ is given by an Arrhenius equation:

$$k(T) = k_0 \cdot \exp\left(-\frac{E_\mathrm{A}}{\mathrm{R}T}\right)\left[\mathrm{s}^{-1}\left(\mathrm{mol\ m}^{-3}\right)^{-n}\right] \tag{2.16}$$

k_0 : pre-exponential factor

E_A : activation energy

R : gas constant

n : order of oxygen concentration dependence.

At this point, the three individual steps that make up oxidation - adsorption, oxygen vacancy reaction, and diffusion - are reiterated. With the experiments used, these individual steps cannot be separated. Therefore, the resulting activation energy is referred to as an effective activation energy.

The reaction model $f(X)$ depends on the conversion extent X. Furthermore, in this approach, the assumption is made that this is the only information known about the reaction model due to the fact that only the activation energy is to be determined. In contrast, Subsec. 2.6.2 presents an approach considering a defined model.

The pressure dependence $h(p)$ is replaced with a dependence on the oxygen concentration $h(c_{\mathrm{O}_2})$, as concentration dependence is a more conventional approach in analyzing chemical kinetics.[71] Using the ideal gas law, the oxygen concentration c_{O_2} for a fixed oxygen partial pressure p_{O_2} and varying temperatures T can be derived by:

$$c_{\mathrm{O}_2} = \frac{n_{\mathrm{O}_2}}{V_{\mathrm{O}_2}} = \frac{p_{\mathrm{O}_2}}{\mathrm{R}T} \left[\mathrm{mol\ m^{-3}}\right]. \tag{2.17}$$

Here, n_{O_2} is the molar amount of oxygen and V_{O_2} is the volume of oxygen. The dependency of the oxygen concentration is: $h(c_{\mathrm{O}_2}) = c_{\mathrm{O}_2}^n$. Now, eq. 2.15 is rewritten by inserting the determined functions.

The isoconversional principle states that the reaction rate at a constant extent of conversion is only a function of temperature.[69] The differential isoconversional method is applied by this principle, and therefore, for a fixed value of conversion extent X, all functions are inserted into eq. 2.15, this is reformulated, and a logarithm is taken on both sides. This gives:

$$\log\left({c_{\mathrm{O}_2}}^{-n}\left(\frac{\mathrm{d}X}{\mathrm{d}t}\right)_{X=\mathrm{const.}}\right) = -\frac{E_\mathrm{A}}{\mathrm{R}T} + \log\left(k_0 f(X)_{X=\mathrm{const.}}\right). \tag{2.18}$$

A logarithmic plot of ${c_{\mathrm{O}_2}}^{-n}\left(\frac{\mathrm{d}X}{\mathrm{d}t}\right)_{X=\mathrm{const.}}$ vs. $\frac{10^3}{\mathrm{R}T}$ results in a line which can be fitted giving the activation energy as the slope (details in Sec. 3.7, p. 41).

2.6.2. Kinetic Model

In contrast to the isoconversional method, the model fitting method indeed assumes that a specific reaction model exists. It represents the dependence of the conversion extent on the reaction rate.[69] Earlier kinetic measurements on $\mathrm{CaMnO}_{3-\delta}$ and $\mathrm{Ca_{0.8}Sr_{0.2}MnO}_{3-\delta}$[66]

are analyzed, following the recommendation of the *ICTAC Kinetics Committee* to identify a suitable reaction model. They are displayed in Fig. 2.7.

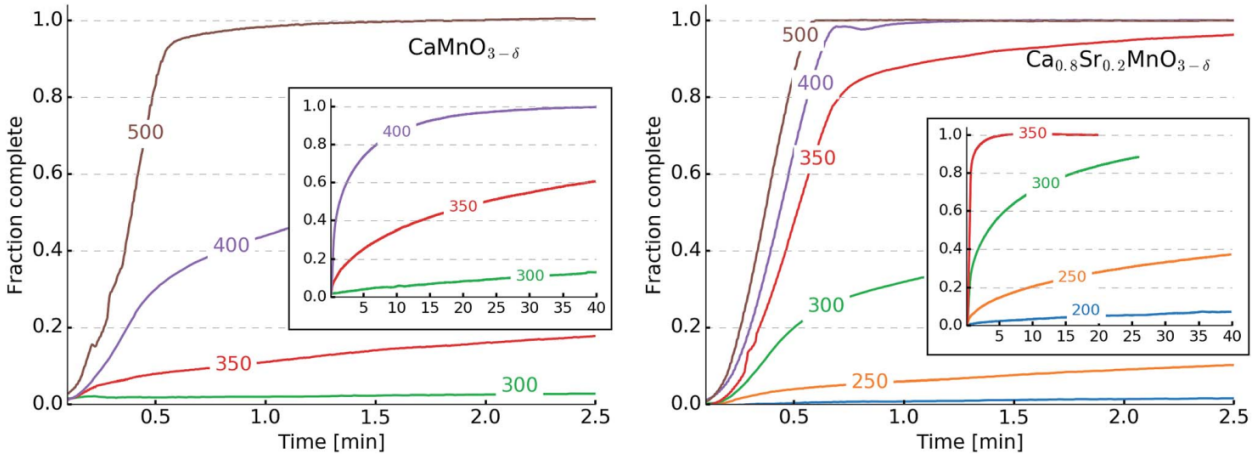

Figure 2.7.: Oxidation kinetics of $CaMnO_{3-\delta}$ and $Ca_{0.8}Sr_{0.2}MnO_{3-\delta}$ by *Bulfin et al.*. Reproduced from ref.[51] with permission from The Royal Society of Chemistry. They are used to identify a suitable reaction model. The curve exhibits no inflection point and represents a slowed-down process.

The earlier study shows no inflection points in the oxidation curve. Therefore, it is concluded that the process either depends on only one step or that one step is the limiting step so that the following steps are not recognizable. Additionally, the oxidation curves show that it is a decelerated process. The results of the isoconversional method show that the activation energy is not highly dependent on the extent of conversion. These observations result in the reaction model:

$$f(X) = (1 - X)^{\beta} \tag{2.19}$$

where β is the reaction order. Applying this reaction model to eq. 2.15 and using the aforementioned expressions for the other dependence, gives the rate equation:

$$\begin{gathered} \frac{\mathrm{d}X}{\mathrm{d}t} = \left(\frac{\mathrm{d}X}{\mathrm{d}t}\right)_{t=0} (1 - X)^{\beta} \\ \text{and} \\ \left(\frac{\mathrm{d}X}{\mathrm{d}t}\right)_{t=0} = {c_{\mathrm{O_2}}}^{n} k_0 \exp\left(-\frac{E_{\mathrm{A}}}{\mathrm{R}T}\right). \end{gathered} \tag{2.20}$$

Taking the logarithm of both sides of the equation gives:

$$\log\left(\frac{\mathrm{d}X}{\mathrm{d}t}\right) = \beta \log(1 - X) + \log\left(\left(\frac{\mathrm{d}X}{\mathrm{d}t}\right)_{t=0}\right). \tag{2.21}$$

A log-log plot of $\frac{\mathrm{d}X}{\mathrm{d}t}$ vs. $1-X$ is linear with a slope of β and an intercept of $\log\left(\left(\frac{\mathrm{d}X}{\mathrm{d}t}\right)_{t=0}\right)$. Each temperature is initially fit linearly to determine β. The average value of these individual values is taken to get a material specific β. This is used to fit the whole dataset for one material.

After fixing the reaction order, the entire data set $\frac{\mathrm{d}X}{\mathrm{d}t}$ vs. $1-X$ is fitted to get the intercepts $\left(\frac{\mathrm{d}X}{\mathrm{d}t}\right)_{t=0}$. With an Arrhenius plot based on eq. 2.20, the activation energy and the pre-exponential factor k_0 are extracted (details in Sec. 3.7, p. 41).

2.7. Introducing $CaMnO_{3-\delta}$

After setting the relevant theoretical background for analyzing important properties of perovskites for thermochemical cycles, this section introduces a suitable material for the application. $CaMnO_{3-\delta}$ has been studied for oxygen partial pressure adjustment like oxygen pumping and air separation.[21,32,66] They exhibit proper thermodynamic and kinetic properties.[66] Moreover, it is a promising material since it is non-toxic, abundant, and cheap.[72]

A disadvantage of $CaMnO_{3-\delta}$ is the decomposition to $CaMn_2O_4$ and Ca_2MnO_4 when applied to low oxygen partial pressure and high temperatures.[73] This decomposition is unfavorable for the air separation process because, on the one hand, this decomposition can generate stress in the material. The stress can lead to the instability of macroscopic structures. On the other hand, the decomposition products cannot be oxidized under the prevailing conditions,[66] so this part of the material is no longer available for the redox process. The decomposition can be reversed at high temperatures and high oxygen partial pressures.[66] *Bulfin et al.*[66] proofed that a 20 % substitution of Ca^{2+} by Sr^{2+} avoided the decomposition. Moreover, it was qualitatively shown that this Sr-substitution led to a decreased change in reduction enthalpy and an improved oxidation kinetics.[28,66] Nevertheless, the impact of the Sr content over a broader range and the underlying mechanisms have not yet been discussed.

The crystal structure of $CaMnO_3$ is characterized, in part, by the space group. The space group describes the symmetry of a crystal pattern. The Schönflies symbol of the space group of $CaMnO_3$ is D_{2h}^{16}. D_{2h} describes that a 2-fold vertical rotation axis is accompanied by two symmetry-equivalent horizontal twofold rotation axes and a horizontal symmetry plane.[74] Since the Schönflies notation only directly addresses the crystal class, the different space groups are differentiated by a superscript. Here, the superscript is 16; thus, the Schönflies symbol displays the space-group symmetry only partly.

A more detailed description is embedded in the Hermann-Mauguin symbol. The complete Hermann-Mauguin symbol is often abbreviated by the short Hermann-Mauguin symbol. The abbreviation omits some symmetry information but is more handy in everyday use. For

$CaMnO_3$, the complete Hermann-Mauguin symbol is $P2_1/n2_1/m2_1/a$, and the short symbol is $Pnma$. The full Hermann-Mauguin symbol is explained in the following to understand the symmetry of the crystal. Later in this thesis, only the short version will be used.

The first constituent always identifies the conventional cell of the translation lattice of the space group.[74] P characterizes a primitive lattice. The slash indicates that the corresponding lattice vector has two symmetry operations.[74] For an orthorhombic crystal, the directions of the basis vectors are symmetry independent. Therefore, there are all representative and mark a symmetry direction. 2_1 identifies a screw ax. n identifies a sliding mirror plane with translation along half a surface diagonal. m identifies a mirror plane, and a identifies a sliding mirror plane with translation along half a lattice vector $\vec{a}$.

$CaMnO_{3-\delta}$-based compositions are not only used for oxygen partial pressure adjusting applications but also for other thermochemical processes, such as thermochemical heat storage,[28,29] chemical looping combustion[75] and chemical looping partial oxidation of methane.[76] Besides the application of $CaMnO_{3-\delta}$ in thermochemical processes, researchers have as well investigated $CaMnO_{3-\delta}$ for thermoelectric applications[77] and as an electrocatalyst for rechargeable batteries.[78] This demonstrates that this material is relevant for many types of applications.

2.8. Thermochemical Process for the Production of Ammonia

One example of applying a thermochemical cycle is the production of feedstock for ammonia. As mentioned previously, ammonia is a vital chemical commodity. Thus, to decarbonize the industry, the production of it needs to be fossil-free as well. *MacFarlane et al.*[17] divided the transition to fossil-free ammonia into three 'Generations'. The project *SESAM*[2] focuses on the 2. Generation, namely the fossil-free production of the feedstock nitrogen.

As presented above, this is possible by a thermochemical process where the heat is provided by concentrated solar radiation. Still, earlier work showed that pre-purifying the air reduces the energy requirement.[18] Therefore, in the project *SESAM* the air is pre-purified. The complete process is summarized in Fig. 2.8.

The process starts with the pre-purification of the air by pressure swing adsorption (PSA). The gas with a residual oxygen content of about 1 % enters a solar thermochemical cycle. This cycle produces pure oxygen during reduction and nitrogen with an oxygen concentration of less than 10 ppm during oxidation. This low oxygen concentration is essential not to poison the catalyst in the Haber-Bosch process. The ammonia produced in the Haber-Bosch process

[2]Project identification number: EFRE-0801808

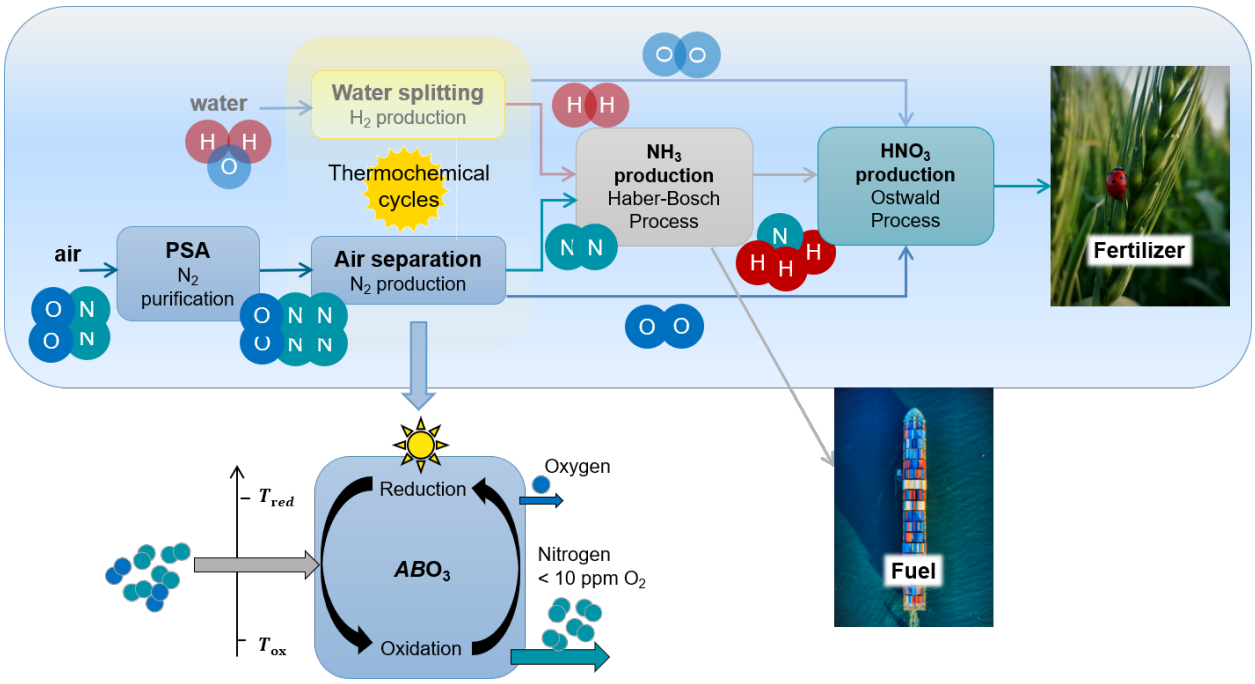

Figure 2.8.: Overview over the fertilizer production process applied in the project *SESAM*. It starts with the pre-purification of air with pressure swing adsorption (PSA). It is followed by a thermochemical cycle which reduces the oxygen content in the nitrogen stream to the ppm level. The final product is either ammonia or fertilizer.

can either be used directly as a fuel, e.g., in maritime applications, or further processed into fertilizer.

A recently published work underlines the energetic advantage of this combined PSA-thermochemical system compared to purification via a PSA alone.[19] This enables the high-purity production of nitrogen on a medium scale.

2.9. Thermodynamic-based Energy Calculations

The thermodynamic-based energy calculations are performed for the system presented above, where a PSA and a thermochemical cycle are combined. In order to perform a thermodynamic energy calculation, some values must first be specified, namely the amount of redox material m_{redox}, the purity of the final product $p_{\mathrm{O_2,product}}$, the inlet oxygen partial pressure $p_{\mathrm{O_2,inlet}}$ and the efficiencies for gas heat exchanger η_{gas}:

$$m_{\text{redox}} = 5\,\text{kg}$$
$$p_{\text{O}_2,\text{product}} = 10 \times 10^{-6}\,\text{bar}$$
$$p_{\text{O}_2,\text{inlet}} = 0.01\,\text{bar}$$
$$\eta_{\text{gas}} = 0.8.\,[19]$$

The choice of m_{redox} is based on a lab-scale reactor design. $p_{\text{O}_2,\text{product}}$ is selected since it is an oxygen impurity fraction which is applicable in the Haber-Bosch-Process.[79] $p_{\text{O}_2,\text{inlet}}$ results from earlier packed-bed experiments.[18] Gas stream pre-purification is assumed to be performed by PSA.

As presented in Sec. 2.5 on p. 15, the perovskite material class permits varying oxygen vacancy concentrations (eq. 2.8, p. 15). Therefore, it is used to remove the oxygen from the inlet gas stream to produce highly pure nitrogen. First, the amount of purified gas must be calculated to compute the energetic contributions to produce the product gas. This is done by calculating the equilibrium non-stoichiometry δ for the oxidized δ_{ox} and the reduced δ_{red} state according to eq. 2.14 on p. 16. The required material-dependent properties are extracted from thermodynamic calculations and are displayed in Tab. A.6 on p. 149.

Besides the here presented and analyzed material $\text{Ca}_{1-x}\text{Sr}_x\text{MnO}_{3-\delta}$, $\text{SrFeO}_{3-\delta}$ is also a material recently studied for air separation. The advantage of $\text{SrFeO}_{3-\delta}$ compared to $\text{Ca}_{1-x}\text{Sr}_x\text{MnO}_{3-\delta}$ is that it requires lower temperatures to be reduced, which comes with a lower oxygen affinity.

Fig. 2.9 displays the equilibrium non-stoichiometries for both $\text{Ca}_{1-x}\text{Sr}_x\text{MnO}_{3-\delta}$ and $\text{SrFeO}_{3-\delta}$. Only the extreme total pressures of the oxidation and reduction and the ambient pressure for reference are shown. If the total pressure is equal to or greater than 1, the oxygen molar fraction is $x_{\text{O}_2} = 0.01$, and for vacuum, the oxygen molar fraction is $x_{\text{O}_2} = 1$. Eq. 2.14 on p. 16 is used for $\text{Ca}_{1-x}\text{Sr}_x\text{MnO}_{3-\delta}$. *Bulfin et al.* developed an empirical model with a better agreement between experiment and calculated values for $\text{SrFeO}_{3-\delta}$.[19] Naturally, this model is used for $\text{SrFeO}_{3-\delta}$. Still, the model is only valid up to 1100 K for low oxygen partial pressures and, therefore, only used and displayed up to this threshold. For the sake of clarity, the study focuses on the two extreme cases with $x = 0$ and $x = 0.4$ in $\text{Ca}_{1-x}\text{Sr}_x\text{MnO}_{3-\delta}$. $x = 0.4$ arises from the solubility limit.[80,81]

The change in non-stoichiometry $\Delta\delta = \delta_{\text{red}} - \delta_{\text{ox}}$ is correlated to the amount of oxygen absorbed n_{O_2} during oxidation by the molar amount of redox material n_{redox}:

$$n_{\text{O}_2} = n_{\text{redox}} \cdot \frac{\Delta\delta}{2}. \tag{2.22}$$

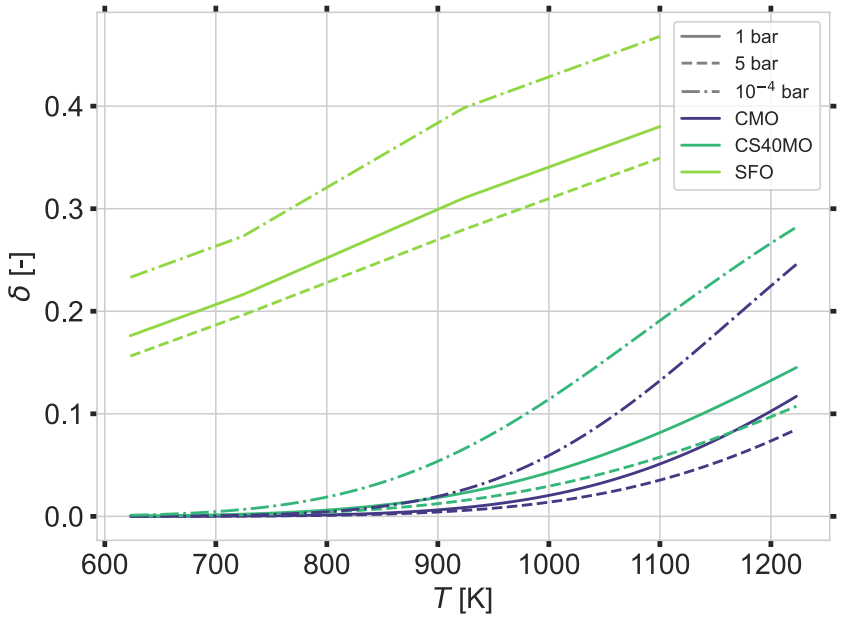

Figure 2.9.: Equilibrium δ-values dependent on temperature and total pressure (linestyle) calculated with eq. 2.14 on p. 16 for $Ca_{1-x}Sr_xMnO_{3-\delta}$ and with an empirical model[19] for $SrFeO_{3-\delta}$ (color code). Adapted from *Klaas et al.*[82] with permission from the Royal Society of Chemistry.

The factor $\frac{1}{2}$ results from the fact that the quantity of oxygen molecules O_2 is of interest. The volume of the absorbed oxygen V_{O_2} is calculated from this molar amount by applying the ideal gas law. All volumes mentioned in this thesis are specified at norm conditions, such that $T = 273\,\mathrm{K}$ and $p = 1\,\mathrm{bar}$, if not otherwise stated. Since the inlet oxygen partial pressure $p_{O_2,\mathrm{inlet}}$, the product oxygen partial pressure $p_{O_2,\mathrm{product}}$ and the volume of the absorbed oxygen V_{O_2} are known, the amount of the inlet gas V_{in} is computed through a mass balance:

$$V_{\mathrm{in}} = V_{O_2} \cdot \frac{1 - p_{O_2,\mathrm{product}}}{p_{O_2,\mathrm{inlet}} - p_{O_2,\mathrm{product}}}. \tag{2.23}$$

The volume of the product gas is then easily determined by subtracting the volumes of inlet gas and oxygen absorbed.

The total energy Q_{tot} required for air separation by the thermochemical cycle is composed of several contributions:

$$Q_{\mathrm{tot}} = Q_{\mathrm{sens}} + Q_{\mathrm{chem}} + W_{\mathrm{pump}} + Q_{\mathrm{gas}}. \tag{2.24}$$

Each of them will be presented in the following. Any losses are neglected in this analysis because they depend on the heat losses of the reactor design and the operating parameters. For the same reason, the energy required to heat and cool the reactor shell is not considered. In the first analysis, the focus lies solely on the thermochemical cycle and the impact of the

different materials. Therefore, the work to compress the gas is ignored since the gas coming from the PSA is already pressurized to typically 7–10 bar. Moreover, the energy demand of the PSA is neglected.

In the parametric study of one selected material, the work of the PSA is indeed included since here as well, the oxygen inlet purity is varied. The energy demand of a PSA for the production of one mole nitrogen with an oxygen impurity mole fraction x_{O_2} is defined by:

$$W_{\mathrm{PSA}}\left(x_{O_2}\right) = \frac{W_{\mathrm{comp}}}{x_{N_2,\mathrm{air}} \cdot \eta_{\mathrm{PSA-recov}}\left(x_{O_2}\right)}.^{[20]} \tag{2.25}$$

$x_{N_2,\mathrm{air}}$ denotes the nitrogen mole fraction in air and $\eta_{\mathrm{PSA-recov}}$ denotes the nitrogen recovery fraction.[20] The energy to compress gas W_{comp} is calculated with an adiabatic compression in a single-stage compressor with an efficiency of 84 % and the adiabatic compression work $W_{\mathrm{adiabatic}}$ is computed using the thermodynamic software cantera:[83]

$$W_{\mathrm{Comp}} = \frac{W_{\mathrm{adiabatic}}}{0.84}.^{[20]} \tag{2.26}$$

The sensible energy Q_{sens} is the sensible heat stored in the material for the temperature swing ΔT:

$$Q_{\mathrm{sens}} = c_p \cdot n_{\mathrm{redox}} \cdot \Delta T. \tag{2.27}$$

The heat capacity c_p is approximated by the high-temperature limit of the Debye approximation.[84] Fig. 2.10 displays the Debye approximation for the oxidized Perovskite $CaMnO_3$ and the reduced Brownmillerite $Ca_2Mn_2O_5$ with $c_V = c_p$. The assumption of the specific heat capacity is reasonable because only solid oxides are used. The required Debye temperature is calculated from the elastic tensor with data available from *The Materials Project*.[23,34] In addition, the high-temperature limit of both phases is presented. From this presentation, the high-temperature approximation is reasonable in the present application since the applied temperatures are sufficiently high. Moreover, this approximation only overestimates the required energies.

The energy required to reduce the material is given by

$$Q_{\mathrm{chem}} = \Delta h_\delta^\circ \cdot \Delta\delta \cdot n_{\mathrm{redox}}. \tag{2.28}$$

The aforementioned partial molar change in enthalpy at standard pressure is Δh_δ°. The energy required to reduce the material is equivalent to the energy released during oxidation in case of air separation. For this reason, a solid-solid heat recuperation can be applied, but since this is technically difficult to implement, it is not implemented in the current analysis.

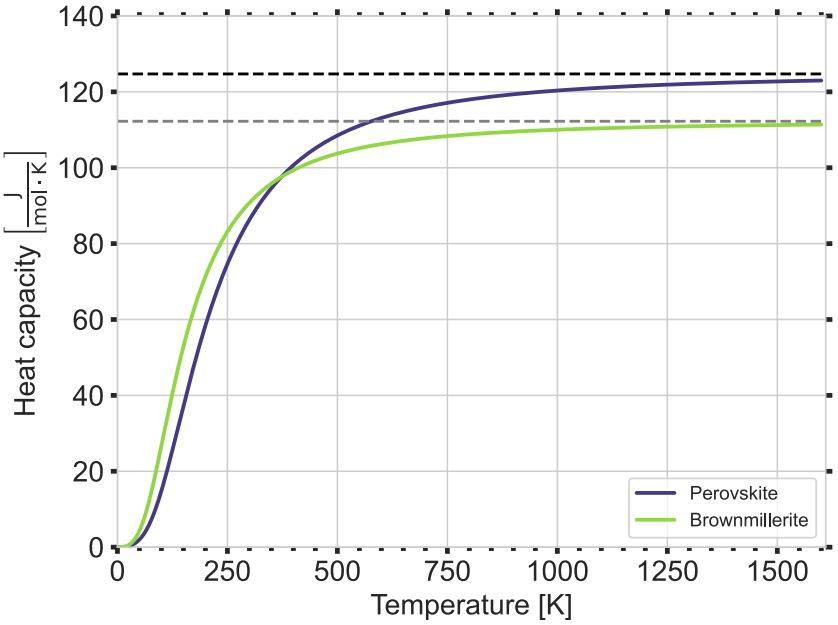

Figure 2.10.: Heat capacity of $CaMnO_3$ and the concerning Brownmillerite $Ca_2Mn_2O_5$ calculated by the Debye model. The dashed line indicates the high-temperature limit of the Debye model for Brownmillerite (grey) and Perovskite (black).

The energy to pump the gases W_{pump} consists of two contributions, namely the energy required to pump the gas during reduction $W_{\text{pump,red}}$ and during oxidation $W_{\text{pump,ox}}$. An isothermal approximation for an ideal gas calculates the required work during oxidation:

$$W_{\text{pump,ox}} = -\int_1^2 V \mathrm{d}p = p_1 V_1 \cdot \ln \frac{p_2}{p_1}. \tag{2.29}$$

This is the baseline of the minimal pumping work. Since the pumps are not part of this study and are not further defined, this simplification was applied. The volume V_1 equals $V_{\text{in}}(T = T_{\text{ox}})$, p_1 equals the total pressure during oxidation $p_{\text{tot,ox}}$ and p_2 equals the change of the total pressure due to the pressure drop Δp within the reactor.

The pressure drop Δp during oxidation at 1–5 bar and reduction at 1 bar is calculated based on the Ergun equation.[85] The necessary input values are based on an existing reactor design and are listed in the following:

- length of the packed bed ΔL : 500 mm
- fluid velocity in the empty pipe ν : 0.422 m/s
- porosity of the filling ψ : 0.4
- Sauter particle diameter d : 1.5 mm

The temperature and pressure-dependent dynamic viscosity and fluid density are based on the material properties of air and extracted from.[86] The resulting pressure drop Δp is listed in table 2.3.

Table 2.3.: Pressure drop Δp in bar. Calculated by the Ergun equation[85] for the applied temperatures and pressures during oxidation and reduction.

		Temperature [K]					
		623	873	973	1023	1173	1223
pressure [bar]	1	0.0143	0.0248	0.0295	0.0319	0.0395	0.0423
	2	0.0073		0.0145	0.0155		
	3	0.0049		0.0096	0.0103		
	4	0.0037		0.0072	0.0077		
	5	0.0030		0.0057	0.0060		

The work necessary to pump the gas during reduction at $p_{\mathrm{red}} = 1\,\mathrm{bar}$ is calculated with eq. 2.29 as well. In order to remove the released oxygen, a purge gas with a gas flow of $1\,\mathrm{Nm^3/h}$ for 30 min is assumed. Besides the purge gas, the released volume of oxygen is pumped. For reduction pressures lower than 1 bar, an empirical approach by *Brendelberger et al.*[87] is used. This model is valid in the range of 0.7–10^{-6} bar. Here, only the volume of the released gas is pumped.

The energy required to heat the gas consists of the contribution of heating the gas during reduction and oxidation. Here, heat recovery with an efficiency of η_{gas} is implemented. The energy required to heat the gas during oxidation or reduction is calculated by:

$$Q_{\mathrm{gas}} = Q(T_{\mathrm{ox/red}}) \cdot n_{\mathrm{in,ox/red}} - \eta_{\mathrm{gas}} \cdot Q(T_{\mathrm{ox/red}}) \cdot n_{\mathrm{out,ox/red}}, \tag{2.30}$$

where $n_{\mathrm{in,ox/red}}$ is the inlet molar amount of gas and $n_{\mathrm{out,ox/red}}$ is the outlet molar amount of gas. The molar heat $Q(T_{\mathrm{ox/red}})$ is given by:

$$Q(T_{\mathrm{ox/red}}) = \int_{T_1}^{T_2} c_p(T)\mathrm{d}T. \tag{2.31}$$

The heat capacity $c_p(T)$ is calculated based on the values of nitrogen and oxygen from the *NIST Chemistry WebBook*.[88] As nitrogen and oxygen have similar heat capacities with a maximal difference of 6 % in the relevant temperature regime and to reduce the complexity of the calculation, the gas is postulated to always consist of 1 % O_2 and 99 % N_2.

3. Experimental Methods

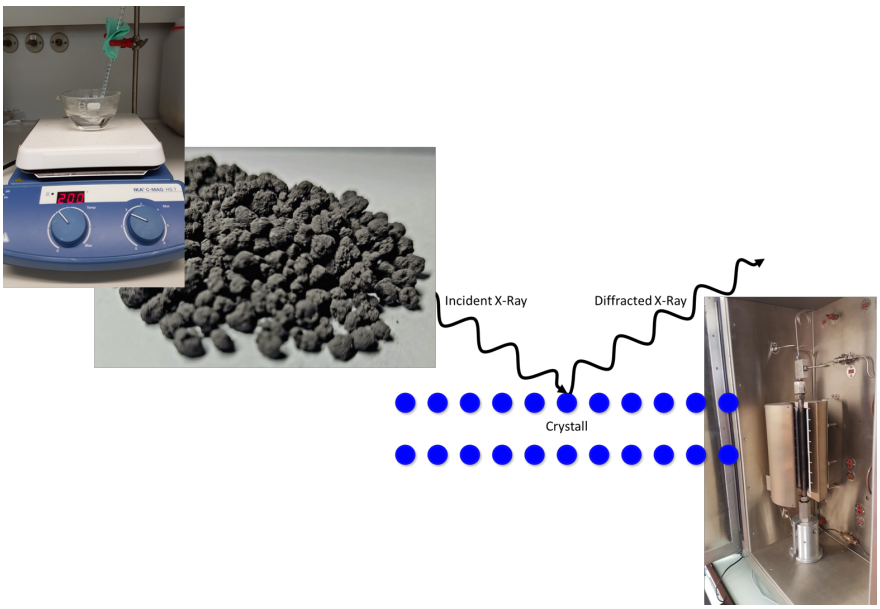

Figure 3.1.: Illustrative representation of some experimental methods used. From top left to bottom right: Some samples were synthesized by the auto-combustion method. In addition to the analysis of powders, macrostructures such as granules were studied. The analytical methods utilized ranged from analysis of the crystal structure by X-ray diffraction to application of the material in a small-scale test reactor.

This chapter is partially based on the following peer-reviewed publications, which are authored by the author of this thesis:

L. Klaas, M. Pein, P. Mechnich, A. Francke, D. Giasafaki, D. Kriechbaumer, Ch. Agrafiotis, M. Roeb, and Ch. Sattler. Controlling thermal expansion and phase transitions in $Ca_{1-x}Sr_xMnO_{3-\delta}$ by Sr content. Physical chemistry chemical physics: PCCP, 24(45):27976-27988, 2022. doi: 10.1039/D2CP04332G.

L. Klaas, B. Bulfin, D. Kriechbaumer, M. Roeb and Ch. Sattler. Impact of the Sr content on the redox thermodynamics and kinetics of $Ca_{1-x}Sr_xMnO_{3-\delta}$ tailored properties. Physical chemistry chemical physics: PCCP, 25(13):9188-9197, 2023. doi: 10.1039/D3CP00267E.

L. Klaas, B. Bulfin, D. Kriechbaumer, N. Neumann, M. Roeb and Ch. Sattler. Energetic optimization of thermochemical air separation for the production of sustainable nitrogen. Reaction Chemistry & Engineering, 8(8):1843-1854, 2023. doi: 10.1039/D3RE00087G.

This chapter presents the experimental methods used. At the beginning, the synthesis of the perovskites and the production methods of the macrostructures are described. Then, the crystallographic analysis method and Raman spectroscopy are presented. Then the thermodynamic analysis methods, microstructure analysis and kinetic analysis are introduced. The chapter concludes with the details of the fixed bed reactor experiments.

3.1. Synthesis of Perovskites

$Ca_{1-x}Sr_xMnO_3$ is prepared by two different methods - the sol-gel auto-combustion method and the solid-state method because each method has advantages and disadvantages regarding scalability and expected purity. Therefore, the individual synthesis route was selected for each study, which is explained in more detail below.

3.1.1. Sol-gel Auto-combustion Method

The auto-combustion method is established to produce perovskites with different compositions.[89–92] It is a variant of the sol-gel method.[92] An advantage of this method is the mixing at an atomic level. A disadvantage is that a maximal quantity of several 100 mg can be produced with the available laboratory equipment. Still, it was used when only small quantities were necessary.

Fig. 3.2 shows a visualization of the different steps. First, 0.1 M aqueous solutions of calcium(II) nitrate (*Alfa Aesar*), strontium(II) nitrate (*Alfa Aesar*), and manganese(II) nitrate (*Acros Organics*) were mixed according to the desired stoichiometries in order to get 500 mg perovskite (quantities in Sec. A.1, p. 133). Additionally, 10 ml of 1.0 M citric acid (*Merck*) was added to have an excess compared to the nitrates. Under constant stirring with a magnetic stirrer, the solution is heated below boiling temperature around 353 K in a glass beaker to evaporate the water (a). The stirrer was removed immediately after a gel was formed (b), and the glass beaker was partially covered with a lid to restrict the oxygen supply. The temperature was increased to 573–773 K to decrease the humidity further and to initiate auto-combustion (c). Due to the release of gases, the volume of the solid expands, and a sponge-like product results. After the auto-combustion, the sponge-like product was pulverized in an agate mortar, and the resulting powder was transferred to an alumina crucible (d). The final calcination was done in a *RHF1400, Carbolite* muffle furnace. The powder was heated two times at 1073 K for 10 h with intermediate cooling to room temperature. The heating and cooling rates were 2 K/min. Subsequently, the powder was heated at 1573 K for 20 h with a heating and cooling rate of 5 K/min. The whole process occurred under air. As the sample was sintered during the temperature treatment, the final product was ground by hand in an agate mortar to obtain powder (e).

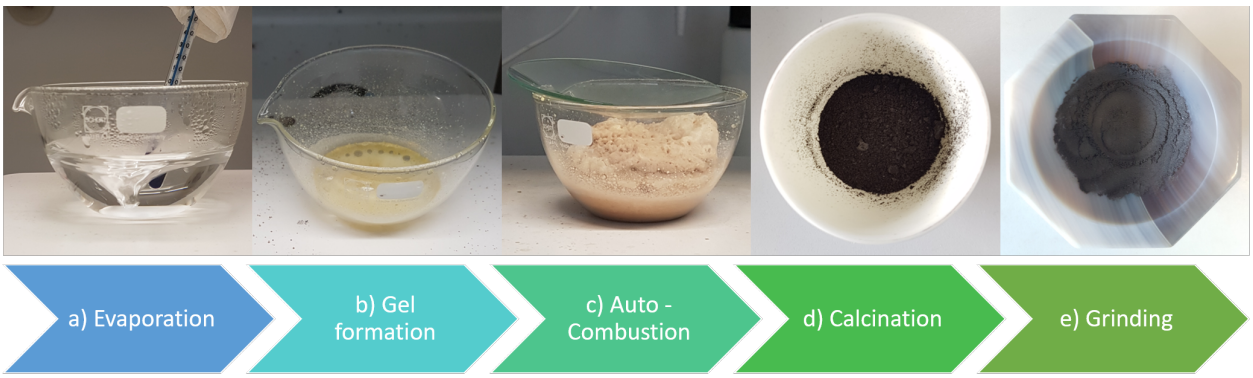

Figure 3.2.: The different steps of the auto-combustion method. Starting from the mixing of the solutions and the evaporation (a) and ending at the grinding of the final powder (b).

3.1.2. Solid-state Method

The solid-state method was mainly used when larger quantities of the material were required, e.g., to produce macroscopic structures.

The required mass according to the desired final stoichiometry of the precursors $CaCO_3$ (*Merck*), $SrCO_3$ (*VWR International GmbH*) and Mn_3O_4 (*ERACHEM*) with purities higher than 98 % were weighted. The materials were first wet-mixed to ensure high phase purity, to prevent the formation of side phases, and to reproduce the result. This wet-mixing facilitates the homogenization of the feedstocks. Therefore, $SrCO_3$ was dispersed in isopropanol and constantly stirred with a stirring rod at 333 K. When the powder was agglutinated, it was further refined by sieving it into the isopropanol. After 15 min of mixing, $CaCO_3$ and Mn_3O_4 were added and constantly mixed for 24 h. The relation between powder and isopropanol was 1:2 wt-ratio. This ratio is maintained until the end of the process, i.e., more isopropanol is added when the suspension becomes thicker due to evaporation.

The dispersion was filtered and afterward dried first at room temperature for 24 h and then at 353 K for 24 h. The dried powder was heated in an alumina crucible for 48 h at 1473 K in the air in the same *Carbolite* muffle furnace. The heating and cooling rate was 5 K/min. As the powder was sintered during the temperature treatment, the final product was ground by hand in an agate mortar to obtain powder again.

3.2. Production Methods of Macrostructures

To conduct various experimental studies on $Ca_{1-x}Sr_xMnO_{3-\delta}$, powders and macrostructures are examined. The term 'macrostructure' defines whether the material is granule, foam, or pellet. Macrostructures can be better utilized in the application since they are easier to handle than powder. In addition, they can prevent the formation of preferential flow tunnels through which gas can flow with less interaction with the material. The same powder

prepared by the solid-state method was used to produce all macrostructures with identical Sr content.

3.2.1. Production Method of Granules

Figure 3.3.: Representative image of a granule.

A wet granulation method[93] was used for the production of granules. Fig. 3.3 displays a representative image of the resulting granule. This process has been successfully used in earlier work.[18] The required powder was prepared by the solid-state method.

For the preparation of granules, 77 wt% perovskite powder were mixed with 23 wt% microcrystalline cellulose (*Serva, d*=0.05 mm) as a binder in an *Eirich EL1* mixing system. These powders were homogeneously mixed. Subsequently, H_2O was added at about 50 wt% of the solid mass with continuous stirring until granules were formed. The formation of granules was visually observed.

The resulting granules were dried under atmospheric conditions and sintered in the aforementioned *Carbolite* furnace. The heating rate was 1 K/min. To first decompose the organic material and to avoid rapid gas formation, the granules were heated to 553 K, then to 773 K and held for 2 h at both temperatures. Afterward, to sinter the granules, they were heated to 1573 K for 24 h. The cooling rate to room temperature was 2 K/min.

3.2.2. Production Method of Foams

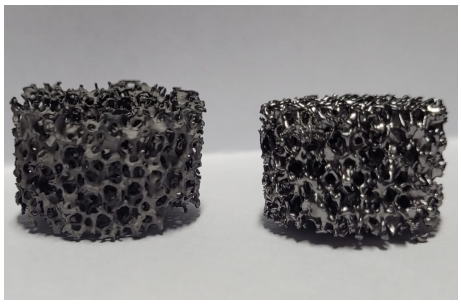

Figure 3.4.: Image of foams produced via two routes. The dull foam (left) was produced with a magnetic stirrer and the glossy foam (right) with a ball mill.

The polyurethane (PU) foam replica method[94] was used to manufacture the foams, as $CaMnO_3$ foams have been successfully produced using this method in previous work.[95] This approach requires a fine particle size of redox powder with a diameter of $d \leq 10\,\mu m$ to form stable slurries that do not sediment and develop free fluid under gravity. Fig. 3.4 displays a representative image of foams produced via two variations of this approach.

To get fine powder, the powder of $Ca_{0.8}Sr_{0.2}MnO_3$ prepared through the solid-state method was further ground in a planetary ball mill (*Pulverisette 6, FRITSCH GmbH Milling and Sizing*) with zirconia spheres with a diameter of 1 mm for 30 min to reduce the particle size to $d \approx 10\,\mu m$. After grinding, water was added to the powder in a 5:1 powder:water ratio. A dispersant (*DOLAPIX CE 64, Zschimmer*

& Schwarz) of 0.84 wt% of the solid load was added to the mixture, and the mixture was then blended for 3 h at a rotation speed of 450 rpm. Foams whose suspension has undergone this treatment are referred to as Foam_{BM}. In one variant of the manufacturing process, this homogenization was carried out with a magnetic stirrer. Foams whose suspension has undergone this treatment are referred to as Foam_{MS}. The following steps were identical in both methods. Afterward, the suspension and mixing balls were separated using a sieve into a beaker. To the suspension 1.5 wt% of solid binder (*Optapix PA 4 G, Zschimmer& Schwarz*) were added. The mixture was heated to 353 K for 2 h with constant stirring and subsequently cooled for 1 h, also under continuous stirring. The PU foams (*Regicell 30, FoamPartner GmbH*) were then immersed into the suspension, and the excess suspension was removed using a two-plate squeezing machine. The coated foams were air dried for 24 h. The air-dried foams were transferred to a muffle furnace (*L40/11-BO, Nabertherm*) for debinding and pre-sintering. The heating and cooling rates were 2 K/min. They were first heated to 353 K for 2 h in order to remove any residual humidity. They were then heated to 553 K for 1 h, then to 773 K for 1 h and finally to 1623 K for 2 h. Afterward, the foams were cooled to room temperature and transferred to the *Carbolite* muffle furnace for the final sintering at 1623 K for 2 h. The heating and cooling rates were 5 K/min. Foams with different pore densities ranging from 20–60 ppi were manufactured (Fig. 3.5). All samples have a diameter of 20.7 mm and a height of $h \approx 14$ mm. The mass for the sample with 20 ppi is 4.46 g, with 30 ppi is 5.25 g and with 60 ppi is 8.01 g.

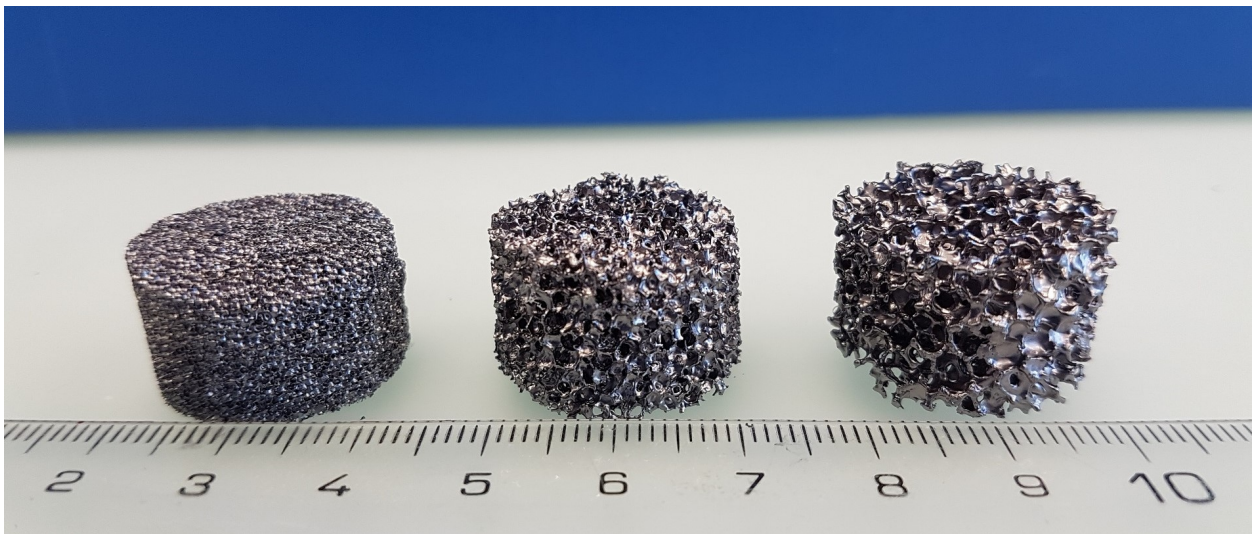

Figure 3.5.: Foams with different pore densities, starting from the left with 60 ppi, followed by 30 ppi to 20 ppi on the right.

3.2.3. Production Method of Pellets

The pellets were produced using a *Perkin-Elmer* hydraulic press. Therefore, the required amount of perovskite powder of $Ca_{0.8}Sr_{0.2}MnO_3$ prepared through the solid-state method was weighted and then inserted into a pressure mold. The masses were 2.25 g and 1.25 g. A total load of 4×10^4 N was applied to the pressing die. The resulting green bodies were sintered in the same *Carbolite* furnace at 1623 K for 20 h. The heating and cooling rate was 5 K/min. The resulting pellets have a diameter of 15 mm. Fig. 3.6 displays a representative image of the pellets.

Figure 3.6.: Image of pellets with height of 0.5 mm (left) and 0.25 mm (right).

The used powder was either coarser powder which was manually ground, and then the pellet is referred to $Pellet_M$, or finer powder which was ground in the aforementioned planetary ball mill with zirconia spheres for 30 min at 450 rpm with a ball to powder ratio of 2:1, then the pellet is referred to $Pellet_{BM}$. Two different sizes of a pellet made out of fine powder were manufactured, with one sample having a height of 0.25 mm and one sample having a height of 0.5 mm.

3.3. Crystallographic Structure Analysis Methods

The crystallographic structure of the samples was analyzed via powder X-ray diffraction (XRD) using a *D8-Advance (A25)* instrument from *Bruker* with either a copper or a cobalt anode. The detector for both setups was a *Lynxeye XE-T* from *Bruker*. The samples were prepared on Si single crystal powder specimen holder. The scanned range was 20–120° and the steps were in the range of 0.005–0.02°. In the appendix, a list specifying the experimental details for every measurement can be found (Sec. A.6, p. 138).

The qualitative phase analysis was performed with *DIFFRAC.EVA V5.2* with the *PDF2 - Release 2019 RDB* database from the *International Center for Diffraction Data* (ICCD). The Rietveld refinement [96,97] for the quantitative phase analysis was applied using the software *DIFFRAC.TOPAS V5.0*. The data set from the *Inorganic Crystal Structure Database* (ICSD) with the most similar composition was used as the start structure (details in Sec. A.7, p. 139). The Sr content was set to the stoichiometric composition.

Two different *R*-factors judged the quality of the Rietveld refinement. First, the quality of the fit of the whole profile was assessed with the weighted profile factor: [97]

$$R_{\mathrm{wp}} = \frac{\sum_{i=1}^{N} w_i \left(y_{\mathrm{obs},i} - y_{\mathrm{calc},i}(\mathbf{p})\right)^2}{\sum_{i=1}^{N} w_i \left(y_{\mathrm{obs},i}\right)^2}. \tag{3.1}$$

Here, w_i is the weight, $y_{\mathrm{obs},i}$ and $y_{\mathrm{calc},i}$ are the observed and calculated intensities, respectively, at point i of N data points. The parameter vector $\mathbf{p}$ contains all independent parameters.

Second, the quality of the fit compared to a single crystal is done with the Bragg-R-value:[97]

$$R_{\mathrm{Bragg}} = \frac{\sum_{i=1}^{N} |I_{\mathrm{obs},i} - I_{\mathrm{calc},i}|}{\sum_{i=1}^{N} I_{\mathrm{obs},i}}. \tag{3.2}$$

Here, $I_{\mathrm{obs},i}$ and $I_{\mathrm{calc},i}$ are the observed and calculated intensities of the kth reflection of K total reflections. In the case of overlapping reflections, the intensity of the individual (hkl) reflections is divided according to the ratio of the calculated intensities. Here, the error adjustments of the individual reflection intensities are averaged, but this can lead to a biased or overly optimistic estimation of the Bragg-R value. Therefore, this value must be viewed critically and only considered a guiding indicator. The bond length and bond angle were calculated after the refinement with the in-built function of *DIFFRAC.TOPAS V5.0*.

The in-situ high-temperature XRD (HT-XRD) were collected with a *D8-Advance (A25)* instrument from *Bruker* with a copper anode and a *Lynxeye XE-T* from *Bruker*. Therefore, the indirect heating chamber *HTK1200N* from *Anton Paar* with a motorized sample stage was used. The highest possible temperature is 1473 K. A range of 20–85° with steps of 0.04° was scanned. The measured temperature range was 303–1378 K with a heating and cooling rate of 20 K/min. Here, for the sample $CaMnO_{3-\delta}$, $Ca_{0.9}Sr_{0.1}MnO_{3-\delta}$ and $Ca_{0.8}Sr_{0.2}MnO_{3-\delta}$ a scan at 303 K, 773 K, 873 K and 973 K was collected. In the range 973–1378 K, the temperature steps vary for all samples.

Before the recording of the diffraction pattern, no equilibration time was applied. Except for the investigations of the decomposition of $Ca_{0.9}Sr_{0.1}MnO_{3-\delta}$ and $Ca_{0.6}Sr_{0.4}MnO_{3-\delta}$, an equilibration time of 10 min is applied to exclude the possibility that secondary phases are not observed for kinetic reasons. Diffraction patterns were collected both during cooling and heating. To adjust the oxygen partial pressure, a constant gas stream of calibration gas with the required O_2 in N_2 concentration was applied. All measurements were done at ambient pressure.

3.4. Experimental Details of Raman Spectroscopy

The Raman spectra were obtained at room temperature with a *XploRA Plus* and a *Syncerity OE* detector with a grating of 1200 lines/mm. A 532 nm laser with a 10 % intensity was the excitation source, and the spectra were recorded in backscattering geometry. The excitation laser was focused with a 10 x objective onto the sample surface (415 µm x 380 µm). The samples $Ca_{1-x}Sr_xMnO_3$ with $x \in [0, 0.1, 0.2, 0.4]$ were measured with an acquisition time of 30 s and three accumulations. The sample $Ca_{0.6}Sr_{0.4}MnO_3$ was measured with an acquisition time of 60 s and four accumulations due to a decreased signal intensity.

The peak position of all samples was identified without any baseline correction applied. In order to analyze the full width at half maximum (FWHM), a linear baseline correction was applied using *Origin 2017*. Afterward, the data is normalized by the highest peak. Using the program *Origin 2017*, a Lorentzian distribution is fitted to mode 1 at 249 cm^{-1} and mode 4 at 566 cm^{-1} individually to get the FWHM. Mode 4 of $Ca_{0.9}Sr_{0.1}MnO_3$, $Ca_{0.8}Sr_{0.2}MnO_3$ and $Ca_{0.6}Sr_{0.4}MnO_3$ could only be fitted with an additional mode at 542 cm^{-1}, 521 cm^{-1} or 524 cm^{-1}, respectively. As the Lorentzian line fitting failed, a Pseudo-Voigt distribution is fitted to mode 2 at 466 cm^{-1} and mode 3 at 488 cm^{-1}. More details about the fitting can be found in Sec. A.8 on p. 140. Since $Ca_{0.7}Sr_{0.3}MnO_3$ was measured separately after changes in the experimental setup, it was excluded from this analysis.

No internal standards are used in this work, so qualitative rather than quantitative analysis of the peak intensities is performed.

3.5. Thermodynamic Analysis Methods

The samples $Ca_{0.7}Sr_{0.3}MnO_3$ and $Ca_{0.6}Sr_{0.4}MnO_3$ for the thermodynamic analysis were produced via the auto-combustion method (Sec. 3.1.1, p. 30) and the samples $CaMnO_3$, $Ca_{0.95}Sr_{0.05}MnO_3$, $Ca_{0.9}Sr_{0.1}MnO_3$ and $Ca_{0.8}Sr_{0.2}MnO_3$ were produced via the solid-state method (Sec. 3.1.2, p. 31). The sample did not show any major side phases (details in Sec. A.9, p. 144).

The thermogravimetric measurements were conducted with a *STA 449 F3 Jupiter Netzsch* thermobalance. This was done by placing 80–96 mg of powder of the sample on a flat ceramic sample holder covered with a platinum foil. The used furnace was an air-cooled silicon carbide (SiC) furnace. The samples were heated to temperatures between 873–1473 K with a heating rate of 20 K/min. Each temperature was held for 30 min to ensure that thermodynamic equilibrium was reached. After a completed reduction with the final temperatures of 1473 K, the samples were cooled to 673 K. This data point was used as a reference point where $\delta = 0$ to detect and correct any instrumental drift. Afterward, the gas flows were adjusted to change the oxygen partial pressure, and the whole cycle was redone with the new oxygen

partial pressure. To limit buoyancy effects on the weighing system, 20 ml/min of Ar (*Linde*, 5.0) constantly flows through the balance chamber. To adjust the oxygen partial pressures between 0.83–10^{-4} bar, O_2 (*Linde*, 5.0), N_2 (*Linde*, 5.0) and synthetic air (80:20 N_2:O_2 mol%, *Linde*) were mixed. Here, the total volume flow of the process gases is fixed at 100 ml/min.

In order to remove the mass changes due to buoyancy changes and the sample holder, a blank measurement with specimen holder but without specimen was performed for each measurement record. This blank measurement was then subtracted from the actual measurement, and the aforementioned drift correction was applied. The drift showed a nearly linear behavior and varied for each measurement. Different temperatures and pressures in the laboratory may cause it. The varying drift was discussed and observed before.[34]

A *SETNAG Gen'Air* oxygen pump-gauge measured the outlet oxygen partial pressure. Since the maximum oxygen partial pressure, which is measurable with this device, is 0.25 bar, the oxygen partial pressures above this limit were calculated based on the applied gas flow rates. An example of a measurement for the higher oxygen partial pressures (p_{O_2} =0.83–0.1 bar) is displayed in Fig. 3.7a. Fig. 3.7b shows an example for the lower oxygen partial pressures (p_{O_2} =0.01–10^{-4} bar). This separation of measurements was necessary since pure oxygen was used to reach the high oxygen partial pressures, and synthetic air was used to reach the low oxygen concentrations. Thus, an intermediate switching of gases was necessary. The kinetics were too slow for the lowest oxygen partial pressure to reach equilibrium in a reasonable time frame. Therefore, the sample was first heated to a higher temperature and then cooled to the desired temperature to support faster equilibration. Here, the blank subtraction and drift correction was already applied for both measurements. The cross indicates the selected equilibrium value $\mathrm{d}m(T, p_{O_2})$. Severe pressure changes in the lab caused spikes in the measured mass changes. They were neglected in the following analysis.

For perovskites, a mass change is induced by a release or uptake of oxygen. Therefore, the change in mass can directly be related to the change in reduction extent or oxygen non-stoichiometry $\Delta\delta$:

$$\Delta\delta = \frac{\Delta m \cdot \mathrm{M_{Sample}}}{m \cdot \mathrm{M_O}} \tag{3.3}$$

m : sample mass

$\mathrm{M_{Sample}}$: molar mass of sample

$\mathrm{M_O}$: molar mass of oxygen.

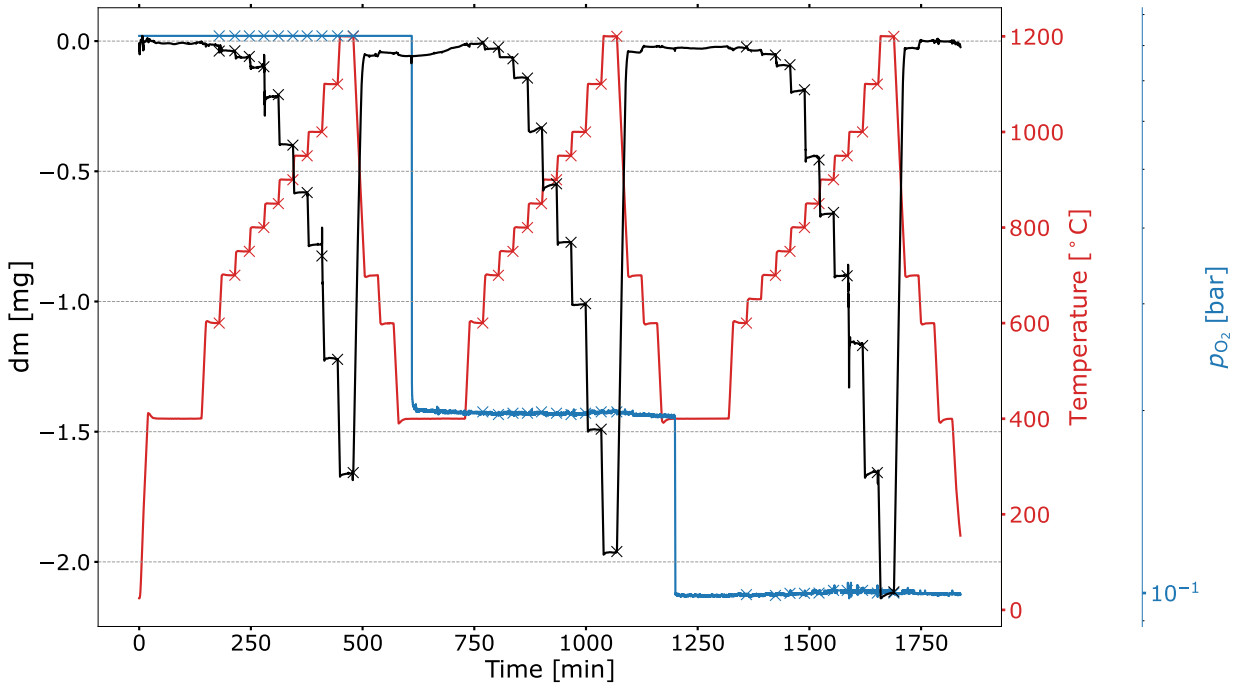

(a) p_{O_2} =0.83–0.1 bar

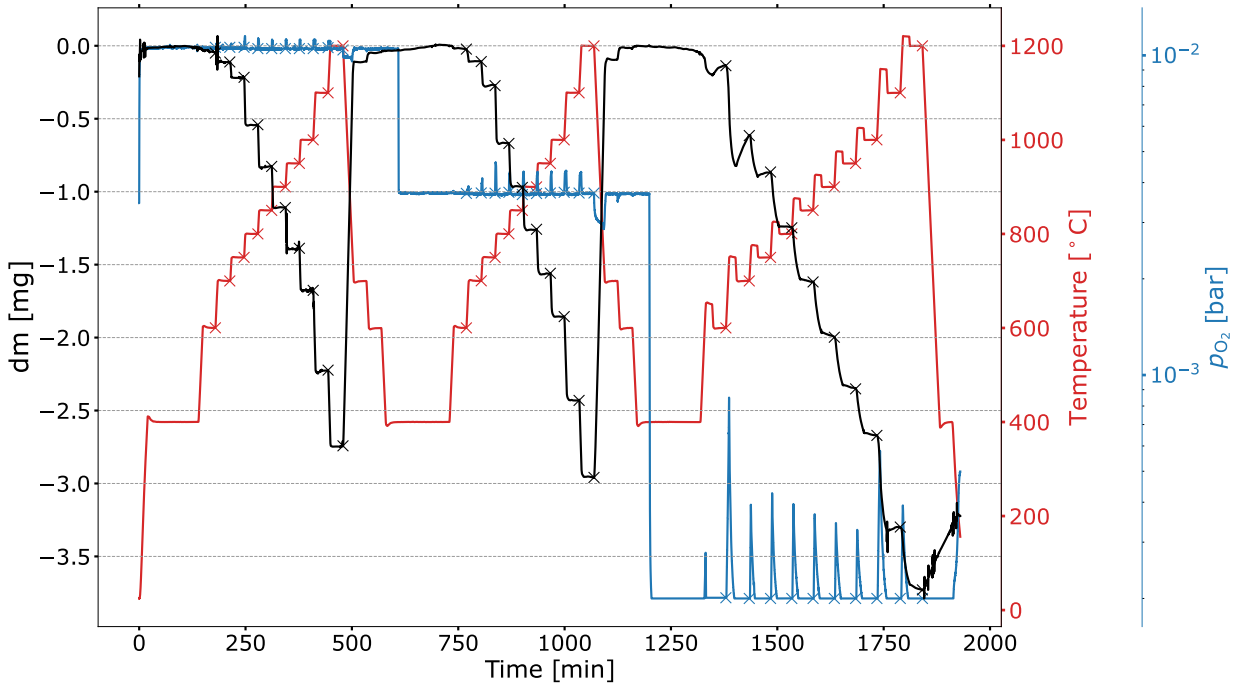

(b) p_{O_2} =0.01–10^{-4} bar

Figure 3.7.: Thermogravimetric scans of $Ca_{0.9}Sr_{0.1}MnO_{3-\delta}$. A blank measurement subtraction and a linear drift correction were already applied. The crosses identify the selected equilibrium values. Reproduced from *Klaas et al.*[98] with permission from the PCCP Owner Societies.

Since $Ca_{1-x}Sr_xMnO_{3-\delta}$ is assumed to be wholly oxidized at room temperature[51,99] and for convenience, in the following, the change in non-stoichiometry is set equal to the non-stoichiometry.

The thermodynamic measures enthalpy and entropy are extracted from the thermogravimetric measurements via the *van't Hoff* method.[27,66,67,100,101] Therefore, the mass changes are first converted to the reduction extent δ (eq. 3.3). Afterwards, the experimental values $\delta(T = \text{const.}, p_{O_2})$ are sorted and interpolated for each temperature. This procedure serves to obtain a higher number of triples for temperature, oxygen partial pressure, and reduction extent. In the following, the oxygen partial pressure and the temperature for a constant reduction extent are extracted. This is shown in Fig. 3.8. Here, the symbols indicate the value gained through interpolating the experimental values. The lines show the linear fit results for each constant δ.

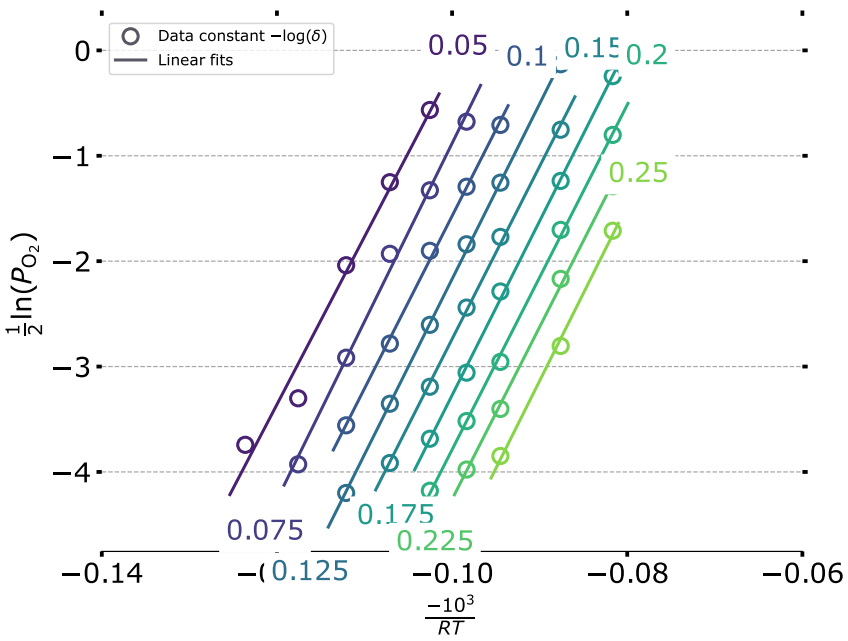

Figure 3.8.: Arrhenius plot for applying the van't Hoff method to $Ca_{0.9}Sr_{0.1}MnO_{3-\delta}$. The numbers on the line refer to the oxygen non-stoichiometry δ. The symbols indicate the value which was gained through the interpolation of the experimental values. The line is a linear fit. Here, the slopes result in the enthalpy and the intercept in the entropy.

Using the expression of the Gibbs-Helmholtz equation 2.11 on p. 16 and assuming that in the thermodynamic equilibrium $\Delta g_\delta = 0$, results into:

$$\frac{1}{2}\ln\left(\frac{p_{O_2}}{p}\right)\bigg|_{\delta=\text{const}} = -\frac{\Delta h_\delta^\circ}{RT}\bigg|_{\delta=\text{const}} + \frac{\Delta s_\delta^\circ}{T}\bigg|_{\delta=\text{const}} \tag{3.4}$$

Thus, the linear fit of Fig. 3.8 results in the enthalpy from the slope and the entropy from the intercept at constant reduction extents.

3.6. Microstructure Analysis Methods

The term 'microstructure' is defined as structures above the atomic level. The microstructure of the materials is analyzed through a variety of different experimental approaches. These serve to get a comprehensive picture of the structure of the material. These structures can influence both the kinetic properties and the mechanical properties of a material.

3.6.1. Particle Size Distribution

The particle size distribution was analyzed using a laser scattering particle size distribution analyzer (*Horiba Scientific Partica LA-960, Retsch Technology GmbH*). Therefore, the powder was dispersed in water and subjected to the measuring chamber. The light source is a 650 nm laser diode with approximately 5 mW. The detector is a silicon photodiode. The refractive index used is 1.67. It is based on the refractive index of $CaMnO_3$.[102] From the results of *Pawar et al.*[103] it is anticipated that at the frequencies used, the refractive index is independent of the Sr content.

3.6.2. Scanning Electron Microscopy

Microstructural analysis of the powders as well as the granules with different Sr contents (Fig. 6.3, p. 78 and Fig. 6.5, p. 80) by scanning electron microscopy (SEM) was performed using a *ZEISS ULTRA 55 FEG* instrument coupled to an *INCA Pentafet x3* energy dispersive X-ray spectroscopy (EDS) system from *Oxford Instruments*.

The different macrostructures, e.g., pellet and foam, (Fig. 6.8, p. 85 and 6.2, p. 76) were analyzed using a *Hitachi SU3900* with a tungsten cathode coupled to an *Ultim Max 40* from *Oxford Instruments*.

3.6.3. Porosimetry

The porosity and the pore size distribution were measured by mercury porosimetry using a *Porotec Pascal 140–440* Hg porosimeter from *ThermoFisher Scientific*. The accuracy is 0.25 %. The specific surface area and the meso- / micropore size distribution were measured via nitrogen porosimetry using a *Porotec Surfer* nitrogen porosimeter from *ThermoFisher Scientific*. The accuracy is 0.15 %.

3.7. Kinetic Analysis Methods

The samples for the kinetic analysis were produced via the solid-state method (Sec. 3.1.2, 31). A granulate was formed (Sec. 3.2.1, p. 32) to prevent inhomogeneous oxygen concentration due to the formation of dense piles when using powder. The samples had phase purity (Sec. A.11, p. 148).

The kinetics were analyzed by the thermogravimetric analysis using a *Netzsch STA 409 CD* thermobalance for the investigation of the impact of the Sr content, the impact of the granular size, and the effect of different pore densities, and by a *STA 449 F3 Jupiter Netzsch* thermobalance for the investigation of the effect of different microstructures. One layer of granules with a total mass of 197–203 mg was placed on a flat ceramic sample holder. If not otherwise stated, the granules used had a diameter of 1.25–1.6 mm.

Like the thermodynamic measurements, the oxygen partial pressure needed adjustment. Therefore, O_2, Ar and synthetic air (80:20 N_2:O_2 mol %) were mixed. As well, a constant flow through the balance chamber was applied to limit buoyancy effects. For the *Netzsch STA 409 CD* thermobalance, the outlet of this protective gas was not through the furnace and thus did not affect the oxygen concentration at the sample.

The samples were reduced at 1173 K under a constant flow of 1 % O_2 in Ar and a total mass flow of 200 ml/min. Afterward, the sample was cooled to the oxidation temperature with a constant flow of 50 ml/min Ar to prevent re-oxidation during the cooling. The heating and cooling rate was 20 K/min. The oxidation temperatures were used in the range of 473–673 K. This temperature window is chosen as in this range; the oxidation is neither too slow so that an oxidation-re-oxidation cycle would take too long nor too fast so that transport limitations due to the mass flow of the reaction gas became relevant.

After cooling the sample, the temperature was stabilized, and afterward, 100 ml/min O_2 was inserted to oxidize the sample. Following a complete redox cycle as described here, the sample was heated to 873 K under 20 % O_2 in N_2. This step was executed at the beginning of the measurement as well. It serves as a reference state for linear drift correction. A thermogravimetric scan for the kinetic analysis can be found in Fig. 3.9.

Similar to the thermodynamic analysis, a blank measurement was conducted to eliminate all parasitic mass changes. This correction has yet to be applied in Fig. 3.9, but drift correction has already been applied. However, for further analysis, only the oxidation segments were used.

The reduction kinetics should be investigated as well. Therefore, the sample was heated to temperatures in the range of 873–1023 K in 100 ml/min O_2. After the stabilization of the temperature, the gas flow was switched to 200 ml/min of 1 % O_2 in Ar. This reduction in oxygen partial pressure leads to an isothermal reduction.

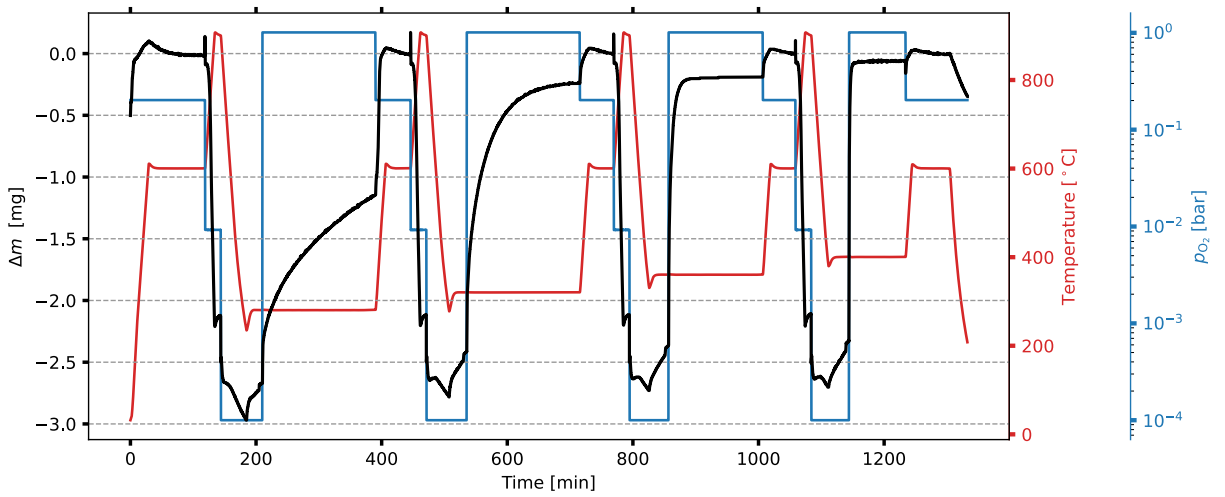

Figure 3.9.: Thermogravimetric scan for kinetic analysis of $Ca_{0.9}Sr_{0.1}MnO_{3-\delta}$. A linear drift correction was already performed. Reproduced from *Klaas et al.*[98] with permission from the PCCP Owner Societies.

To extract the activation energy based on both presented methods (Sec. 2.6, p. 17), the derivative of the conversion extent needs to be taken. Taking the numerical derivative is problematic since noise is apparent in the raw data. If the complete data set were used for some measurements, the fully-oxidized part would be overrepresented. For that reason, a subset of the experimental values is extracted with a discrete step size of 0.05 over the entire range of $X(t)$. This subset is exemplified in figure 3.10 for $Ca_{0.8}Sr_{0.2}MnO_{3-\delta}$. For this subset, the numerical derivative is computed using accurate second-order central differences in the interior points and accurate first-order one-side differences at the edges. This method has been used in previous work.[70]

The previously described step is the same for both methods. To apply the isoconversional method, ${c_{O_2}}^{-n}\left(\frac{dX}{dt}\right)_{X=\text{const.}}$ vs. $\frac{10^3}{RT}$ is plotted logarithmically as one can see in Fig. 3.11 for $Ca_{0.8}Sr_{0.2}MnO_{3-\delta}$. Here, the squares denote the experimental data sets for each X. The color code specifies the X value. To extract the activation energy, these experimental data are linearly fitted for each X, where the slope is the activation energy. A fit is just applied if at least three data points are available. The material-specific activation energy is calculated by taking the mean value.

The application of the kinetic models requires other calculations. First, the following eq. 2.21 on p. 19, $\frac{dX}{dt}$ vs. $1-X$ is plotted for each temperature (Fig. 3.12a). The squares indicate the experimental data, and the color code denotes the oxidation temperature. Each temperature is fit linearly to get β. The average of these individual fit values was taken and fixed for the whole dataset.

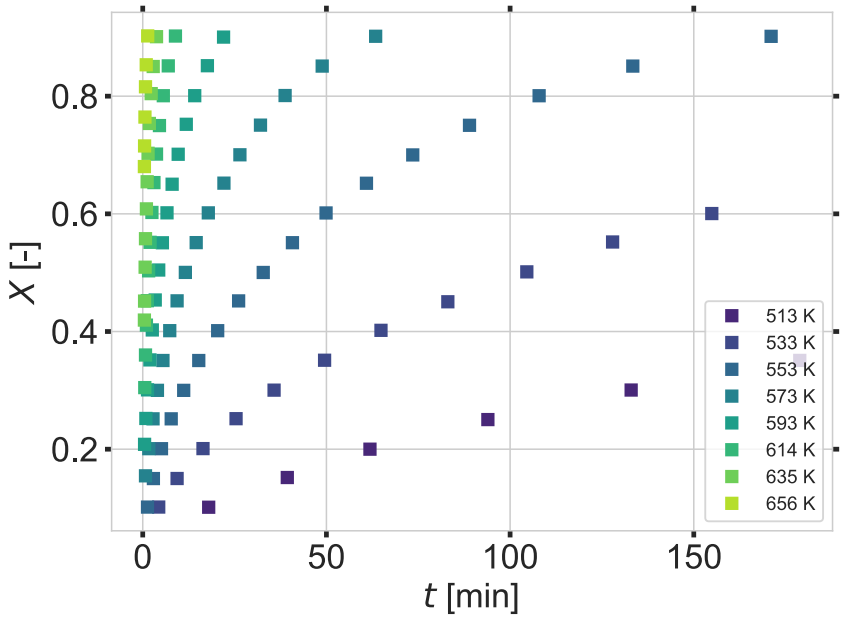

Figure 3.10.: Subset of $X(t)$ of $Ca_{0.8}Sr_{0.2}MnO_{3-\delta}$ for the kinetic analysis. This subset is meant to reduce noise and over-representation of the fully oxidized sections of the measurement.

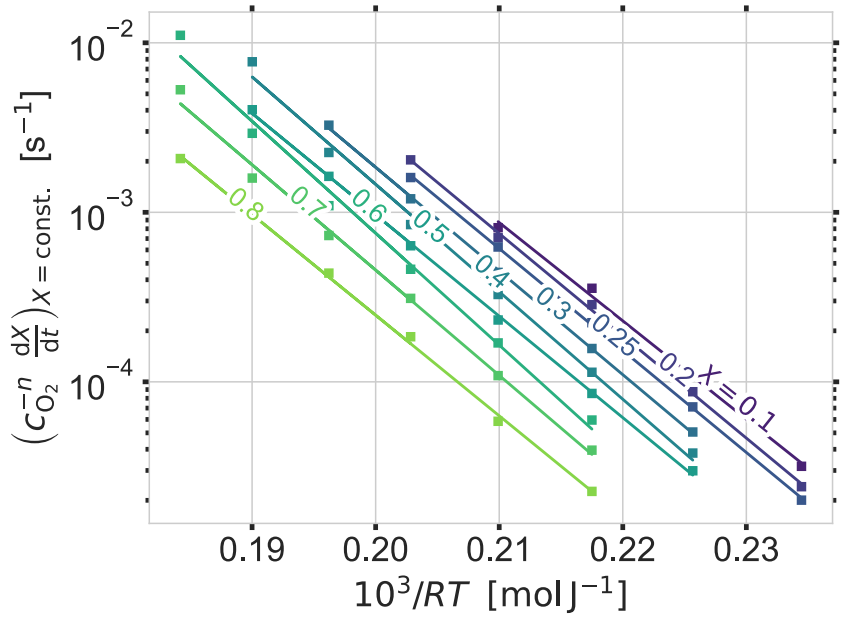

Figure 3.11.: Application of the isoconversional method to calculate the activation energy of $Ca_{0.8}Sr_{0.2}MnO_{3-\delta}$. The squares denote the experimental values, and the color code specifies the X value. The lines are the linear fit of the experimental data for each X. The slope of the fit results in the activation energy.

After fixing the reaction order, the entire data set (Fig. 3.12a) is again fitted to get the intercepts $\left(\frac{dX}{dt}\right)_{t=0}$. These intercepts are plotted with an Arrhenius plot (Fig. 3.12b). A

linear fit of this plot results in the activation energy and the pre-exponential factor k_0 based on eq. 2.20 on p. 19. Again the squares are the experimental values, and the line is the linear fit.

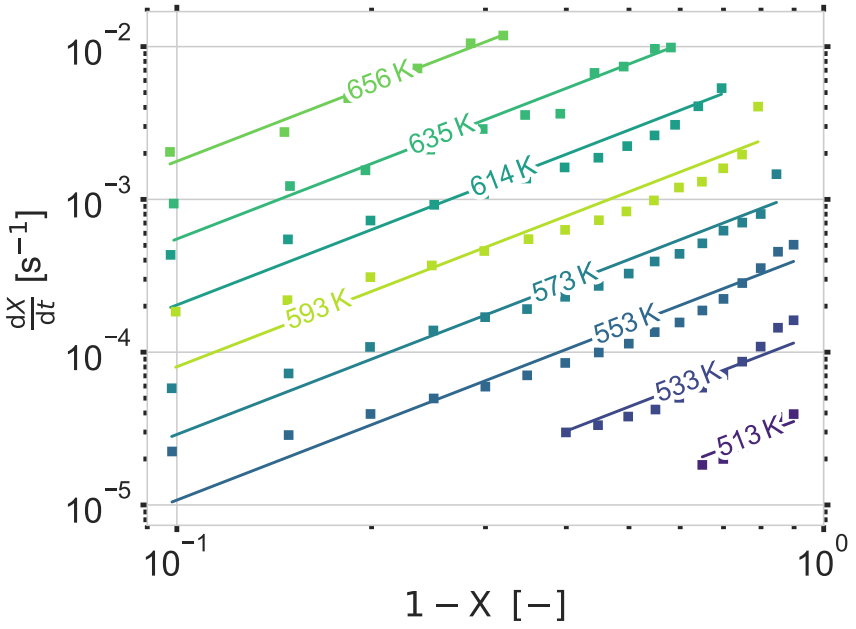

(a) The squares are experimental data. The color code denotes the oxidation temperature, and the lines are a linear fit. The slope of the fit results into the reaction order.

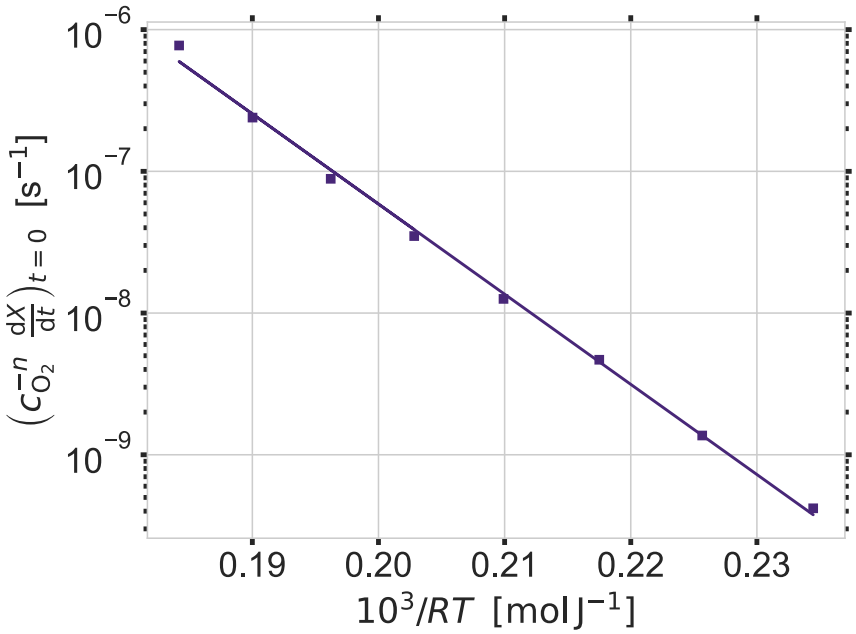

(b) The squares are experimental data. The line is a linear fit whose slope is the activation energy.

Figure 3.12.: Application of the model fitting method to calculate the activation energy of $Ca_{0.8}Sr_{0.2}MnO_{3-\delta}$.

3.8. Packed-bed Reactor Experiments

The experiments with the packed-bed reactor could not be carried out with $Ca_{1-x}Sr_xMnO_{3-\delta}$ because the required temperatures could not be reached with the available laboratory reactor. Therefore $SrFeO_{3-\delta}$ was used. It was manufactured with the solid-state method (Sec. 3.1.2, p. 31). The precursors were $SrCO_3$ (*Alfa Aesar*) and Fe_3O_4 (*Alfa Aesar*). From this powder, granules were produced (Sec. 3.2.1, p. 32). The sample had the desired composition without major side phases (Sec. A.12, p. 149).

The experimental setup used for the packed-bed reactor experiments is displayed schematically in Fig. 3.13. It consists of two main components, a *PID Eng&Tech MicroEffi system* (PID), which is a PID-controlled reactor, and a *Setnag - Jok'Air* oxygen sensor. The oxygen sensor measures the oxygen concentration at standard conditions and has an accuracy of 2 % relative. The PID enables automated pressure, temperature, and volume flow rate control. The gases used are synthetic air (80:20 N_2:O_2 mol %) and N_2. The gases enter the reactor through mass flow controllers (MFC), and by adjusting the flow rates, the oxygen concentration in the inlet gas can be adjusted. With a pneumatically activated bypass valve, the gas can enter or bypass the reactor.

The pressure in the reactor can be adjusted. Therefore, a relative pressure sensor measures the gas in the reactor, and a PID controller controls the needle valve at the system output. [104] The system was operated with varying total pressure of 1–10 bar.

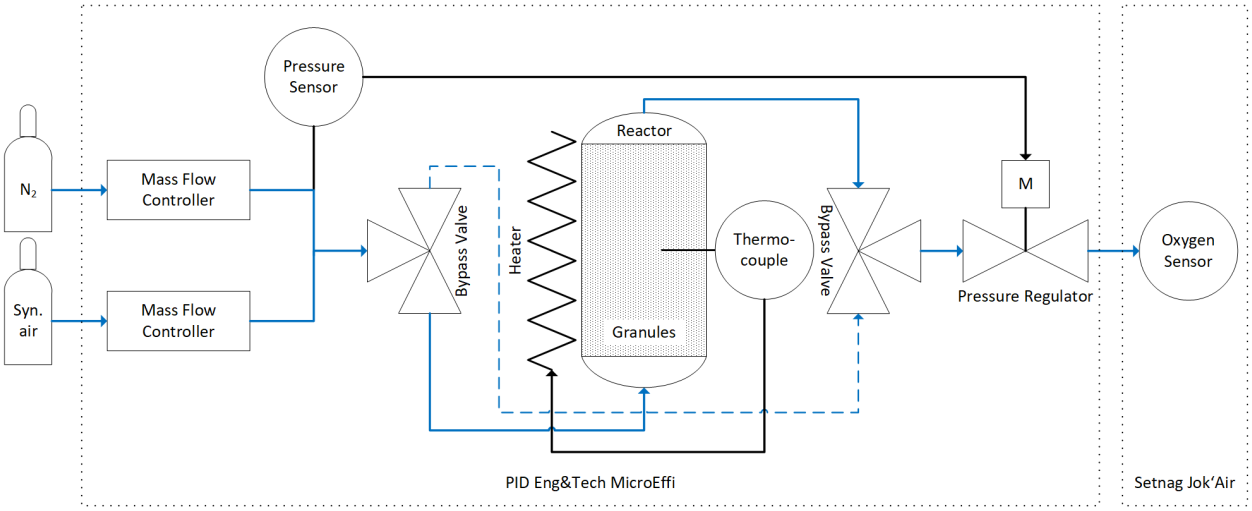

Figure 3.13.: Schematic of the experimental setup used for the packed-bed reactor experiments. Reproduced from *Klaas et al.* [82] with permission from the Royal Society of Chemistry.

The reactor is placed in a furnace heated with an electrical heater. The uniformly heated zone inside the reactor tube is 50 mm long. A K-type thermocouple is entered from the top

into the reactor to measure the temperature inside the reactor. The reactor has an inner diameter of 9 mm, is vertically located, and consists of 316 stainless steel tubes.[104]

The reactor was filled with 4.548 g of $SrFeO_{3-\delta}$ particles with a diameter of 1.25–1.6 mm, and the bed length was 51 mm.

For the packed bed reactor experiments, the heating and cooling rate was 10 K/min. The starting temperature for each experiment was 623 K. The sample was then reduced at the set reduction temperature for 30 min. The total pressure during the reduction was 1 bar. The inlet oxygen concentration and inlet flow rate were identical during heating and reduction. Subsequently, the reactor was cooled while no gas flow was supplied. The reactor was first pressurized with nitrogen when oxidation was performed at elevated pressure. After reaching the pressure within 5 min, the oxidation was carried out at 623 K and a constant gas flow of the oxidizing atmosphere.

The total amount of purified inlet gas $V_{\mathrm{in,exp}}$ was calculated using the oxidation time t_{ox} and the inlet mass flow rate $\dot{V}_{\mathrm{ox}}$. The oxidation time is defined as the time between the time at which oxidation begins and when the oxygen partial pressure exceeds 10 ppm. The adsorbed oxygen flow $\dot{V}_{\mathrm{O_2}}$ is calculated by a mass balance of the input $x_{\mathrm{O_2,inlet}}$ and the output oxygen concentration $x_{\mathrm{O_2,outlet}}$:

$$\dot{V}_{\mathrm{O_2}} = \dot{V}_{\mathrm{ox}} \cdot (x_{\mathrm{O_2,inlet}} - x_{\mathrm{O_2,outlet}}). \tag{3.5}$$

The total volume of the absorbed oxygen $V_{\mathrm{O_2,exp}}$ is calculated by integrating the absorbed oxygen stream.

4. Crystal Structure Analysis

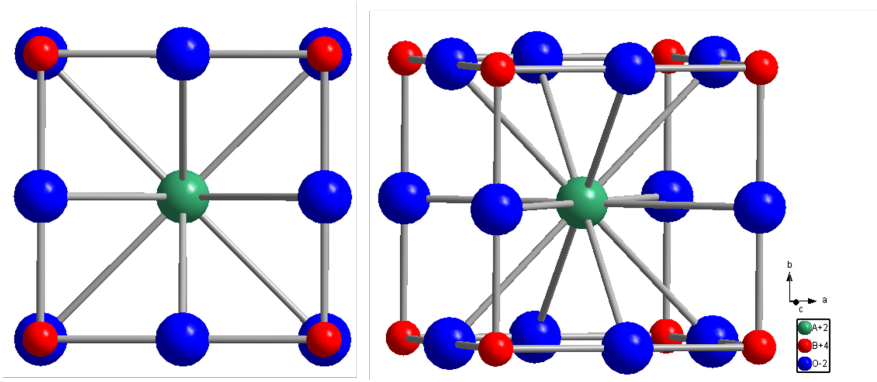

Figure 4.1.: Sketch of the crystal structure. The cubic perovskite crystal structure consists of a centered A-ion (green) in a cube of B-ions (red). The B-ions themselves are surrounded by oxygen ions (blue). The composition of the material influences the bond length and the angle between the bonds.

This chapter is partially based on the following peer-reviewed publication, which is authored by the author of this thesis:

L. Klaas, M. Pein, P. Mechnich, A. Francke, D. Giasafaki, D. Kriechbaumer, Ch. Agrafiotis, M. Roeb, and Ch. Sattler. Controlling thermal expansion and phase transitions in $Ca_{1-x}Sr_xMnO_{3-\delta}$ by Sr content. Physical chemistry chemical physics: PCCP, 24(45):27976-27988, 2022. doi: 10.1039/D2CP04332G.

This chapter thoroughly investigates the impact of the Sr content on the crystal structure of the material. First, the impact at room temperature is analyzed employing XRD. Second, the impact of temperature and oxygen partial pressure on the crystal structure for different Sr contents is examined by in-situ HT-XRD. Finally, the chapter is concluded by investigating the impact of the Sr content on the molecular vibrations using Raman spectroscopy.

4.1. Room Temperature Crystal Structure

The samples $Ca_{1-x}Sr_xMnO_3$ with $x \in [0, 0.4]$ are investigated with XRD. The materials were investigated in the form of powder. The preparation method of the sample is summarized in Tab. 4.1. Experimental details about the XRD can be found in Sec. 3.3 on p. 34.

Table 4.1.: The prepared samples with the corresponding preparation method. The auto-combustion method is described in Sec. 3.1.1 on p. 30, and the solid-state method is described in Sec. 3.1.2 on p. 31.

Sample	Auto-combustion	Solid-state
$CaMnO_{3-\delta}$		**x**
$Ca_{0.95}Sr_{0.05}MnO_{3-\delta}$		**x**
$Ca_{0.9}Sr_{0.1}MnO_{3-\delta}$		**x**
$Ca_{0.85}Sr_{0.15}MnO_{3-\delta}$	**x**	
$Ca_{0.8}Sr_{0.2}MnO_{3-\delta}$		**x**
$Ca_{0.75}Sr_{0.25}MnO_{3-\delta}$	**x**	
$Ca_{0.7}Sr_{0.3}MnO_{3-\delta}$	**x**	
$Ca_{0.6}Sr_{0.4}MnO_{3-\delta}$	**x**	

The analysis of the XRD pattern of all $Ca_{1-x}Sr_xMnO_{3-\delta}$ samples reveals an orthorhombic structure with space group *Pnma* (details about space group in 2.7, p. 20). The impact of the Sr content on the cell volume is presented in Fig. 4.2. A linear increase with the increase of the Sr content is apparent as predicted by *Vegard's law*[105] due to the different ionic radii of $^{XII}Ca^{2+} = 1.34\,Å$[60] and $^{XII}Sr^{2+} = 1.44\,Å$.[60] Therefore, a shift of the 2Θ angles to smaller values is predicted.

Fig. 4.3 shows a part of the XRD patterns. This part is selected as it includes the (211)-peak, which indicates an orthorhombic distortion of the ideal cubic perovskite. The counts of the highest peak normalize each diffraction pattern; no further corrections are applied. Due to different step sizes in the experiment (0.005° and 0.02°; exp. details see Sec. 3.3, p. 34), the $K_{\alpha 2}$-contribution is visible to varying degrees. The displayed peak shifts from 40.1° for 0 % Sr to 39.69° for 40 % Sr. Thus, the prediction of the increasing unit cell is observed. Besides, a decreasing peak intensity with an increasing Sr content is observed.

The XRD patterns are further analyzed through Rietveld refinement (Sec. 3.3, p. 34). The results are shown in Tab. 4.2. The lattice parameters are in good agreement with literature

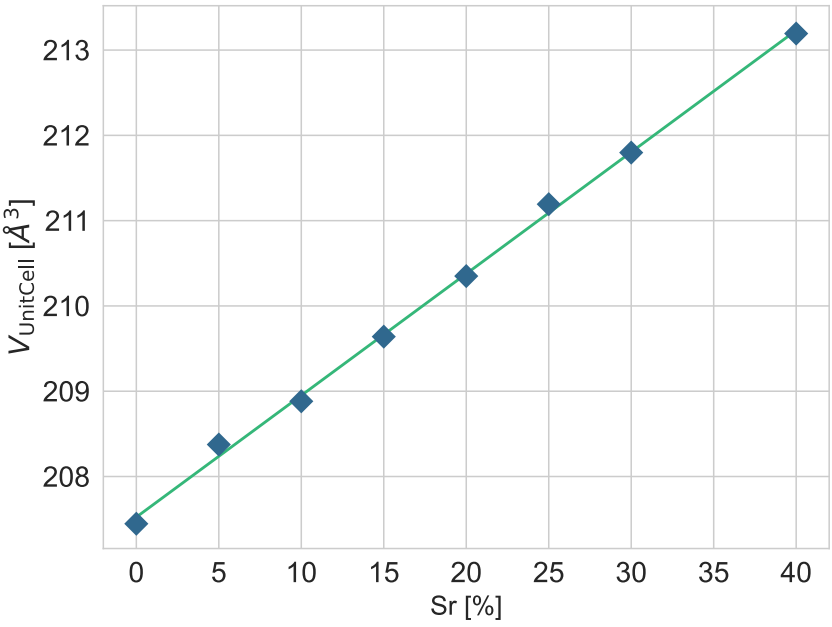

Figure 4.2.: Evolution of the unit cell volume with increasing Sr content. The results are gained through Rietveld refinement. The linear increase is predicted by Vegard's law[105] because Sr has a bigger ionic radius than Ca. Adapted from *Klaas et al.*[45] with permission from the PCCP Owner Societies.

values.[106] Four of the samples show a minor marokite ($CaMn_2O_4$) side phase. This phase is known to form under reducing conditions as part of a decomposition process.[73] Still, one would expect that two decomposition products, namely $CaMn_2O_4$ and Ca_2MnO_4, would form to maintain the overall nominal cation ratio. Since these compositions exhibit similar major diffraction peaks (2Θ) at 32.6° and 32.5° (Cu-K_α),[107,108] and the patterns are difficult to distinguish, it may be that both phases are apparent. As the fraction of this side phase is small and is expected to have negligible impact, they are not further analyzed.

A representation of the orthorhombic lattice distortion is the relative magnitudes of the lattice parameters (Sec. 2.2, p. 9): $\frac{\sqrt{2}c}{b}$ and $\frac{c}{a}$. The results for $CaMnO_{3-\delta}$ in Tab. 4.2 are in good agreement with literature values.[61] The relative magnitudes approach the value one when increasing the Sr content up to 20–25 %. A relative magnitude equal to one implies that the lattice parameters are approximately equal, and therefore, the structure is nearly undistorted but cubic. Increasing the Sr content further diverges this undistorted state and increases the distortion but with reversed axial ratios, meaning:

$$c > a \text{ and } c > \frac{b}{\sqrt{2}}.$$

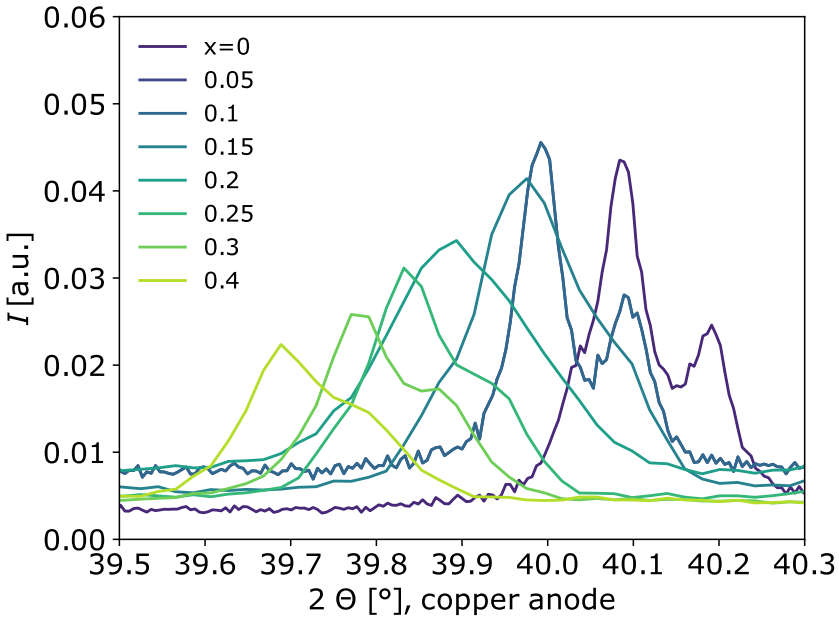

Figure 4.3.: Evolution of the peak of the orthorhombic phase with Sr content. Displayed is a part of the XRD pattern of $Ca_{1-x}Sr_xMnO_{3-\delta}$ with $x \in [0, 0.4]$. The range is selected because it contains a peak assigned to the orthorhombic distortion. The (hkl) value is (211). Increasing the Sr content leads to a shift of the peak to lower 2Θ values and a decreasing intensity. Due to different step sizes in the experiment (0.005° and 0.02°; exp. details see Sec. 3.3, p. 34), the $K_{\alpha 2}$-contribution is visible to varying degrees. The highest peak intensity normalizes the values. No further corrections are applied. Reproduced from *Klaas et al.*[45] with permission from the PCCP Owner Societies.

Using the results of the Rietveld refinement and further investigating the impact of the Sr content, the bond length and bond angles between the oxygen ions and the cations are calculated. A labels both, Sr and Ca, since they are assumed to be in the same position. First, the development of the bond length is considered (Fig. 4.4). The values of the Mn-oxygen bond length are in good agreement with literature values.[106] Similar to *Taguchi et al.*,[106] no trend is apparent. Contrary, the A-O1/2 bond length shows an increasing trend for an increasing Sr content. This increase is particularly evident for the A-O1 bond length. A linear approximation reveals a slope of $3.1(1) \times 10^{-3}$ Å.

Second, the development of the bond angle is studied (Fig. 4.5). In agreement with the different evolutions of the A-O1 and A-O2 bond lengths, the O1-A-O2 bond angle slightly increases with an increasing amount of Sr content. The bond angle between A and one type of oxygen, namely the bond angle O1-A-O1, scatters around 90°. The values for the Mn-O1/2-Mn bond angles are in good agreement with literature values.[106]

The larger mean ionic radius of Sr compared to Ca $\big(r(\mathrm{Sr}) > r(\mathrm{Ca})\big)$ influences the lattice parameters by increasing them. The increasing lattice parameters become apparent by the

Table 4.2.: Lattice parameters of the samples $Ca_{1-x}Sr_xMnO_3$ gained by Rietveld refinement. The error margins are extracted from *DIFFRAC.TOPAS*. The equations of R_{wp} and R_{Bragg} are eq. 3.1 and eq. 3.2 on p. 35. The side phase is marokite ($CaMn_2O_4$).

Sr [%]	a [Å]	b [Å]	c [Å]	R_{wp}	R_{Bragg}	Marokite [wt%]	c/a	$\sqrt{2}c/b$
0	5.281 48(2)	7.457 16(3)	5.267 16(2)	9.85	3.317	3.14(4)	0.9973	0.9989
5	5.286 59(3)	7.469 05(5)	5.277 21(3)	8.11	6.845		0.9982	0.9992
10	5.288 44(4)	7.475 43(8)	5.283 68(4)	7.98	7.097		0.9991	0.9996
15	5.292 06(8)	7.487 54(8)	5.290 66(9)	13.64	3.834	3.6(2)	0.9997	0.9993
20	5.2950(4)	7.4996(3)	5.2972(4)	9.77	2.325	5.663(14)	1.0004	0.9989
25	5.299 84(4)	7.504 86(6)	5.309 76(4)	9.54	2.326	4.069(9)	1.0019	1.0006
30	5.304 21(4)	7.511 24(7)	5.316 04(4)	8.02	2.707		1.0022	1.0009
40	5.313 95(3)	7.526 55(5)	5.330 41(3)	6.93	2.502		1.0031	1.0016

shift of the peak (Fig. 4.3) and the increase of the unit cell (Fig. 4.2). The substitution of Ca by Sr slightly influences the MnO_6 octahedra. *Taguchi et al.*[106] observe an increasing trend in the Mn-O1/2-Mn bond angle with an increasing Sr content. The presented data do not directly support this statement. This may be due to experimental variations and the fact that more Sr concentrations were measured in the data presented here. The XRD results and the nearly constant Mn-O1/2 bond length indicate that Sr substitution has no trend-like effect on the MnO_6 octahedra. On the contrary, the Sr substitution clearly affects the A-O bond lengths by increasing them. Since the O2-A-O2 bond angle scatters around 90°, the A-ion is centered within the MnO_6 octahedron for all Sr contents investigated.

The *Goldschmidt* tolerance factor (eq. 2.2, p. 9) indicates that the fully oxidized composition $Ca_{0.89}Sr_{0.11}MnO_3$ has a cubic structure since the tolerance factor equals one (Tab. 2.1, p. 10). An increase in the Sr content is expected to result in a hexagonal form because $SrMnO_3$ has a hexagonal structure.[109] In contrast, all analyzed samples with Sr content up to 40 % show orthorhombic distortion. Nevertheless, the decreasing peak intensity indicate a decreasing distortion through the substitution of Ca by Sr. One possibility of distortion is the tilting of the MnO_6-octahedron as described by the model of basic structural distortions (Sec. 2.4, p. 13). As the bond angles, Mn-O1-Mn and Mn-O2-Mn deviate from 180° over the whole range of Sr content investigated, a tilting of the MnO_6-octahedra is indicated. To compensate for the limitation of the *Goldschmidt* tolerance factor, the relative magnitudes of the lattice parameters serve as an additional measure to predict the distortion of the structure. Moreover, a previous study showed a phase transition from orthorhombic to tetragonal to cubic for $CaMnO_{3-\delta}$.[53,54] For Sr concentrations between 15 % and 20 %, the ratio $\frac{c}{a} \approx 1$, points to a tetragonal structure.

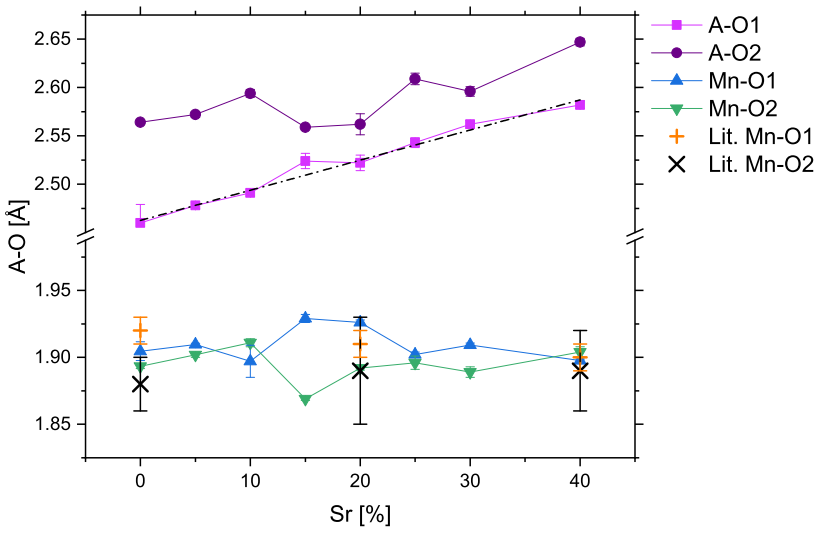

Figure 4.4.: Evolution of the bond length between the cations and the two distinct oxygen ion positions for $Ca_{1-x}Sr_xMnO_{3-\delta}$ with $x \in [0, 0.4]$. As Ca and Sr are assumed to be located at the same position, A represents both. The dotted line is a linear fit to the A-O1 bond length with a slope of $3.1(1) \times 10^{-3}$ Å. The assigned literature values can be found in ref.[106] Adapted from *Klaas et al.*[45] with permission from the PCCP Owner Societies.

Still, this approach has limitations. For example, focusing on the ratio $\frac{\sqrt{2}c}{b}$ and $\frac{c}{a}$, one would conclude that the sample $Ca_{0.85}Sr_{0.15}MnO_3$ has a cubic structure. However, this is not the case, as the orthorhombic peak is still clearly visible.

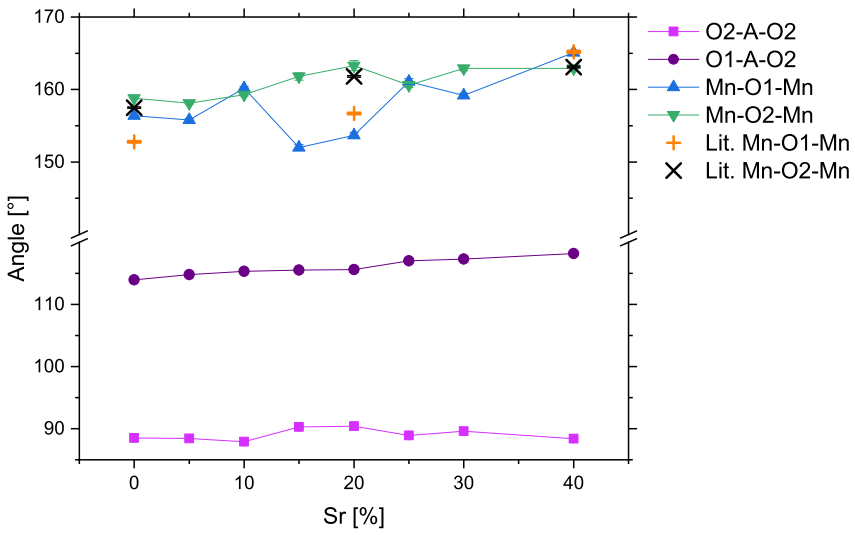

Figure 4.5.: Evolution of the bond angle between the cations and the two distinct oxygen ion positions for $Ca_{1-x}Sr_xMnO_{3-\delta}$ with $x \in [0, 0.4]$. As Ca and Sr are assumed to be located at the same position, A represents both. The assigned literature values can be found in.[106] Adapted from *Klaas et al.*[45] with permission from the PCCP Owner Societies.

4.2. Evolution of Crystal Structure with Temperature and Oxygen Partial Pressure

The samples $Ca_{1-x}Sr_xMnO_3$ with $x \in [0, 0.2]$ were investigated with HT-XRD. These Sr concentrations were chosen because DSC studies indicated a disappearance of the phase change between the distortions in this concentration range.[21] The materials were investigated in the form of powder. The preparation methods of the samples were equivalent to the previous section. Experimental details about the HT-XRD can be found in Sec. 3.3 on p. 34.

The analysis of $CaMnO_{3-\delta}$, $Ca_{0.9}Sr_{0.1}MnO_{3-\delta}$, and $Ca_{0.8}Sr_{0.2}MnO_{3-\delta}$ in both applied atmospheres show no side phases. Especially, no decomposition into a AMn_2O_4 and A_2MnO_4 is observed. What is seen is a transformation from an orthorhombic to a cubic phase.

Here, the two phases, orthorhombic and cubic, are distinguished by the presence of the orthorhombic (211)-peak at $2\Theta \approx 40°$ (copper anode). In the HT-XRD results, a decreasing peak height over a temperature range of the orthorhombic peak is observed. The decrease over a temperature range indicates the smearing of the phase transition, which can be associated with an intermediate tetragonal phase. An example is displayed in Fig. 4.6. Here, the orthorhombic peak of $CaMnO_{3-\delta}$ is shown. The measurement occurred in air. The color code represents the intensity of the peak in arbitrary units. Besides the peak shift with

increasing temperature, the gradual vanishing of the peak with increasing temperature is evident.

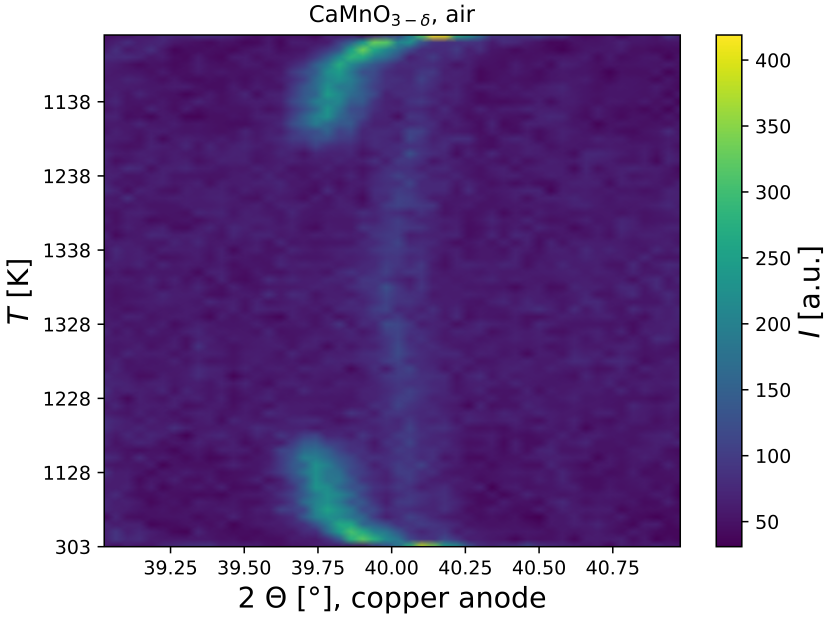

Figure 4.6.: Divergence and re-occurrence of the orthorhombic peak (211) in $CaMnO_{3-\delta}$ in air measured with a copper anode. The color code represents the intensity of the peak in arbitrary units.

Powder samples were reduced at 1223 K and $p_{O_2} = 0.01$ bar and then rapidly cooled under an inert atmosphere to investigate if the phase change persists at room temperature. The reduced samples were analyzed via XRD with cobalt anode (Sec. 3.3, p. 34) at ambient conditions. Fig. 4.7 shows that the orthorhombic peak is still not present, and, therefore, the sample is, in fact, still cubic.

In the following, the phase change temperature T_{PT} is defined as the mean value of the highest temperature at which the orthorhombic peak is observed and the lowest temperature at which the cubic peak is observed. The reversible phase transition was also investigated by *Klaas et al.*[45] through differential scanning calorimetry (DSC). The phase transition temperature can be found in table 4.3. $Ca_{0.8}Sr_{0.2}MnO_{3-\delta}$ is omitted since the DSC measurement did not reveal a phase change through an endothermic peak.[45] Considering the difference between the methods, they are in good agreement. In addition, *Klaas et al.*[45] likewise observed a smearing of the phase transition.

Only the lattice parameters extracted via Rietveld refinement during the initial heating cycle are used for further analysis because the impact on the as-prepared samples is investigated. To be able to directly compare the lattice parameters of the orthorhombic and cubic phase, the orthorhombic lattice parameter a is converted into a pseudo-cubic parameter (eq. 2.3, p. 10):

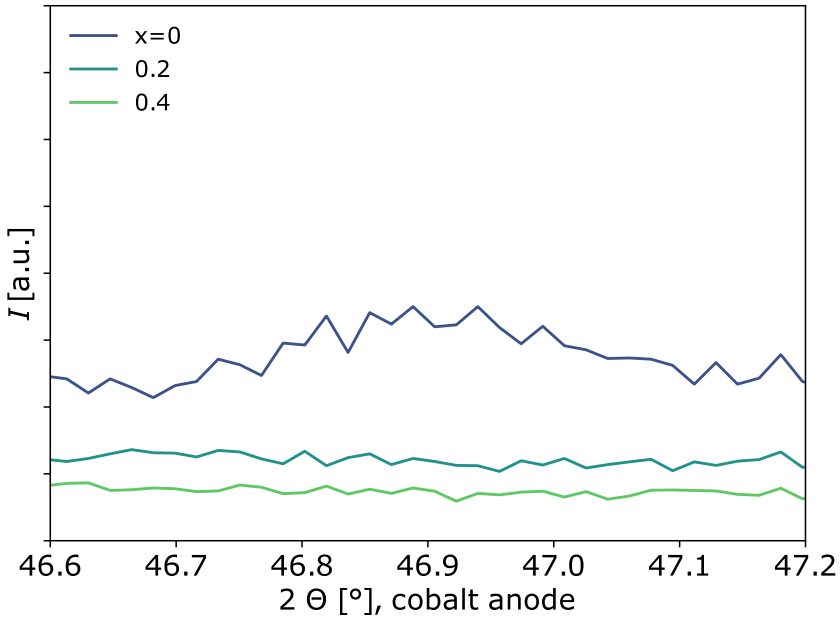

Figure 4.7.: XRD (cobalt anode) of reduced $Ca_{1-x}Sr_xMnO_{3-\delta}$ at room temperature. The color code of the line assigns the Sr content of the sample. The orthorhombic peak (211) is still not present. Therefore, the conclusion is that the sample retains its cubic structure.

$$a_{\text{pseudo-cubic}} = \frac{a}{\sqrt{2}}. \tag{4.1}$$

The cubic and pseudo-cubic lattice parameters can be found in the Appendix in Sec. A.3 on p. 134. The expansion coefficients are calculated separately to compare the expansion of the material for both phases. A linear fit is applied to the pseudo-cubic lattice parameter (eq. 2.3) in the temperature range 773–973 K because all samples investigated are orthorhombic in this temperature range. The slope is Δa_{ortho}. Since only diffraction patterns for three

Table 4.3.: Temperatures of phase transition T_{PT} between the orthorhombic and cubic phase of $Ca_{1-x}Sr_xMnO_{3-\delta}$ ($x \in [0, 0.1]$) in air and 1% O_2 in N_2 as determined by DSC and HT-XRD. The results of the DSC measurements are extracted from.[45]

x	Atmosphere	T_{PT} [K]	
		DSC	HT-XRD
0	Air	1165.6	1183
0	1% O_2	1120.8	1113
0.1	Air	1101.1	1080.5
0.1	1% O_2	1095.9	1043

temperatures are recorded in this temperature range, the error margins are relatively big, and the validity is limited. Nevertheless, the overall trend is a valuable measure.

Analogously, a linear fit is applied to the temperature range 1173–1373 K, to get Δa_{cubic}. Both values, Δa_{ortho} and Δa_{cubic}, are divided by the room temperature lattice parameter of the corresponding sample and atmosphere. The results are summarized in Tab. 4.4.

Table 4.4.: Expansion coefficients of $Ca_{1-x}Sr_xMnO_{3-\delta}$ $x \in [0, 0.2]$ in air and 1 % O_2 in N_2 for the cubic and the orthorhombic phase. a_0 assigns the lattice parameter at 303 K under the specified atmosphere.

Atmosphere	x	$\Delta a_{\text{ortho}}/a_0[\frac{\%}{\text{K}}]$	$\Delta a_{\text{cubic}}/a_0[\frac{\%}{\text{K}}]$
Air	0	0.0016(0)	0.00321(3)
1% O_2	0	0.0014(1)	0.00323(2)
Air	0.1	0.0017(0)	0.00311(4)
1% O_2	0.1	0.0016(8)	0.00318(4)
Air	0.2	0.0008(4)	0.00301(3)
1% O_2	0.2	0.0010(2)	0.00305(2)

The two different atmospheres do not affect the expansion coefficients of both phases. The expansion of the orthorhombic phase Δa_{ortho} is 2-3 times smaller than the corresponding Δa_{cubic} for both atmospheres and all samples. Δa_{cubic} decreases with an increasing Sr content for both atmospheres.

The lattice parameters of the cubic phase for all samples and both applied atmospheres are displayed in Fig. 4.8. The different initial temperatures result from the different phase change temperatures. From this plot, it is clear that the temperature of the phase change depends on both the Sr content and the atmosphere. For $Ca_{0.8}Sr_{0.2}MnO_{3-\delta}$, the phase transitions is between 873 K and 973 K. Since no XRD pattern is recorded in between, the phase change temperature cannot be determined with higher precision.

Comparing the lattice parameters at one temperature shows that they increase with an increasing Sr content, $a_{\text{CS20MO}} > a_{\text{CS10MO}} > a_{\text{CMO}}$, and with a reduced oxygen concentration of the atmosphere, $a_{1\%O_2} > a_{\text{air}}$.

The thermodynamics are summarized in Sec. 2.5 on p. 15 and visualized in Fig. 4.9. The thermodynamic values used are displayed in Tab. A.6 on p. 149. In Fig. 4.9 the reduction extent of the phase change is denoted by a star. The material is strongly reduced after the phase change temperature. The model does not take the crystal structure into account, but only thermodynamic data. The reduction extent depends not only on the temperature but also on the surrounding oxygen partial pressure. Therefore, the materials have a higher reduction extent when measured under 1 % than measured under 20 % at the same temperature. Increasing the reduction extent results in an increased amount of Mn^{3+} compared to Mn^{4+}. The relations of the ionic radius is: $r(Mn^{3+}) > r(Mn^{4+})$.[60] Thus, the

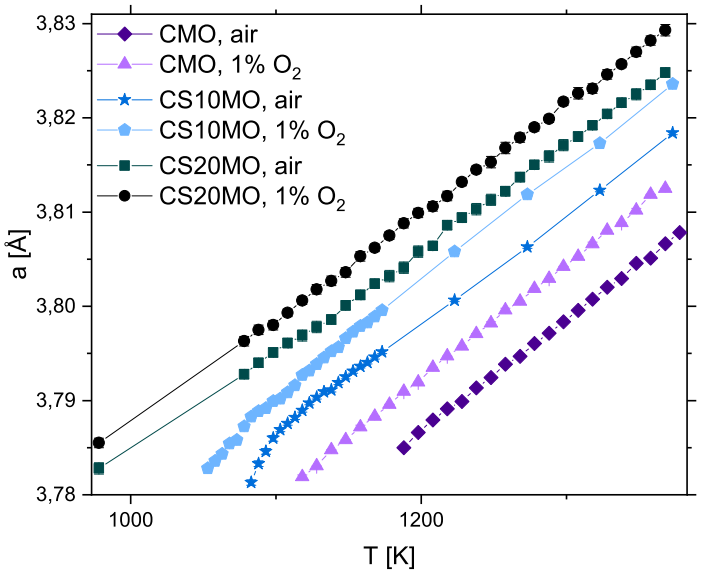

Figure 4.8.: Evolution of the cubic lattice parameter over the temperature range of 973–1378 K dependent on $x \in [0, 0.2]$ in $Ca_{1-x}Sr_xMnO_{3-\delta}$ and the oxygen partial pressure. Reproduced from *Klaas et al.*[45] with permission from the PCCP Owner Societies.

enhancement of the lattice parameter only by decreasing the oxygen partial pressure, $a_{1\%O_2} > a_{air}$, is explained by the increased reduction extent. Moreover, the enhanced expansion of the lattice parameter after the phase change may be mainly favored by the enhanced reduction.

As shown in section 4.1 on p. 50, the lattice expands through the substitution of Ca by Sr due to the increased ionic radius of Sr compared to Ca. The results of the HT-XRD reveal the same behavior, as $a_{CS20MO} > a_{CS10MO} > a_{CMO}$. Moreover, the thermodynamic analysis of the impact of the Sr content on the reduction extent indicates that increasing the Sr content increases the reduction extent under otherwise same experimental conditions (Chap. 5, p. 69). Thus, similar to the impact of the decreased oxygen partial pressure, the lattice parameters are also enhanced by the increased reduction extent through the substitution of Ca by Sr. Meaning that the impact of the Sr content has two contributions: on the one hand, the increased ionic radius compared to Ca and on the other hand, the increased reduction extent under otherwise same experimental conditions. The latter aspect loses significance at the final reduction level ($\delta = 0.5$). Here, the material transforms to the brownmillerite state $A_2B_2O_5$,[52] which has another reduction behavior. This state was never reached in this study.

Investigations on monolithic samples revealed a lower expansion coefficient for the orthorhombic than for the cubic phase.[45] This expansion is caused by the thermal expansion and the expansion due to the reduction. Additionally, they observed increased expansion

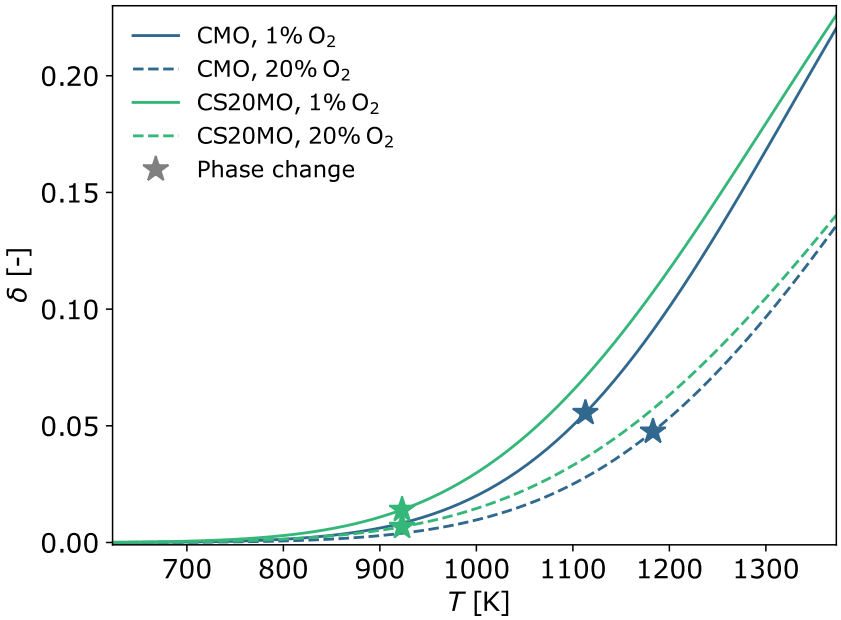

Figure 4.9.: Calculation of the non-stoichiometry δ for the temperature range investigated and both applied oxygen partial pressures based on Sec. 2.5 on p. 15. The thermodynamic values used are displayed in Tab. A.6 on p. 149. The star indicates the phase change reduction extent.

with increased Sr content. The expansion effects are mainly determined by the degree of reduction of the material. Therefore, the conclusion is that the lattice parameter changes have a macroscopic effect and thus can be crucial for applying these materials since expansion can induce mechanical stress and lead to cracking and deformation of the material.

For technical applications, the material must be stable against decomposition. Decomposition can on the one hand lead to a decreased redox performance as the resulting phase may not be able to be reduced and oxidized under the applied conditions. On the other hand, a decomposition may lead to decreased mechanical stability since the decomposition is most likely accompanied by expansion of the material. Therefore, in the framework of a collaboration project, *GTT-technologies* performed chemical thermodynamic equilibrium calculations using the software *FactSage*™ to investigate if any decomposition is expected to occur. The resulting phase diagram of $Ca_{0.9}Sr_{0.1}MnO_{3-\delta}$ and $Ca_{0.6}Sr_{0.4}MnO_{3-\delta}$ is shown in Fig. A.2 on p. 136. Since for $CaMnO_{3-\delta}$, the decomposition is already well-established[73,75] and since no side phases were calculated for $Ca_{0.8}Sr_{0.2}MnO_{3-\delta}$ and $Ca_{0.7}Sr_{0.3}MnO_{3-\delta}$; these compositions will not be considered further in the following. Table 4.5 and table 4.6 show the quantities of formed side-phases of $Ca_{0.9}Sr_{0.1}MnO_{3-\delta}$ and $Ca_{0.6}Sr_{0.4}MnO_{3-\delta}$, respectively, for selected temperatures. The oxygen partial pressure is fixed at 0.0001 bar. The tables highlight that considerable amounts of side phases are expected to form while reducing the material.

Table 4.5.: Calculated amounts of side phases for $Ca_{0.9}Sr_{0.1}MnO_3$ occurring during reduction under $p_{O_2} = 0.0001$ bar for selected temperatures.[110]

	973 K	1123 K	1273 K
Perovskite [wt.%]	99.67	67.8	93.39
$Ca_3Mn_2O_7$ [wt.%]		18.6	2.38
$CaMn_2O_4$ [wt.%]		11.6	1.49

Table 4.6.: Calculated amounts of side phases for $Ca_{0.6}Sr_{0.4}MnO_3$ occurring during reduction under $p_{O_2} = 0.0001$ bar for selected temperatures.[110]

	873 K	923 K	973 K	1023 K	1073 K	1173 K
Perovskite [wt.%]	82.39	79.47	80.71	83.01	86.82	98.34
$SrMnO_3$ [wt.%]	27.53					
$CaMn_2O_4$ [wt.%]		4.82	4.49	3.9	2.92	
$Sr_4Mn_3O_{10}$ [wt.%]		1.52	1.42	1.23	0.9	

To investigate the predicted occurrence of side-phases, in-situ HT-XRD were performed with the same conditions as were used for the calculations (Exp. details see Sec. 3.3, p. 34). The results are shown in Fig. 4.10. The vertical lines mark the position of the main peaks. They are extracted from *PDF 01-074-8781* for $Ca_{0.9}Sr_{0.1}MnO_{3-\delta}$ and *PDF 50-1748* for $Ca_{0.6}Sr_{0.4}MnO_{3-\delta}$.

The increasing temperature leads to both an expansion of the unit cell and, therefore, a shift of the peak to lower 2Θ-values and the vanishing of the orthorhombic peak. However, contrary to what the thermodynamic calculations predicted, no measurable minor phases occur. In conclusion, both materials are considered stable against decomposition. Nevertheless, the calculations show minor phases in thermodynamic equilibrium. The formation of the calculated minor phases could therefore be kinetically inhibited, so that minor phases could form after multiple cycles or long residence times.

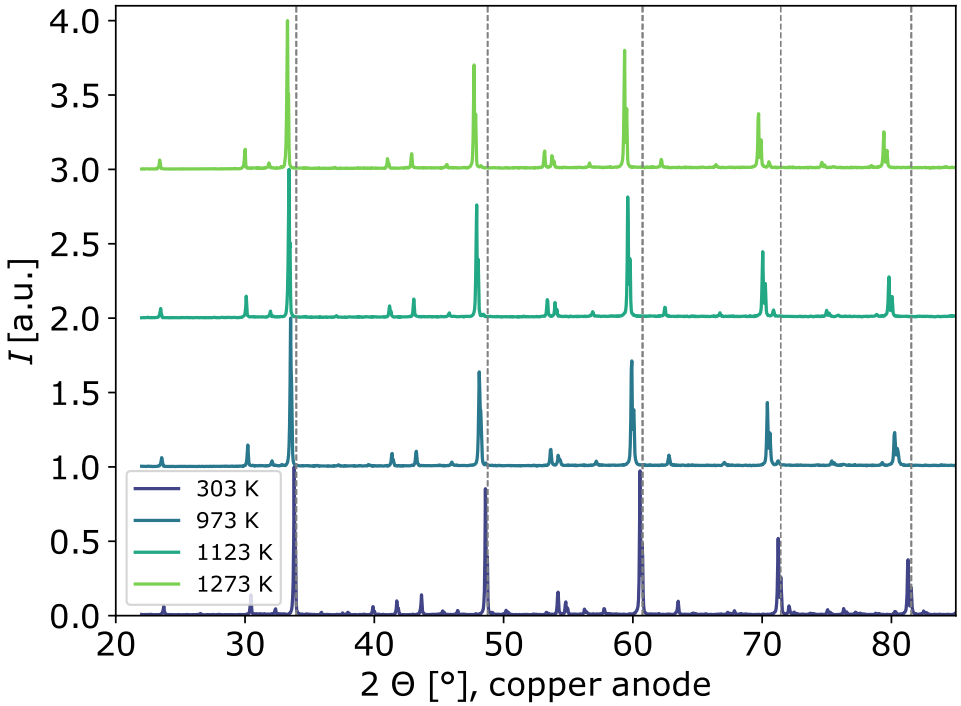

(a) $Ca_{0.9}Sr_{0.1}MnO_{3-\delta}$

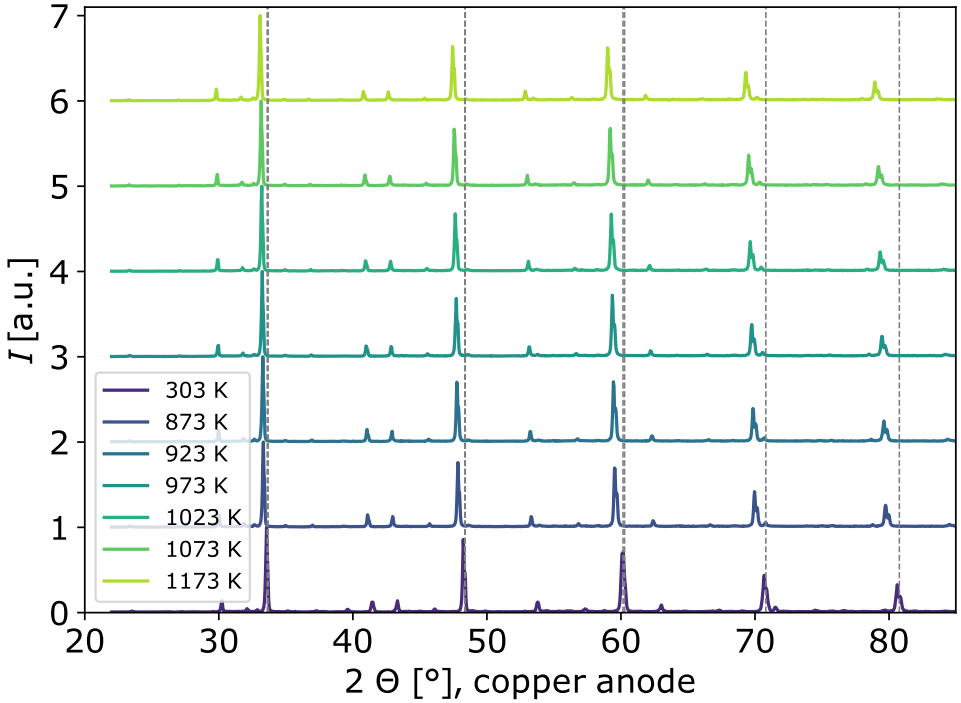

(b) $Ca_{0.6}Sr_{0.4}MnO3$-δ

Figure 4.10.: HT-XRD pattern to investigate the predictions of Tab. 4.5 and 4.6. The vertical dashed lines indicate the main peaks of the phase. They are extracted from *PDF 01-074-8781* for $Ca_{0.9}Sr_{0.1}MnO_{3-\delta}$ and *PDF 50-1748* for $Ca_{0.6}Sr_{0.4}MnO_{3-\delta}$. No side phases are observed.

4.3. Molecular Vibrations

The samples $Ca_{1-x}Sr_xMnO_3$ with $x \in [0, 0.4]$ are investigated with Raman spectroscopy. The materials were produced via the solid-state method (Sec. 3.1.2, p. 31) and investigated in the form of pellets (Sec. 3.2.3, p. 34). Experimental details about the Raman measurement can be found in Sec. 3.4 on p. 36.

The phase purity of the samples was analyzed via XRD (Sec. 3.3, p. 34). The results are shown in Sec. A.5 on p. 137. The samples $Ca_{1-x}Sr_xMnO_3$ with $x \in [0, 0.3]$ are pure with no side phases. On the contrary, $Ca_{0.6}Sr_{0.4}MnO_3$ has a minor $SrMnO_3$ side phase. Thus, all the samples have a primary *Pnma* structure (details about space group in 2.7, p. 20).

Figure 4.11 shows the result of the Raman measurement. No correction is applied. The vertical dashed lines indicate the center of the peaks of $CaMnO_3$. The numbers with black background indicate the Raman bands that will be examined in more detail below.

First, the present modes of $CaMnO_3$ are assigned. Following *Abrashev et al.*,[65] the lines at $152\,cm^{-1}$ and $488\,cm^{-1}$ have A_g symmetry (explanations of symmetry in Sec. 2.3). The lines $317\,cm^{-1}$ and $566\,cm^{-1}$ have B_{1g} or B_{3g} symmetry. The line at $466\,cm^{-1}$ have B_{2g} symmetry. In *Abrashev et al.*[65] one line lies at $242\,cm^{-1}$ with A_g symmetry and one line lies at $259\,cm^{-1}$ with B_{2g} symmetry. In the current measurement, only one peak at $249\,cm^{-1}$ is apparent. As this peak is relatively broad, this peak is likely to be a superposition of both lines. Overall, the spectra are comparable to other earlier reported spectra of $CaMnO_3$.[111,112]

Second, the evolution of the lines in the spectra of $Ca_{1-x}Sr_xMnO_3$ with increasing amounts of Sr is described. Overall, the signal intensities of all identified Raman modes in this study decrease when Sr is present, compared to $CaMnO_3$. Especially, the intensity of the modes at $249\,cm^{-1}$ (A_g and B_{2g}), $317\,cm^{-1}$ (B_{1g} or B_{3g}) and $566\,cm^{-1}$ (B_{1g} or B_{3g}) clearly decreases. Moreover, all modes are softened with increasing Sr content, meaning that they shift to lower wavenumbers. The A_g mode at $152\,cm^{-1}$ either vanishes or moves to a wavenumber outside of the recorded spectra. In $Ca_{0.8}Sr_{0.2}MnO_3$ an additional mode appears at $515\,cm^{-1}$ with a weak intensity and in $Ca_{0.6}Sr_{0.4}MnO_3$ an additional mode appears at $652\,cm^{-1}$.

Figure 4.12 displays the evolution of the wavenumbers of selected Raman modes with an increasing Sr content. These modes are selected as they do not vanish over the Sr range studied. Here, as well as in Fig. 4.11, the softening of the Raman modes with increasing Sr content is apparent. The highest change in peak position is $28\,cm^{-1}$ for the A_g mode and lowest change in peak position is $12\,cm^{-1}$ for the B_{1g} or B_{3g} mode. The red dotted lines represent the linear fit. The slopes a_{sl} of the linear fit are summarized in Tab. 4.7.

As the slope of mode 3 is the steepest, this mode experiences the strongest softening with an increase in Sr content. Because of the overlap of peaks 2 and 3, these results should be evaluated cautiously. However, mode 4 has by far the weakest softening.

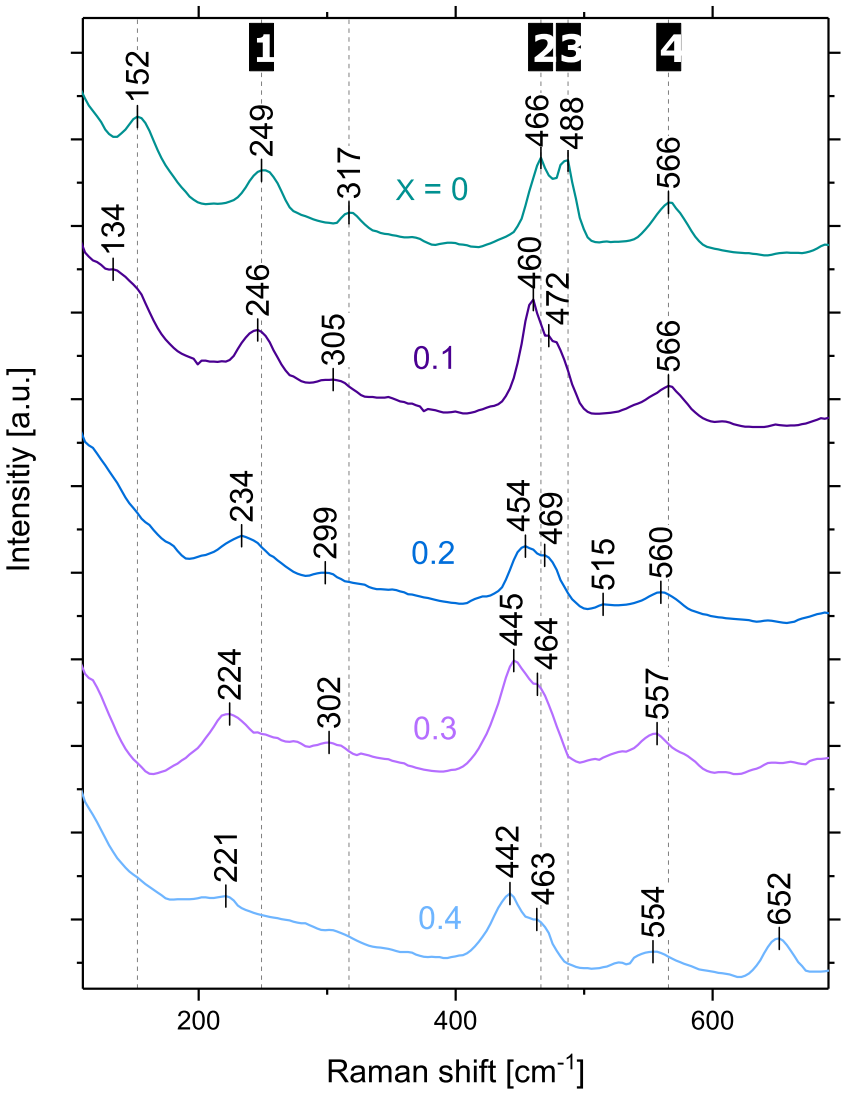

Figure 4.11.: Raman spectra of $Ca_{1-x}Sr_xMnO_3$ with $x \in [0, 0.4]$. No correction is applied. The numbers above the modes indicate the peak center. The vertical dashed lines serve as a guide to the eye to observe the evolution of the modes with increasing Sr content. The numbers with black background highlight the Raman bands that will be examined in more detail below.

Figure 4.13 shows the evolution of the FWHM of the selected modes with increasing Sr content. Since $Ca_{0.7}Sr_{0.3}MnO_3$ was measured separately after changes to the device, it was excluded from this analysis. As the intensity decreased too much, a fitting of Peak 1 for $Ca_{0.6}Sr_{0.4}MnO_3$ was not successful. Moreover, for Sr contents $\geq 10\,\%$ an additional peak needed to be included to achieve a good line fitting of Peak 4 (Sec. A.8, p. 140). The required addition of a peak indicates that a new mode may appear when Sr is added. Overall, an increasing trend with an increasing amount of Sr content is observed, except for the Raman mode 3 at the highest Sr content. However, the reliability of the fits is limited due to the

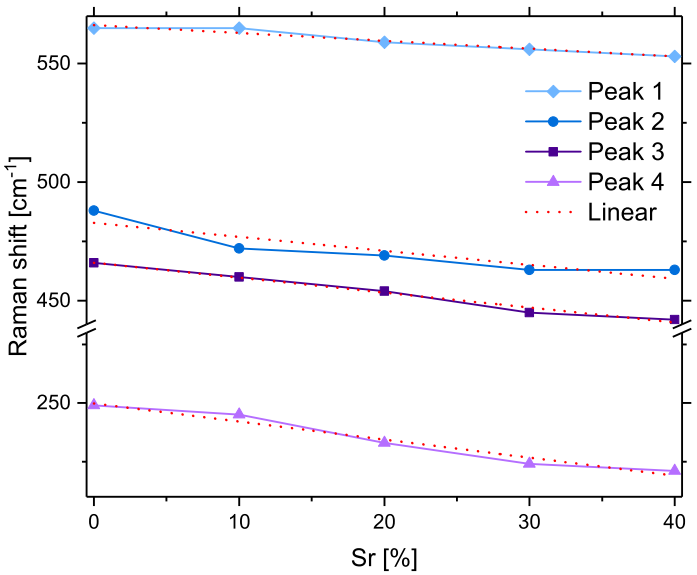

Figure 4.12.: Evolution of the modes wavenumber of $Ca_{1-x}Sr_xMnO_3$ with $x \in [0, 0.4]$. The red dotted lines represent a linear fit. The slopes a_{sl} of the linear fit are summarized in Tab. 4.7.

Table 4.7.: Slopes a_{sl} of the linear regression of the Raman modes with increasing Sr content.

Model number [-]	a_{sl} [cm^{-1}/%Sr]
1	-0.63
2	-0.59
3	-0.77
4	-0.33

significantly low peak intensity, especially in the case of Peak 1 and Peak 4 at high Sr content. In addition, there is a high possibility that the new peaks added to compensate for the fit accuracy might have influenced the FWHM of Peak 4. Therefore, the following discussion will be focused on the peak position rather than the FWHM.

The analysis of the phase purity of $Ca_{0.6}Sr_{0.4}MnO_3$ shows a $SrMnO_3$ side phase (Sec. A.5, p. 137). *Sacchetti et al.*[113] investigated the Raman spectrum of $SrMnO_3$. They found the major Raman mode at 644 cm^{-1}. Therefore, the additional Raman mode in $Ca_{0.6}Sr_{0.4}MnO_3$ is assigned to the side phase. Since the additional Raman modes of $SrMnO_3$ have considerably lower intensity, they are not apparent.

As presented in Sec. 2.4 on p. 13, the orthorhombic distortion can be divided into four basic distortions. Combining lattice-dynamical calculations with group-theoretical analysis, the Raman active modes of the orthorhombic structure are assigned to the Raman active modes of a basic distortion.[65] Thus, the intensities of the Raman lines can be utilized

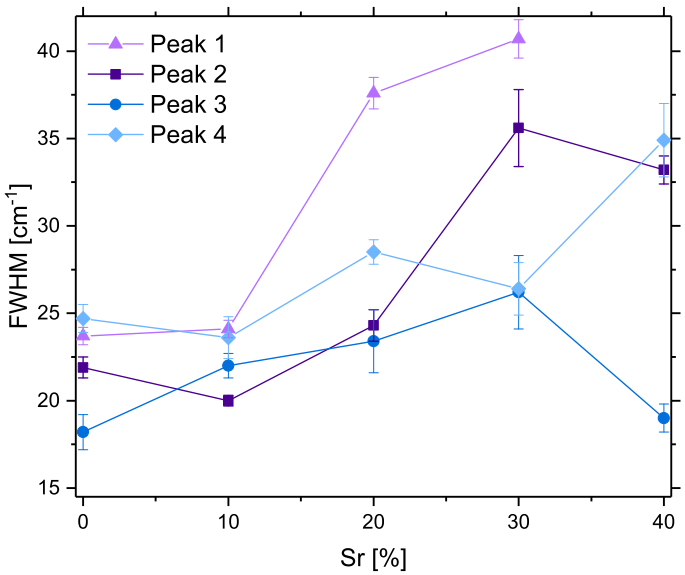

Figure 4.13.: Evolution of the modes FWHM of $Ca_{1-x}Sr_xMnO_3$ with $x \in [0, 0.4]$. The error bars assign the numerical errors of the fit.

as a measure for the basic distortions. Table 4.8 summarizes the correlation between the wavenumber and the basic distortion. As the intensities of the line 152 cm^{-1}, 249 cm^{-1}, 317 cm^{-1} and 566 cm^{-1} (Fig. 4.11) clearly decrease with an increasing amount of Sr content, the hypothesis is that the overall orthorhombic distortion decreases. In the following, the individual basic distortions are discussed in more detail.

Table 4.8.: Summary of the correlation between the wave number and the basic distortion.

Wavenumber [cm^{-1}] This thesis	Wavenumber [cm^{-1}] Ref.[65]	Activating distortion Ref.[65]
152	160	rot. [010], JT
249	258	A-shift
317	320	rot. [010], JT
466	465	rot. [101]
488	487	rot. [101]
566	564	rot. [101]

As presented in Sec. 2.4 on p. 13, the basic structural distortions can also be described by analyzing the deviations of the apparent ion position from the ideal cubic ion position. Using the results of the Rietveld refinement (Sec. A.2, p. 133), the values of the basic distortion as presented in Tab. 2.2 on p. 15 are calculated. The results are shown in Tab. 4.9. For

clarity, the corresponding formula is again displayed here. For further details, the reader is referred to the section mentioned above.

Table 4.9.: Basic distortions of $Ca_{1-x}Sr_xMnO_3$.

Sr [%]	$D_{[101]}$	$D_{[101]}$	$D_{[010]}$	D_{JT}	$D_{\mathrm{A-shift}}$
	$2\sqrt{2}\left\lvert z_{\mathrm{O}(1)}\right\rvert$	$4\sqrt{2}\left\lvert y_{\mathrm{O}(2)}\right\rvert$	$2\left\lvert x_{\mathrm{O}(2)} - z_{\mathrm{O}(2)}\right\rvert$	$2\left\lvert x_{\mathrm{O}(2)} + z_{\mathrm{O}(2)}\right\rvert$	$2x_A$
0	0.2082(17)	0.163(2)	0.148(2)	0.0016(17)	0.066 02(18)
10	0.1734(3)	0.171(3)	0.137(3)	0.0060(34)	0.054 04(2)
20	0.2328(6)	0.111(6)	0.124(17)	0.0002(170)	0.041 80(60)
30	0.1830(40)	0.130(4)	0.119(5)	0.0054(45)	0.035 52(32)
40	0.1307(34)	0.150(3)	0.106(4)	0.0006(40)	0.027 42(30)

The values of $CaMnO_3$ are in good agreement with literature values.[65] For all Sr contents, the tilting ($D_{[101]}$) and the rotation ($D_{[010]}$) of the MnO_6-octahedra have the greatest impact. The $D_{\mathrm{A-shift}}$ basic distortion has a weaker impact, and the Jahn-Teller basic distortion D_{JT} is the weakest but also has the highest relative error. Thus, this distortion has the lowest impact on the crystal structure, but the precise value has limited validity and, therefore, is excluded from the following discussion.

Both $D_{[101]}$ (tilting) and the $D_{[010]}$ (rotation) values decrease with an increasing Sr content (Tab. 4.9). The assigned modes (Tab. 4.8) show both a decreasing peak intensity (Fig. 4.11) and a softening (Fig. 4.12 and Tab. 4.7). This trend shows that there has been a decrease in distortion. Concerning *Woodward et al.*,[47] the orthorhombic distortion minimizes the repulsive A-O1/2 overlap and maximizes the A-O1/2 covalent bonding. Substituting Ca by Sr, which has a bigger ionic radius $\Big(r(\mathrm{Sr}) > r(\mathrm{Ca})\Big)$,[60] leads to an increased repulsive interaction and thereby the cubic system becomes energetically more stable.[47] This explains why the Sr substitution leads to a reduced octahedral tilting observed in XRD and in Raman spectroscopy. Surprisingly, although the $D_{[010]}$ values indicate an octahedral rotation for $Ca_{0.6}Sr_{0.4}MnO_3$ as well, the assigned Raman modes have already vanished.

The basic distortion $D_{\mathrm{A-shift}}$ decreases strictly monotonously (Tab. 4.9). The value at 40 % Sr is less than half of the value at 0 % Sr. As well, the assigned modes (Tab. 4.8) show both a decreasing peak intensity (Fig. 4.11) and a softening that has the second largest slope (Fig. 4.12 and Tab. 4.7). In general, displacement of the A-ion is caused by the repulsive force between the A-ion and the oxygen ion, which can arise when the octahedral tilt becomes too large.[48] Based on the observations, it is, therefore, conclusive that a decreasing displacement of the A-ion accompanies the decreasing octahedral tilt and rotation.

In conclusion, combining the analysis of the modes and the basic structural distortion reveals that the A-shift is most relaxed through the substitution of Ca by Sr. This is in

line with the observation that the Sr substitution mainly influences the A-O1/2 bond length (Sec. 4.1, p. 50). At 40 % Sr content, the predominant distortion is the rotation and tilting of the MnO_6-octahedra.

4.4. Summary of the Crystal Structure Analysis

This chapter analyzed the effects of Sr content on the crystal structure. The effects at room temperature, elevated temperatures, and reduced oxygen partial pressures were discussed. This chapter shows that, in contrast to the prediction by the *Goldschmidt* tolerance factor, the orthorhombic distortions at room temperature persist over the entire range of Sr content studied. However, the orthorhombic distortion decreases with increasing Sr content. The additional measure of the relative sizes of the lattice parameters to determine the distortion of the structure is applied. It proves to be a helpful additional measure but still has limitations in accuracy. Thus, if the exact crystal structure is particularly important, the complete XRD spectrum analysis remains inevitable. Nevertheless, for an initial screening and categorizing of materials, the introduced measure is a helpful tool to facilitate the analysis of the crystal structure of a material.

The Sr substitution mainly affects the A-O1/2 bond length by elongating it. It also leads to a decreased phase change temperature between the orthorhombic and cubic phases. The HT-XRD proves that an increased reduction extent leads to increased unit cell expansion. Moreover, the Sr content affects thermal expansion. This is important for the application, as expansion can cause mechanical stresses that lead to deformation or the formation of cracks and thus reduce the mechanical stability of a macrostructure.

Except for $CaMnO_{3-\delta}$, the diffraction patterns prove that no decomposition occurs during reduction for all the samples studied. Therefore, it is emphasized that no significant changes in material properties are to be expected during the application, as would be the case in the event of decomposition.

Additional analysis of the molecular vibrations revealed that the distortion is governed by the tilting and rotation of the MnO_6-octahedra. This distortion decreases with an increasing Sr content and is assigned to elongating the *A*-O bond length. The reduced tilting and rotation of the MnO_6-octahedra, in turn, leads to a lower displacement of the *A*-ion from the central position.

5. Thermodynamic Analysis

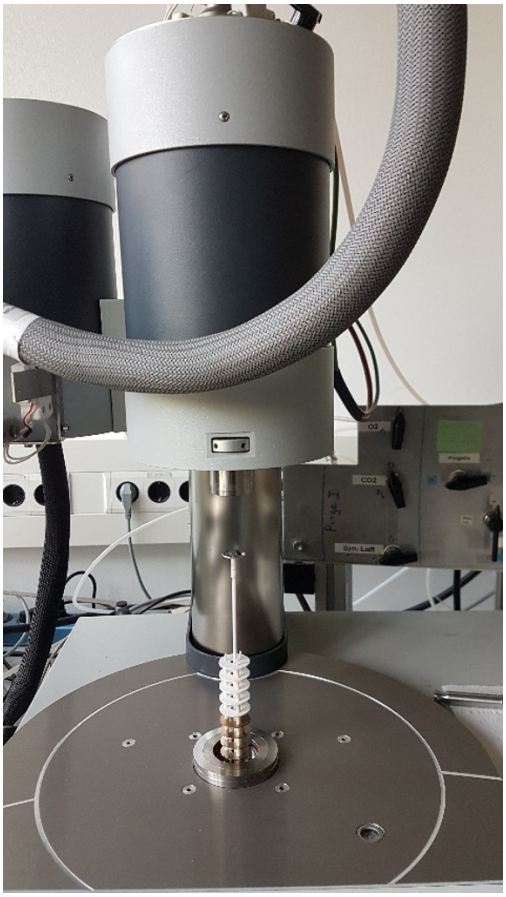

Figure 5.1.: The thermodynamics of $Ca_{1-x}Sr_xMnO_{3-\delta}$ were measured by thermogravimetric analysis. Displayed is the used device with a powder sample. In the figure, the furnace is at the top position where the loading and unloading of a sample is enabled.

This chapter is partially based on the following peer-reviewed publication, which is authored by the author of this thesis:

L. Klaas, B. Bulfin, D. Kriechbaumer, M. Roeb and Ch. Sattler. Impact of the Sr content on the redox thermodynamics and kinetics of $Ca_{1-x}Sr_xMnO_{3-\delta}$ tailored properties. Physical chemistry chemical physics: PCCP, 25(13):9188-9197, 2023. doi: 10.1039/D3CP00267E.

After demonstrating the effects of Sr content on the crystal structure of the material, this chapter considers the effects of Sr content on thermodynamic properties, enthalpy and entropy, by applying the *van't Hoff* method. Details about the experimental configuration can be found in Sec. 3.5 on p. 36.

The non-stoichiometries of the materials are calculated with eq. 3.3 on p. 37 for all experimental conditions investigated. Afterwards, the equilibrium values $\delta\left(T, p_{O_2}\right)$ are selected based on the equilibrium conditions for temperature $\Delta T < 10^{-2}\,\mathrm{K}$ and mass $\Delta m < 10^{-4}\,\mathrm{mg}$. Fig. 5.2 shows the experimental selected equilibrium values of $Ca_{0.9}Sr_{0.1}MnO_{3-\delta}$, together with the fit of eq. 2.14 on p. 16. All other samples can be found in Sec. A.9 on p. 144. As predicted, the non-stoichiometry δ depends on the temperature T and the oxygen partial pressure p_{O_2}. This dependency is comparable to earlier studies on $Ca_{1-x}Sr_xMnO_{3-\delta}$.[66]

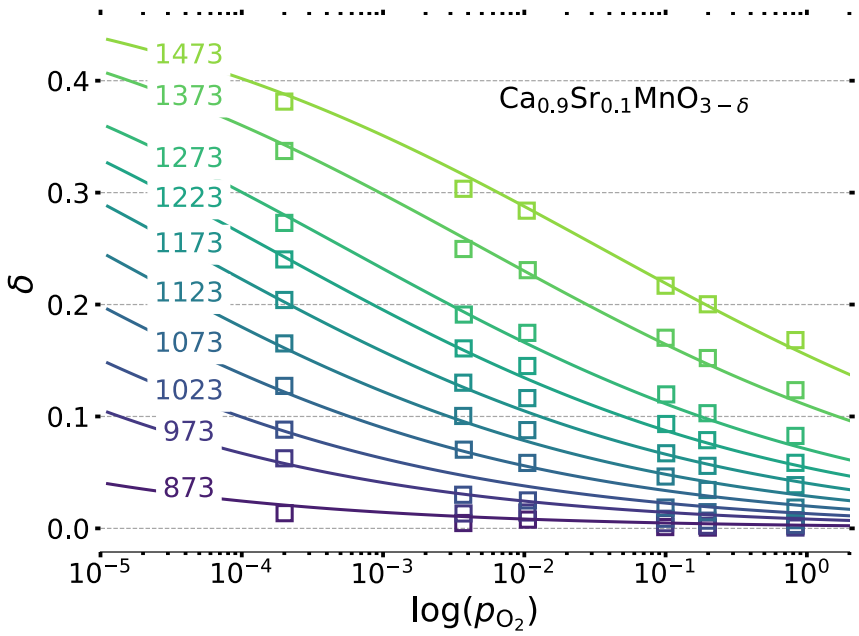

Figure 5.2.: Equilibrium non-stoichiometries $\delta\left(T, p_{O_2}\right)$ of $Ca_{0.9}Sr_{0.1}MnO_{3-\delta}$ depending on temperature T and oxygen partial pressure p_{O_2}. The temperature is displayed on the line in K. The squares indicate the experimental values which are selected as they fulfill the equilibrium conditions. The lines are the fit of eq. 2.14, p. 16. Reproduced from *Klaas et al.*[98] with permission from the PCCP Owner Societies.

Using the *van't Hoff* approach (Sec. 2.5, p. 15), the enthalpy Δh_δ° and entropy Δs_δ° of the reduction reaction at fixed δ values is calculated. The δ values investigated are in the range of 0.05–0.3. Here, the lower boundary is selected to avoid small mass changes. These small mass changes have more significant uncertainties, amplified in the *van't Hoff* method. Additionally, fits must pass at least three data points. This criterion leads to a material-dependent maximum δ value. Fig. 5.3 displays the enthalpy Δh_δ° and entropy Δs_δ° of $Ca_{0.9}Sr_{0.1}MnO_{3-\delta}$. Both enthalpy and entropy values exhibit a development over the non-

stoichiometric range studied, as reported in previous studies.[66] The enthalpy is constant. On the contrary, the entropy decreases with an increasing reduction extent. Therefore, model 2.12 on p. 16 is fitted to the experimental data of the entropy (blue line). The resulting thermal entropy $\Delta s^\circ_{\mathrm{th}}$ and the dimensionless parameter γ are used for further analysis. The mean value is calculated to get a reduction extent independent enthalpy Δh° (black line).

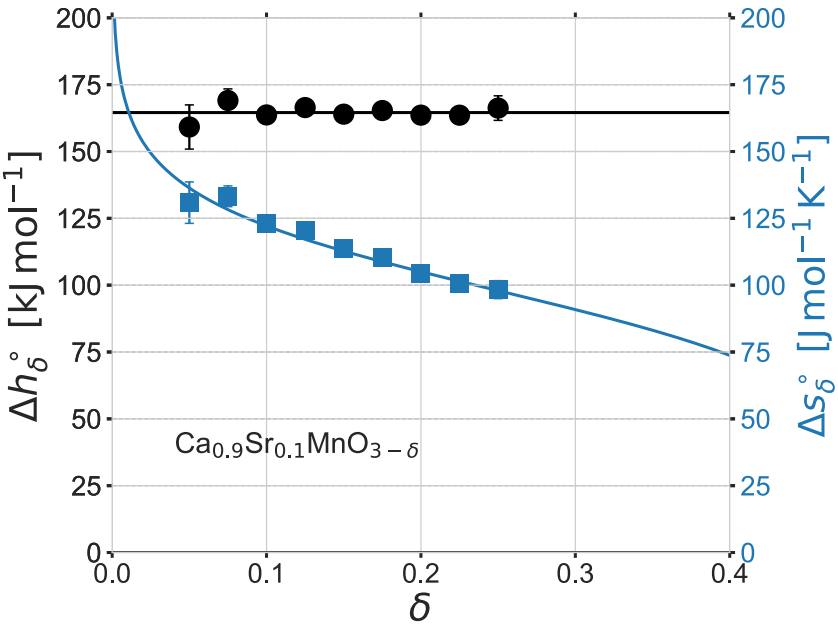

Figure 5.3.: The black circles display the experimental enthalpy Δh°_δ and and the blue squares the experimental entropy Δs°_δ of $Ca_{0.9}Sr_{0.1}MnO_{3-\delta}$. The values are gained through the *van't Hoff* approach. The error bars assign the numerical errors of the fit. Due to the independence of the enthalpy on the reduction extent, the material-dependent enthalpy is the data's mean value. The black line indicates this mean value. The model eq. 2.12 on p. 16 (blue line) represents the reduction extent dependent behavior of the entropy. Reproduced from *Klaas et al.*[98] with permission from the PCCP Owner Societies.

The described procedure is carried out for all materials with different Sr content. This results in an enthalpy Δh° (Fig. 5.4a) and thermal entropy $\Delta s^\circ_{\mathrm{th}}$ (Fig. 5.4b) dependent on the Sr content. Both thermodynamic values have a decreasing trend with an increasing Sr content.

The dimensionless parameter γ is summarized in table 5.1. All values are around one, which means that most of the defects form clusters.[66]

Comparing the results of $CaMnO_{3-\delta}$ with previous studies,[66,109] the enthalpy Δh° calculated in this study is found to be about 20 kJ/mol higher and the thermal entropy $\Delta s^\circ_{\mathrm{th}}$ to be about 20 J/mol higher. In contrast, they are about the same order of magnitude as the values of *Goldyreva et al.*[114] Moreover, the results of $Ca_{0.95}Sr_{0.05}MnO_{3-\delta}$,[28] $Ca_{0.9}Sr_{0.1}MnO_{3-\delta}$[28] and $Ca_{0.6}Sr_{0.4}MnO_{3-\delta}$[115] are comparable as well. Therefore, the conclusion is that the

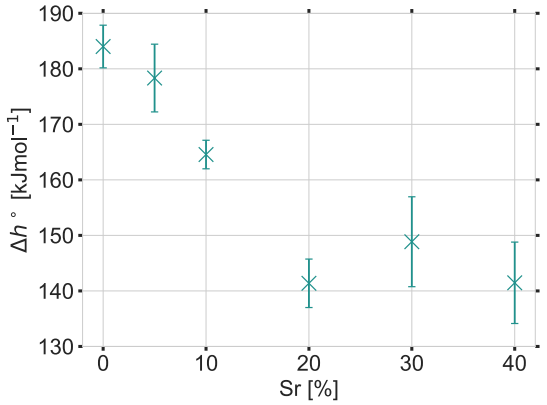

(a) Dependence of the enthalpy Δh° on the Sr content.

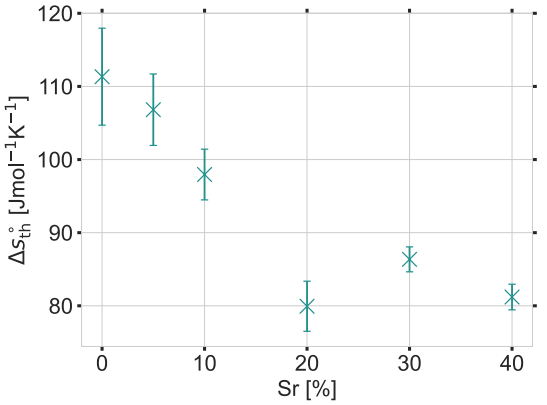

(b) Dependence of the thermal entropy $\Delta s^\circ_{\mathrm{th}}$ on the Sr content.

Figure 5.4.: Thermodynamic values in dependence of the Sr content. The error bars assign the standard deviation of Δh°_δ and the numerical error of the fit of Δs°_δ. Both thermodynamic values show a decreasing tendency with increasing Sr content. Reproduced from *Klaas et al.*[98] with permission from the PCCP Owner Societies.

Table 5.1.: Dimensionless parameter γ which represents the number of moles being mixed (Sec. 2.5, p. 15).

Sr [%]	γ [-]
0	0.98(3)
5	1.07(2)
10	1.04(2)
20	1.05(2)
30	1.10(1)
40	1.09(1)

discrepancies are assigned to experimental deviations. This conclusion is supported by the enthalpy obtained with DFT calculations. Its value of $\Delta h^\circ = 173\,\mathrm{kJ/mol}$[34] lies between the two experimental values.

Imponenti et al.[28] and *Albrecht et al.*[115] discuss a reduction extent and temperature dependent enthalpy. This dependence is particularly evident at small reduction extents, especially at $\delta < 0.1$ for $Ca_{0.95}Sr_{0.05}MnO_{3-\delta}$ and $\delta < 0.05$ for $Ca_{0.6}Sr_{0.4}MnO_{3-\delta}$. The reduction extent and temperature-dependent enthalpy is not observed in the measurements presented here (Fig. 5.3), which may be related to the lack of accuracy of the *van't Hoff* method in this regime.

As presented in Sec. 4.1, the substitution of Ca by Sr leads to a variation of the crystal structure. First, the orthorhombic distortion of the ideal cubic perovskite decreases with an increasing amount of Sr content. *Curnan et al.*[116] use DFT studies to analyze that the energy for forming oxygen vacancies is higher for orthorhombic structures than for cubic

structures. Thus, the observed decreasing enthalpy can be caused by the transition to the cubic structure. Second, the increasing Sr content leads to an elongation of the bond length between the *A*-site ion and the oxygen ion O1 located in the *A*-plane. This elongation leads to a lower binding energy, which facilitates the release of oxygen and thus reduces the enthalpy of reduction.

The oxygen gas entropy is assumed to be constant $\frac{1}{2}s^{\circ}_{O_2} = 124(3)\,\mathrm{J/molK}$ [88] over the temperature range investigated (873–1473 K) because it only varies slightly in this range. Furthermore, the thermal entropy $\Delta s^{\circ}_{\mathrm{th}}$, which is composed of the vibrational entropy and the oxygen gas entropy, is always below this value (Fig. 5.4b). Overall, the thermal entropy decreases with an increasing Sr content. These results show that first, the oxygen release leads to a negative change in the vibrational entropy, and second, the amount of Sr enhances this effect.

In summary, the *van't Hoff* approach is a viable tool for extracting the thermodynamic properties of a material. Their validity is limited at low reduction levels. Moreover, due to the divergence of literature values on thermodynamic properties, the exact values appear to depend on the experimental conditions. Nevertheless, it provides crucial trends.

Due to decreasing enthalpy and entropy with an increasing Sr content, the reduction extent increases under the same experimental conditions. This means that, for example, in the case of air separation, more nitrogen can be produced by the same amount of material. On the contrary, the reduced enthalpy as well decreases the oxygen affinity and thus reduces the equilibrium oxygen partial pressure. The correlation between enthalpy and oxygen affinity must be considered for the required purities.

The observed correlation between the change in crystal structure and the change in thermodynamic properties is of particular interest, as it may serve to predict changes in thermodynamic properties from knowledge of crystal structure changes alone. Therefore, an extension of the materials studied is required to investigate this hypothesis further.

6. Microstructure Analysis

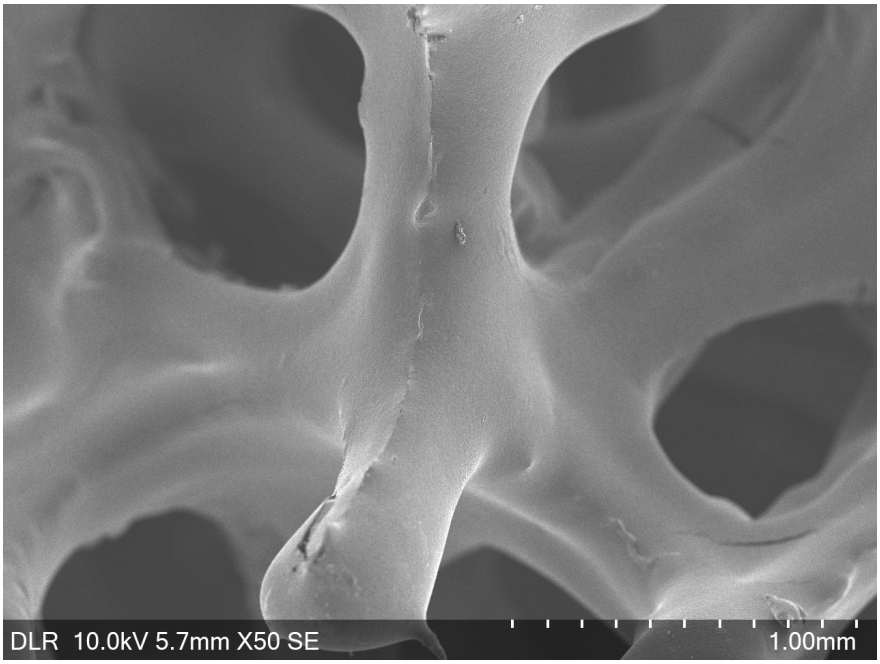

Figure 6.1.: Exemplary scanning electron microscopy image of a foam. Shown are the struts of a foam. Scanning electron microscopy reveals the structure of the surface of the material. This chapter uses additional methods besides scanning electron microscopy to analyze the microstructure.

To recap, the term 'microstructure' is defined by structures above the atomic level. The term 'macrostructure,' on the other hand, refers to foams, pellets, or granules. Knowledge and understanding of the microstructure are relevant for applying redox materials, as they can influence essential properties such as mechanical stability or redox kinetics. Therefore, this chapter will focus first on the impact of the Sr content on the microstructure and second on the impact of different macrostructures and production procedures on the microscopic structure.

Before analyzing the impact of the Sr content, macrostructures, and production procedures on the microscopic structure, the distribution of the elements in the material is investigated. This is done through EDS (Sec. 3.6.2, p. 40). A representative result of a foam made out of $Ca_{0.8}Sr_{0.2}MnO_{3-\delta}$ can be found in Fig. 6.2. All elements are distributed homogeneously. Thus, the result underlines that a strontium ion substitutes the calcium ion without forming two separate phases. This implies that the microstructure is not assumed to be determined by individual phases but that the influence of the elements is homogeneously distributed. This statement holds for all samples analyzed.

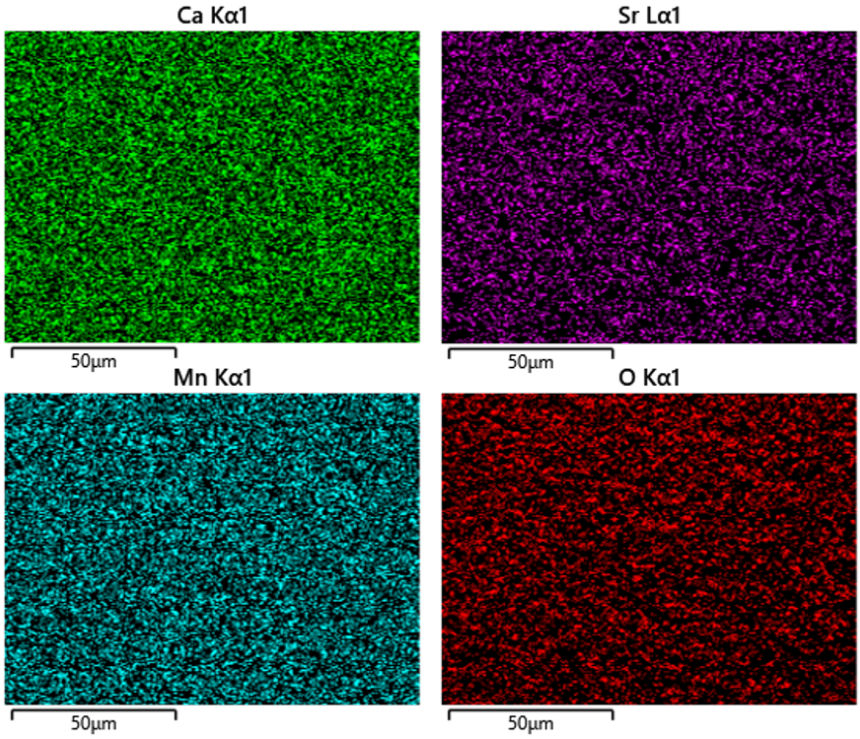

Figure 6.2.: EDS analysis of a $Ca_{0.8}Sr_{0.2}MnO_3$ foam. All elements are distributed homogeneously.

6.1. Material Composition Dependent Microstructure

Fig. 6.3 displays the SEM image (details in Sec. 3.6.2, p. 40) of powder of $Ca_{1-x}Sr_xMnO_3$ with varying Sr concentrations. The powder was prepared via the solid-state method (Sec. 3.1.2, p. 31). Starting with Fig. 6.3a, which displays $CaMnO_3$ without any Sr substitution. The surface morphology reveals a porous surface with an agglomeration of small particles. The size of the small particles is spread over a range of $d \approx$3–70 µm. Remarkably, the larger particles feature holes with a diameter of $d \approx 1$ µm and grain boundaries. The size of the grain is similar to that of the small particles $d \approx 3$ µm and larger with up to $d \approx 10$ µm.

Analyzing the evolution of the microstructure with increasing Sr content, the surface remains porous. However, it is important to note that the size distribution of the small particles changes, as seen in Fig. 6.3. For example, considering Fig. 6.3e, which shows the composition with the highest Sr content of 40 %. The powder consists solely of agglomerates of smaller, strongly branched particles. Their size is comparable to the smaller particles mentioned above ($d \approx 3$ µm). The larger particles with holes and grain boundaries are no longer identifiable, resulting in a homogeneous size distribution.

Generally, a substituent may be partially soluble in the principal component, but finally, the solubility limit is reached above which segregation occurs at grain boundaries. The mobility of the ions at the grain boundaries is slowed down by segregated substituents.[117] Here, Sr is the substituent, and $CaMnO_3$ is the principal component. The decreased mobility leads to smaller crystallites and more grain boundaries for an increasing Sr content.

In addition, the defects in the crystal lattice caused by the substitution can serve as nucleation sites, increasing the number of crystallites and resulting in smaller particles with increasing Sr content. Moreover, several in-situ experiments, such as XRD and SEM, as described by *Li et al.*,[118] would be beneficial to investigate the underlying growth mechanisms further.

The crystallite size D of the different samples is analyzed by applying the Scherrer formula from X-ray line width:

$$D = \frac{S\lambda}{\mathrm{FWHM}} \cos(\theta).^{[119,120]} \tag{6.1}$$

Here, $S = 0.89$ is the shape factor,[103] λ is the wavelength of the X-ray, FWHM is the full width at half maximum of the major peak, and θ is the Bragg's angle of the major peak.

The required XRDs were performed using a cobalt anode (details in Sec. 3.3, p. 34). The results for the different Sr contents are shown in Tab. 6.1. Samples without Sr content, medium Sr content, and maximum Sr content were analyzed to identify the trend. Similar to *Pawar et al.*,[103] the increasing Sr content leads to a decreasing crystallite size. This

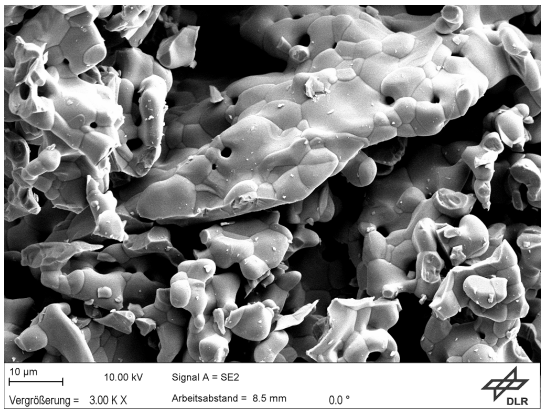

(a) CMO

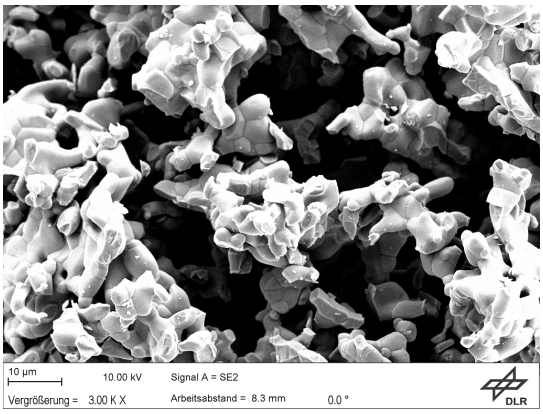

(b) CS10MO

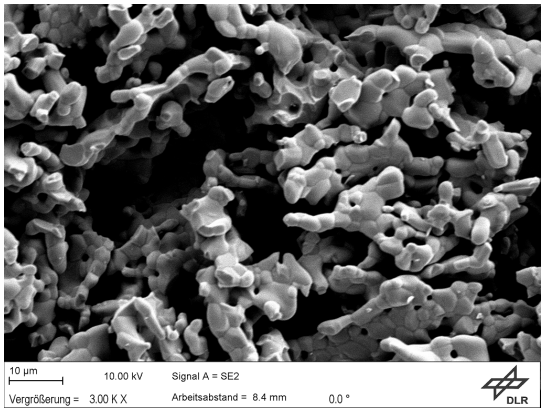

(c) CS20MO

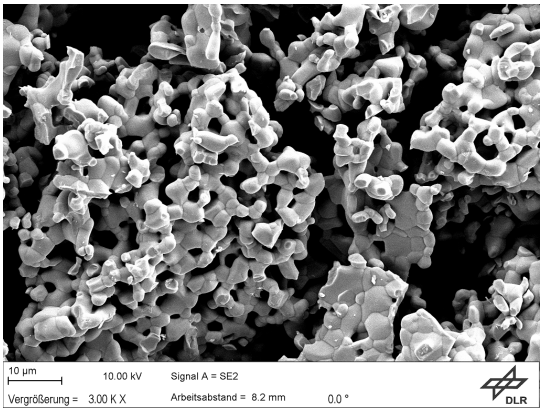

(d) CS30MO

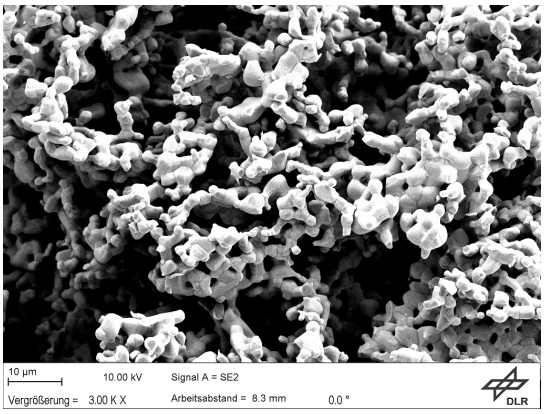

(e) CS40MO

Figure 6.3.: SEM image of powder with varying Sr content. All powders exhibit an agglomeration of particles. However, the size of the particles depends on the amount of Sr. Increasing Sr content decreases the particle size, and the particle size distribution becomes more homogeneous than samples with less Sr content.

trend directly supports the previously mentioned hypothesis that the defects decrease the crystallites' size.

Table 6.1.: Crystallite size D of different Sr contents calculated by the Scherrer equation 6.1. Besides, the full width at half maximum FWHM and Bragg's angle θ of the major peak are displayed.

Sample	FWHM [°]	θ [°]	D [nm]
CMO, powder	0.085(8)	39.874(7)	232(22)
CS20MO, powder	0.088(5)	39.531(2)	170(9)
CS40MO, powder	0.099(7)	39.401(7)	140(10)

After analyzing the impact of the Sr content on powder, granules with different Sr contents are examined as well (Fig. 6.5). The granules have a diameter of d =1.25–1.6 mm, except of the granule displayed in Fig. 6.5b which has a diameter of d >2.24 mm. All samples are porous. Similar to the powders, agglomeration of particles is observed. This is shown exemplarily in Fig. 6.4. It displays a close-up of the granule in Fig. 6.5b. As well, the inhomogeneities in porosity become apparent. Some areas are sintered more densely than others. It is noted that the magnification is smaller in this figure compared to the image of the powders.

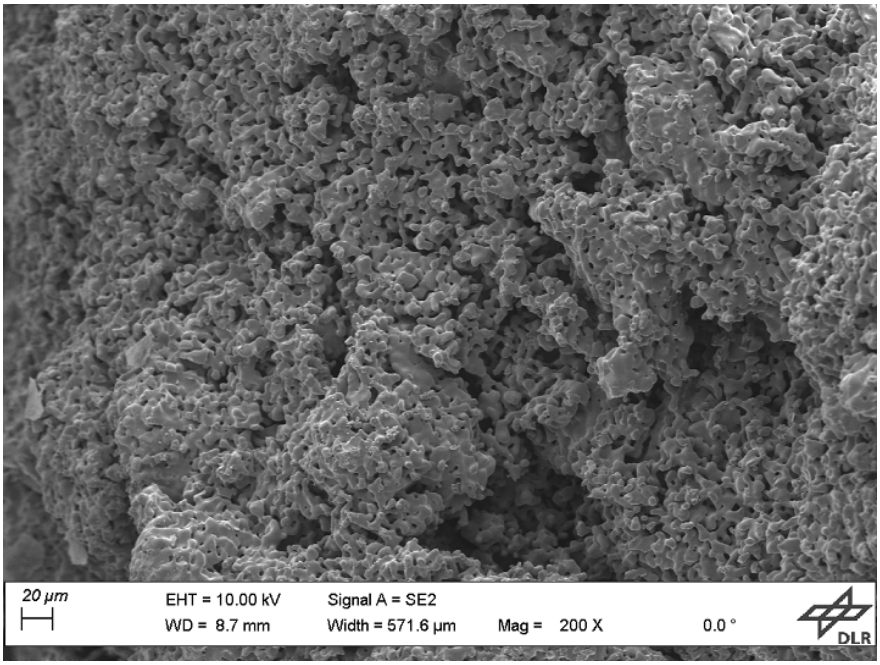

Figure 6.4.: Close-up of the granule displayed in Fig. 6.5b. The surface appears to be an agglomeration of particles. Whereby some surfaces are sintered more densely and others less densely.

The granule with 0 % Sr, shown in Fig. 6.5a, has an inhomogeneous surface with big trenches which have a width of approximately 95 µm. Besides the trenches, denser areas are

apparent. This appearance is independent of the total size of the granule (Fig. 6.5b). The granule with 40 % Sr still features trenches, but they are narrower and less apparent. Moreover, no dense areas are observed. All in all, the surface appears to be more homogeneous.

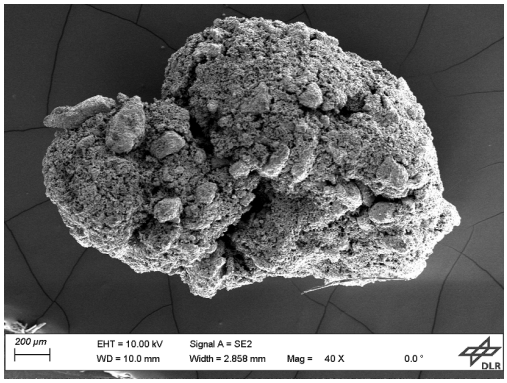

(a) CMO

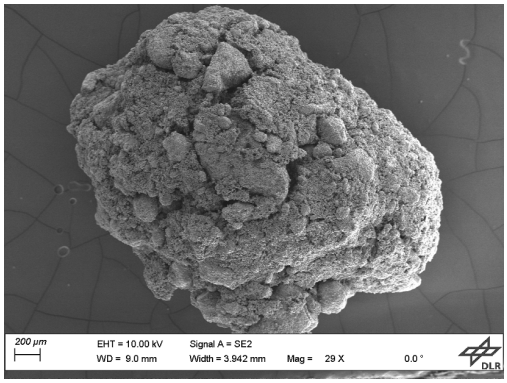

(b) CMO, $d > 2.24\,\mathrm{mm}$

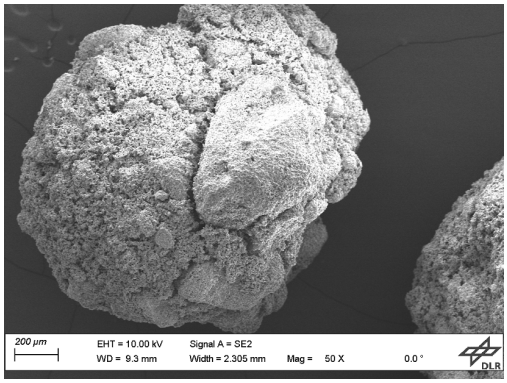

(c) CS10MO

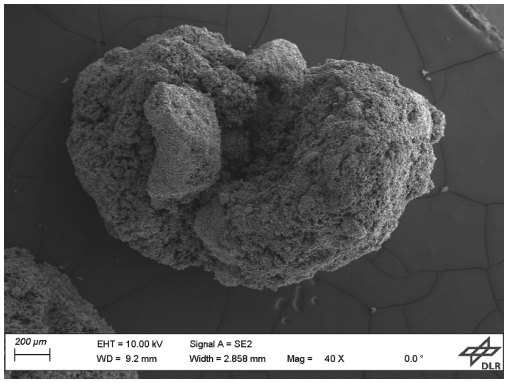

(d) CS20MO

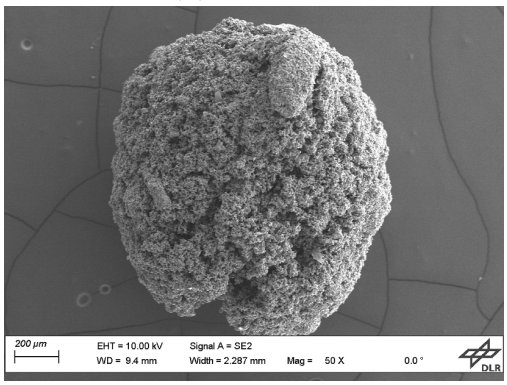

(e) CS30MO

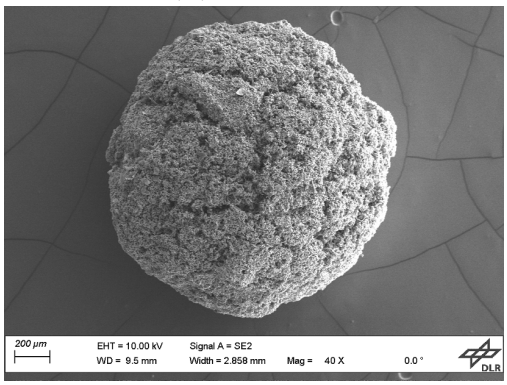

(f) CS40MO

Figure 6.5.: SEM image of granules with varying Sr content. All granules exhibit a rough surface, but the homogeneity of the surface depends on the content of Sr.

Analyzing the evolution of the granules with increasing Sr content, a gradual increase in homogeneity of the surface is evident. The implication is that the powder substantially affects the homogeneity of the granules.[117] The broader distribution of the size of the particles

for 0 % Sr results in a more inhomogeneous surface. As the homogeneity of the particles increases, the resulting granule becomes more homogeneous.

The homogeneity of the granules can influence mechanical stability. For example, trenches can be seen in the granules with 0 % Sr, as described previously. Under mechanical or thermal stress, this can lead to the easier breakage of the material at these points. In addition, under mechanical load, the more densely sintered areas may be more stable and thus persist, resulting in larger particles in the event of a fracture. In contrast, the more homogeneous sample, e.g., $Ca_{0.6}Sr_{0.4}MnO_3$, might be more resilient to mechanical stress, and in the event of fracture, it results in more homogeneous fragments.

To examine if the different shapes of the granules result in different specific surface areas, N_2 porosimetry was conducted (Sec. 3.6.3, p. 40). The results are displayed in Tab. 6.2. At this point, it is emphasized that the results are close to the detection limit of a total surface area of 1 m^2 since only a few grams (2–4 g) can be used due to the size of the sample holder.

The total size of the granules does not affect the surface area. Since not enough sample of $Ca_{0.6}Sr_{0.4}MnO_3$ with a diameter of 1.25–1.6 mm was available and the measurement revealed that the diameter does not affect the surface area, $Ca_{0.6}Sr_{0.4}MnO_3$ granule with $d > 2.24$ mm was used. The Sr content as well does not impact the surface area, although $Ca_{0.6}Sr_{0.4}MnO_3$ has a slightly higher surface area. However, this might be assigned to the inaccuracy due to the small total surface area. None of the samples showed meso- or micropores.

Table 6.2.: Specific surface area of samples depending on Sr content. The data was gained by N_2 porosimetry (exp. details in Sec. 3.6.3).

Sample	surface area [m^2/g]
CMO, granule d =1.25–1.6 mm	0.311
CS20MO, granule d =1.25–1.6 mm	0.292
CS20MO, granule d >2.24 mm	0.249
CS40MO, granule d >2.24 mm	0.513

The results of mercury porosimetry (Sec. 3.6.3, p. 40) for the impact of different amounts of Sr are summarized in Fig. 6.6. The left y-axis displays the normalized cumulative pore volume per g of material, which measures the porosity. Moreover, the total macro-porosity is shown above each curve. The right y-axis displays the differential pore volume distribution. For clarity, the curves are plotted with an offset.

The porosity of all samples is similar, and no discernible trend emerges. The pore diameters are primarily in the range of 3–40 $\times 10^3$ nm. A significantly smaller proportion of pores have a diameter around the value of 10 nm. The d50 value (Tab. 6.3) is similar for all samples and likewise does not reveal any trend. These observations show that the Sr content does not influence the porosity and pore distribution. This result is expected since all specimens

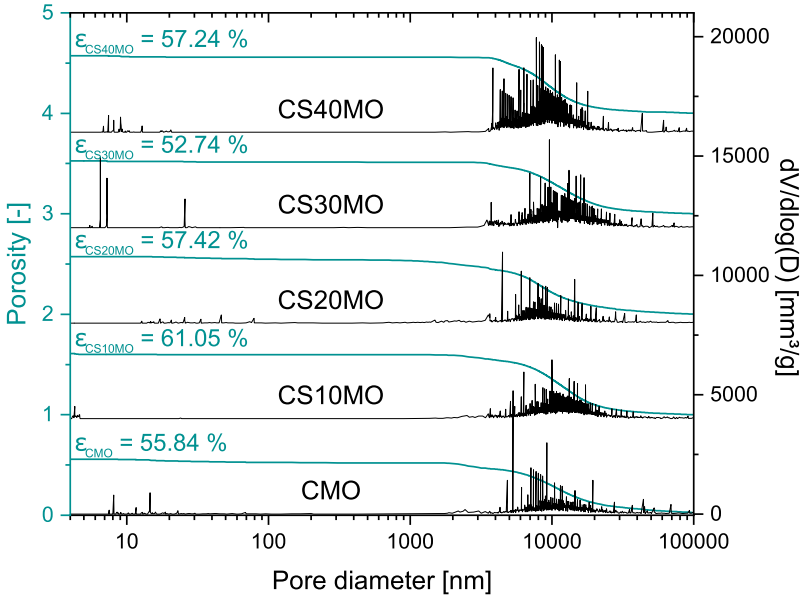

Figure 6.6.: Sr content dependent porosity determined by Hg porosimetry (exp. details in Sec. 3.6.3). Displayed are the normalized cumulative pore volume per g of material which is a measure for the porosity (left axis) and the differential pore volume distribution (right axis). Additionally, the total porosity is assigned for each sample.

were produced with the same process, and the sintering temperature and time were identical for all specimens. Additionally, the diameter of the granules does not affect the porosity (Sec. A.10, p. 148). Moreover, the result highlights that the manufacturing process is reproducible.

Table 6.3.: d50 pore diameter determined by Hg porosimetry (exp. details in Sec. 3.6.3) dependent on Sr content. The granules with different Sr contents have comparable values and do not reveal a trend.

Sample	d50 [nm]
CMO, granule d =1.25–1.6 mm	10475
CS10MO, granule d =1.25–1.6 mm	11259
CS20MO, granule d =1.25–1.6 mm	8224
CS30MO, granule d =1.25–1.6 mm	11447
CS40MO, granule d =1.25–1.6 mm	9292

6.2. Macrostructure and Production Dependent Microstructure

For the applications, not only are granules of interest, but also foams are considered.[95] Therefore, the microstructure of foams produced via two different routes (Sec. 3.2.2, p. 32) is covered in the following. The foam whose slurry was processed with a ball mill is called $Foam_{BM}$, and the foam whose slurry was processed with a magnetic stirrer is called $Foam_{MS}$. To focus on the impact of the macrostructure, $Ca_{0.8}Sr_{0.2}MnO_{3-\delta}$ is used for all samples. $Ca_{0.8}Sr_{0.2}MnO_{3-\delta}$ was selected since it has an intermediate Sr concentration of the samples investigated.

The particle size distribution (PSD) of the powder used for the production of the samples is analyzed via a laser scattering particle size distribution analyzer (details in Sec. 3.6.1, p. 40). Four different treated powders of $Ca_{0.8}Sr_{0.2}MnO_3$ were analyzed. P_M is a manual grounded powder, P_{BM} is a ball-milled powder (details in Sec. 3.2.2, p. 32), P_{2BM} is a ball-milled powder that has been ball-milled a second time as a slurry (details in Sec. 3.2.2, p. 32) and $P_{BM,MS}$ is a ball-milled powder that has been magnetically stirred as a slurry (details in Sec. 3.2.2, p. 32).

Table 6.4.: Particle size distribution of used powders measured via a laser scattering particle size distribution analyzer (details in Sec. 3.6.1, p. 40).

Sample	d10 [µm]	d50 [µm]	d90 [µm]	Mean [µm]	Standard Dev. [µm]
P_M	7.1	16.7	323.6	108.8	139.2
P_{BM}	4.5	6.6	9.9	6.9	2.2
P_{2BM}	1.7	3.1	5.4	3.4	1.5
$P_{BM,MS}$	2.8	5.0	8.2	5.3	2.2

The PSD shows that, as expected, the manually ground powder P_M has the largest mean particle size (d50), and the PSD is the widest for this powder. Ball-milling the powder decreases both the mean particle size and the width of the distribution of the particle sizes. An additional ball-milling of the suspension also decreases the PSD's width and reduces the average particle size by half. An additional magnetic stirring, instead, only slightly reduces the mean particle size and has no impact on the width of the PSD.

In Fig. 6.7 are the $Ca_{1-x}Sr_xMnO_3$ foams produced by the two stated procedures. Both structures are similar. They are composed of struts with a triangular shape. Although these samples have not been investigated in detail, the struts are hollow since this has been observed before for similar materials with the same production procedure.[95] This structure is typical for ceramic foams manufactured via the polyurethane replica method and a result

of the sublimation of the PU foam template used.[121,122] Some defects in the surface, such as cracks and holes, are noticeable.

Already indicated here is the difference between the two samples. $Foam_{MS}$, made out of $P_{BM,MS}$, has a rougher and $Foam_{BM}$, made out of P_{2BM}, has a smoother surface. The different structures of the surface will be analyzed in more detail in the following.

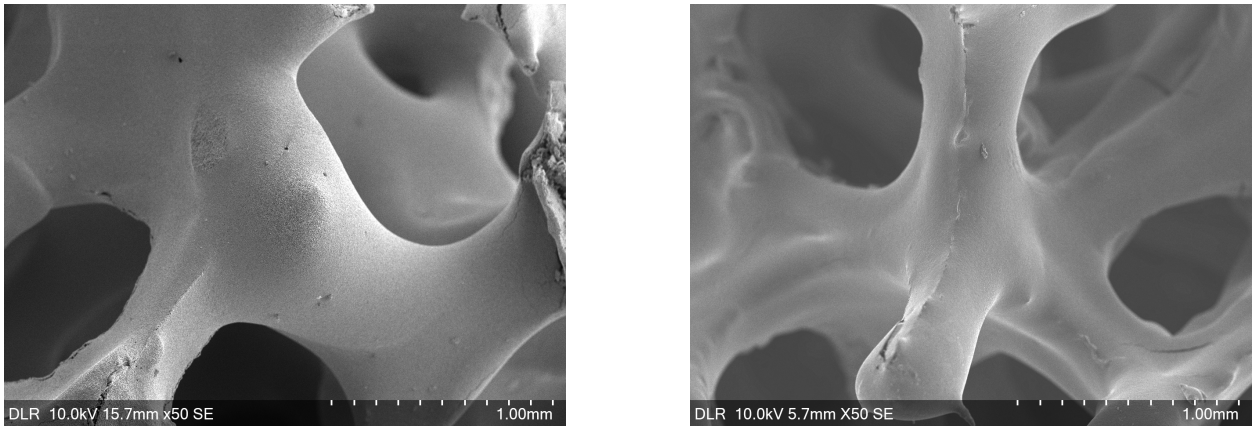

(a) $Foam_{MS}$ **(b)** $Foam_{BM}$

Figure 6.7.: SEM of the shape of the foams. Both foams exhibit a typical structure with struts having a triangular shape. Already indicated here is a difference in the surface since foam $Foam_{MS}$ appears to have a rougher surface.

After analyzing the shape of the foams, the focus lies on the different surface properties of the samples. To compare the effect of the shape, pellets were produced additionally, again with two different treatments of the powder (Sec. 3.2.3, p. 34). Here, the pellet whose powder was milled with a ball mill (P_{BM}) is called $Pellet_{BM}$ and the pellet whose powder was milled manually (P_M) is called $Pellet_M$.

A close-up of the surface of the samples is displayed in Fig. 6.8. All samples consist of $Ca_{0.8}Sr_{0.2}MnO_3$. The $Pellet_{BM}$ has a densely sintered surface with several holes of $d \approx 1\,\mu m$ (Fig. 6.8a). Grain boundaries are visible. Contrary, the $Pellet_M$ (Fig. 6.8b) has a porous surface. However, some areas exhibit a densely sintered surface. In general, the surface appears to be a mesh of individual grains sintered.

The $Foam_{BM}$ (Fig. 6.8c) has as well a densely sintered surface and visible grain boundaries, similar to the $Pellet_{BM}$. Still, no holes are apparent in the foam, but a trench with a width below 1 µm. This trench could be caused by the evaporation of gas during debinding.

In contrast, the surface of the $Foam_{MS}$ (Fig. 6.8d) has a similar appearance as $Pellet_M$. The surface is rough without any densely sintered areas. The grains are smaller than the grains of $Foam_{BM}$ and have a diameter $d \approx 5\,\mu m$.

The granule also has a porous surface and is a mesh of individual particles with a coral-like appearance.

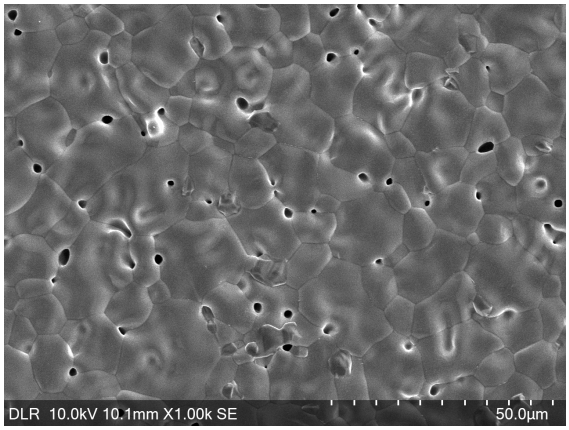

(a) $\text{Pellet}_{\text{BM}}$

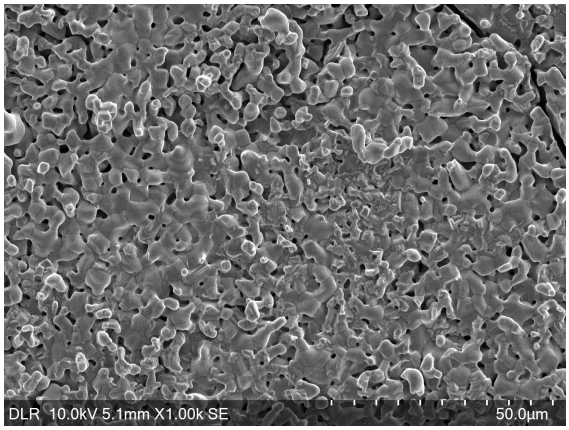

(b) Pellet_{M}

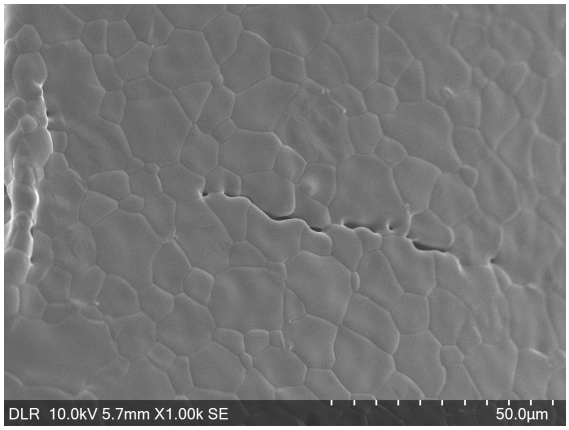

(c) Foam_{BM}

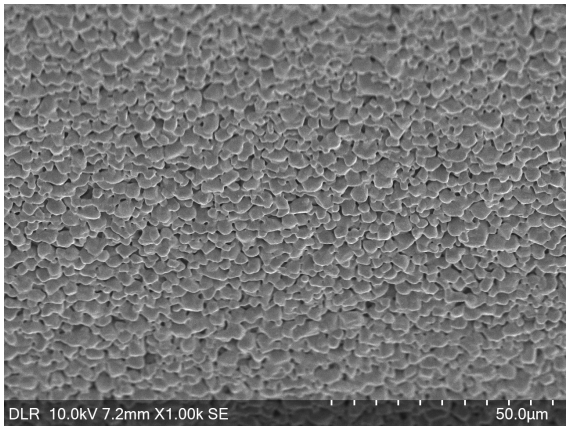

(d) Foam_{MS}

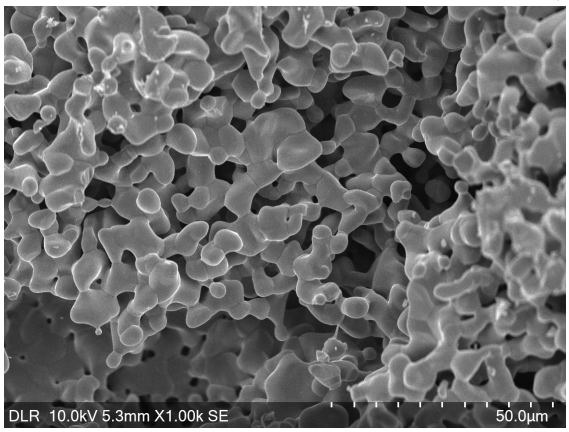

(e) granule

Figure 6.8.: SEM close-up of different macrostructures and production procedures. All samples are $Ca_{0.8}Sr_{0.2}MnO_3$. Highlighted is that the underlying powder governs the difference in the surface structure. Finer powder results in a densely sintered surface, and coarser powder produces a rough surface.

For the different shapes, the crystallite size was investigated (Tab. 6.5). Supporting the results of the SEM, the sample with the densely sintered surface, $Foam_{BM}$, has the biggest crystallite size, and the corresponding $Foam_{MS}$ has a smaller crystallite size. Here, the granule and the $Foam_{MS}$ have similar crystallite size and is even similar to the crystallite size of the powder. The crystallite size of $Foam_{BM}$ is significantly higher than the powder.

Table 6.5.: Crystallite size D of different macrostructures and production procedures, calculated by the Scherrer equation 6.1 on p. 77. Besides, the full width at half maximum FWHM and Bragg's angle θ of the major peak are displayed.

Sample	FWHM [°]	θ [°]	D [nm]
CS20MO, powder	0.088(5)	39.531(2)	170(9)
CS20MO, granule d =1.25–1.6 mm	0.086(3)	39.530(1)	175(7)
CS20MO, $Foam_{BM}$	0.055(2)	39.472(1)	262(9)
CS20MO, $Foam_{MS}$	0.092(4)	39.478(3)	158(7)

The surface area for different macrostructures is summarized in Tab. 6.6 to further analyze the morphology. The surface area is the highest for $Foam_{MS}$. This is expected due to the rough surface. The $Foam_{BM}$ has half of the surface area. The granules have a slightly smaller surface area. The reason for this is that the foams have hollow struts. When these are cracked open, the inside provides additional surface area. Although the exact values should not be taken for granted because of the proximity to the detection limit, this deviation is sufficiently clear that an increased surface area of $Foam_{MS}$ should be assumed. Similar to the granules, the foams do not exhibit micro- or mesopores.

Table 6.6.: Specific surface area of samples depending on the macrostructure and production procedure. The data was gained by N_2 porosimetry (exp. details in Sec. 3.6.3).

Sample	surface area [m^2/g]
CS20MO, granule d =1.25–1.6 mm	0.292
CS20MO, $Foam_{MS}$	1.117
CS20MO, $Foam_{BM}$	0.598

Analyzing the porosity of the different macrostructures and production procedures, the samples with a smaller powder size distribution exhibit a smaller porosity than the corresponding sample with higher powder size distribution. The smallest porosity is 2.77 % for $Pellet_{BM}$. The highest porosity is 57.42 % for $Foam_{MS}$, which is comparable to the porosity of the granule. The porosity trends support those mentioned above of the surface analyzed via SEM.

The d50 value of the pore size distribution is displayed in Tab. 6.7. The high value of $Foam_{BM}$ (d50=45 059 nm) indicates that the highest number of pores measured is the filling

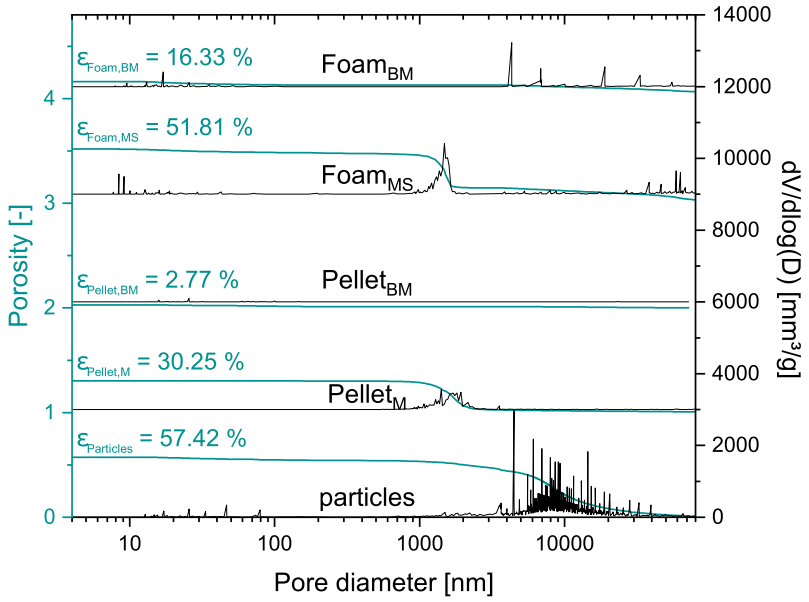

Figure 6.9.: Macrostructure dependent porosity for $Ca_{0.8}Sr_{0.2}MnO_3$. Displayed are the normalized cumulative pore volume per g of material, which measures the porosity (left axis) and the differential pore volume distribution (right axis). Additionally, the total porosity is assigned for each sample.

of the hollow struts. Whereas, d50 of $Foam_{MS}$ and $Pellet_M$ have a similar d50 value. d50 of the granules is slightly higher, which is explained by the high amount (23 wt%) of binder used for the production. $Pellet_{BM}$ has the smallest d50, which supports the results of the SEM.

Table 6.7.: d50 pore diameter determined by Hg porosimetry (exp. details in Sec. 3.6.3) dependent on the macrostructure.

Sample	d50 [nm]
CS20MO, granule d =1.25–1.6 mm	8224
CS20MO, $Foam_{MS}$	1528
CS20MO, $Foam_{BM}$	45059
CS20MO, $Pellet_M$	1689
CS20MO, $Pellet_{BM}$	143

The powder's PSD for producing the different macrostructures governs the sample's microstructure. The finer powder results in a denser sintered surface, whereas the coarse powder results in more porous structures with a rough surface under otherwise the same conditions. The positive impact of finer powder on the sintering behavior has been shown for the production of ceramic pellets.[123] The additional difference between the macrostructures, e.g., pellet and foam, is explained by, first, the addition of organic material, which

is decomposed during the following process. This results in less dense material since the organics are evaporated and, therefore, creates voids on the one hand because of the lack of material and on the other hand because the gas can form tunnels in the material. Second, the pressure applied to the pellets compresses the material and therefore leads to a higher density which is supporting for sintering.[124]

6.3. Summary of the Microstructure Analysis

This chapter first focuses on the impact of the material composition on the macroscopic structure. Therefore, samples of $Ca_{1-x}Sr_xMnO_3$ with different Sr contents are qualitatively analyzed. An increasing Sr content resulted in smaller crystallites and a powder with a more homogeneous particle size distribution. No analysis of the underlying growth mechanism is possible with the experiments available. The more homogeneous powder, in turn, led to more homogeneous granules, which were produced from the same powders. Finally, the inhomogeneity of the granules is discussed to have a negative impact on mechanical stability.

All granules are highly porous. Here, the porosity is similar for all compositions. The pores are in the macro range. No meso- or micropores are detected. Due to the similar porosity results, the manufacturing process's reproducibility is given. In addition, the similarity of all the samples implies that in thermochemical processes, the surface adsorption is not affected by the Sr content of the material.

Second, the impact of the macrostructure and the production procedure is analyzed. Foams with a typical structure for the method used are successfully manufactured, and the macrostructure is independent of the fineness of the powder used.

Contrary, the finer powder resulted in bigger crystallite size and denser sintered samples. This observation is underlined by the increased surface area and higher porosity for samples produced with coarser powder. Therefore, the microstructure can be tuned by the fineness of the powder. No meso- or micropores are detectable in any of the specimens. The different microstructures may impact the kinetic properties of the material.

7. Kinetic analysis

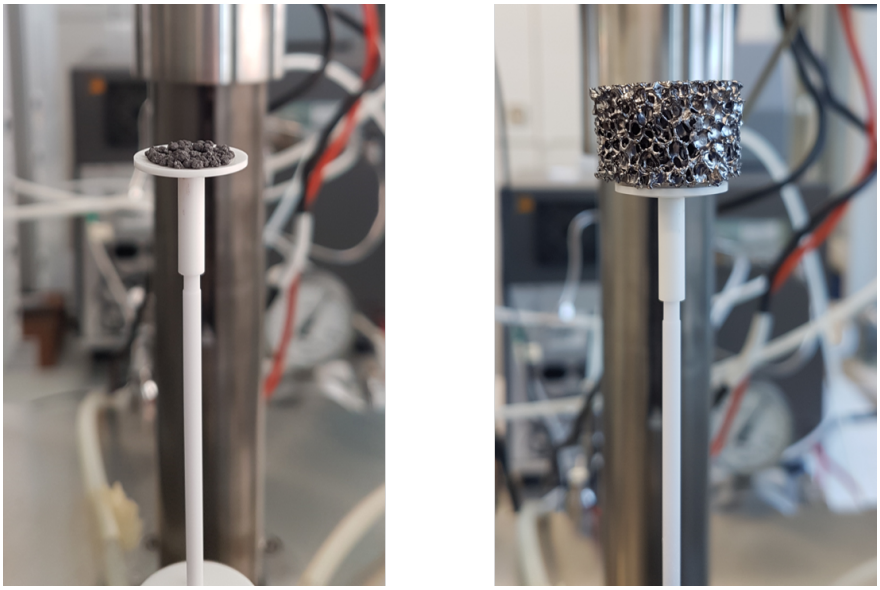

Figure 7.1.: A thermogravimetric analyzer also measured the kinetics of $Ca_{1-x}Sr_xMnO_{3-\delta}$. In contrast to thermodynamics, however, no powder was used, but various macrostructures, such as granules or foams.

This chapter is partially based on the following peer-reviewed publication, which is authored by the author of this thesis:

L. Klaas, B. Bulfin, D. Kriechbaumer, M. Roeb and Ch. Sattler. Impact of the Sr content on the redox thermodynamics and kinetics of $Ca_{1-x}Sr_xMnO_{3-\delta}$ tailored properties. Physical chemistry chemical physics: PCCP, 25(13):9188-9197, 2023. doi: 10.1039/D3CP00267E.

The kinetics of the material are investigated with an isothermal relaxation kinetic study. First, in this chapter, the material composition-dependent kinetics are analyzed to identify the impact of the Sr content. Here, the impact of temperature and oxygen partial pressure on the oxidation kinetics is of interest. The measures used are the evolution of the conversion extent X (eq. 7.1), the reaction half-lives (eq. 7.2), and the activation energy which is gained through the isoconversional method (Sec. 2.6.1, p. 17) and the fitting of a kinetic model (Sec. 2.6.2, p. 18). Moreover, the temperature-dependent reduction kinetics are analyzed.

Granules were used to study the material composition-dependent kinetics to avoid time-varying inhomogeneities in the surrounding oxygen concentration due to a dense packing of powder piles.

Subsequently, the impact of different macrostructures and microstructures on the oxidation kinetics is analyzed.

7.1. Material Composition Dependent Kinetics

Details on the experimental configuration for the kinetic analysis can be found in 3.7 on p. 41. Throughout this study, the impact of the minor particle size distribution of the granules 1.25–1.6 mm is first identical for all compositions analyzed and second is assumed to be negligibly small. Proof of this assumption can be found in Sec. 7.2, and the author concludes that the results presented in this section are based solely on composition.

The extent of conversion $X(t)$ is a quantity that indicates the progress of oxidation. It is calculated by:

$$X(T) = \frac{\delta_0 - \delta(t)}{\delta_0 - \delta_\infty} \tag{7.1}$$

δ_0 : non-stoichiometry at $t = 0$

δ_∞ : equilibrium non-stoichiometry the sample converges to.

$\delta(t)$ is the time-dependent non-stoichiometry calculated by eq. 3.3 on p. 37 based on thermogravimetric measurements.

The extent of conversion $X(t) \in [0, 1]$ equals zero when the material is still in the reduced state, and no re-oxidation occurred. It reaches one when the material is completely oxidized. Its evolution gives evidence about the oxidation kinetics and is a convenient measure for the kinetic analysis.[70]

δ_0 is the non-stoichiometry of the reduction $\delta_0 = \delta_{\mathrm{red}}(T = 1173\,\mathrm{K}, p_{\mathrm{O_2}} = 0.01\,\mathrm{bar})$. The thermodynamic analysis revealed that for all investigated oxidation temperatures and sam-

ples, the equilibrium non-stoichiometry δ_∞ equals zero. Additionally, the curves of the change in mass show that this state is reached if the oxidation time is sufficient.

The impact of the temperature on the oxidation kinetics for $Ca_{0.8}Sr_{0.2}MnO_{3-\delta}$ is displayed in Fig. 7.2. For temperatures below 553 K, the oxidation is not completed within 150 min. Contrary, for oxidations at temperatures above 633 K, the oxidation takes less than 10 min. The general trend is that an increase in temperature leads to faster oxidation kinetics. Naturally, higher oxidation temperatures can be used for the application. However, higher temperatures are not suitable for studying oxidation kinetics since the reaction proceeds primarily in a time window when a change in the gas atmosphere due to residual gases in the system occurs. Moreover, restrictions on mass transport due to a limited gas flow become relevant.

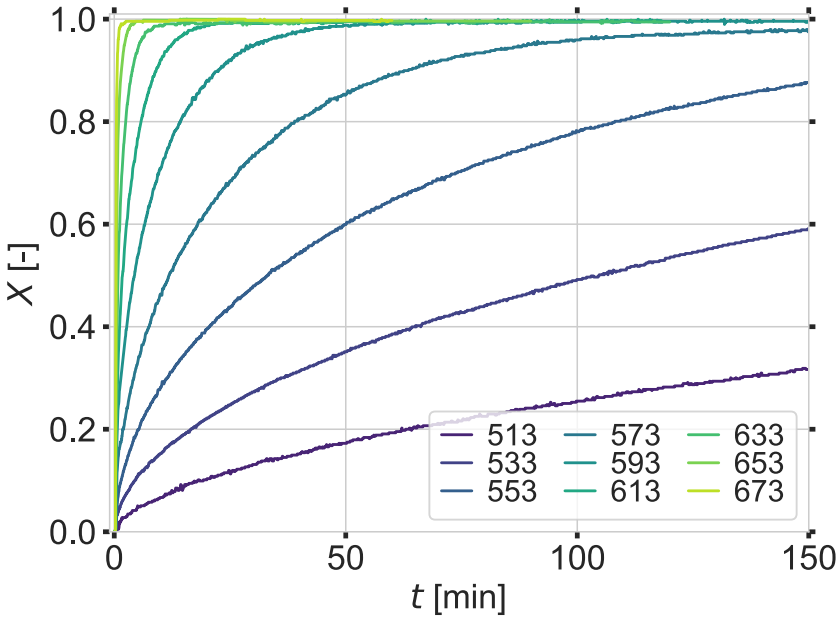

Figure 7.2.: Temperature dependent evolution of the conversion extent $X(t)$ (eq. 7.1) for $Ca_{0.8}Sr_{0.2}MnO_{3-\delta}$. The lines are labeled with the oxidation temperature in Kelvin. The increasing oxidation temperature leads to faster oxidation. Reproduced from *Klaas et al.*[98] with permission from the PCCP Owner Societies.

To identify if there are any degradations of the sample during the measurement, one oxidation curve in the beginning and one oxidation curve at the end of the measurement at the same oxidation temperature $T_{ox} = 593$ K was recorded for $Ca_{0.8}Sr_{0.2}MnO_{3-\delta}$ (Fig. 7.3).

Since the oxidation curves at the beginning and at the end are almost identical, no sample degradation is observed during the measurement. Consequently, the order in which the temperatures are recorded does not interfere with the measured kinetic properties.

Fig. 7.4 displays the impact of the Sr content on the oxidation kinetics for an oxidation temperature of 593 K. The oxidation behavior becomes faster with an increasing Sr content.

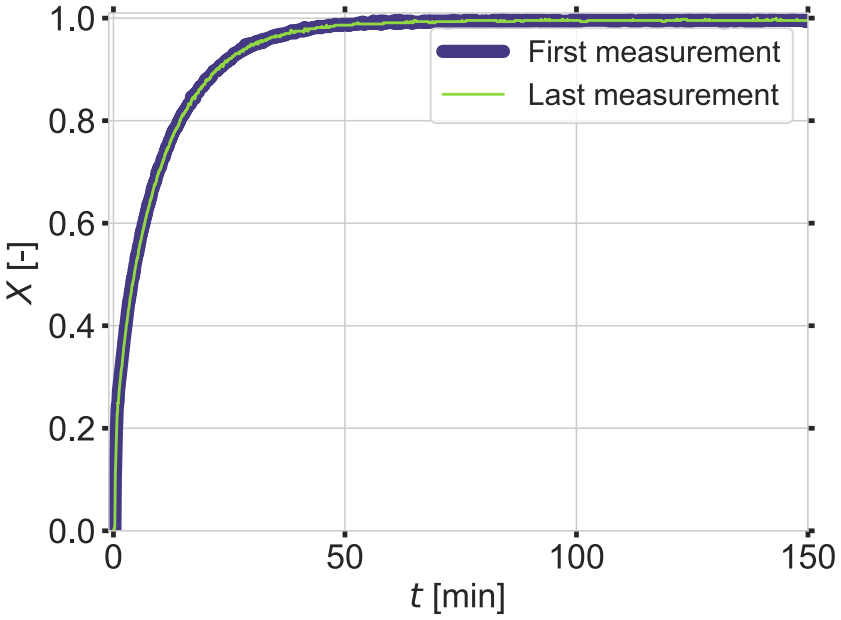

Figure 7.3.: Study of the change in kinetic properties during the measurement period. The oxidation of $Ca_{0.8}Sr_{0.2}MnO_{3-\delta}$ at $T_{ox} = 593\,K$ was measured at the beginning and at the end of the measurement. Since the curves almost completely overlap, no degradation is observed.

The influence of the Sr content and the temperature on the oxidation kinetics can be first analyzed by the half-life $t_{1/2}$. It is calculated by:

$$X(t_{1/2}) = 0.5. \tag{7.2}$$

Fig. 7.5 depicts the half-life depending on the Sr content and the temperature. The presentation of half-lives is limited to cases where the condition $X = 0.5$ was met during the oxidation measurement at the specified temperature and sample.

For $T = 553\,K$ ($10^3/RT \approx 0.22$), the half life changes from $t_{1/2} \approx 263\,s$ ($Ca_{0.6}Sr_{0.4}MnO_{3-\delta}$) to $t_{1/2} \approx 6579\,s$ ($Ca_{0.9}Sr_{0.1}MnO_{3-\delta}$). Thus, the oxidation is highly dependent on the Sr concentration, as indicated before (Fig. 7.4). In addition, for Sr contents of 10–30 % at $673\,K$ ($10^3/RT \approx 0.38$) the data points of the half-lives overlap and the curves appear to saturate. The linear correlation between half-live and temperature is no longer present.

Eq. 2.15 highlights that oxidation behavior depends on the temperature and oxygen concentration. To study this dependence, a measurement with fixed oxidation temperature ($T_{ox} = 573\,K$), but varying oxygen partial pressure (p_{O_2} =0.05–0.97 bar) for $Ca_{0.8}Sr_{0.2}MnO_{3-\delta}$ was conducted. Fig. 7.6 shows the results of this measurement.

Although the oxygen partial pressure varies over a wide range, it does not affect the oxidation kinetics. Therefore, the oxygen concentration dependence $h(c_{O_2})$ is omitted by setting $n = 0$ (eq. 2.18, p. 18) for all studied compositions.

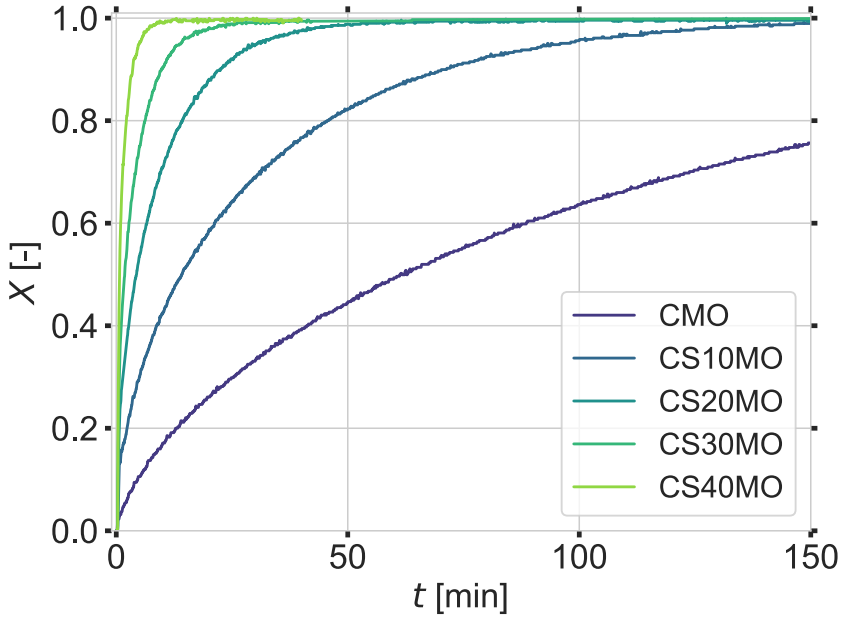

Figure 7.4.: Influence of the Sr content x in $Ca_{1-x}Sr_xMnO_{3-\delta}$ on the evolution of the conversion extent $X(t)$ (eq. 7.1) at 593 K. With an increase in the Sr content, the conversion speeds up. Reproduced from *Klaas et al.*[98] with permission from the PCCP Owner Societies.

The gas switching at the beginning of the oxidation process cannot occur instantly since the remaining inert gas needs to be flushed out. Therefore, the sample's inhomogeneous and time-dependent oxygen concentration is present until the atmosphere exchange is completed. The varying oxygen concentration can affect the kinetics, and therefore, the analysis will exclude the data gathered during the gas switching period. *Bulfin et al.* used the same experimental set-up and calculated a gas switching time of 20 s.[70] This time is as well applied in this study. Besides, the oxidation curves with temperatures where the linear behavior of the Arrhenius-like plot (Fig. 7.5) is not apparent are neglected since this indicates a change in the reaction regime.

Another experimental aspect that could affect the results is the limitation of oxygen mass transfer. The supply of oxygen limits the maximum change:

$$\left.\frac{\mathrm{d}m}{\mathrm{d}t}\right|_{\mathrm{max}} = \dot{n}_{\mathrm{O_2}} \mathrm{M}_{\mathrm{O_2}}. \tag{7.3}$$

Here, $\dot{n}_{\mathrm{O_2}}$ is the molar feed rate of oxygen and $\mathrm{M}_{\mathrm{O_2}}$ is the molar mass of oxygen. Since the mass flow rate was kept constant for all measurements, this value is constant for all temperatures. To know if the mass transfer limit affected the experimental results, the maximum mass change of each experiment was extracted and compared with the mass transfer limit. All samples are illustrated in Figure 7.7.

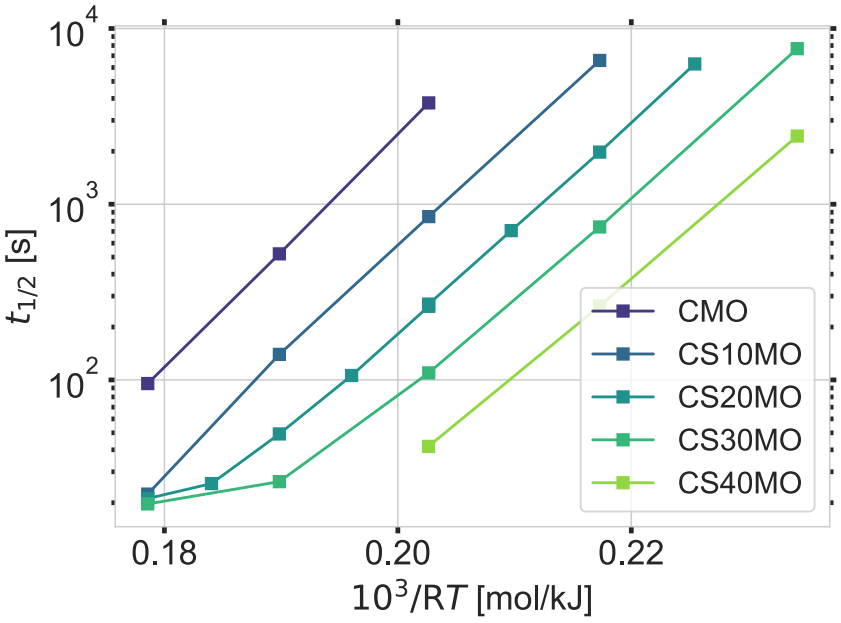

Figure 7.5.: Arrhenius-like plot of the half lives $t_{1/2}$ for different Sr contents in $Ca_{1-x}Sr_xMnO_{3-\delta}$. R is the gas constant. The half-lives decrease with an increase in Sr at equal temperatures. The curves seem to converge for higher temperatures or smaller $\frac{10^3}{RT}$ values, depending on the sample.Reproduced from *Klaas et al.*[98] with permission from the PCCP Owner Societies.

The experimental values of the maximum mass change are consistently far below the mass transfer limit, so it is concluded that it has no effect on the measured mass changes and that the kinetic properties of the sample determine the change in mass rates.

To extract the activation energy based on both presented methods (Sec. 2.6, p. 17), first a subset is taken, and then the numerical derivative is computed (Sec. 3.7, p. 41).

The isoconversional method (Sec. 2.6.1, p. 17) is applied for all samples to extract the activation energy. In order to apply a linear fit, the requirement is that there must be a minimum of three data points provided. The results can be compared in Figure 7.8. Here, the average of the slopes results in the activation energy, and the standard deviation is the uncertainty. The standard deviation is likewise a measure of how much the activation energy depends on the conversion extent. For example, the dependence is negligible if the standard deviation is slight. Fig. 7.8 additionally depicts the activation energy extracted by the model fitting method (Sec. 2.6.2, p. 18).

The values for both methods overlap with the uncertainties. This means that the reaction model (eq. 2.19, p. 19) represents the existing kinetics sufficiently. Additionally, a clear decreasing activation energy with an increasing Sr content is evident. The other model fitting parameters are given in table 7.1.

β is similar for all materials and k_0 does not show an apparent trend.

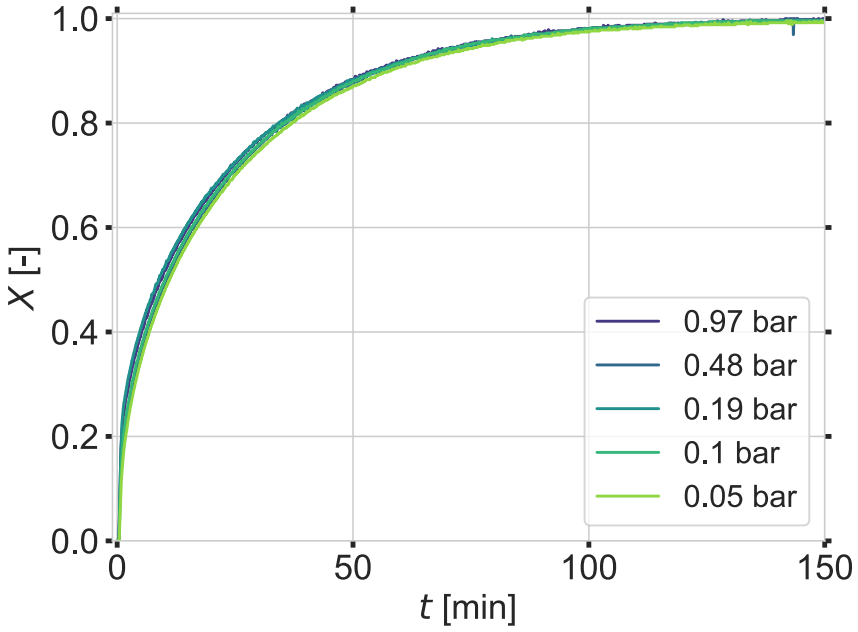

Figure 7.6.: Dependence of the conversion extent $X(t)$ on the oxygen partial pressure p_{O_2} for $Ca_{0.8}Sr_{0.2}MnO_{3-\delta}$. The oxidation temperature is 573 K. No dependence is apparent. Reproduced from *Klaas et al.*[98] with permission from the PCCP Owner Societies.

Table 7.1.: Oxidation kinetic parameters determined by the model fit parameters.

Material	β [-]	k_0 $[s^{-1}(mol\ m^{-3})^{-n}]$
CMO	1.6(7)	4.813×10^9
CS10MO	1.6(5)	3.855×10^9
CS20MO	1.6(5)	3.115×10^{10}
CS30MO	1.6(4)	2.036×10^{10}
CS40MO	2.1(8)	8.150×10^9

The oxidation process starts with the adsorption and dissociation of an oxygen molecule at the sample's surface to be oxidized.[68] This step is determined by the surface properties and the gas phase oxygen concentration since it occurs at the interface between redox material and the gaseous surrounding. Then the absorbed oxygen reacts at the surface with the oxygen vacancy layer and diffuses into the bulk. The diffusion through the bulk depends on the continued supply of oxygen at the surface of the redox material.

The thermodynamic analysis reveals that the oxidized equilibrium state for all temperatures and oxygen partial pressures studied is $\delta(T, p_{O_2}) \approx 0$. Therefore, the final state depends neither on the material composition nor the oxygen partial pressure. The oxidation curve (Fig. 7.6), which is independent of the oxygen partial pressure, permits the conclusion that the surface reaction is rapid compared to diffusion and that the surface of the granules is entirely and immediately oxidized. As a result, oxygen ion diffusion is the rate-limiting step.

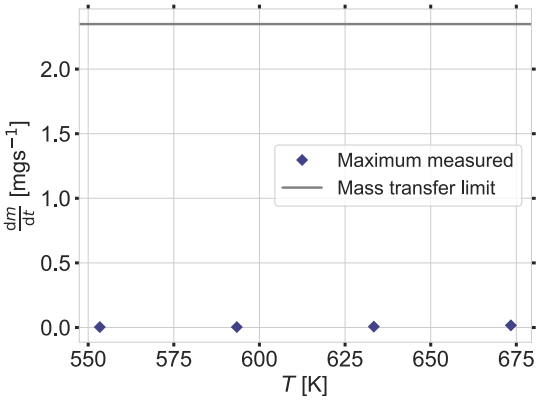

(a) $CaMnO_{3-\delta}$

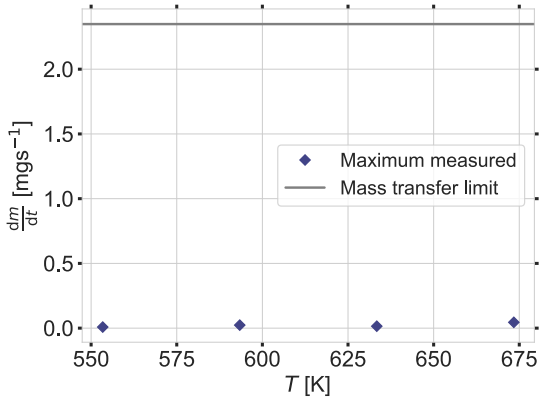

(b) $Ca_{0.9}Sr_{0.1}MnO_{3-\delta}$

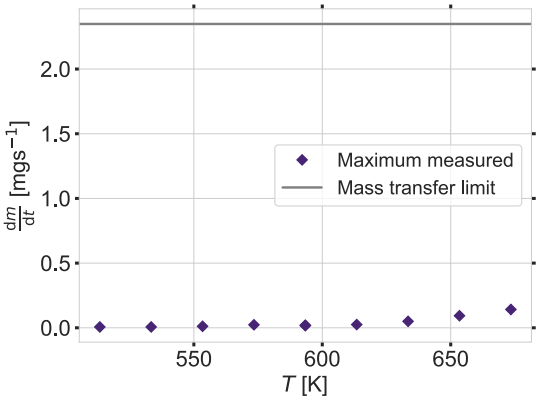

(c) $Ca_{0.8}Sr_{0.2}MnO_{3-\delta}$

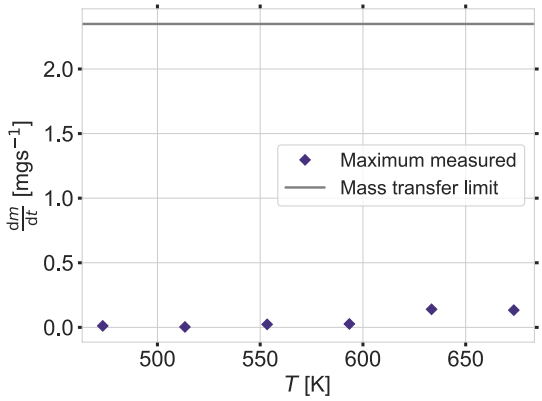

(d) $Ca_{0.7}Sr_{0.3}MnO_{3-\delta}$

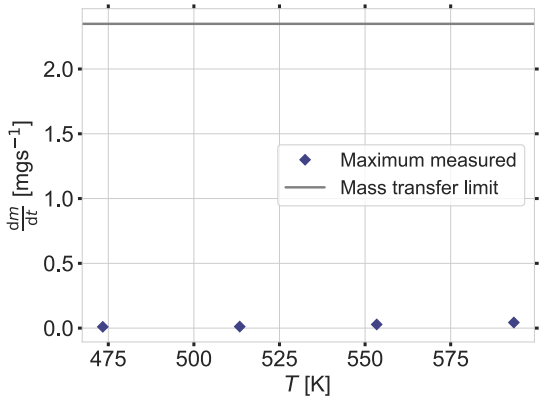

(e) $Ca_{0.6}Sr_{0.4}MnO_{3-\delta}$

Figure 7.7.: Analysis of the mass transfer limitation for all samples and temperatures investigated. The line indicates the mass transfer limit calculated by eq. 7.3 and the squares the maximum measured mass change of each temperature. The mass transfer limit is never reached; thus, it does not affect the observed kinetic properties.

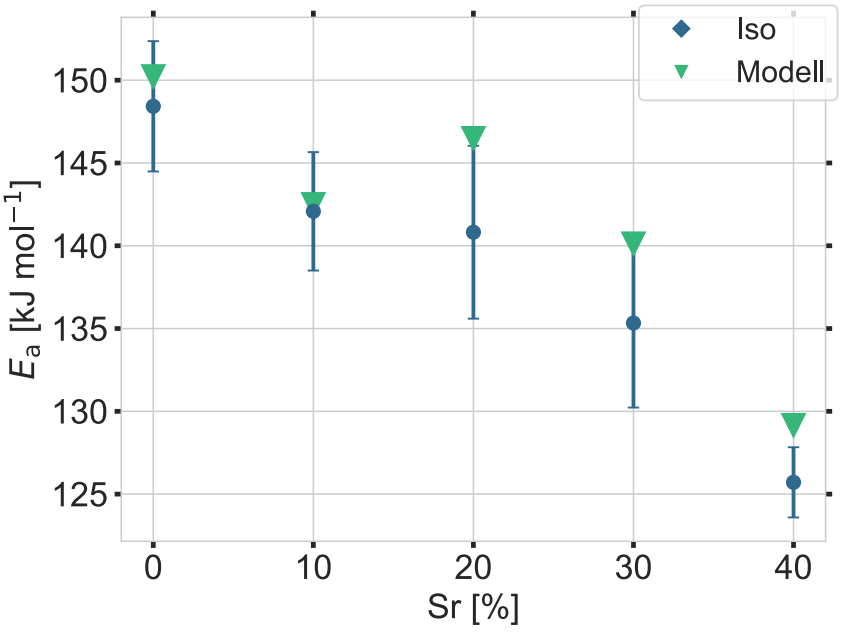

Figure 7.8.: Calculated oxidation activation energies of all samples $Ca_{1-x}Sr_xMnO_{3-\delta}$. 'Iso' refers to the isoconversional method (Sec. 2.6.1, p. 17) and 'Model' to the kinetic model fitting (Sec. 2.6.2, p. 18). Within the experimental uncertainty, both methods result in the same activation energy. A decrease in the activation energy with increased Sr content is observed. Reproduced from *Klaas et al.*[98] with permission from the PCCP Owner Societies.

Thus, the applied oxygen partial pressure does not influence the material's performance in applications.

Kuganathan et al. investigated different pathways of oxygen ion migration through $CaMnO_{3-\delta}$. They showed that diffusion along the *a*-axis within the plane of Mn ions has the lowest migration energy with a value of 1.25 eV or 121 kJ/mol.[125] This migration energy is in the order of the activation energies calculated, supporting the conclusion that diffusion is the rate-limiting step. Since diffusion occurs preferentially along particular axes, the reduction in distortion due to the substitution of Ca by Sr (Sec. 4.1, p. 50)[45] may also result in decreased migration energy. In addition, the increased A-O1 bond length (Sec. 4.1, p. 50) may facilitate oxygen ion diffusion.

After analyzing the oxidation kinetics, the focus now lies on the analysis of the reduction kinetics. Therefore, the conversion extent $X(t)$ (eq. 7.1) is calculated again. Contrary to the oxidation measurements, δ_0 equals zero and $\delta_\infty = \delta(p_{O_2} = 0.01\,\text{bar}, T)$ depends on the reduction temperature. More experimental details can be found in Sec. 3.7 on p. 41. The effect of the reduction temperatures on the reduction of $Ca_{0.8}Sr_{0.2}MnO_{3-\delta}$ is shown in Fig. 7.9. Here, $X(t) = 0$ assigns complete oxidation, and $X(t) = 1$ assigns complete reduction.

Since the lines overlap greatly, the measured rate is not dependent on the temperature. The different δ_∞ can explain the small deviation of the curvature near the saturation value.

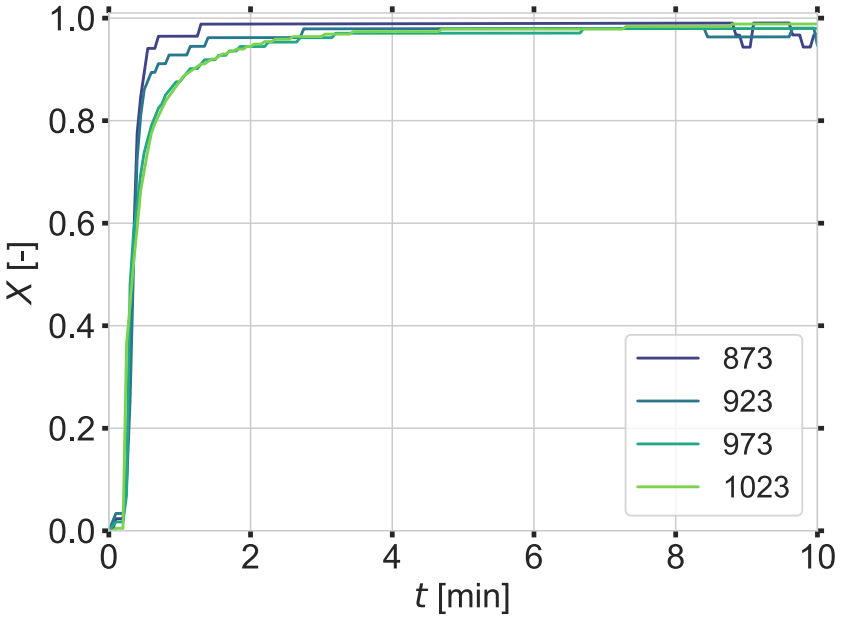

Figure 7.9.: Evolution of the conversion extent for the reduction of the granules of $Ca_{0.8}Sr_{0.2}MnO_{3-\delta}$. The oxygen partial pressure is $p_{O_2} = 0.01$ bar. Contrary to the oxidation measurements, $X(t) = 0$ indicates complete oxidation, and $X(t) = 1$ indicates complete reduction. The reactions appear to be nearly temperature independent. Reproduced from *Klaas et al.*[98] with permission from the PCCP Owner Societies.

This means that equilibrium is reached faster at lower temperatures. δ_∞ ranges from 0.007–0.035 for 873–1023 K respectively. The half lives $t_{1/2}$ (eq. 7.2) is 21 s for all temperatures. The reduction is completed after only ≈ 3 min. Since the half-life is in the order of the gas exchange times and the rates appear to be independent of temperature, they are limited by the mass transfer of the TGA system.

7.2. Microstructure Dependent Kinetics

In the section mentioned above, the kinetics are determined based on granules. To investigate if the minor particle size distribution 1.25–1.6 mm may impact the kinetics, granules with different diameter ranges (d =1.25–1.6 mm, d =1.6–2.24 mm and d >2.24 mm) of $Ca_{0.8}Sr_{0.2}MnO_{3-\delta}$ are measured. Fig. 7.10 displays the evolution of the conversion extent $X(t)$ at $T_{ox} = 593$ K. Since the lines overlap, the extent of conversion is strikingly independent of the size of the granules. As predicted previously, the independence of the oxidation kinetics on the granular size (Fig. 7.10) indicates that the minor size distribution of the granules used for the composition-dependent study does not affect the measured activation energy.

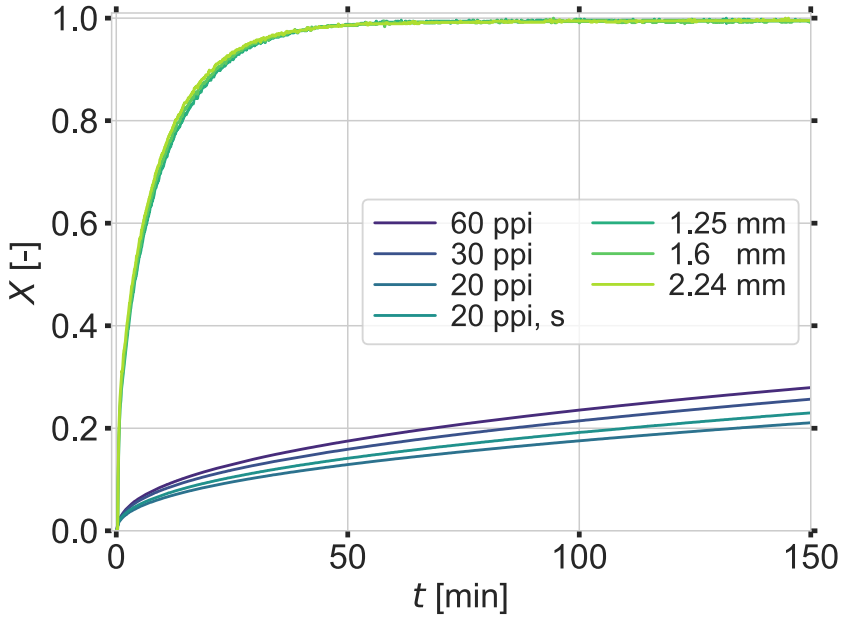

Figure 7.10.: Evolution of the conversion extent for different sizes of granules of $Ca_{0.8}Sr_{0.2}MnO_{3-\delta}$ and foams of $Ca_{0.8}Sr_{0.2}MnO_{3-\delta}$ with different pore densities at T_{Ox} = 593 K. The displayed diameter is the minimal diameter of the particle size distribution. The conversion extent is independent of the granular size within the measured particle size distribution. Moreover, the different pore densities do not highly affect the oxidation behavior. Contrary, the difference between the granule and the foams is striking.

Moreover, Fig. 7.10 displays the oxidation curve of foams with different pore densities. All foams displayed here are produced by a ball-milled slurry (exp. details in Sec. 3.2.2). To identify if the total mass impacts the oxidation curve, the sample '20 ppi, s' weighs 57 % of sample '20 ppi'. The reduced mass results in slightly faster oxidation kinetics.

The oxidation rate increases slightly with increasing pore density. Increasing pore density is accompanied by increasing total sample mass as the size of the pores decreases, and the foam becomes more compact (see Fig. 3.5, p. 33). Since a decrease in mass leads to slightly faster oxidation kinetics, the trend toward an increase in oxidation rate with increasing pore density is opposite to the effect of mass. Nevertheless, the different oxidation behavior for the different pore densities can be attributed to changing heat transfer properties. The effect is small compared to the change in pore density. At this point, it should be emphasized that all the results presented in this section are below the mass transfer limit.

Not only a single temperature was analyzed and compared, but the activation energy was additionally extracted by the isoconversional method (Sec. 2.6.1, p. 17). Fig. 7.11 emphasizes that the activation energy of all granules is identical within the experimental uncertainty. The activation energy of all foams is also comparable. Comparing the activation energy of both macrostructures, granules and foam, shows that they overlap within the

experimental error. Furthermore, the foams appear to have slightly higher activation energy, but since the mass change from mg for granules to g for foams is enormous, this small change should not be over-interpreted.

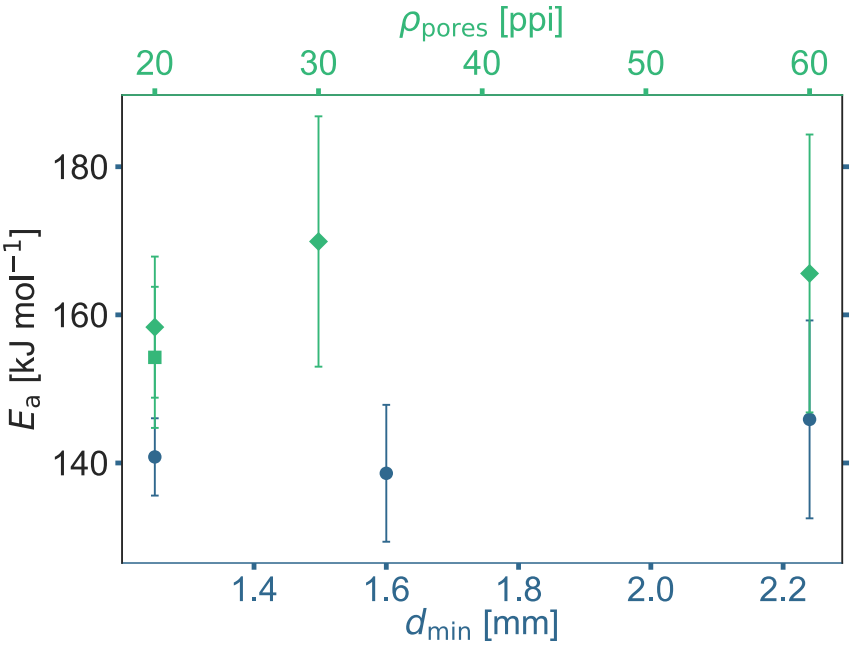

Figure 7.11.: Activation energy of the oxidation for different granules and foams. The lower blue x-Axis shows the minimal diameter of the granule, and the upper green x-Axis shows the pore density. The square assigns the smaller foam of 20 ppi with 57 % of the weight.

To further investigate the impact of the material's structure, foams and pellets are analyzed beside granules. Similar to the structures in Chap. 6 on p. 75, the foams of $Ca_{0.8}Sr_{0.2}MnO_{3-\delta}$ were fabricated via two different routes (Sec. 3.2.2, p. 32). The foam whose slurry was processed with a ball mill is called $Foam_{BM}$, and the foam whose slurry was processed with a magnetic stirrer is called $Foam_{MS}$. Pellets of $Ca_{0.8}Sr_{0.2}MnO_{3-\delta}$ with two different treatments of the powder (Sec. 3.2.3, p. 34) were manufactured. Here, the pellet whose powder was milled with a ball mill is called $Pellet_{BM}$, and the pellet whose powder was milled manually is called $Pellet_{M}$. For $Pellet_{BM}$, two different sample heights are produced. $Pellet_{BM,0.25}$ has a height of 0.25 mm and $Pellet_{BM,0.5}$ has a height of 0.5 mm. The terms are equivalent to the terms in Chap. 6 and are listed here for easier comprehension. The oxidation kinetics for $T_{ox} = 593\,K$ are displayed in Fig. 7.12.

Focusing first on the different pellets, the faster kinetics for the thinner $Pellet_{BM,0.25}$ compared to $Pellet_{BM,0.5}$ is expected, but the impact is negligible. Contrary, the increased oxidation kinetics of $Pellet_{M}$ is striking. The same trend holds comparing $Foam_{MS}$ with fast kinetics compared to $Foam_{BM}$ with slow kinetics. The samples with slow kinetics are not fully oxidized within 150 min, and $Foam_{BM}$ has the slowest oxidation kinetics. The kinetics

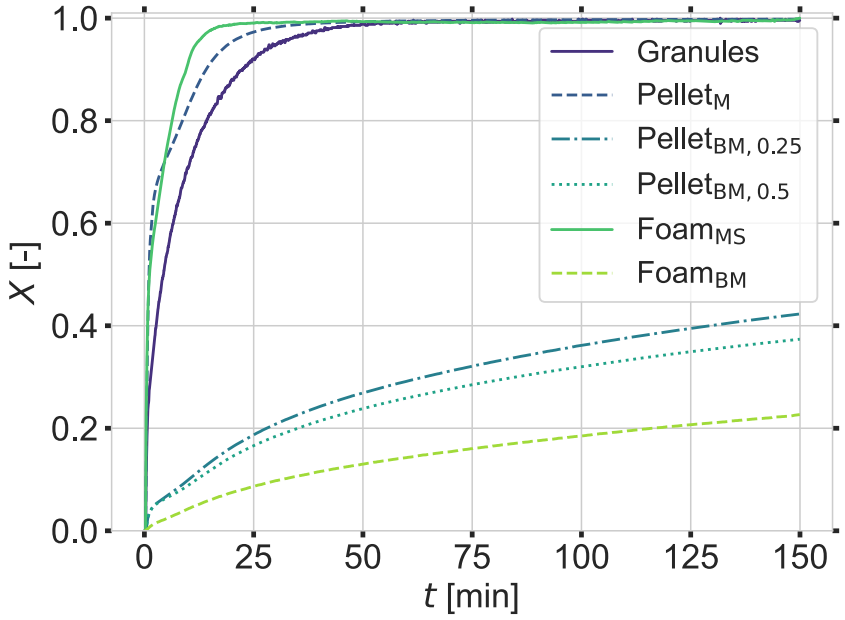

Figure 7.12.: Oxidation curves for different structures and production procedures for $T_{Ox} = 593\,K$. Microstructural changes govern the changing oxidation kinetics.

of the granules is comparable to both, $Foam_{MS}$ and $Pellet_{M}$. Here, $Foam_{MS}$ has the fastest kinetics, followed by $Pellet_{M}$ and granule.

The similar activation energy of granules and foam supports the assumption that the determined activation energy is a material characteristic quantity independent of the specimen's macrostructure.

Nevertheless, the oxidation kinetics depends on the specimen's macrostructure. The striking difference between the samples is their microstructure (Fig. 6.8, p. 85). The ball-milled samples have a densely sintered surface, and the others have a porous and rough surface. *Yang et al.*[126] as well observed microstructure-dependent oxidation kinetics in perovskites, although they used CO_2 as the oxygen source.

The independence of oxidation from $Ca_{0.8}Sr_{0.2}MnO_{3-\delta}$ from the oxygen partial pressure implies that oxidation is not limited by adsorption but by bulk diffusion (Sec. 7.1, p. 90). *Kimura et al.*[127,128] described that the oxidation kinetics is inversely proportional to the particle size of the sample. The term 'particle' will be used in the following to describe the size of the individual unit of a macrostructure. E.g. for the granule, the term 'particle' describes the individual small particle which is discussed in the microstructure. Thus, considering the presented samples as an agglomeration of particles, where the particle size is different for each sample, the oxidation kinetics follows the proposed trend.

To reconsider the different microstructures, the reader is referred to Sec. 6.2 on p. 83. The sample $Foam_{BM}$ is densely sintered and thus has the biggest particle size. For this sample,

the particle size of the sample is determined by the thickness of the struts. This sample shows the slowest oxidation kinetics. The corresponding Foam_{MS} has smaller particles and faster oxidation kinetics. The same statement holds for the granules. Pellet_{M} consists of mainly smaller particles and some sintered areas with larger particles. This explains the initial faster oxidation kinetics and decelerating after 1 min.

Additionally, diffusion of ions along crystallite boundaries proceeds faster than diffusion of ions through the bulk.[128,129] The samples with less dense sintered surface areas have more boundaries, leading to faster kinetics.

The depth-dependent diffusion of oxygen may be analyzed to investigate the above hypothesis further. This can be realized by ^{18}O-secondary ion mass spectrometry. For this purpose, a sample is reduced, then partially oxidized with the tracer oxygen ^{18}O, and subsequently, the depth-dependent ^{18}O concentration is measured. In this way, oxygen diffusion can be studied layer by layer for different oxidation times.

7.3. Summary of the Kinetic Analysis

The first part of the chapter investigates the impact of the material composition on the kinetic properties. The oxidation kinetics are proven to be independent of the ambient oxygen partial pressure. This leads to the conclusion that not the oxygen uptake at the surface but the bulk diffusion is the rate-limiting step.

Increasing the Sr content in $\text{Ca}_{1-x}\text{Sr}_x\text{MnO}_{3-\delta}$ results in faster oxidation kinetics with lower activation energy. Since crystallographic analysis revealed that with increasing Sr content, the distortion also decreases, and diffusion occurs preferentially along a defined axis, the lower activation energy results from this decreasing distortion. In addition, the increasing Sr content elongates the length of the A-O1 bond, which further facilitates the diffusion of the oxygen ions. For different applications, different oxidation kinetics are beneficial. For example, short cycle times are required for air separation, and thus, fast oxidation kinetics are preferred. On the contrary, slower oxidation kinetics are preferred for thermochemical heat storage since this enables a heat supply over an extended period.

The material exhibits rapid reduction kinetics. Further analysis is impossible because the reduction is completed at a time when the external conditions still vary. The fast reduction kinetics is advantageous because, in industrial applications, the cycle time must be short to increase the number of cycles per day.

In the second part, the impact of the microstructure on the kinetics is analyzed. The particle size of the granules does not influence the oxidation kinetics. Moreover, the activation energy for foams with different pore densities and for granules with different diameters is similar. Nevertheless, different oxidation behaviors are recognizable.

Combining the microstructure analysis with the kinetic analysis leads to an explanation of the observed feature. A finer powder used to make the various macrostructures results in a denser sintered surface and, thus, fewer crystallite boundaries and larger particles. Since crystallite boundaries facilitate ion diffusion and larger particles impede ion diffusion, the denser sintered samples exhibit slower oxidation kinetics. Therefore, the oxidation kinetics can be tuned by varying the microstructure.

8. Energetic Requirements

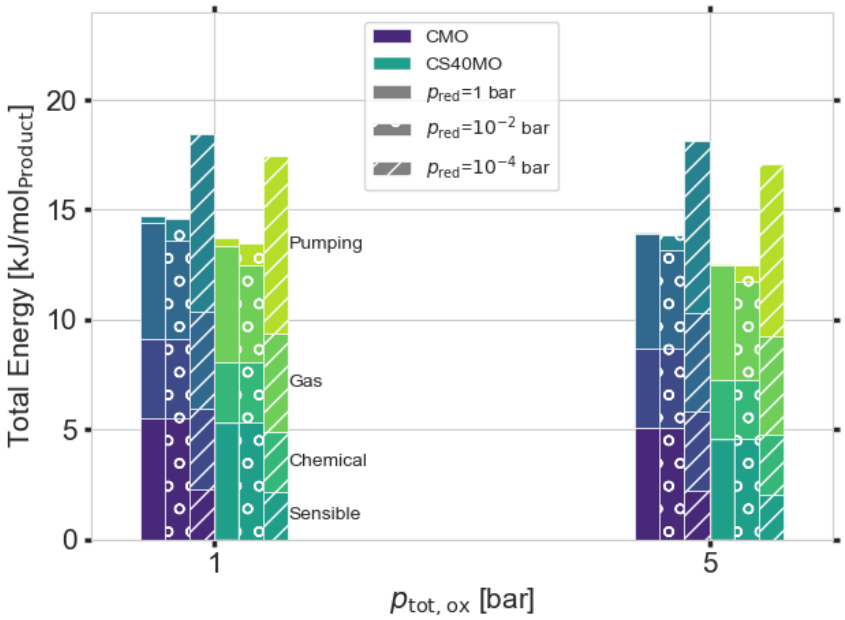

Figure 8.1.: An example of calculating the energy required for producing high-purity nitrogen is demonstrated. A distinction is made between the different energy contributions, such as sensible heat. Influencing factors include the Sr content of the redox material, the pressure during oxidation, and the pressure during reduction.

This chapter is partially based on the following peer-reviewed publication, which is authored by the author of this thesis:

L. Klaas, B. Bulfin, D. Kriechbaumer, N. Neumann, M. Roeb and Ch. Sattler. Energetic optimization of thermochemical air separation for the production of sustainable nitrogen. Reaction Chemistry & Engineering, 8(8):1843-1854, 2023. doi: 10.1039/D3RE00087G.

To determine the best operating parameters, such as reduction and oxidation temperature, for a selected material or to determine the most suitable material, thermodynamic energy calculation, as presented in this chapter, is a good approach. It prevents long-worthy experiments in the laboratory. Thermodynamic-based calculations for thermochemical air separation have been used previously.[19,20] First, small-scale packed-bed experiments are conducted to justify the application of thermodynamic-based calculations. $SrFeO_{3-\delta}$ has been studied extensively thermodynamically and kinetically. Moreover, this material has already been used to study air separation.[18,19] Therefore, it was selected to justify the calculations with experiments conducted in a PID system. Unfortunately, the experiments could not be extended to $Ca_{1-x}Sr_xMnO_{3-\delta}$ because the available system could not reach the required temperatures for these materials.

Afterwards, an energetic calculation for an air separation with $SrFeO_{3-\delta}$ and different redox parameters is carried out. Subsequently, this calculation is extended to $Ca_{1-x}Sr_xMnO_{3-\delta}$. Finally, a detailed parameter study is carried out for the most energy-efficient material, together with $Ca_{0.8}Sr_{0.2}MnO_{3-\delta}$.

8.1. Packed-bed Experiments for Validation

Experimental details about the packed-bed reactor experiments can be found in Sec. 3.8 on p. 46. The redox material used is $SrFeO_{3-\delta}$. Fig. 8.2 visualizes the results of the air separation during the oxidation with different experimental parameters. It reflects how the purity of the oxygen outlet evolves. Details about the experimental parameters can be found in the Tab. 8.1. In each experiment, usually, only one parameter is varied. The standard configuration is:

$$\begin{aligned}
\text{Reduction temperature: } & T_{\text{red}} = 873\,\text{K} \\
\text{Oxidation temperature: } & T_{\text{ox}} = 623\,\text{K} \\
\text{Reduction oxygen partial pressure: } & p_{\text{O}_2,\text{red}} = 0.01\,\text{bar} \\
\text{Oxidation total pressure: } & p_{\text{tot,ox}} = 5\,\text{bar} \\
\text{Oxidation oxygen partial pressure: } & p_{\text{O}_2,\text{ox}} = 0.01\,\text{bar} \\
\text{Oxidation volume flow rate: } & \dot{V}_{\text{ox}} = 169.8\,\text{ml/min}.
\end{aligned}$$

In the best case, several parameters are varied as the highest amount of purified gas will be produced. In this case $T_{\text{red}} = 973\,\text{K}$, $p_{\text{tot,ox}} = 10\,\text{bar}$, $p_{\text{O}_2,\text{ox}} = 0.004\,\text{bar}$ and $\dot{V}_{\text{ox}} = 160.4\,\text{ml/min}$.

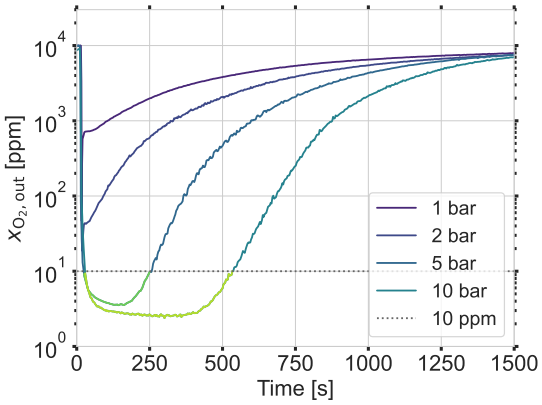

(a) Variation of the total pressure during oxidation $p_{tot,ox}$

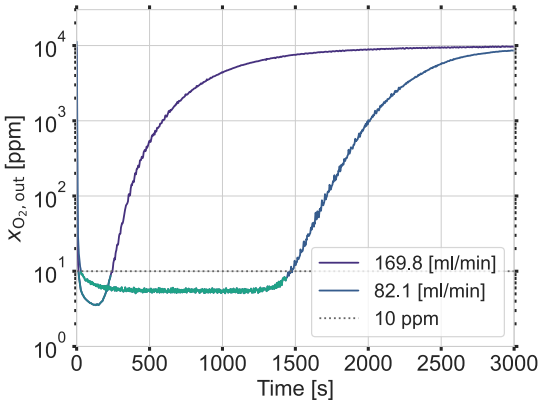

(b) Variation of the volume flow rate $\dot{V}_{ox}$

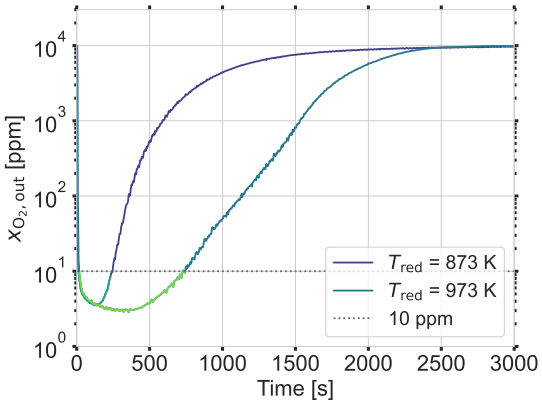

(c) Variation of the reduction temperature T_{red}

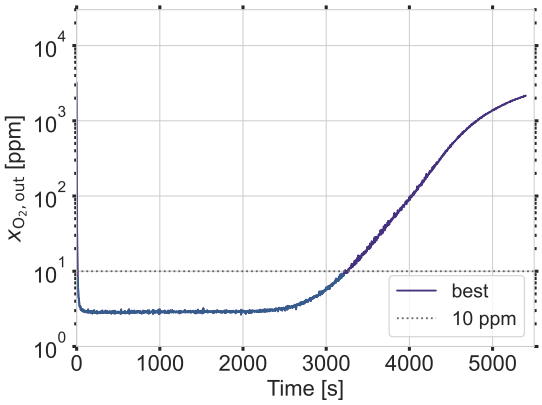

(d) Result of a best case scenario with T_{red} = 973 K, $p_{tot,ox}$ = 10 bar, $p_{O_2,ox}$ = 0.004 bar and $\dot{V}_{ox}$ = 160.4 ml/min

Figure 8.2.: Packed-bed reactor experiments to investigate the impact of different conditions during the oxidation and reduction on the molar outlet oxygen impurity fraction $x_{O_2,out}$. The experimental results are displayed with a solid line. A horizontal dotted line highlights the cut-off criterion.

All experiments show an oxygen-impurity floor. This appearance can be attributed to various causes. First, oxygen leakage into the stream may occur after leaving the reactor. Oxygen leakage cannot be prevented entirely since this setup involves a minimal mass flow at low oxygen partial pressures. Second, there may be preferential flow paths mainly because the ratio of the diameter of the granules to the diameter of the reactor is 1.25–1.6 mm to 9 mm. Finally, kinetics can also be a limiting factor. All these factors are likely to be less significant in a larger reactor.

All figures show the complete oxidation curves. Still, for the application, only the gas stream with an oxygen impurity of less than 10 ppm is of interest since this can be used as a supply for the Haber-Bosch process. The dotted line highlights this cut-off criterion.

Moreover, for further analysis and comparison, the integrated volume flow rates, which are beneath the cut-off criteria, are of interest in order to extract the total volume of purified gas produced. The different colors highlight these flow rates.

The results, as well as the variation of parameters of these experiments, are summarized in Tab. 8.1. Moreover, it includes calculated quantities which are highlighted with *calc.* Therefore, the experimental results and the impact of the different parameters are further discussed before comparing the experimental values with the calculated ones.

Table 8.1.: Summary of the packed-bed reactor experiments and the calculated values. The first four columns show the set of experimental values. T_{red} is the temperature during reduction. $p_{\mathrm{tot,ox}}$ and $p_{\mathrm{O_2,ox}}$ are the total pressure and the oxygen partial pressure during oxidation, respectively. $p_{\mathrm{O_2,red}}$ is the oxygen partial pressure during reduction, and it is kept at 0.01 bar. $\dot{V}_{\mathrm{ox}}$ is the total mass flow of the applied gases during oxidation. $\bar{x}_{\mathrm{O_2}}$ and $x_{\mathrm{O_2,min}}$ are the measured mean molar oxygen fraction and the measured minimal molar oxygen fraction, respectively. $V_{\mathrm{in,exp/calc}}$ is the total volume of the inlet gas either of the experiment (exp) or the calculation (calc, eq. 2.23, p. 24) which is purified. $V_{\mathrm{O_2,exp/calc}}$ is the volume of the absorbed oxygen (calc, eq. 2.22, p. 23).

T_{red} [K]	$p_{\mathrm{tot,ox}}$ [bar]	$p_{\mathrm{O_2,ox}}$ [bar]	$\dot{V}_{\mathrm{ox}}$ [ml/min]	$\bar{x}_{\mathrm{O_2}}$ [ppm]	$x_{\mathrm{O_2,min}}$ [ppm]	$V_{\mathrm{in,exp}}$ [l/g]	$V_{\mathrm{in,calc}}$ [l/g]	$V_{\mathrm{O_2,exp}}$ [ml/g]	$V_{\mathrm{O_2,calc}}$ [ml/g]
873	1	0.01	169.8	-	-	-	0.655	-	6.5
873	2	0.01	169.8	-	-	-	0.706	-	7.1
873	5	0.01	169.8	5	4	0.141(1)	0.773	1.4(1)	7.7
873	10	0.01	169.8	3	2	0.314(2)	0.824	3.1(1)	8.2
973	5	0.01	169.8	4	3	0.450(3)	1.031	4.5(2)	10.3
873	5	0.01	82.1	6	5	0.424(3)	0.773	4.2(4)	7.7
973	10	0.004	160.4	3	3	1.881(13)	2.540	7.5(3)	10.1

The theoretical minimal oxygen molar fraction $x_{\mathrm{O_2,min,calc}}$ which can be calculated based on an empirical model by *Bulfin et al.*[19] is only dependent on the oxidation temperature, the reduction temperature and the oxygen partial pressure during reduction. Here, the oxidation temperature and the oxygen partial pressure during reduction are not varied. Therefore, in this case, the minimal molar fraction is a function of the reduction temperature. The calculated minimal oxygen molar fraction is summarized in Tab. 8.2.

Table 8.2.: Calculation of minimal molar fraction for the packed-bed experiment based on an empirical model of $SrFeO_{3-\delta}$.[19] $p_{\mathrm{O_2,red}}$ equals 0.01 bar and T_{ox} equals 623 K for all conducted experiments.

T_{red} [K]	$x_{\mathrm{O_2,min,calc}}$ [ppm]
873	1
973	0.04

The theoretical minimal oxygen molar fraction is not reached in any experiment, although the experiments with a reduction temperature of 873 K are in a similar ppm range. Increasing the total pressure during oxidation results in a decreased minimal oxygen molar fraction, a longer oxidation time, and, thus, an increase in the volume of the adsorbed oxygen. This is equivalent to an increased amount of purified gas. For a total pressure of 1 bar and 2 bar during oxidation, the required oxygen molar fraction of 10 ppm is not reached.

An increase in the reduction temperature leads to longer oxidation times and, therefore, to an increased amount of absorbed oxygen. This behavior is expected since a higher reduction temperature leads to an increased reduction extent (Fig. 2.9, p. 24) and, therefore, to a tremendous change in non-stoichiometry.

Decreasing the total mass flow increases the amount of the absorbed oxygen. The set oxygen partial pressure decrease during oxidation has two experimental effects. The first effect is the reduced amount of oxygen the material must absorb, and the second is the reduced total volume flow rate.

The theoretical minimum oxygen partial pressure may not be reached due to experimental limitations, as preferential flow tunnels may form. Through these tunnels, the gas can flow directly through the reactor and interacts only with a small number of particles that may already be oxidized. Furthermore, oxygen leakage into the stream may occur after leaving the reactor. In addition, kinetic limitations could prevent lower oxygen partial pressures. These three factors have already been discussed in the analysis of the shape of the curve of oxygen concentration of the outlet gas (Fig. 8.2).

Whether preferential flow tunnels are formed cannot be investigated because when the reactor is opened, the thermocouples in the bed are removed simultaneously. Removing them changes the packing inside the reactor and destroys the preferential flow tunnels.

Concerning the kinetic limitations, the residence time of the gas in the reactor is calculated with the dimensions of the packed bed and the prevalent gas flow $\dot{V}_{\mathrm{ox}} = 169.8\,\mathrm{ml/min}$. It equals 1.1 s. Kinetic studies on $SrFeO_{3-\delta}$ showed that the complete re-oxidation of 260 mg powder in an atmosphere of 90 % O_2 required 1 min.[18] Therefore, the kinetic limitations are important in the presented experimental setup since the kinetics of $SrFeO_{3-\delta}$ depends as well on oxygen partial pressure[19] and thus becomes slower at lower oxygen partial pressures. This reasoning is supported by the fact that lower volume flow rates and, thus, longer residence times increase the amount of absorbed oxygen. Furthermore, higher pressure leads to longer residence time, and again the amount of absorbed oxygen follows the proposed trend. Nevertheless, the increased pressure may have a further contribution. Indeed, in similar materials, it increases the kinetic performance.[20]

The observed trend that an increase in pressure leads to lower achievable oxygen partial pressures could additionally be explained by the fact that the input oxygen concentration,

as well as the equilibrium oxygen partial pressure, remains constant, but due to the high total pressure, the output N_2 concentration increases.

Afterward, the experimental results are compared with the calculations. The general trend observed in the experiments is reflected in the calculations. For example, increasing the reduction temperature from 873 K to 973 K leads to an almost identical change in the amount of absorbed oxygen in the experiment as in the calculations; all other conditions remain the same.

Nevertheless, the overall values deviate from the experimental values. The experimental observations indicate that one reason for this is kinetic limitation. Since the change in flow rate leads to an approximation of the experimental values to the calculated values. Furthermore, the calculations are based on thermodynamic equilibria and neglect dynamic developments. Since dynamic developments are neglected, there is also no cut-off condition; in contrast to the experiments, the final oxygen partial pressure is used as the average value. This increases the total amount of calculated oxygen absorbed. If the experiments were performed with a buffer between the reactor and the oxygen sensor, this approach could be adopted, and the yield would increase.

In summary, although elementary, the calculations satisfactorily reproduce the experimental results. They reveal significant trends and can be used to calculate optimal experimental conditions. Finally, deviations of experimental volumes from calculated volumes may indicate that kinetics limit reactor performance.

8.2. Energetic Calculations for $SrFeO_{3-\delta}$

Since the experiments with the packed-bed reactor have shown that the thermodynamic calculations assign essential trends in terms of the amount of purified gas, the thermodynamic calculations are used to determine the most energetically efficient operating conditions for $SrFeO_{3-\delta}$.

Details for the energetic contributions can be found in Sec. 2.9 on p. 22. The oxygen molar fraction during the oxidation is $x_{O_2} = 0.01$, and the oxidation temperature is $T_{ox} = 623\,K$ for all configurations. Whereas the reduction temperature, T_{red} =873 K or 973 K, the total pressures during oxidation, $p_{tot,ox}$ =1–5 bar, and the total pressures during reduction, p_{red} =1–10^{-4} bar are changed. For the reduction at 1 bar, a purge gas flow of 1 Nm^3/h with an oxygen molar fraction of 0.01 for 30 min is applied. Fig. 8.3 presents the results of the energetic calculations for the different configurations.

Comparing first the contribution of the different energies in Fig. 8.3 (a)-(c), the contribution of the sensible energy is the largest, followed by the energy required to heat the gas. Except for $p_{red} = 10^{-4}$ bar, where the energy to pump the gas is significantly increased and

comparable to the contribution of the sensible energy. The chemical energy is smaller than the previously mentioned energies. This distribution can be seen for all parameters studied. Due to the isothermal simplification of the pumping work, this value may be slightly underestimated for $p_{red} = 1\,bar$. In addition, it must be taken into account that, in this case, additional work is required to generate the purge gas; thus, an additional energy contribution is required.

The total energy demand for $p_{red} = 1\,bar$ and $p_{red} = 10^{-2}\,bar$ is comparable, but increases for $p_{red} = 10^{-4}\,bar$ because of the energy required to pump the gas. Hence, the higher reduction ratio due to the lower oxygen partial pressure (Fig. 2.9, p. 24) does not compensate for the increased total energy demand.

For all $p_{tot,ox}$, the higher reduction temperature results in a lower total energy demand. The decreased total energy demand also appears for all p_{red}. The increased reduction temperature leads to an increased reduction extent (Fig. 2.9, p. 24). This, in turn, increases the total amount of purified gas. As the calculations show, the increased reduction extent compensates for the increased total energy demand due to the increased temperature.

An increase in $p_{tot,ox}$ lowers the total energy demand for all cases studied. This indicates that increasing the total pressure during oxidation positively influences the energy demand. As shown by the fixed bed experiment, it also increases the total residence time, benefiting the absorption process.

Fig. 8.3d serves as a summary of Fig. 8.3 (a)-(c), since it illustrates the total energy demand for all configurations investigated. In this function, it emphasizes the trends for the individual parameters already observed. In particular, it appears that the higher total pressures during oxidation have a stronger influence on the total energy demand for $p_{red} = 1\,bar$ and $10^{-2}\,bar$ than for $p_{red} = 10^{-4}\,bar$. As mentioned earlier, the total energy demand for $p_{red} = 1\,bar$ and $10^{-2}\,bar$ is close to each other. This is due to the same level of reduction since, in both scenarios, the oxygen partial pressure is $10^{-2}\,bar$. In one case, this is achieved by purging and in the other by vacuum pumping. Therefore, the contributions of sensible and chemical energy are the same in both processes. Only the energy contributions for heating the inlet gas and for pumping the gases differ. In the case of $p_{red} = 1\,bar$, the PSA must generate an additional $0.5\,Nl$ for purging. This leads to an additional energy contribution of $1.8\,kJ/mol_{Product}$ for $T_{red} = 973\,K$ and $p_{tot,ox} = 5\,bar$ (eq. 2.25, p. 25). From this follows that the lowest energy requirement is for $p_{red} = 10^{-2}\,bar$, $T_{red} = 973\,K$ and $p_{tot,ox} = 5\,bar$.

Fig. 8.3e plots the total amount of purified gas $V_{product}$ per kg of $SrFeO_{3-\delta}$ for all cases presented. The values of $p_{red} = 1\,bar$ and $10^{-2}\,bar$ are identical since they share the same oxygen partial pressure during reduction. As expected, the total amount of product gas increases with increasing total pressure during oxidation. In addition, a lower p_{red} and a

higher T_{red} lead to an increased product gas amount, where p_{red} has a more considerable influence than T_{red} for the selected parameter range.

The lowest energy demand and an average yield for $SrFeO_{3-\delta}$ occur at the highest reduction temperature $T_{\mathrm{red}} = 973\,\mathrm{K}$, the average total pressure during reduction $p_{\mathrm{red}} = 10^{-2}\,\mathrm{bar}$, and the highest total pressure during oxidation $p_{\mathrm{tot,ox}} = 5\,\mathrm{bar}$.

Based on Fig. 8.3d and Fig. 8.3e, decisions about the most suitable parameters for the experimental conversion can be made and whether the energy requirement or the volume of the product gas should be optimized. Additionally, whether $SrFeO_{3-\delta}$ is stable at the lowest p_{red} has to be investigated to prevent the material's decomposition.

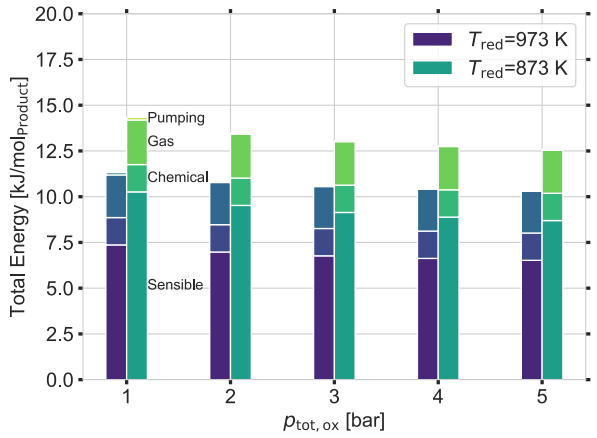

(a) p_{red}=1 bar with purge gas

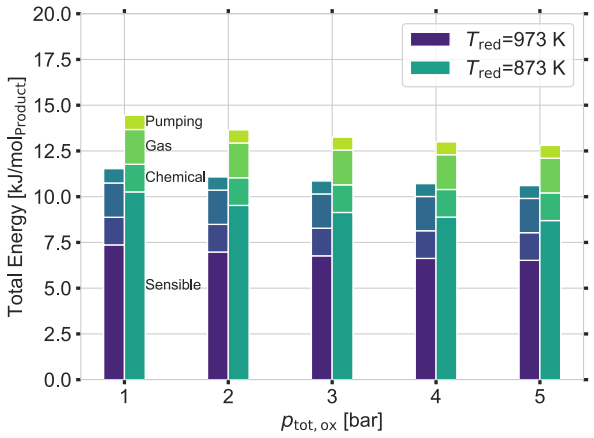

(b) p_{red}=10^{-2} bar

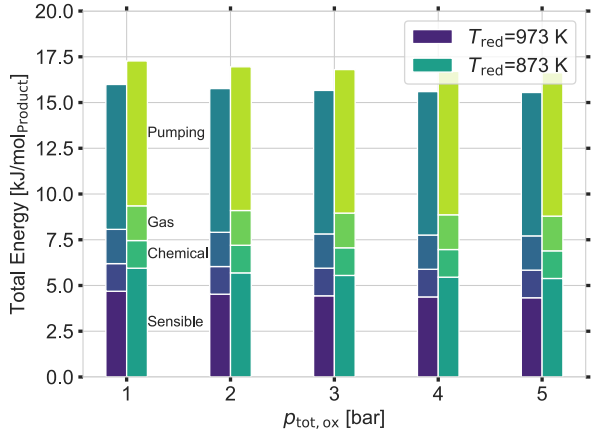

(c) p_{red}=10^{-4} bar

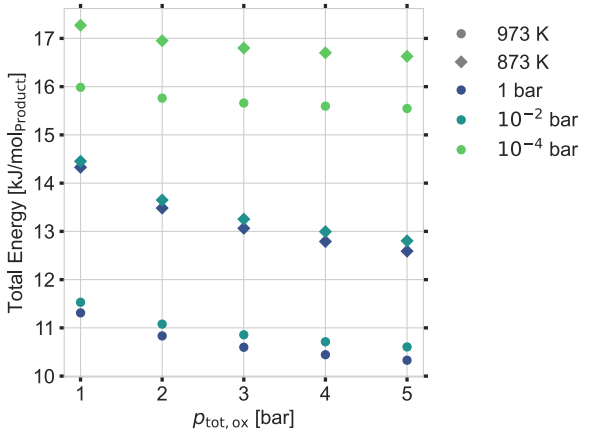

(d) The total energy demand for all conditions analyzed.

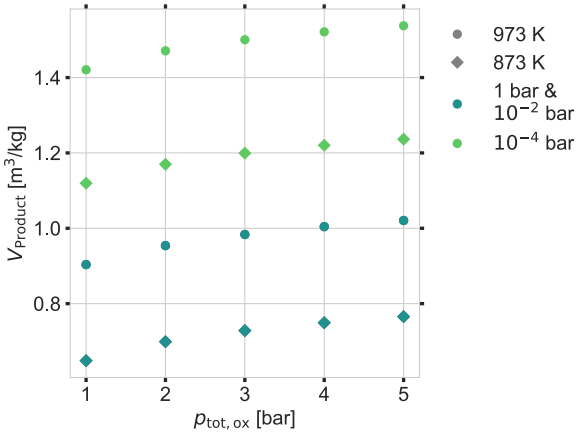

(e) Volume of product gas per kg of $SrFeO_{3-\delta}$ for all conditions analyzed. The values of p_{red} = 1 bar and 10^{-2} bar share the same oxygen partial pressure.

Figure 8.3.: Thermodynamic-based energy calculations for $SrFeO_{3-\delta}$ with different applied total reduction pressures p_{red}. The formulas of the energy distributions are shown in Sec. 2.9 on p. 22. The temperature indicates the reduction temperature. The oxidation temperature is 623 K. The oxygen fraction during oxidation is 1 %. The molar fraction of oxygen in the product gas is 10 ppm. Reproduced from *Klaas et al.*[82] with permission from the Royal Society of Chemistry.

8.3. Energetic Calculations for $Ca_{1-x}Sr_xMnO_{3-\delta}$

Since $Ca_{1-x}Sr_xMnO_{3-\delta}$ is also a studied material for air separation and oxygen delivery [21,22] and in this work, the influence of Sr content on redox performance is analyzed in detail, the energetic calculations are extended to this class of materials in the current section. As mentioned previously, for clarity, this section focuses on the two extreme cases with $x = 0$ and $x = 0.4$ for $Ca_{1-x}Sr_xMnO_{3-\delta}$.

As the volume V_{product} in the calculations for $SrFeO_{3-\delta}$ (Fig. 8.3e) already suggests, the reduced pressure relative to ambient pressure during reduction has a stronger effect on δ than the increased pressure during oxidation. The profile of the equilibrium curves (Fig. 2.9, p. 24) depends on both the material and the total pressure. Therefore, the temperature change required for a suitable change in δ depends on both. In this context, the substitution of Ca by Sr in $Ca_{1-x}Sr_xMnO_{3-\delta}$ results in a curve shift in the direction of $SrFeO_{3-\delta}$. This shift is due to the decrease in enthalpy with an increase in Sr (Sec. 5, p. 69). The change in enthalpy leads to different equilibria and, thus, to different purities of the nitrogen effluent during oxidation. The purity can be calculated by converting the equation 2.14 on p. 16. This results into: for $CaMnO_{3-\delta}$: $p_{O_2,\text{equ.}}(T_{\text{ox}} = 623\,\text{K}, \delta = 0.12) = 2 \times 10^{-17}\,\text{bar}$ and for $Ca_{0.6}Sr_{0.4}MnO_{3-\delta}$: $p_{O_2,\text{equ.}}(T_{\text{ox}} = 623\,\text{K}, \delta = 0.12) = 2 \times 10^{-13}\,\text{bar}$. Sr substitution thus reduces the achievable purity of the exhaust gas but also leads to lower required energies. The latter is reflected in the reduced enthalpy, which, for example, lowers the required reduction temperature for an identical degree of reduction and whose effects will become clearer in the following.

Since the change in stoichiometry between 623 K and 1073 K is less than 0.1, different reduction and oxidation temperatures must be chosen for $Ca_{1-x}Sr_xMnO_{3-\delta}$. In reactor designs, it is difficult to handle both high temperatures and high total pressure or vacuum due to, e.g., valves and reactor materials. Therefore, a reduction temperature of 1173 K and 1223 K is chosen for analysis, although thermodynamically, a higher reduction temperature would be preferable. To take advantage of the steepest slope of δ (Fig. 2.9, p. 24) between oxidation temperature and reduction temperature, an oxidation temperature of 973 K and 1023 K is chosen. The kinetic studies on this class of materials showed fast oxidation kinetics at the selected temperatures (Chap. 7, p. 89).

Fig. 8.4 compares the energy demand contributions for the different temperature variations. For each temperature change, the results for both Sr contents and the highest (5 bar) and lowest (1 bar) total pressure during oxidation are shown. Since the trend is similar to $SrFeO_{3-\delta}$, the intermediate pressures are not included for clarity. In addition, the different total pressures during reduction are analyzed for each material, starting on the left with 1 bar, moving through 10^{-2} bar to 10^{-4} bar. The relationship of the different contributions to the total energy is identical to that already discussed for $SrFeO_{3-\delta}$ (Sec. 8.2, p. 110).

Except when comparing the total energies between $p_{red} = 1\,bar$ and $10^{-2}\,bar$. Here, the $p_{red} = 10^{-2}\,bar$ case has a lower total energy requirement, even without considering the additional energy for the generation of the purge gas. Furthermore, in the direct comparison of these two cases, the identical contribution of sensible and chemical energy for both cases, as mentioned before, is noticeable.

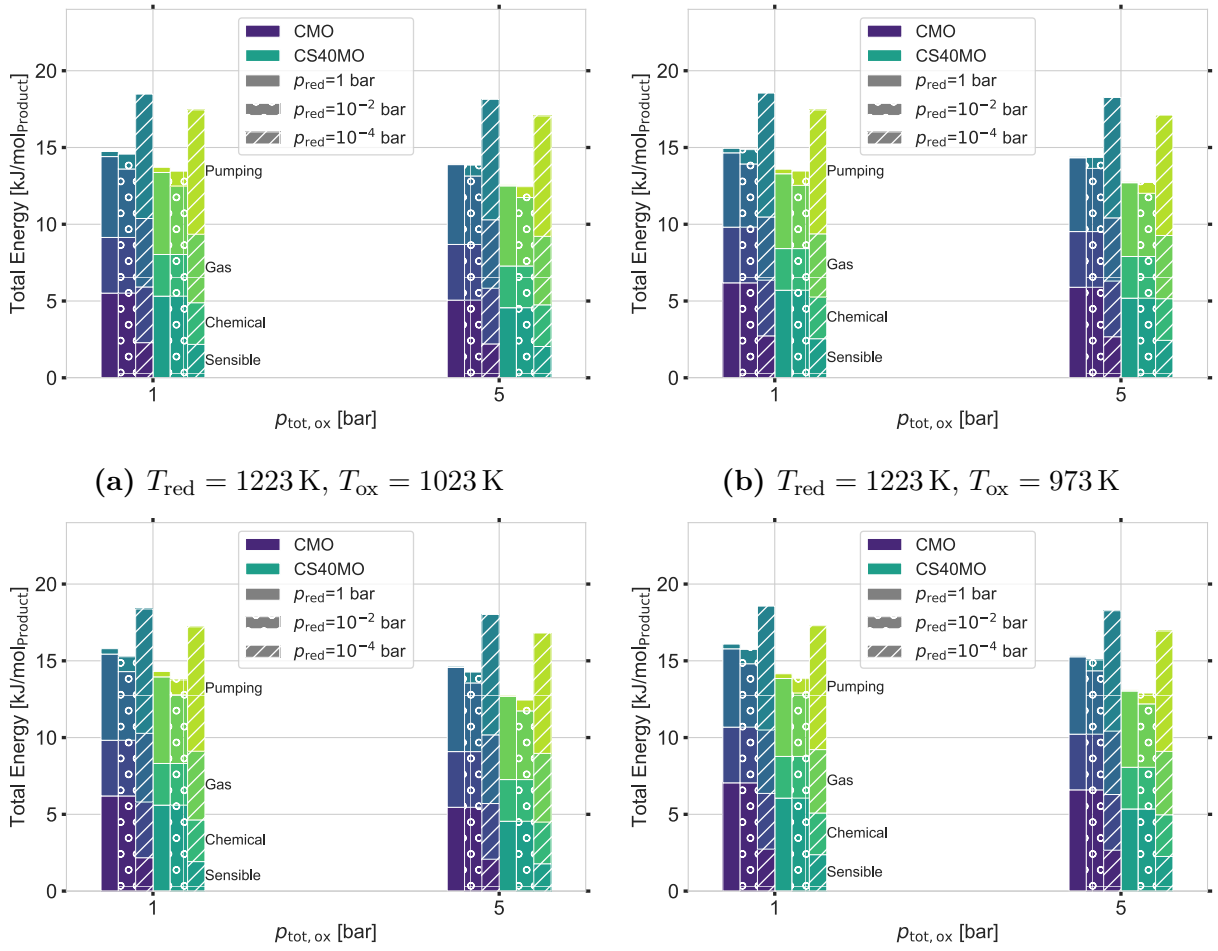

(a) $T_{red} = 1223\,K$, $T_{ox} = 1023\,K$ **(b)** $T_{red} = 1223\,K$, $T_{ox} = 973\,K$

(c) $T_{red} = 1173\,K$, $T_{ox} = 1023\,K$ **(d)** $T_{red} = 1173\,K$, $T_{ox} = 973\,K$

Figure 8.4.: Thermodynamic-based energy calculation of $Ca_{1-x}Sr_xMnO_{3-\delta}$ with energetic contributions for both Sr-contents and the discussed temperature swings. The respective temperatures are displayed in the caption. For each temperature swing, the highest (5 bar) and lowest (1 bar) total pressure during oxidation are included. Additionally, the different total pressures during reduction are analyzed for each material. They are displayed by different hatches starting with 1 bar on the left, through 10^{-2} bar to 10^{-4} bar on the right. Reproduced from *Klaas et al.*[82] with permission from the Royal Society of Chemistry.

$CaMnO_{3-\delta}$ has a higher energy consumption compared to $Ca_{0.6}Sr_{0.4}MnO_{3-\delta}$, which is due to the higher enthalpy of reduction (Chap. 5, p. 69). The higher enthalpy of reduction leads to smaller changes in the non-stoichiometry $\Delta\delta$, thus lowering the yield. It also directly increases Q_{chem} (eq. 2.28, p. 25), since Q_{chem} is proportional to enthalpy. The trends for

$p_{\mathrm{tot,ox}}$ and p_{red} are similar to those for $SrFeO_{3-\delta}$. A similar trend is anticipated since the calculations are based on the same model. The optimum reduction and oxidation temperature depends on the applied pressure. The higher reduction temperature reduces the energy required for both temperatures for reduction and oxidation at ambient pressure. In addition, the larger temperature variation has a higher energy requirement.

The lowest energy demand is for $Ca_{0.6}Sr_{0.4}MnO_{3-\delta}$ with $T_{\mathrm{red}} = 1173\,\mathrm{K}$ and $T_{\mathrm{ox}} = 1023\,\mathrm{K}$, $p_{\mathrm{red}} = 10^{-2}\,\mathrm{bar}$ and $p_{\mathrm{tot,ox}} = 5\,\mathrm{bar}$. Nevertheless, experiments are needed to validate the calculated product gas amounts and to verify that the nitrogen outlet purities are sufficient. Another advantage of using Sr-substituted $CaMnO_{3-\delta}$ is the prevention of decomposition at high temperatures and low oxygen partial pressures.[66]

8.4. Comparison of the Materials

Table 8.3 summarizes the lowest total energy required per mole of product for each material discussed in this chapter and the corresponding experimental operating parameters. It also contains additional information for Sr contents of $x \in [0.1, 0.3]$. In a recent publication by *Capstick et al.*,[20] $Sr_{0.8}Ca_{0.2}FeO_{3-\delta}$ was investigated for the production of high-purity nitrogen. Since this material can produce nitrogen with oxygen impurities of 10 ppm, it is included in the comparison of materials. To calculate the non-stoichiometries for the reduced and oxidized states, their empirical model is used.[20] The enthalpy used can be found in Sec. A.12 on p. 149. The oxidation and reduction temperatures are fixed to their selected test case scenario. To facilitate comparison between materials, the reduction and the oxidation pressure are aligned with the best parameters of the other materials analyzed in this chapter; $p_{\mathrm{red}} = 10^{-2}\,\mathrm{bar}$ and $p_{\mathrm{tot,ox}} = 5\,\mathrm{bar}$.

In addition, table 8.3 provides a summary of the total masses m_{Redox} of redox material required to produce V_{ProdRate} =24 000 $\mathrm{Nm^3/d}$[20] product gas. These masses are calculated according to the following:

$$m_{\mathrm{redox}} = V_{\mathrm{ProdRate}} \cdot t_{\mathrm{cycle}} \cdot \frac{1}{V_{\mathrm{Product}}}. \tag{8.1}$$

Here, t_{cycle} denotes the time for completion of a redox cycle and is assumed to be 10 h following *Capstick et al.*[20]

The optimum experimental parameters are identical for all the $Ca_{1-x}Sr_xMnO_{3-\delta}$ materials investigated. Except for $Ca_{0.6}Sr_{0.4}MnO_{3-\delta}$, here, the lower reduction temperature ($T_{\mathrm{red}} = 1173\,\mathrm{K}$) leads to lower total energy. This deviation can be explained by the different slope of the δ-curves, which is influenced by the Sr content (Fig. 2.9, p. 24). Increasing the Sr content leads to a decrease in the required energy. It should be kept in mind that a decreasing lowest possible nitrogen purity may accompany this.

Table 8.3.: Optimal experimental parameters for all materials investigated within the energetic study. SFO denotes $SrFeO_{3-\delta}$, and CMO denotes $CaMnO_{3-\delta}$. In addition to the results for the Sr contents discussed here, the results for the Sr contents in between (e.g., CS10MO denotes $Ca_{0.9}Sr_{0.1}MnO_{3-\delta}$) and $Sr_{0.8}Ca_{0.2}FeO_{3-\delta}$ (SC20FO) are also presented. The total energy E_{tot} is in $\text{kJ/mol}_{\text{Product}}$. The reduction and oxidation pressure are $p_{\text{red}} = 10^{-2}\,\text{bar}$ and $p_{\text{tot,ox}} = 5\,\text{bar}$ for all results presented.

Material	T_{red} [K]	T_{ox} [K]	E_{tot} [kJ\mol]	m_{redox} [kg]
SFO	973	623	10.605	9798
SC20FO	873	623	9.295	7905
CMO	1223	1023	13.852	12769
CS10MO	1223	1023	13.461	12769
CS20MO	1223	1023	13.096	12811
CS30MO	1223	1023	12.758	12906
CS40MO	1173	1023	12.445	17353

Both $SrFeO_{3-\delta}$ and $Sr_{0.8}Ca_{0.2}FeO_{3-\delta}$ have lower total energy demand than $Ca_{1-x}Sr_xMnO_{3-\delta}$ regardless of Sr content. In addition, less redox material is required to produce $24\,000\,\text{Nm}^3/\text{d}$. The increasing trend in mass required with increasing Sr content is due to the increasing molar mass of the material with increasing Sr content. The lowest total energy requirement and mass of redox material are required for $Sr_{0.8}Ca_{0.2}FeO_{3-\delta}$.

8.5. Parametric Study for Selected Materials

As mentioned in the prior section, $Sr_{0.8}Ca_{0.2}FeO_{3-\delta}$ has the lowest total energy demand and total mass of redox material required to produce $24\,000\,\text{Nm}^3/\text{d}$ of N_2 at an oxygen impurity level of 10 ppm. However, due to the lower enthalpy (Sec. A.12, p. 149), this material may not be suitable when lower oxygen impurities are required since a lower enthalpy is accompanied by a lower oxygen affinity.[23]

A more detailed parameter study will be conducted[1] to identify the best parameters for this material. Since the overall process will be considered, the energy demand of the PSA (eq. 2.25, p. 25) will be included in this parameter study. The PSA outlet pressure is 7 bar. For pressures above 7 bar, the energy requirement for compressing the gas is calculated according to eq. 2.26 on p. 25.

Fig. 8.5 presents the results of the parameter study. E_{redox} is the sum of the energy contributions associated with the redox process: $E_{\text{redox}} = Q_{\text{sens}} + Q_{\text{chem}} + Q_{\text{gas}} + W_{\text{vac}}$.

[1] The initial python script for this detailed parameter study was written by Dr. Brendan Bulfin and adjusted by the author.

Where W_{vac} is the energy demand of the vacuum pump. E_{total} is the total energy demand: $E_{\mathrm{tot}} = E_{\mathrm{redox}} + W_{\mathrm{comp}} + W_{\mathrm{PSA}}$.

The oxygen impurity of 10 ppm in the product gas is fixed. Similar to the above studies, the reduction temperature T_{red}, the pressure during reduction p_{red}, and the total pressure during oxidation p_{ox} will be varied. This time, the variation will be over a more extensive range and a quasi-continuous parameter change. In addition, the PSA output oxygen mole fraction x_{O2} and thus the oxygen partial pressure during oxidation will be varied. The standard parameters are:

$$\begin{aligned} T_{\mathrm{red}} &= 873\,\mathrm{K} \\ p_{\mathrm{red}} &= 0.01\,\mathrm{bar} \\ p_{\mathrm{tot,ox}} &= 7\,\mathrm{bar} \\ x_{\mathrm{O_2}} &= 0.01 \end{aligned}$$

The default total pressure during oxidation $p_{\mathrm{tot,ox}}$ is chosen so that $W_{\mathrm{comp}} = 0$ since the outlet pressure of the PSA is 7 bar.

As shown in the previous sections, the pressure increase during oxidation reduces the total energy demand. Therefore, the effect of an additional pressure increase using a compressor after the PSA is investigated (Fig. 8.6a). The increasing oxidation pressure causes the heat required to heat the gas to diminish and approach zero as the compression also heats the gas. This decreasing effect is eroded by the increasing energy demand of the compressor, so pressures above 7 bar do not reduce the total energy. However, additional compression of the incoming gas may be advantageous if the end user requires high-pressure nitrogen, for example, for producing ammonia using the Haber-bosch process. In addition, this increases the residence time of the gas in the reactor and increases the oxygen partial pressure, which leads to increased oxidation.

The reduction of pressure during reduction (Fig. 8.6b) has two competing contributions. First, it increases the change in non-stoichiometry and thus the molar amount of N_2 produced. This effect is most noticeable in the decrease in Q_{sens}. On the other hand, it increases the work of the vacuum pump. Therefore, balancing these two contributions, the minimum required energy is for p_{red} =0.023 bar.

When choosing the reduction temperature (Fig. 8.6c), it has to be ensured that the change in non-stoichiometry never reaches zero. Mathematically, this would lead to an infinite required energy. Therefore, the choice of reduction temperature always depends on the reduction pressure. In addition, the reduction degree also determines which oxygen partial pressures can be reached at the outlet. In the standard case, this means that the required

oxygen impurity of 10 ppm is only achieved at reduction temperatures above 725 K. In the present case, the energy requirement increases with an increasing reduction temperature; therefore, a reduction temperature of 725 K should be selected.

Regarding the energy contributions shown, higher reduction temperatures are likewise feasible since they lead only to a slight increase in energy demand. However, higher temperatures also require additional heating of the reactor shell. This heating is an additional energy contribution that explains why the lowest possible reduction temperature is preferred. Furthermore, lower temperatures are preferred due to design considerations.

The amount of oxygen coming from the PSA determines how much work is done by either the PSA or the redox cycle. As seen from Fig. 8.5d, the redox cycle's energy demand increases steeply as more oxygen comes from the PSA. However, if the work is performed solely by the PSA, the energy requirement also increases steeply. The work done when a PSA is used alone is $W_{\mathrm{PSA}}\,(10\,\mathrm{ppm}) = 85\,\mathrm{kJ/mol_{N_2}}$. Between these extreme cases, there are several suitable transition oxygen impurities. The lowest energy requirement is for a transition oxygen impurity of $x_{\mathrm{O_2,PSA}} = 0.0096$.

Parallel to $\mathrm{Sr_{0.8}Ca_{0.2}FeO_{3-\delta}}$, a parameter study for $\mathrm{Ca_{0.8}Sr_{0.2}MnO_{3-\delta}}$ is conducted in order to compare these two materials classes. $\mathrm{Ca_{0.8}Sr_{0.2}MnO_{3-\delta}}$ is selected because it is in the middle of the Sr proportions studied.

Based on Sec. 8.4 on p. 116, the oxidation temperature is $T_{\mathrm{ox}} = 1023\,\mathrm{K}$ and the standard reduction temperature is $T_{\mathrm{red}} = 1223\,\mathrm{K}$. All other standard parameters stay equal to the calculation of $\mathrm{Sr_{0.8}Ca_{0.2}FeO_{3-\delta}}$. The results are displayed in Fig. 8.6.

The results of $\mathrm{Ca_{0.8}Sr_{0.2}MnO_{3-\delta}}$ are similar to $\mathrm{Sr_{0.8}Ca_{0.2}FeO_{3-\delta}}$ and show the same trends as discussed above. As expected, due to the higher enthalpy of $\mathrm{Ca_{0.8}Sr_{0.2}MnO_{3-\delta}}$, the required energies are higher than for $\mathrm{Sr_{0.8}Ca_{0.2}FeO_{3-\delta}}$. Still, the total energy demand is competitive with a PSA alone. Nevertheless, experiments are needed to determine if the required oxygen purity can be achieved with the proposed parameters or if, for example, lower oxidation temperatures are required.

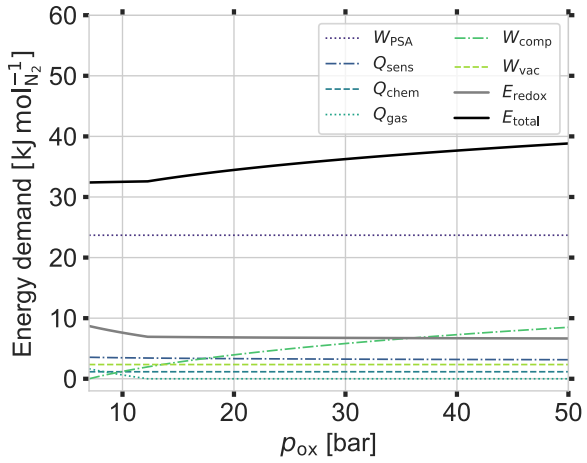

(a) Variation of the pressure during oxidation p_{ox}

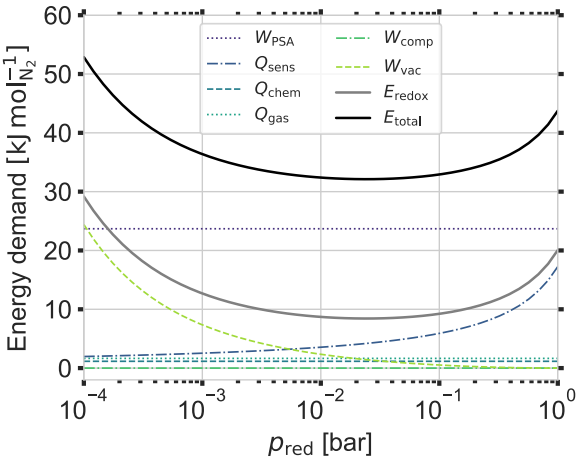

(b) Variation of the pressure during reduction p_{red}

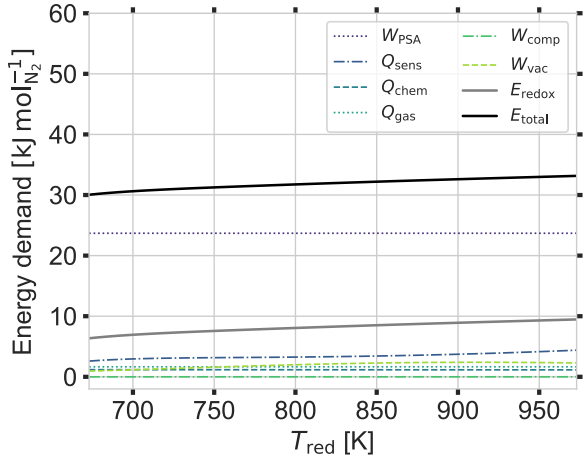

(c) Variation of the reduction temperature T_{red}

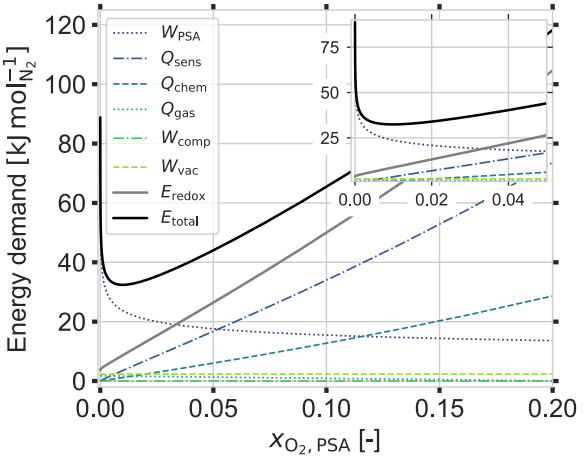

(d) Variation of the PSA outlet oxygen x_{O2} mole fraction and thus oxygen partial pressure during oxidation

Figure 8.5.: Parameter study for $Sr_{0.8}Ca_{0.2}FeO_{3-\delta}$. E_{redox} is the sum of the energy contributions associated with the redox process: $E_{redox} = Q_{sens} + Q_{chem} + Q_{gas} + W_{vac}$. E_{total} is the total energy demand: $E_{tot} = E_{redox} + W_{comp} + W_{PSA}$. Every graph displays the variation of one parameter, which is highlighted in the caption. The other parameters are fixed to their default values. Both diagrams from Fig. 8.5d are displayed separately in Sec. A.12 on p. 149. Reproduced from *Klaas et al.*[82] with permission from the Royal Society of Chemistry.

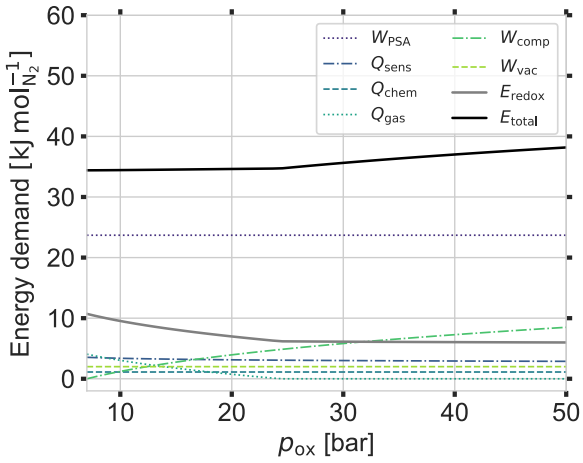

(a) Variation of the pressure during oxidation p_{ox}

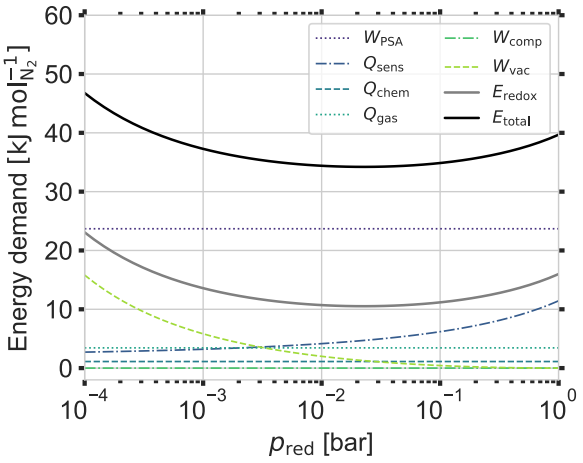

(b) Variation of the pressure during reduction p_{red}

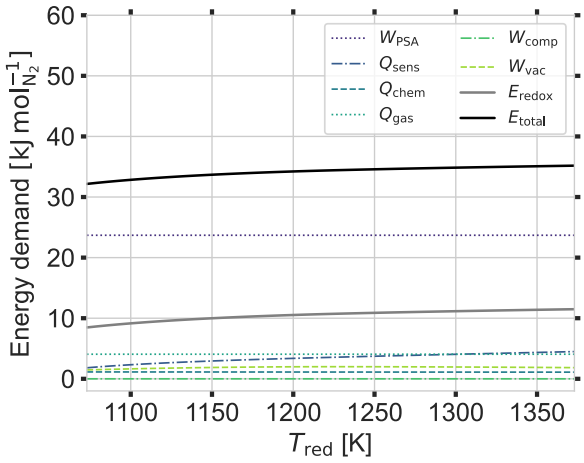

(c) Variation of the reduction temperature T_{red}

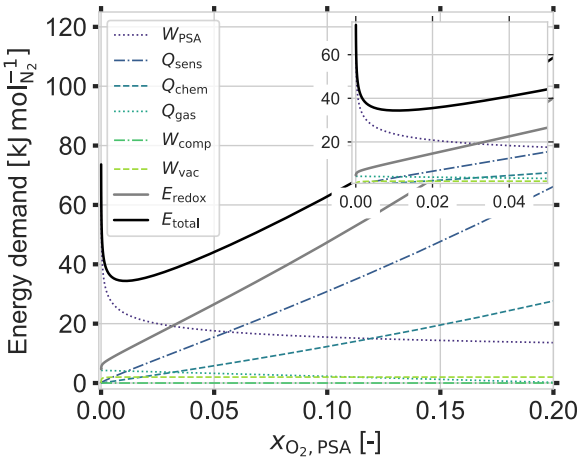

(d) Variation of the PSA outlet oxygen x_{O2} mole fraction and thus oxygen partial pressure during oxidation

Figure 8.6.: Parameter study for $Ca_{0.8}Sr_{0.2}MnO_{3-\delta}$. E_{redox} is the sum of the energy contributions associated with the redox process: $E_{redox} = Q_{sens} + Q_{chem} + Q_{gas} + W_{vac}$. E_{total} is the total energy demand: $E_{tot} = E_{redox} + W_{comp} + W_{PSA}$. Every graph displays the variation of one parameter, which is highlighted in the caption. The other parameters are fixed to their default values. Both diagrams from Fig. 8.6d are displayed separately in Sec. A.12 on p. 149.

8.6. Summary of the Energetic Requirements

This chapter demonstrated the energetic effects of different material compositions on a thermochemical cycle. First, packed-bed experiments proved that thermodynamic-based calculations represent experimental trends. However, there were deviations in the values between the calculation and the experiment due to kinetic limitations and the presumed formation of preferential flow tunnels.

After this validation of thermodynamic-based energetic calculations, the effect of different experimental conditions on the energetic requirement for a thermochemical cycle with $SrFeO_{3-\delta}$ to produce nitrogen with less than 10 ppm oxygen was analyzed. A higher reduction extent by increasing the reduction temperature proved to be energetically favorable. Additionally, applying a pressure of 5 bar during oxidation is beneficial for decreasing the energy requirements and increasing the residence time of the gas in the reactor. A moderate vacuum of 10^{-2} bar is better than applying a flush gas with an oxygen partial pressure of 10^{-2} bar. Moreover, for industrial applications, either the amount of purified gas or the energy demand could be optimized by varying the experimental conditions.

Afterward, the calculations are expanded to $Ca_{1-x}Sr_xMnO_{3-\delta}$. Since the same model as for $SrFeO_{3-\delta}$ is applied, the trends are comparable. Still, the higher enthalpy leads to higher total energy requirements. This trend persists within $Ca_{1-x}Sr_xMnO_{3-\delta}$, with higher Sr ratios leading to lower energy consumption due to the decreasing enthalpy. $Sr_{0.8}Ca_{0.2}FeO_{3-\delta}$ has the lowest enthalpy and energy requirement examined for air separation.

Nevertheless, when selecting the redox material, it is not only the energy requirement that is of interest but also the required nitrogen purities. After all, a lower enthalpy not only leads to a lower energy requirement but also to a lower oxygen affinity. The chapter is concluded with an elaborated parameter study to identify the optimal operating parameter for $Sr_{0.8}Ca_{0.2}FeO_{3-\delta}$ and $Ca_{0.8}Sr_{0.2}MnO_{3-\delta}$. Here, the study is expanded so that higher pressures than pressures from the PSA can be applied during oxidation, and different oxygen partial pressures from the PSA are included. The additional compression leads to an increase in the energy demand but is beneficial if downstream processes also require similar or higher pressures.

Both materials, $Sr_{0.8}Ca_{0.2}FeO_{3-\delta}$ and $Ca_{0.8}Sr_{0.2}MnO_{3-\delta}$, revealed lower energy consumption compared to a PSA alone and are, therefore, competitive as an alternative method for air separation with low residual oxygen concentration.

9. Conclusion and Outlook

This work aims to understand the impact of partial element substitution in perovskites to tune the material properties for solar thermochemical applications. Therefore, the effects of substitution on essential material properties for the application are analyzed. $CaMnO_{3-\delta}$ was selected as the base material because it is a material that has been used for solar thermochemical oxygen partial pressure adjustment. In addition, partial substitution of Ca by Sr was chosen. One criterion for selection is the use of non-toxic, abundant, and cheap elements.

The changes in the crystal structure at different Sr concentrations are studied using XRD. In the fully oxidized state and at room temperature, the lattice parameter increases with increasing Sr content due to the larger ionic radius of Sr compared to the ionic radius of Ca. In contrast to the predictions of the *Goldschmidt* tolerance factor, the orthorhombic distortion is preserved over the investigated range but with a decreasing tendency. The substitution mainly affects the length of the A-O bond by elongating it.

The HT-XRD results, analyzing samples with Sr concentrations up to 20 %, exhibit a phase change from orthorhombic to cubic during the reduction of the sample. The phase transition temperature depends on the degree of reduction and the Sr concentration. The latter additionally affects the degree of reduction and thus has a double influence on the phase transformation temperature. In general, the higher the Sr content, the lower the phase change temperature. The phase change is reversible for all samples.

The observed lattice expansion is caused by thermal expansion and by reduction. During reduction, Mn^{4+} converts to Mn^{3+}. Thereby, the ionic radius of Mn^{3+} is greater. This increase in the ionic radius leads to an expansion of the lattice. The expansion of the material is not only observed at the crystallographic level but can also be observed in monolithic samples.[45] Therefore, the changes at the level of the crystal structure have an impact on the application. As the expansion causes mechanical stresses, deformation and cracking may occur.

Decomposition of the phase during reduction should be avoided as this can affect the redox behavior and mechanical stability. Except for $CaMnO_{3-\delta}$, none of the samples decompose during reduction or show minor phases.

Analysis of the molecular vibrations by Raman spectroscopy confirmed the XRD results of decreasing distortion with increasing Sr content. In addition, the nature of the distortion was determined. The most considerable distortion is caused by the tilting and rotation of the MnO_6-octahedra. This distortion decreases with increasing Sr content, which is related to the elongation of the A-O bond. In addition, the lower tilting and rotation lead to less displacement of the A ion from the ideal cubic position.

In the following, the changing of thermodynamics is summarized. The increase in the Sr content leads to a decreasing enthalpy and entropy. These values govern the required temperatures and determine the lowest achievable oxygen partial pressure for the application.

The change in crystal structure explains the decrease in enthalpy. Previous studies have shown that the formation of oxygen vacancies is facilitated in cubic structures compared to an orthorhombic distorted structure.[116] Thus, the decreasing distortion facilitates reduction, resulting in lower enthalpy. In addition, the elongation of the A-O bond leads to a lower binding energy, which likewise facilitates the release of oxygen.

Considering the effects of Sr concentration on the material's microstructure, the crystallite size decreases with increasing Sr content. This change in microstructure is attributed to the reduced ion mobility, which causes the formation of smaller crystallites. The increased Sr content resulted in a more homogeneous powder in terms of the size of the small particles. The more homogeneous the powder, the more homogeneously the surface of the granules is sintered. Thus, the granules with the highest Sr content have the most homogeneous sintered surface. The microstructure of the granules is vital for the behavior under mechanical load. The Sr concentration does not affect the surface area of the porosity. All samples have a small specific surface area of less than $1\,m^2/g$ without meso- or micropores. Moreover, the elements are evenly distributed.

For the application, not only powder but also macroscopic structures are of interest because they can be handled more efficiently. Thus, the microstructure of $Ca_{0.8}Sr_{0.2}MnO_3$ for different macrostructures and production routes is investigated.

Fine powder leads to a densely sintered surface, and coarse powder leads to a rough surface. This trend applies to foams, pellets, and granules. Nevertheless, the different macrostructures have a slightly different appearance due to further processing. Some powders are made more compact, and others have undergone sublimation of the carrier structure. The trend discussed is also reflected in the porosity and surface area. For example, the sample made from the finer powder, which is sintered more densely, has lower porosity and a smaller specific surface area than the sample made from the coarser powder.

In conclusion, the microstructure of different macrostructures can be tuned by the fineness of the powder.

The kinetic analysis of granules made of $Ca_{1-x}Sr_xMnO_3$ revealed that increased Sr content resulted in faster oxidation kinetics and lower activation energy. Since the oxygen ion migration is preferred along defined axes,[125] the decreasing distortion causes this decreasing trend. Additionally, the increased *A*-O bond length facilitates the oxygen bulk diffusion.

The oxidation kinetics are independent of the oxygen partial pressure. Therefore, the surface reaction is fast and bulk diffusion is identified as the rate-limiting step. The reduction kinetics is rapid, so it cannot be investigated in more detail. Moreover, this fast reduction kinetics benefits the application by reducing the required cycle time.

The macrostructure of the sample has no significant influence on the activation energy of $Ca_{0.8}Sr_{0.2}MnO_{3-\delta}$, as it is similar for granules and foams. Nevertheless, the sample exhibits different oxidation curves depending on the microstructure. The denser sintered samples exhibit slower oxidation kinetics. Since mass diffusion is the rate-limiting step and previous studies have shown that oxidation rate is inversely proportional to particle size,[127,128] this behavior can be explained by the difference in particle size. Here, the denser sintered samples have a larger particle size, which means that they have a longer diffusion path and therefore oxidize more slowly. In addition, ion migration occurs faster at the grain boundaries, and less sintered samples have more grain boundaries and therefore oxidize faster. Hence, the oxidation behavior can be tuned for the application by adjusting the microstructure.

The energy requirements are important for the application. Here, the production of highly pure nitrogen by a coupled PSA-thermochemical process is examined. To verify the approach of thermodynamic energy calculations, laboratory-scale experiments with packed beds are performed. They confirm that the thermodynamic calculations identify trends and are thus a reasonable approach.

The calculations demonstrate that a total pressure of up to 5 bar is advantageous for energy consumption. In addition, using a moderate vacuum is better than using a purge gas during reduction. Furthermore, the energy demand or the amount of purged gas can be optimized depending on the application's requirements. The comparison of different material compositions shows that a higher enthalpy leads to higher energy consumption. Using materials with low enthalpy may result in a higher minimum oxygen concentration than using materials with higher enthalpy, posing a disadvantage.

In general, the oxygen concentration from the PSA is a crucial parameter for the energy consumption of a coupled PSA-thermochemical process. Therefore, the energy required for this entire process is competitive with the state-of-the-art fossil-based processes.

In summary, the work reveals that the performance of a thermochemical cycle can be tuned by varying the material composition - changes in structure at the crystal level result in altered thermodynamic and kinetic material properties. In particular, the altered thermodynamic properties affect the energy required for an air separation process to produce

high-purity nitrogen. In addition, the kinetics can be influenced almost independently of the macrostructure by varying the microstructure.

In perspective, the hypothesis about microstructure-dependent oxidation kinetics needs to be further investigated. As mentioned earlier, ^{18}O-secondary ion mass spectrometry is beneficial for analyzing the diffusion of oxygen ions in bulk.

Moreover, the mechanical stability needs to be investigated and optimized at room temperature and under application conditions. Finally, the influence of the Sr content as well as the influence of the microstructure, are of interest here.

In addition, the $Ca_{1-x}Sr_xMnO_{3-\delta}$ will be implemented in a reactor to demonstrate the production of high-purity nitrogen using a coupled PSA thermochemical cycle. In this context, the energetic calculations will be used to determine the best operating conditions and, conversely, to validate the energetic predictions.

List of Figures

List of Tables

A. Appendix

A.1. Quantities for the Auto-combustion Method

Table A.1 shows the required quantities of the 0.1 M solutions to produce $Ca_{1-x}Sr_xMnO_{3-\delta}$ with $x \in [0, 0.4]$. Details on the production method can be found in 3.1.1 on p. 30.

Table A.1.: Quantities for the Auto-combustion method.

Sr-content [%]	$Ca(NO_3)_2$ [ml]	$Mn(NO_3)_2$ [ml]	$Sr(NO_3)_2$ [ml]
0	35	35	
5	32.7	34.4	1.7
10	30.5	33.8	3.4
15	28.3	33.3	5
20	26.2	32.8	6.6
25	24.2	32.3	8.1
30	22.3	31.8	9.5
35	20.4	31.3	11
40	18.5	30.9	12.3

A.2. Results Rietveld Refinement

Table A.2 summarizes the results of the Rietveld refinement, which are relevant for the calculation of the basic distortion in Sec. 4.3 on p. 63.

Table A.2.: Results of the Rietveld refinement used to calculate the basic distortion.

Sample	Site	x-Coordinate	y-Coordinate	z-Coordinate
CMO	Ca	0.03301(9)	0.25000	-0.0069(2)
	Mn	0.00000	0.00000	0.50000
	O1	0.4917(3)	0.25000	0.0736(6)
	O2	0.2873(3)	0.0288(3)	-0.2865(3)
CS10MO	Ca	0.02702(12)	0.25000	-0.0035(5)
	Sr	0.02702(12)	0.25000	-0.0035(5)
	Mn	0.00000	0.00000	0.50000
	O1	0.4937(5)	0.25000	0.0613(12)
	O2	0.2828(6)	0.0303(5)	-0.2858(6)
CS20MO	Ca	0.0209(3)	0.25000	-0.0020(12)
	Sr	0.0209(3)	0.25000	-0.0020(12)
	Mn	0.00000	0.00000	0.50000
	O1	0.4897(14)	0.25000	0.0823(19)
	O2	0.281(3)	0.0197(10)	-0.281(3)
CS30MO	Ca	0.01776(16)	0.25000	-0.0009(5)
	Sr	0.01776(16)	0.25000	-0.0009(5)
	Mn	0.00000	0.00000	0.50000
	O1	0.4963(8)	0.25000	0.0647(14)
	O2	0.2811(8)	0.0229(7)	-0.2784(8)
CS40MO	Ca	0.01371(15)	0.25000	-0.0010(4)
	Sr	0.01371(15)	0.25000	-0.0010(4)
	Mn	0.00000	0.00000	0.50000
	O1	0.4974(7)	0.25000	0.0462(12)
	O2	0.2764(7)	0.0266(6)	-0.2767(7)

A.3. HT-XRD Lattice Parameter

The lattice parameters for the orthorhombic and cubic phases are shown in Fig. A.1. Experimental details can be found in Sec. 3.3 on p. 34.

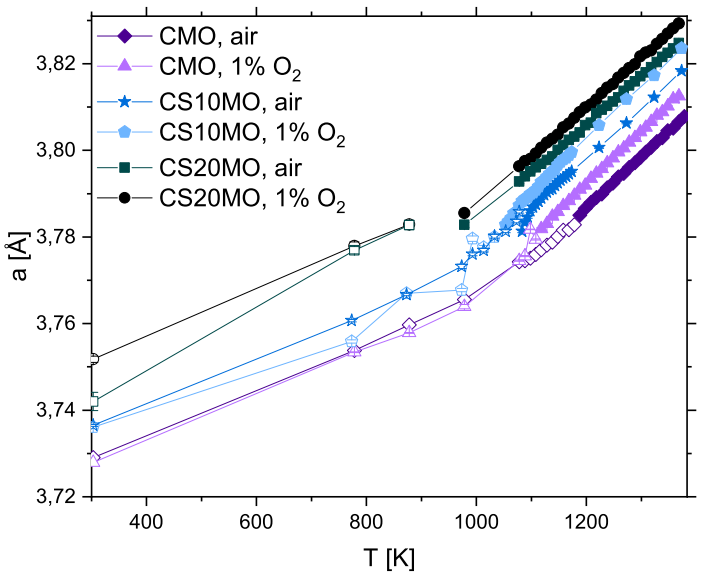

Figure A.1.: Cubic a (filled symbols) and pseudo-cubic a (empty symbols) lattice parameter of the HT-XRD. The lattice parameters are gained through Rietveld refinement.

A.4. Phase Stability

Iin the framework of a collaboration project, *GTT-technologies* performed chemical thermodynamic equilibrium calculations using the software *FactSage*™ to investigate if any decomposition is expected to occur. The resulting phase diagram of $Ca_{0.9}Sr_{0.1}MnO_{3-\delta}$ and $Ca_{0.6}Sr_{0.4}MnO_{3-\delta}$ is shown in Fig. A.2. In addition, the phases of the reduction curves are also displayed. The reduction curves are based on the experimental results presented in Chap. 5 on p. 69. The numbers on the line indicate the applied oxygen partial pressure. The graphs show that for $p_{O_2} = 0.0001$ bar, the reduction curves cross side phases. Therefore, considerable amounts of side phases are expected to be formed.

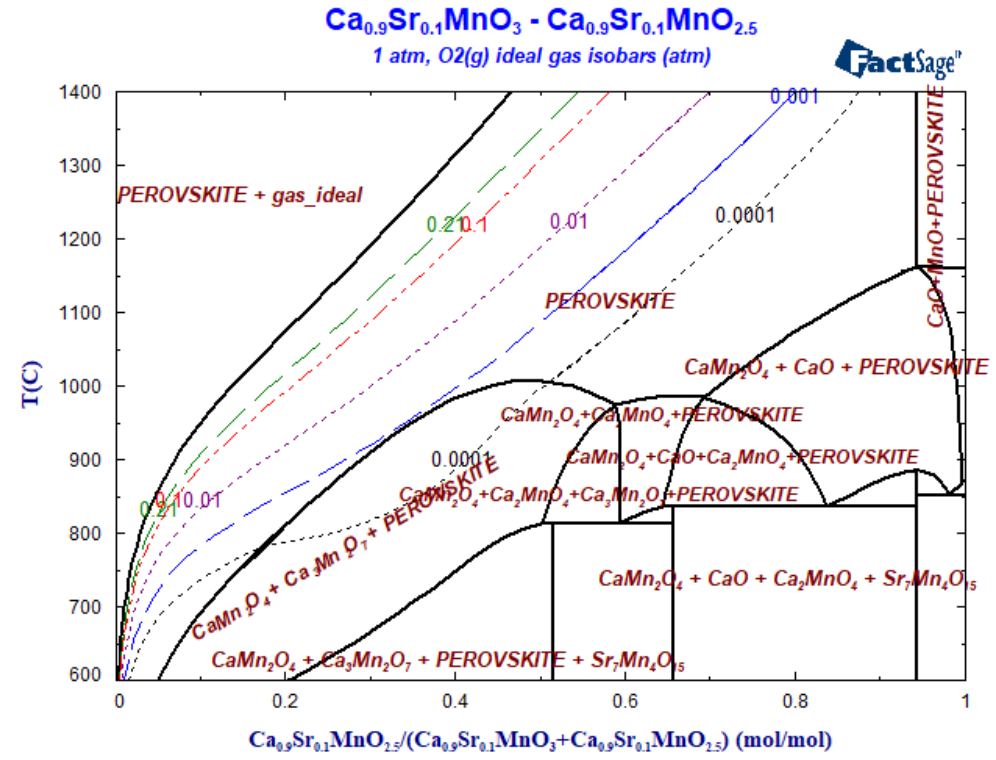

(a) $Ca_{0.9}Sr_{0.1}MnO_3$

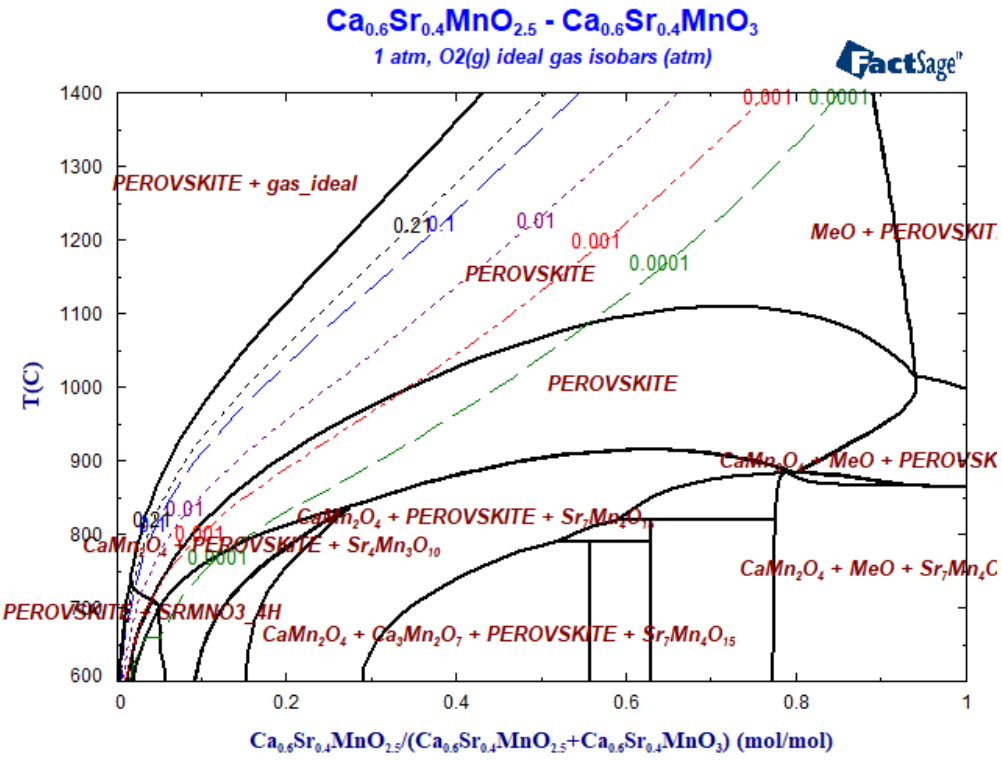

(b) $Ca_{0.6}Sr_{0.4}MnO_3$

Figure A.2.: Phase diagram of two $Ca_{1-x}Sr_xMnO_{3-\delta}$. The total pressure is 1 bar. The lines are the reduction curves. The numbers next to the lines with the corresponding color are the associated oxygen partial pressures. The phase diagrams indicate that especially for $p_{O_2} = 0.0001$ bar side-phases should occur. Printed with permission from *GTT-technologies*.[110]

A.5. XRD of Samples for the Raman Measurement

Fig. A.3 summarizes the qualitative XRD analysis of the samples used for the Raman spectroscopy. All samples do not exhibit any side phase except of $Ca_{0.6}Sr_{0.4}MnO_3$. A close-up in Fig. A.4 highlights the side phase.

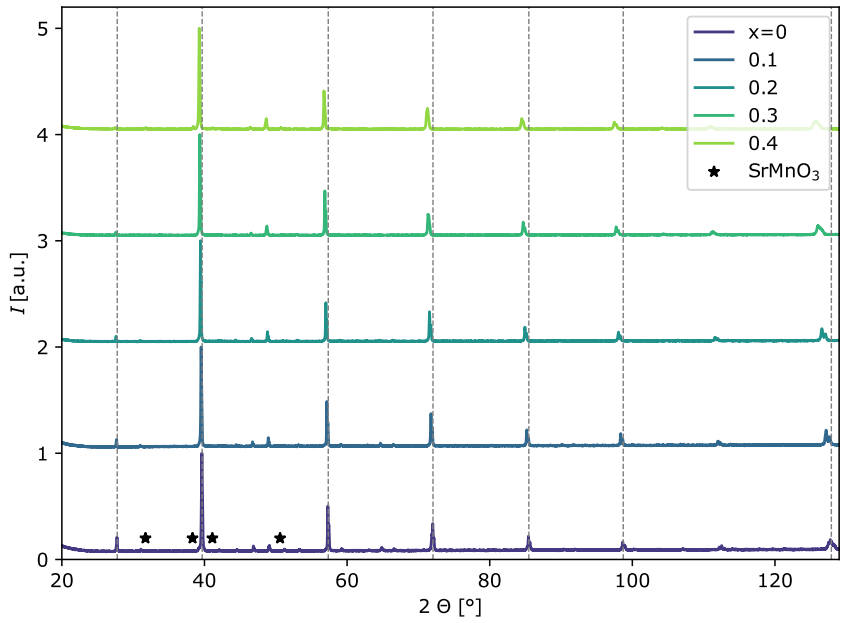

Figure A.3.: XRD pattern of $Ca_{1-x}Sr_xMnO_3$ measured with a cobalt anode. The vertical lines indicate the main peak position of $CaMnO_3$. The samples with $x \in [0, 0.3]$ are pure. $Ca_{0.6}Sr_{0.4}MnO_3$ has a minor secondary phase (Fig. A.4).

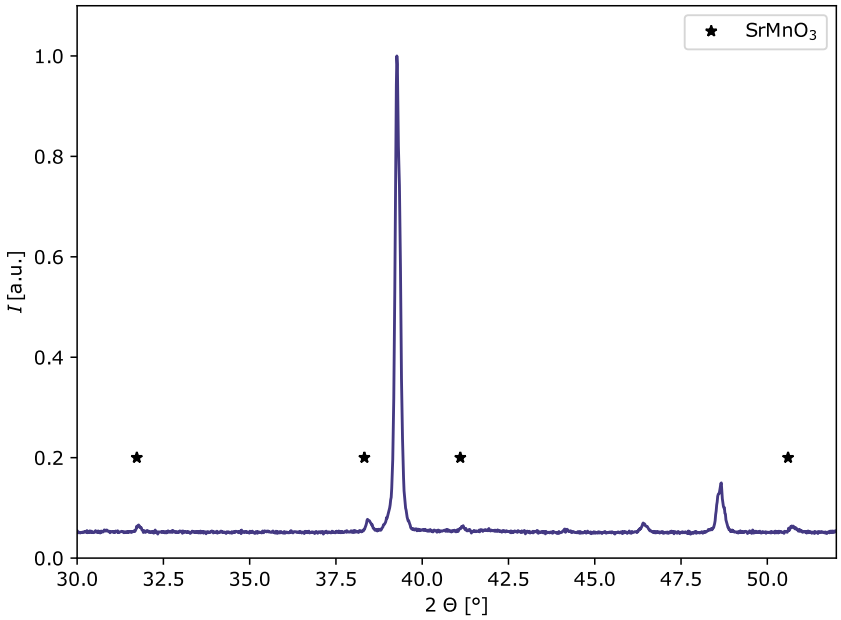

Figure A.4.: Close-up of the pattern of $Ca_{0.6}Sr_{0.4}MnO_3$. The main peaks of the minor $SrMnO_3$ phase are indicated with a star (*PDF 00-024-1213*).

A.6. Experimental Summary for XRD of Chap. 4

The summary of the experimental configuration for all XRDs presented in Chap. 4 can be found in Tab. A.3. More details on the experimental configuration can be found in Sec. 3.3 on p. 34.

Table A.3.: Summary of the experimental configuration for all XRDs presented in Chap. 4.

Description	Sec.	Sample	Anode material	2Θ range [°]	step width [°]
XRD	4.1	CMO	Copper	20–120	0.005
		CS05MO			0.005
		CS10MO			0.005
		CS15MO			0.005 & 0.02
		CS20MO			0.02
		CS25MO			0.02
		CS30MO			0.02
		CS40MO			0.02
HT-XRD	4.2	CMO	Copper	20–85	0.04
		CS10MO			
		CS20MO			
Reduced sample	4.2	CMO	Cobalt	20–130	0.017
		CS20MO			
		CS40MO			
Decomposition	4.2	CS10MO	Copper	20–85	0.04
		CS40MO			
Phase Purity	4.3	CMO	Cobalt	20–130	0.015
		CS10MO			
		CS20MO			
		CS30MO			
		CS40MO			

A.7. CIF for Rietveld Refinement

Table A.4 summarizes the CIF used for the quantitative phase analysis using the Rietveld refinement.

Table A.4.: Summary of the used CIF from the *ICSD* by *FIZ Karlsruhe - Leibniz Institute for Information Infrastructure.*

Sr-content [%]	CIF
0	160305
5	50998
10	50998
15	50998
20	50998
25	50999
30	50999
35	50999
40	50999

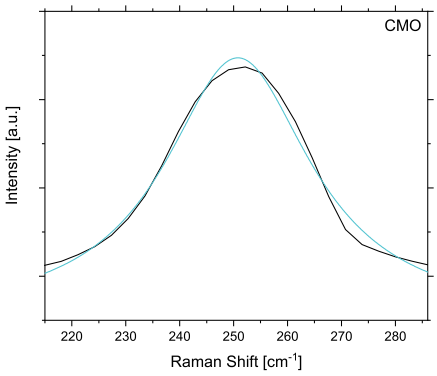

(a) Peak 1

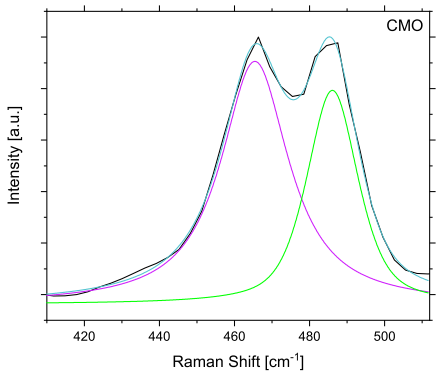

(b) Peak 2 and 3

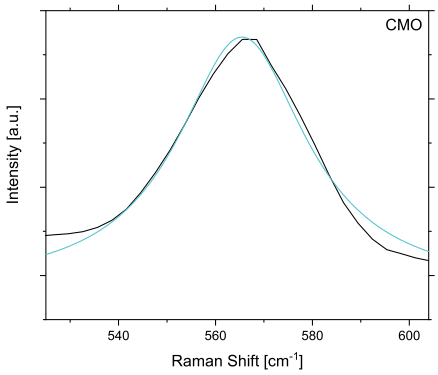

(c) Peak 4

Figure A.5.: Original data (black) of $CaMnO_3$ and fit curve (light green) are displayed. In **b)** also the individual peak fits are shown.

A.8. Fit of Raman Modes

In this section, the fits of the Raman modes are displayed and Tab. A.5 summarizes the goodness of the individual fits.

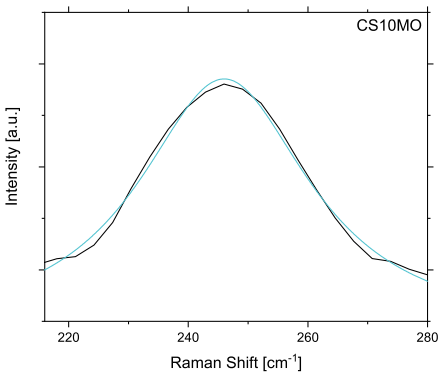

(a) Peak 1

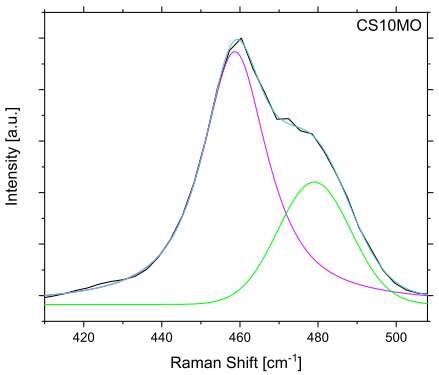

(b) Peak 2 and 3

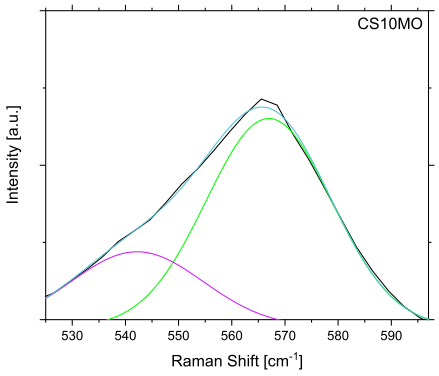

(c) Peak 4

Figure A.6.: Original data (black) of $Ca_{0.9}Sr_{0.1}MnO_3$ and fit curve (light green) are displayed. In **b)** also the individual peak fits are shown. **c)** For peak 4, a second peak (pink) needed to be included to achieve a good line fitting.

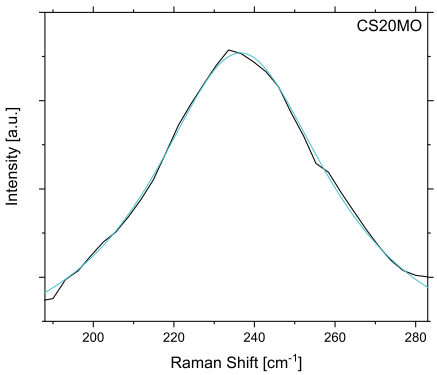

(a) Peak 1

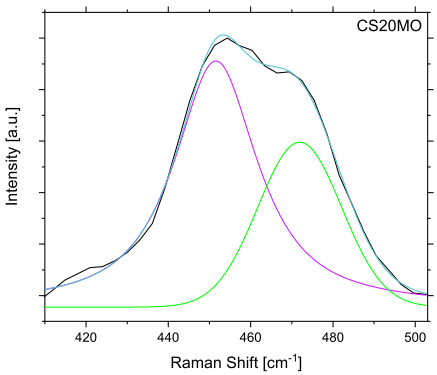

(b) Peak 2 and 3

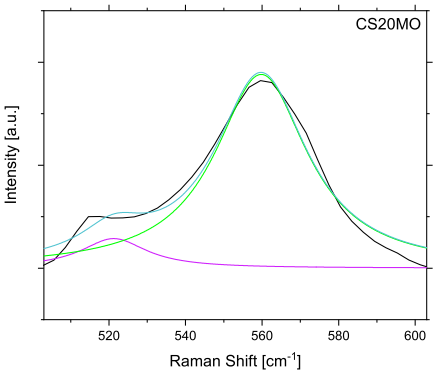

(c) Peak 4

Figure A.7.: Original data (black) of $Ca_{0.8}Sr_{0.2}MnO_3$ and fit curve (light green) are displayed. In **b)** also the individual peak fits are shown. **c)** For peak 4, a second peak (pink) needed to be included to achieve a good line fitting.

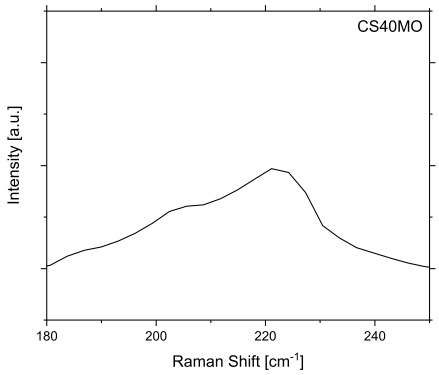

(a) Peak 1

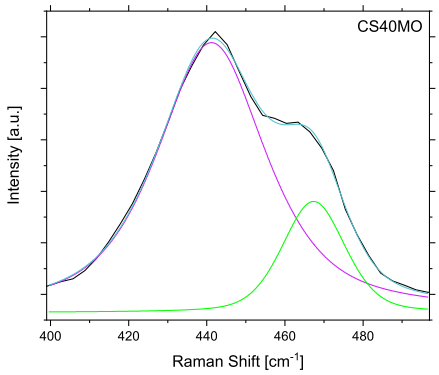

(b) Peak 2 and 3

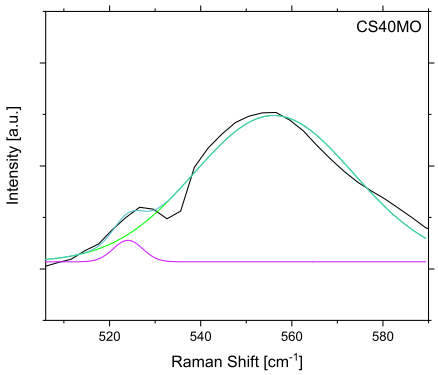

(c) Peak 4

Figure A.8.: Original data (black) of $Ca_{0.9}Sr_{0.1}MnO_3$ and fit curve (light green) are displayed. **a)** The low intensity did not allow a successful fitting. In **b)** also the individual peak fits are shown. **c)** For peak 4, a second peak (pink) needed to be included to achieve a good line fitting.

Table A.5.: Measures for the goodness of fit for the different Raman modes. The measures are extracted from *Origin*.

Sample	Peak	R^2	adjusted R^2
CMO	1	0.9898	0.9882
	2 & 3	0.9982	0.9977
	4	0.9820	0.9798
CS10MO	1	0.9924	0.9912
	2 & 3	0.9994	0.9992
	4	0.9913	0.9623
CS20MO	1	0.9969	0.9966
	2 & 3	0.9976	0.9967
	4	0.9718	0.9657
CS40MO	1		
	2 & 3	0.9988	0.9985
	4	0.9695	0.9659

A.9. Thermodynamic Analysis and Phase Purity of Samples Used

The structure of the perovskite for the thermodynamic analysis was studied with powder X-ray diffraction (XRD) using a *D8-Advance (A25)* instrument from *Bruker* with a copper anode and a *Lynxe-EyeXET-Detector* (Fig. A.9).

The equilibrium non-stoichiometry $\delta(T, p_{O_2})$ values dependent on oxygen partial pressure p_{O_2} and temperature T. The temperatures are displayed in K on the lines in Fig. A.10, A.11, A.12, A.13 and A.14. The squares show the experimental equilibrium values and the lines show the fit of the applied model.

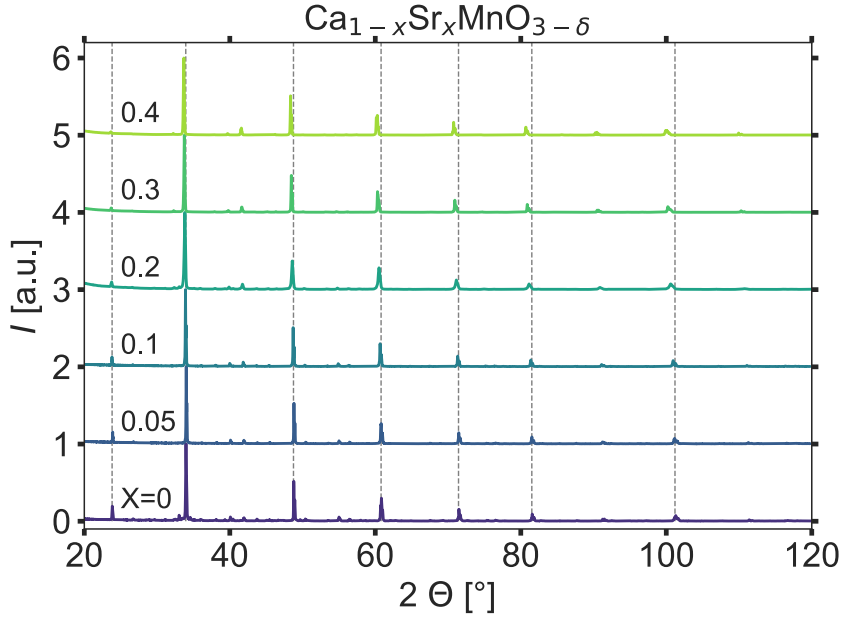

Figure A.9.: XRD-patterns of the perovskites prepared for the thermodynamic analysis. This pattern was measured with a copper anode. The vertical lines indicate the main peaks of $CaMnO_3$. Reproduced from *Klaas et al.*[98] with permission from the PCCP Owner Societies.

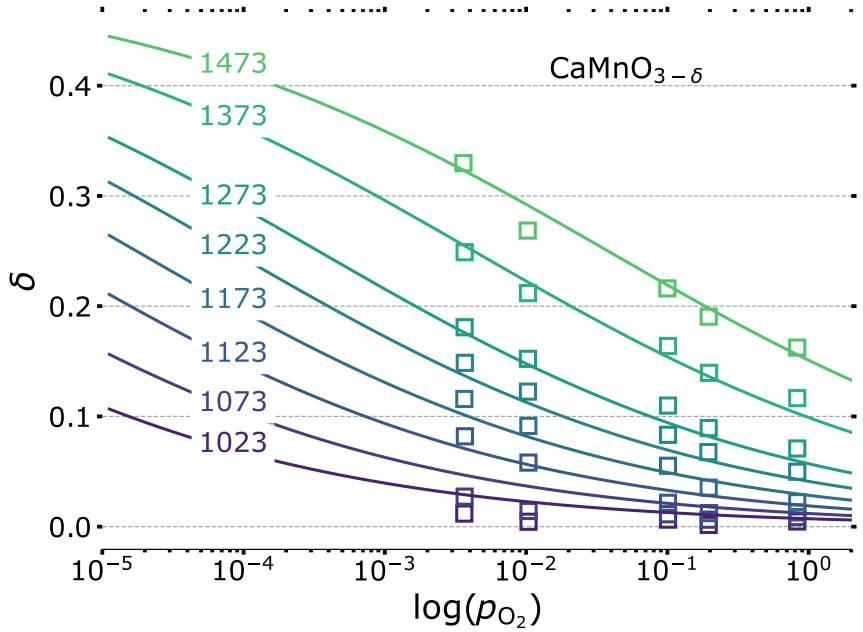

Figure A.10.: Thermodynamic analysis of $CaMnO_{3-\delta}$. Reproduced from *Klaas et al.*[98] with permission from the PCCP Owner Societies.

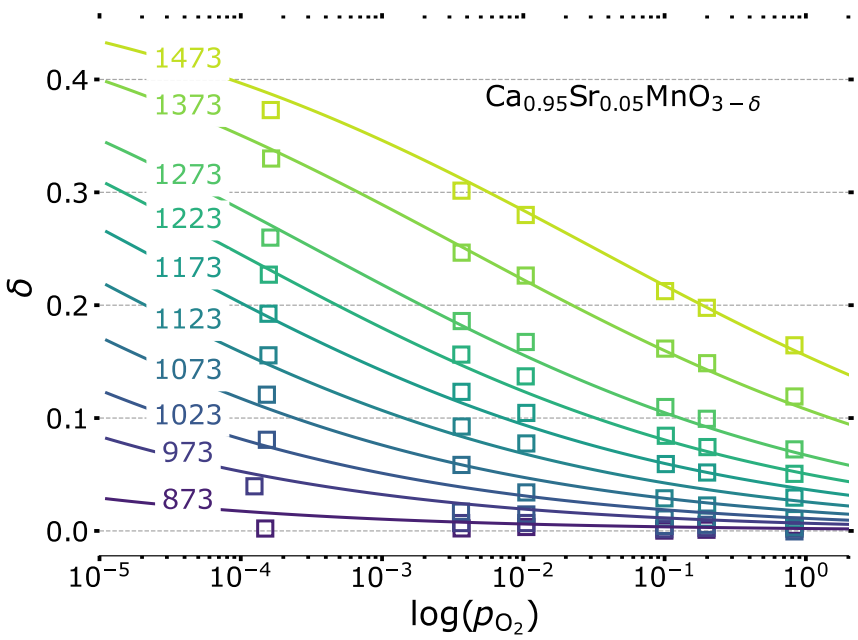

Figure A.11.: Thermodynamic analysis of $Ca_{0.95}Sr_{0.05}MnO_{3-\delta}$. Reproduced from *Klaas et al.*[98] with permission from the PCCP Owner Societies.

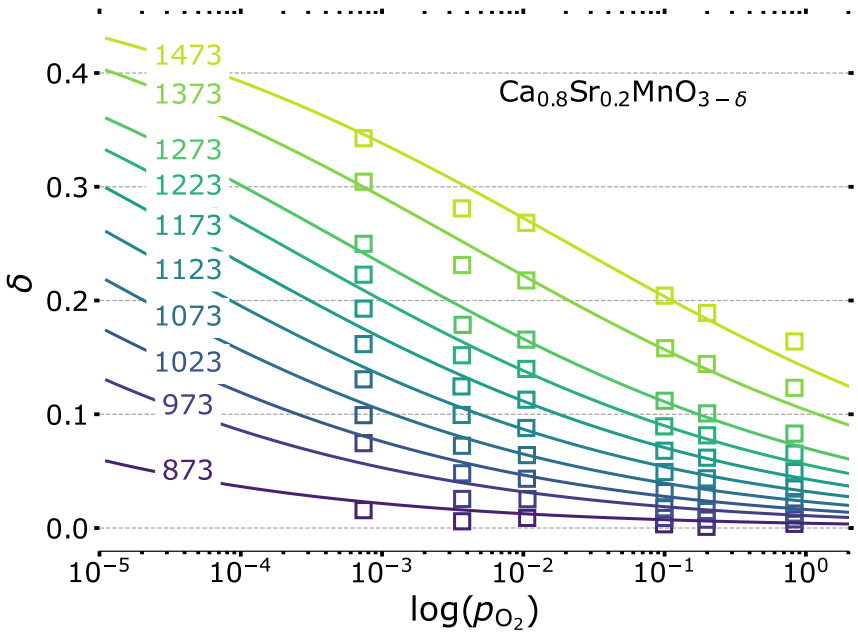

Figure A.12.: Thermodynamic analysis of $Ca_{0.8}Sr_{0.2}MnO_{3-\delta}$. Reproduced from *Klaas et al.*[98] with permission from the PCCP Owner Societies.

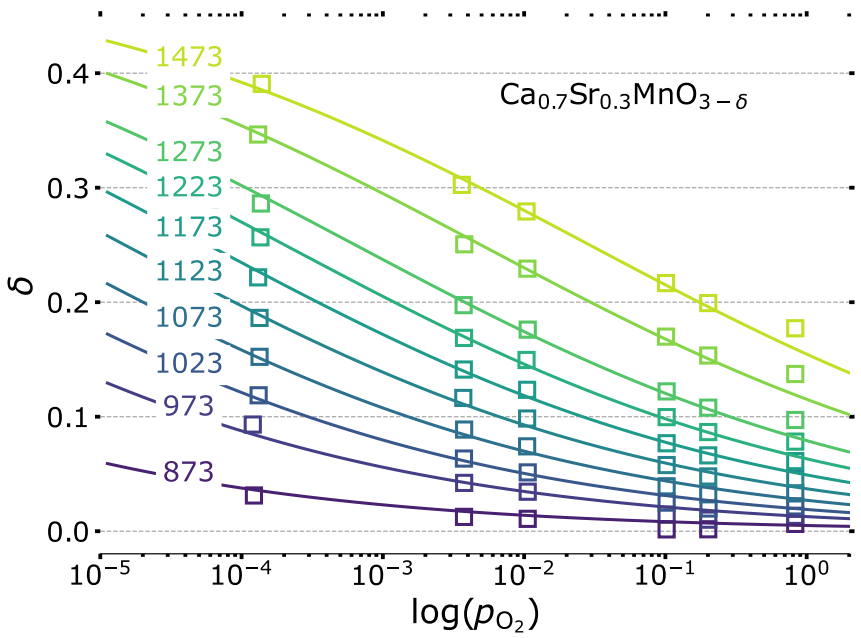

Figure A.13.: Thermodynamic analysis of $Ca_{0.7}Sr_{0.3}MnO_{3-\delta}$. Reproduced from *Klaas et al.*[98] with permission from the PCCP Owner Societies.

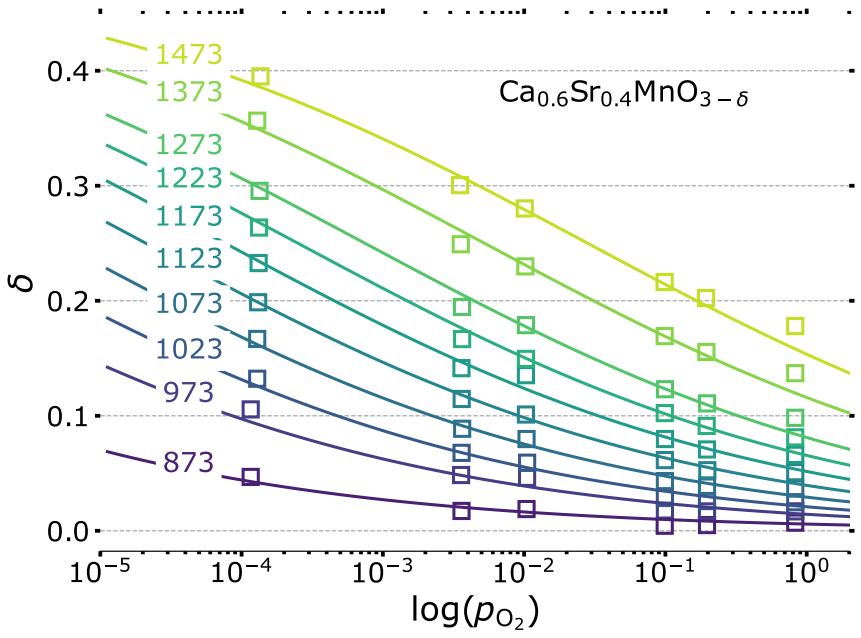

Figure A.14.: Thermodynamic analysis of $Ca_{0.6}Sr_{0.4}MnO_{3-\delta}$. Reproduced from *Klaas et al.*[98] with permission from the PCCP Owner Societies.

A.10. Mercury Porosimetry of Granules

Fig. A.15 displays the porosity dependent on the granule size. The material is $Ca_{0.8}Sr_{0.2}MnO_3$.

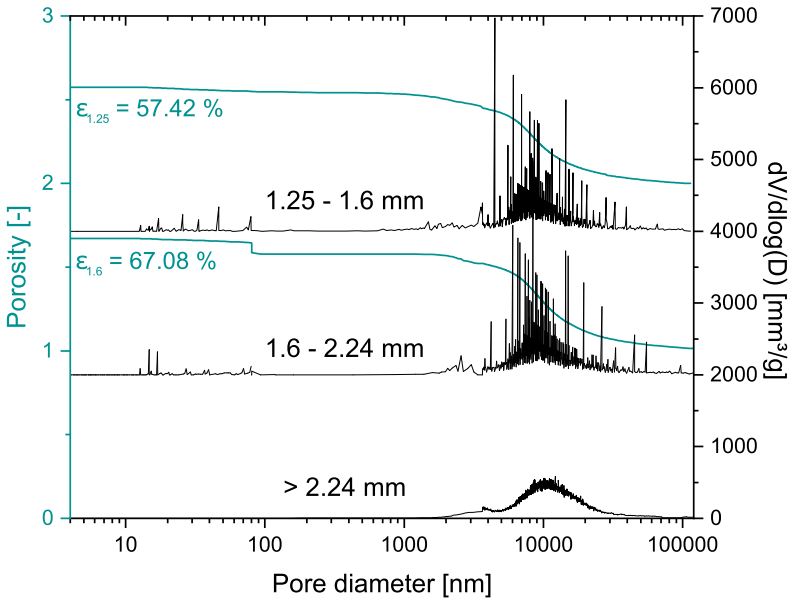

Figure A.15.: Particle size dependent porosity for $Ca_{0.8}Sr_{0.2}MnO_3$. Displayed are the normalized cumulative pore volume per g of material, which measures the porosity (left axis) and the differential pore volume distribution (right axis). Additionally, the total porosity is assigned for each sample.

A.11. Phase Purity of Granules

The crystallographic structure of the perovskite for the kinetic analysis was studied with XRD using a *D8-Advance (A25)* instrument from *Bruker* with a cobalt anode and a *Lynxe-EyeXET-Detector* (Fig. A.16).

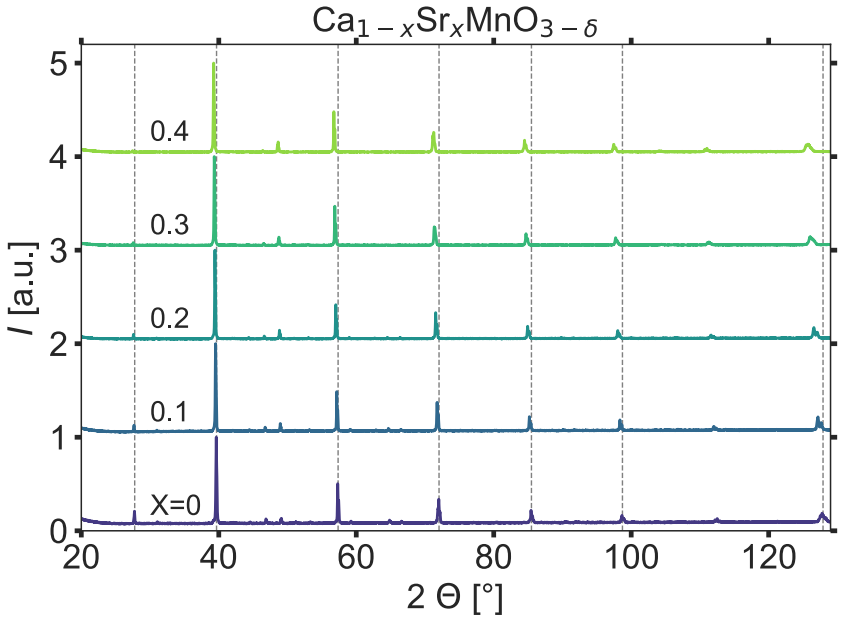

Figure A.16.: XRD-patterns of the perovskites prepared for the granules. This pattern was measured with a cobalt anode. The vertical lines indicate the main peaks of $CaMnO_3$. Reproduced from *Klaas et al.*[98] with permission from the PCCP Owner Societies.

A.12. Thermodynamic-based Calculations

The material composition of the $SrFeO_{3-\delta}$ granules was studied with XRD using a *D8-Advance (A25)* instrument from *Bruker* with a cobalt anode and a *Lynxe-EyeXET-Detector* (Fig. A.17).

Figure A.17 shows that the granules prepared are $SrFeO_{3-\delta}$ granules without major side phases. The vertical lines indicate the peak positions of the PDF 01-081-9514 of the database *PDF 2 - Release 2019 RDB* of the *International Center for Diffraction Data (ICCD)*.

The thermodynamic properties used for the calculations are summarized in Tab. A.6.

Table A.6.: Thermodynamic properties of the materials investigated in the energetic study.

Material	Δh_δ° [kJmol^{-1}]	Δs_δ° [Jmol^{-1}K^{-1}]	γ [-]	extracted from
$SrFeO_{3-\delta}$	74	47	1.07	[34]
$Sr_{0.8}Ca_{0.2}FeO_{3-\delta}$	57.5	-	-	[20]
$CaMnO_{3-\delta}$	180	108	1	[98]
$Ca_{0.9}Sr_{0.1}MnO_{3-\delta}$	168	100	1	[98]
$Ca_{0.8}Sr_{0.2}MnO_{3-\delta}$	157	92	1	[98]
$Ca_{0.7}Sr_{0.3}MnO_{3-\delta}$	146	84	1	[98]
$Ca_{0.6}Sr_{0.4}MnO_{3-\delta}$	135	76	1	[98]

The figures A.18 and A.19 display both graphs of Fig. 8.5 on p. 120 separately.

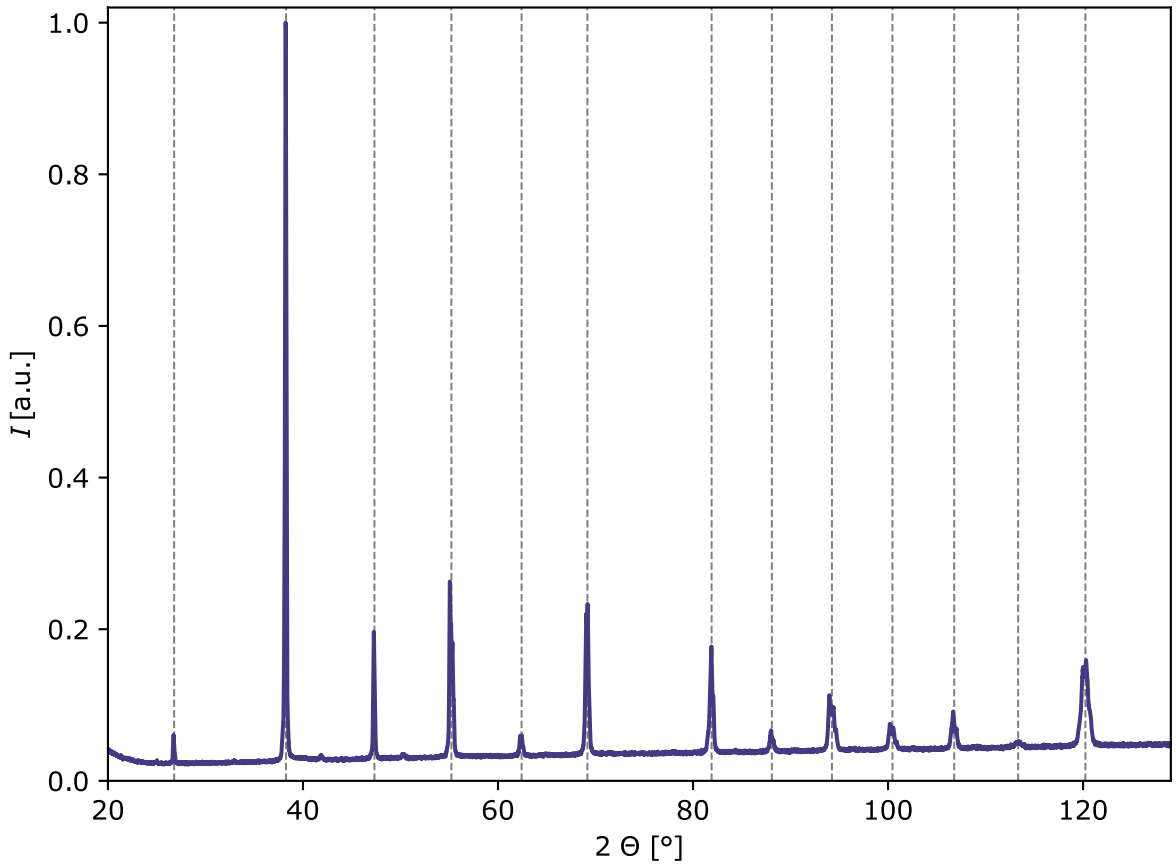

Figure A.17.: XRD-pattern of the $SrFeO_{3-\delta}$ granules. This pattern was measured with a cobalt anode. The vertical lines indicate the main peaks of the structure with which this pattern was identified. They refer to PDF 01-081-9514 of the database *PDF 2 - Release 2019 RDB* of the *International Center for Diffraction Data (ICCD)*. Reproduced from *Klaas et al.*[82] with permission from the Royal Society of Chemistry.

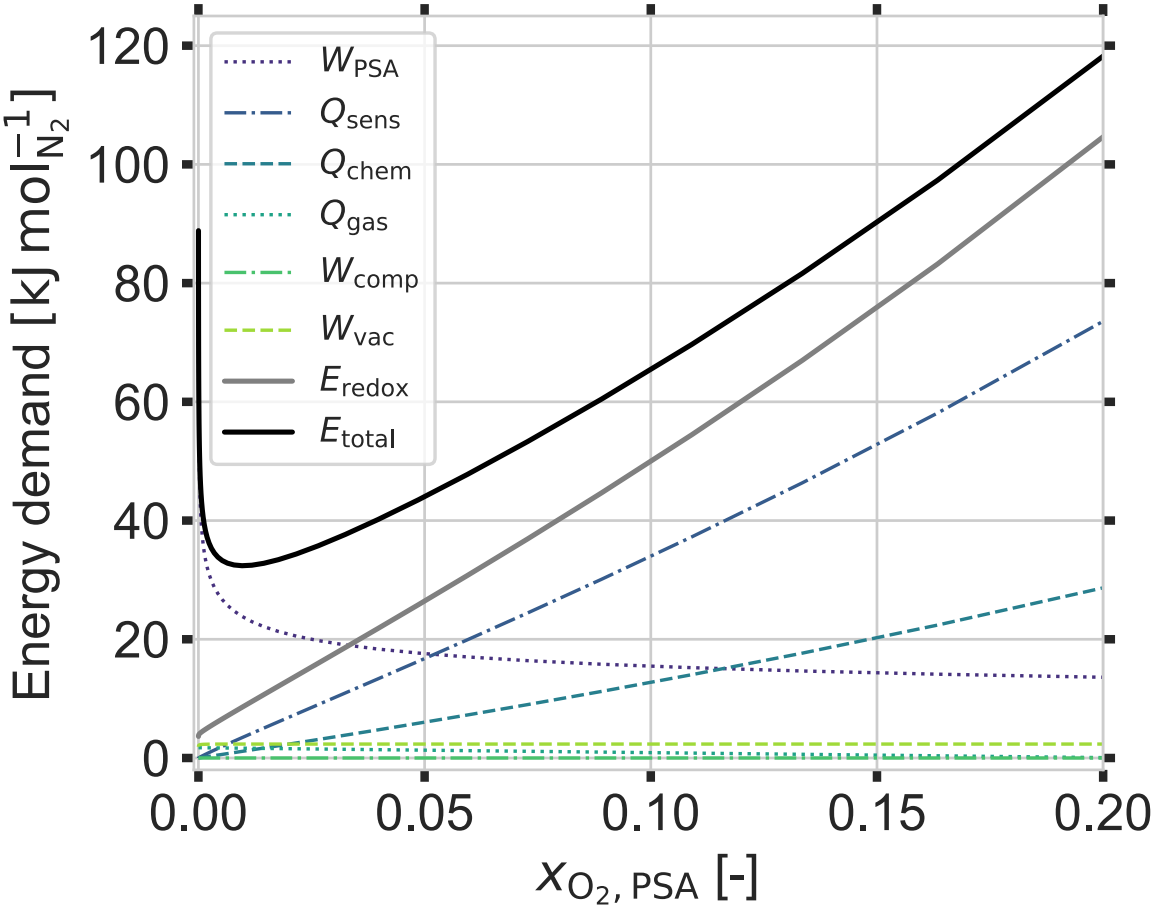

Figure A.18.: Variation of the PSA output oxygen x_{O_2} mole fraction and thus of the oxygen partial pressure during oxidation for $Sr_{0.8}Ca_{0.2}FeO_{3-\delta}$.

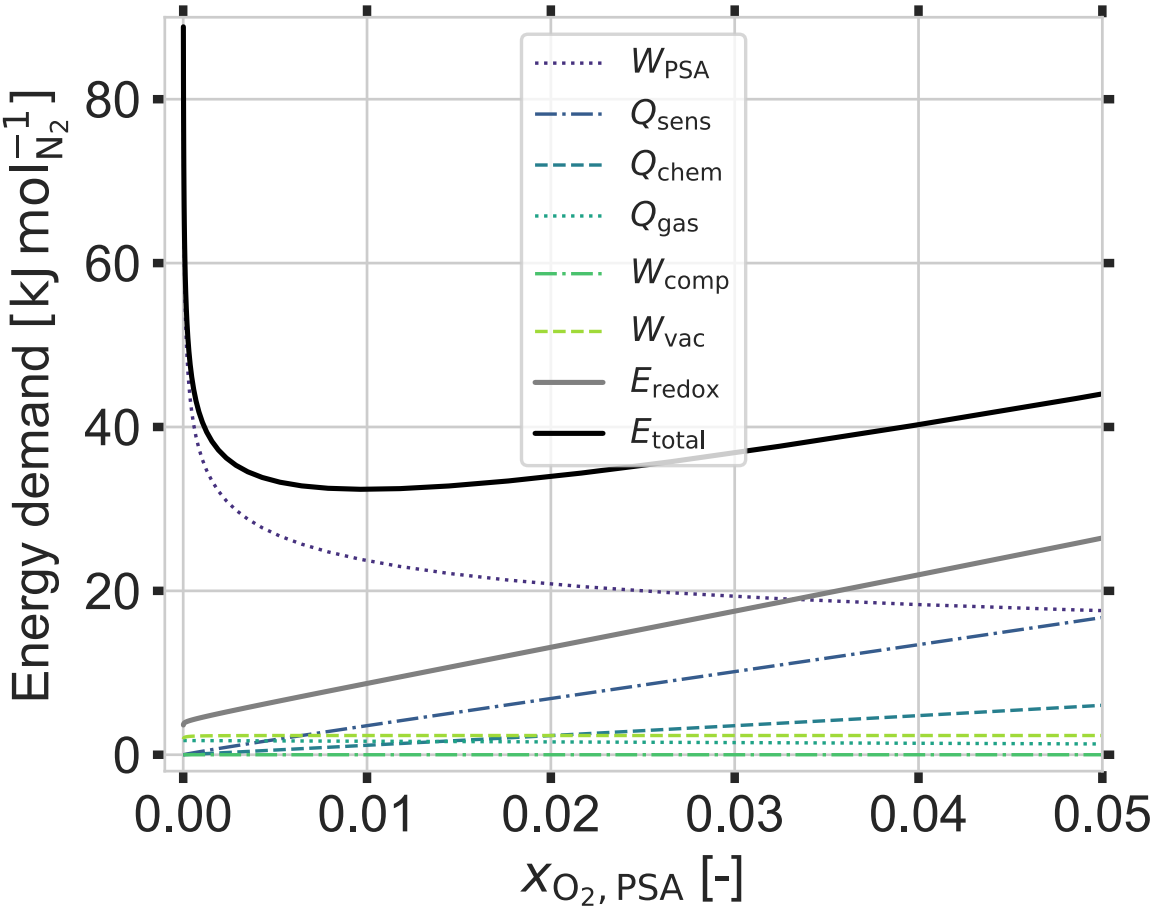

Figure A.19.: Extract from Fig. A.18.

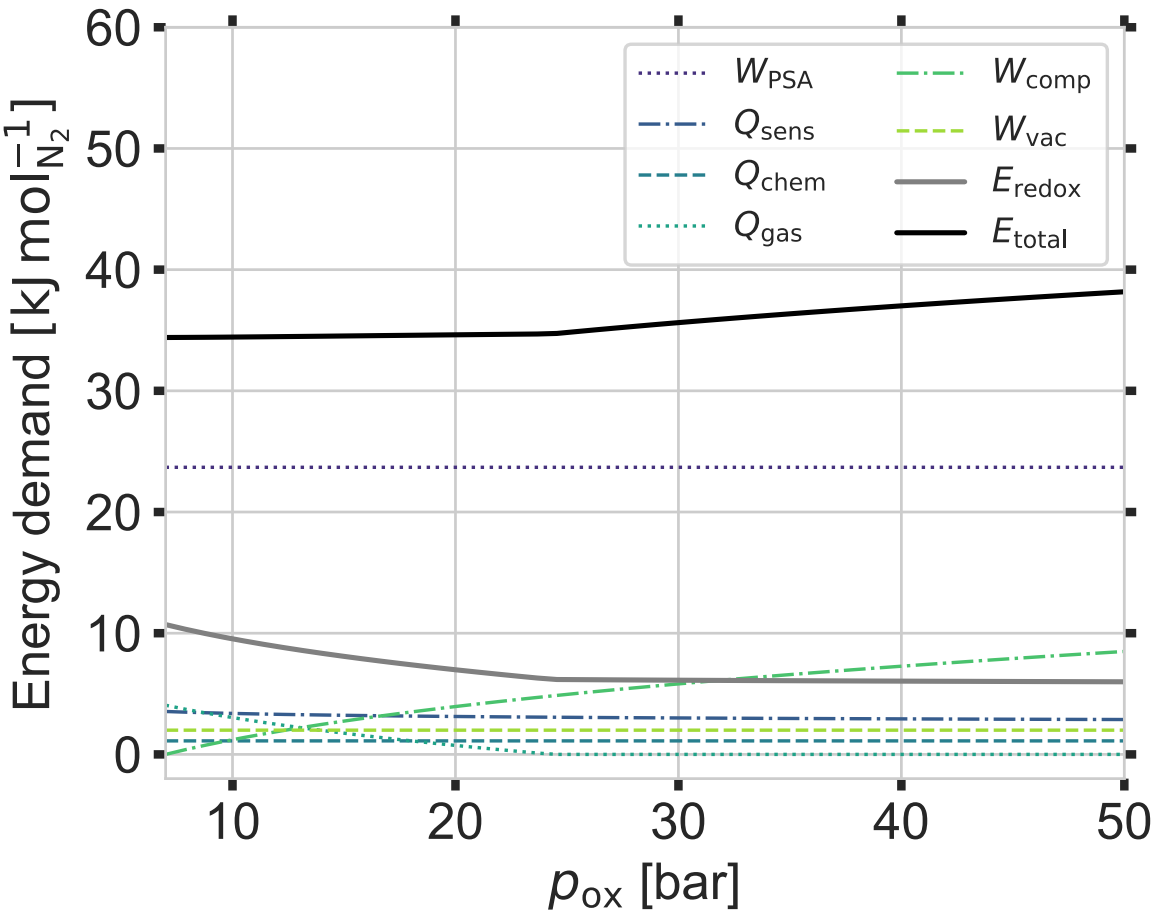

Figure A.20.: Variation of the PSA output oxygen x_{O_2} mole fraction and thus of the oxygen partial pressure during oxidation for $Sr_{0.8}Ca_{0.2}FeO_{3-\delta}$.

The figures A.20 and A.21 display both graphs of Fig. 8.6d on p. 121 separately.

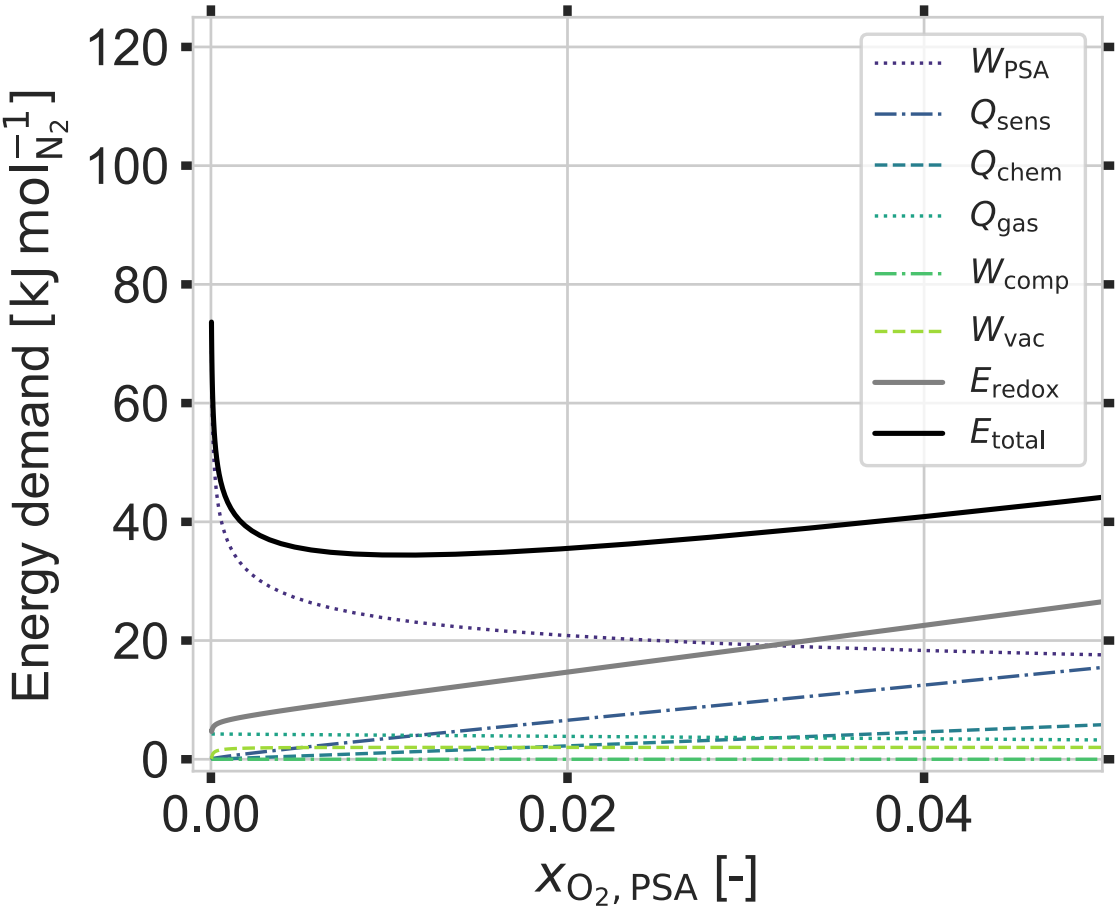

Figure A.21.: Extract from Fig. A.18.

Publications

The following publications were published within the framework of the doctoral thesis:

L. Klaas, B. Bulfin, D. Kriechbaumer, N. Neumann, M. Roeb and Ch. Sattler. Energetic optimization of thermochemical air separation for the production of sustainable nitrogen. Reaction Chemistry & Engineering, 8(8):1843-1854, 2023. doi: 10.1039/D3RE00087G.

A. Eltayeb, **L. Klaas**, L. Klz, J. Vieten, M. Roeb and Ch. Sattler. Thermochemical process and compact apparatus for concentrating oxygen in extraterrestrial atmospheres: a feasibility study. Scientific reports, 13(1), 1-17, 2023. doi: 10.1038/s41598-023-31120-x.

L. Klaas, B. Bulfin, D. Kriechbaumer, M. Roeb and Ch. Sattler. Impact of the Sr content on the redox thermodynamics and kinetics of $Ca_{1-x}Sr_xMnO_{3-\delta}$ tailored properties. Physical chemistry chemical physics: PCCP, 25(13):9188-9197, 2023. doi: 10.1039/D3CP00267E.

L. Klaas, M. Pein, P. Mechnich, A. Francke, D. Giasafaki, D. Kriechbaumer, Ch. Agrafiotis, M. Roeb, and Ch. Sattler. Controlling thermal expansion and phase transitions in $Ca_{1-x}Sr_xMnO_{3-\delta}$ by Sr content. Physical chemistry chemical physics: PCCP, 24(45):27976-27988, 2022. doi: 10.1039/D2CP04332G.

L. Klaas, D. Guban, M. Roeb and Ch. Sattler. Recent progress towards solar energy integration into low-pressure green ammonia production technologies. International Journal of Hydrogen Energy, 46(49): 25121-25136, 2021. doi: 10.1016/j.ijhydene.2021.05.063

Bibliography

[1] E. Foote, *Am. J. Sci. Arts*, 1856, 382–383.

[2] N. Banerjee, L. Song and D. Hasemyer, *Exxon's Own Research Confirmed Fossil Fuels' Role in Global Warming Decades Ago - Inside Climate News*, 27.04.2021, https://insideclimatenews.org/news/16092015/exxons-own-research-confirmed-fossil-fuels-role-in-global-warming/.

[3] G. Supran and N. Oreskes, *Environmental Research Letters*, 2017, **12**, 084019, DOI: 10.1088/1748-9326/aa815f.

[4] G. Supran and N. Oreskes, *Environmental Research Letters*, 2020, **15**, 119401, DOI: 10.1088/1748-9326/ab89d5.

[5] United Nations Framework Convention on Climate Change, *The Paris Agreement*, 13.03.2023, https://unfccc.int/sites/default/files/english_paris_agreement.pdf.

[6] European Commission, *Regulation (EU) 2018/1999 of the European Parliament and of the Council*, 2018.

[7] Die Bundesregierung informiert, *Klimaschutzgesetz: Klimaneutralität bis 2045 - Bundesregierung*, 04.07.2023, https://www.bundesregierung.de/breg-de/schwerpunkte/klimaschutz/klimaschutzgesetz-2021-1913672.

[8] P. E. Miranda, *Science and engineering of hydrogen-based energy technologies - Chap. 5.2: Hydrogen production and practical applications in energy generation*, Academic Press an imprint of Elsevier, London, United Kingdom and San Diego, CA, 2019.

[9] M. Al-Breiki and Y. Bicer, *International Journal of Hydrogen Energy*, 2020, **45**, 34927–34937, DOI: 10.1016/j.ijhydene.2020.04.181.

[10] W. Avery, *International Journal of Hydrogen Energy*, 1988, **13**, 761–773, DOI: 10.1016/0360-3199(88)90037-7.

[11] J.-F. Petit, P. Miele and U. B. Demirci, *International Journal of Hydrogen Energy*, 2016, **41**, 15462–15470, DOI: 10.1016/j.ijhydene.2016.06.097.

[12] R. Lan, J. T. Irvine and S. Tao, *International Journal of Hydrogen Energy*, 2012, **37**, 1482–1494, DOI: 10.1016/j.ijhydene.2011.10.004.

[13] National Minerals Information Center, *Nitrogen Statistics and Information*, 13.03.2023, `https://www.usgs.gov/centers/national-minerals-information-center/nitrogen-statistics-and-information`.

[14] C. Smith, A. K. Hill and L. Torrente-Murciano, *Energy & Environmental Science*, 2020, **13**, 331–344, DOI: 10.1039/C9EE02873K.

[15] G. J. Leigh, in *Catalysts for Nitrogen Fixation*, ed. B. E. Smith, R. L. Richards and W. E. Newton, Springer Netherlands, Dordrecht, 2004, pp. 33–54, DOI: 10.1007/978-1-4020-3611-82.

[16] L. Klaas, D. Guban, M. Roeb and C. Sattler, *International Journal of Hydrogen Energy*, 2021, **46**, 25121–25136, DOI: 10.1016/j.ijhydene.2021.05.063.

[17] D. R. MacFarlane, P. V. Cherepanov, J. Choi, B. H. Suryanto, R. Y. Hodgetts, J. M. Bakker, F. M. Ferrero Vallana and A. N. Simonov, *Joule*, 2020, **4**, 1186–1205, DOI: 10.1016/j.joule.2020.04.004.

[18] B. Bulfin, J. Lapp, S. Richter, D. Gubàn, J. Vieten, S. Brendelberger, M. Roeb and C. Sattler, *Chemical Engineering Science*, 2019, **203**, 68–75, DOI: 10.1016/j.ces.2019.03.057.

[19] B. Bulfin, L. Buttsworth, A. Lidor and A. Steinfeld, *Chemical Engineering Journal*, 2021, **421**, 127734, DOI: 10.1016/j.cej.2020.127734.

[20] S. Capstick, B. Bulfin, J. M. Naik, M. Gigantino and A. Steinfeld, *Chemical Engineering Journal*, 2023, **452**, 139289, DOI: 10.1016/j.cej.2022.139289.

[21] C. Agrafiotis, M. Pein, D. Giasafaki, S. Tescari, M. Roeb and C. Sattler, *Journal of Solar Energy Engineering*, 2019, **141**, 021010, DOI: 10.1115/1.4042226.

[22] M. Pein, C. Agrafiotis, J. Vieten, D. Giasafaki, S. Brendelberger, M. Roeb and C. Sattler, *Solar Energy*, 2020, **198**, 612–622, DOI: 10.1016/j.solener.2020.01.088.

[23] J. Vieten, B. Bulfin, P. Huck, M. Horton, D. Guban, L. Zhu, Y. Lu, K. A. Persson, M. Roeb and C. Sattler, *Energy & Environmental Science*, 2019, **12**, 1369–1384, DOI: 10.1039/C9EE00085B.

[24] M. A. Green, A. Ho-Baillie and H. J. Snaith, *Nature Photonics*, 2014, **8**, 506–514, DOI: 10.1038/nphoton.2014.134.

[25] U. Guth, in *Encyclopedia of Applied Electrochemistry*, ed. G. Kreysa, K.-i. Ota and R. F. Savinell, Springer New York, New York, NY, 2014, pp. 1159–1160, DOI: 10.1007/978-1-4419-6996-5_310.

[26] S. M. Babiniec, E. N. Coker, J. E. Miller and A. Ambrosini, *Solar Energy*, 2015, **118**, 451–459, DOI: 10.1016/j.solener.2015.05.040.

[27] S. M. Babiniec, E. N. Coker, J. E. Miller and A. Ambrosini, *International Journal of Energy Research*, 2016, **40**, 280–284, DOI: 10.1002/er.3467.

[28] L. Imponenti, K. J. Albrecht, J. W. Wands, M. D. Sanders and G. S. Jackson, *Solar Energy*, 2017, **151**, 1–13, DOI: 10.1016/j.solener.2017.05.010.

[29] E. Mastronardo, X. Qian, J. M. Coronado and S. M. Haile, *Journal of Materials Chemistry A*, 2020, **8**, 8503–8517, DOI: 10.1039/D0TA02031A.

[30] R. Buck, C. Agrafiotis, S. Tescari, N. Neumann and M. Schmücker, *Frontiers in Energy Research*, 2021, **9**, 322, DOI: 10.3389/fenrg.2021.694248.

[31] Z. Yang, Y. S. Lin and Y. Zeng, *Industrial & Engineering Chemistry Research*, 2002, **41**, 2775–2784, DOI: 10.1021/ie010736k.

[32] J. Vieten, B. Bulfin, F. Call, M. Lange, M. Schmücker, A. Francke, M. Roeb and C. Sattler, *Journal of Materials Chemistry A*, 2016, **4**, 13652–13659, DOI: 10.1039/C6TA04867F.

[33] H. E. Bush, N. P. Nguyen, T. Farr, P. G. Loutzenhiser and A. Ambrosini, *Solid State Ionics*, 2021, **368**, 115692, DOI: 10.1016/j.ssi.2021.115692.

[34] J. Vieten, *PhD Thesis*, Technische Universität Dresden, 2019.

[35] M. Ezbiri, A. Reinhart, B. Huber, K. M. Allen, A. Steinfeld, B. Bulfin and R. Michalsky, *Reaction Chemistry & Engineering*, 2020, **5**, 685–695, DOI: 10.1039/C9RE00430K.

[36] T. P. Farr, N. P. Nguyen, E. Bush, A. Ambrosini and P. G. Loutzenhiser, *Materials (Basel, Switzerland)*, 2020, **13**, 5123, DOI: 10.3390/ma13225123.

[37] A. H. McDaniel, E. C. Miller, D. Arifin, A. Ambrosini, E. N. Coker, R. O'Hayre, W. C. Chueh and J. Tong, *Energy & Environmental Science*, 2013, **6**, 2424, DOI: 10.1039/C3EE41372A.

[38] A. H. McDaniel, A. Ambrosini, E. N. Coker, J. E. Miller, W. C. Chueh, R. O'Hayre and J. Tong, *Energy Procedia*, 2014, **49**, 2009–2018, DOI: 10.1016/j.egypro.2014.03.213.

[39] A. A. Emery, J. E. Saal, S. Kirklin, V. I. Hegde and C. Wolverton, *Chemistry of Materials*, 2016, **28**, 5621–5634, DOI: 10.1021/acs.chemmater.6b01182.

[40] M. Kubicek, A. H. Bork and J. L. M. Rupp, *Journal of Materials Chemistry A*, 2017, **5**, 11983–12000, DOI: 10.1039/C7TA00987A.

[41] X. Qian, J. He, E. Mastronardo, B. Baldassarri, C. Wolverton and S. M. Haile, *Chemistry of Materials*, 2020, **32**, 9335–9346, DOI: 10.1021/acs.chemmater.0c03278.

[42] A. Riaz, P. Kreider, F. Kremer, H. Tabassum, J. S. Yeoh, W. Lipiński and A. Lowe, *ACS Applied Energy Materials*, 2019, **2**, 2494–2505, DOI: 10.1021/acsaem.8b01994.

[43] A. Eltayeb, L. Klaas, L. Kölz, J. Vieten, M. Roeb and C. Sattler, *Scientific reports*, 2023, **13**, 5148, DOI: 10.1038/s41598-023-31120-x.

[44] A. S. Bhalla, R. Guo and R. Roy, *Materials Research Innovations*, 2000, **4**, 3–26, DOI: 10.1007/s100190000062.

[45] L. Klaas, M. Pein, P. Mechnich, A. Francke, D. Giasafaki, D. Kriechbaumer, C. Agrafiotis, M. Roeb and C. Sattler, *Physical chemistry chemical physics : PCCP*, 2022, **24**, 27976–27988, DOI: 10.1039/d2cp04332g.

[46] A. M. Glazer, *Acta Crystallographica Section B Structural Crystallography and Crystal Chemistry*, 1972, **28**, 3384–3392, DOI: 10.1107/S0567740872007976.

[47] P. M. Woodward, *Acta Crystallographica Section B: Structural Science*, 1997, **53**, 32–43, DOI: 10.1107/S0108768196010713.

[48] P. M. Woodward, *Acta Crystallographica Section B: Structural Science*, 1997, **53**, 44–66, DOI: 10.1107/S0108768196012050.

[49] H. A. Jahn and E. Teller, *Proceedings of the Royal Society of London. Series A - Mathematical and Physical Sciences*, 1937, **161**, 220–235, DOI: 10.1098/rspa.1937.0142.

[50] M. N. Iliev and M. V. Abrashev, *Journal of Raman Spectroscopy*, 2001, **32**, 805–811, DOI: 10.1002/jrs.770.

[51] B. Bulfin, J. Vieten, D. E. Starr, A. Azarpira, C. Zachäus, M. Hävecker, K. Skorupska, M. Schmücker, M. Roeb and C. Sattler, *Journal of Materials Chemistry A*, 2017, **5**, 7912–7919, DOI: 10.1039/C7TA00822H.

[52] A. A. Colville and S. Geller, *Acta Crystallographica Section B Structural Crystallography and Crystal Chemistry*, 1971, **27**, 2311–2315, DOI: 10.1107/S056774087100579X.

[53] H. Taguchi, M. Nagao, T. Sato and M. Shimada, *Journal of Solid State Chemistry*, 1989, **78**, 312–315, DOI: 10.1016/0022-4596(89)90113-8.

[54] E. I. Leonidova, I. A. Leonidov, M. V. Patrakeev and V. L. Kozhevnikov, *Journal of Solid State Electrochemistry*, 2011, **15**, 1071–1075, DOI: 10.1007/s10008-010-1288-1.

[55] J. Klarbring and S. I. Simak, *Physical Review B*, 2018, **97**, 024108, DOI: 10.1103/PhysRevB.97.024108.

[56] V. M. Goldschmidt, *Naturwissenschaften*, 1926, 477–485.

[57] B. Dabrowski, O. Chmaissem, J. Mais, S. Kolesnik, J. D. Jorgensen and S. Short, *Journal of Solid State Chemistry*, 2003, **170**, 154–164, DOI: 10.1016/s0022-4596(02)00056-7.

[58] G. Kieslich, S. Sun and A. K. Cheetham, *Chemical science*, 2015, **6**, 3430–3433, DOI: 10.1039/c5sc00961h.

[59] C. J. Bartel, C. Sutton, B. R. Goldsmith, R. Ouyang, C. B. Musgrave, L. M. Ghiringhelli and M. Scheffler, *Science advances*, 2019, **5**, eaav0693, DOI: 10.1126/sciadv.aav0693.

[60] R. D. Shannon, *Acta Crystallographica Section A*, 1976, **32**, 751–767, DOI: 10.1107/S0567739476001551.

[61] W. Paszkowicz, J. Piętosa, S. M. Woodley, P. A. Dłużewski, M. Kozłowski and C. Martin, *Powder Diffraction*, 2010, **25**, 46–59, DOI: 10.1154/1.3314256.

[62] E. Smith and G. Dent, *Modern Raman spectroscopy: A practical approach*, Wiley, Hoboken, NJ and Chichester, West Sussex, UK, Second edition edn., 2019.

[63] P. Vandenabeele, *Practical Raman spectroscopy: An introduction*, Wiley, Chichester, 2013.

[64] M. N. Iliev, M. V. Abrashev, H.-G. Lee, V. N. Popov, Y. Y. Sun, C. Thomsen, R. L. Meng and C. W. Chu, *Physical Review B*, 1998, **57**, 2872–2877, DOI: 10.1103/PhysRevB.57.2872.

[65] M. V. Abrashev, J. Bäckström, L. Börjesson, V. N. Popov, R. A. Chakalov, N. Kolev, R.-L. Meng and M. N. Iliev, *Physical Review B*, 2002, **65**, 184301, DOI: 10.1103/PhysRevB.65.184301.

[66] B. Bulfin, J. Vieten, C. Agrafiotis, M. Roeb and C. Sattler, *Journal of Materials Chemistry A*, 2017, **5**, 18951–18966, DOI: 10.1039/C7TA05025A.

[67] B. Bulfin, L. Hoffmann, L. de Oliveira, N. Knoblauch, F. Call, M. Roeb, C. Sattler and M. Schmücker, *Physical chemistry chemical physics : PCCP*, 2016, **18**, 23147–23154, DOI: 10.1039/c6cp03158g.

[68] R. A. de Souza, *Physical chemistry chemical physics : PCCP*, 2006, **8**, 890–897, DOI: 10.1039/b511702j.

[69] S. Vyazovkin, A. K. Burnham, J. M. Criado, L. A. Pérez-Maqueda, C. Popescu and N. Sbirrazzuoli, *Thermochimica Acta*, 2011, **520**, 1–19, DOI: 10.1016/j.tca.2011.03.034.

[70] B. Bulfin, J. Vieten, S. Richter, J. M. Naik, G. R. Patzke, M. Roeb, C. Sattler and A. Steinfeld, *Physical chemistry chemical physics : PCCP*, 2020, **22**, 2466–2474, DOI: 10.1039/c9cp05771d.

[71] O. Levenspiel, *Chemical reaction engineering*, Wiley, New York, 2nd edn., 1972.

[72] M. W. Gaultois, T. D. Sparks, C. K. H. Borg, R. Seshadri, W. D. Bonificio and D. R. Clarke, *Chemistry of Materials*, 2013, **25**, 2911–2920, DOI: 10.1021/cm400893e.

[73] E. Bakken, T. Norby and S. Stolen, *Solid State Ionics*, 2005, **176**, 217–223, DOI: 10.1016/j.ssi.2004.07.001.

[74] B. Souvignier, H. Wondratschek, M. I. Aroyo, G. Chapuis and A. M. Glazer, in *International tables for crystallography*, ed. M. I. Aroyo, Wiley, Chichester, 2016, vol. A, pp. 42–74, DOI: 10.1107/97809553602060000922.

[75] N. Galinsky, A. Mishra, J. Zhang and F. Li, *Applied Energy*, 2015, **157**, 358–367, DOI: 10.1016/j.apenergy.2015.04.020.

[76] A. Mishra, N. Galinsky, F. He, E. E. Santiso and F. Li, *Catalysis Science & Technology*, 2016, **6**, 4535–4544, DOI: 10.1039/C5CY02186C.

[77] E. Suprayoga, W. B. Putri, K. Singsoog, S. Paengson, M. Y. Hanna, A. R. Nugraha, D. R. Munazat, B. Kurniawan, M. Nurhuda, T. Seetawan and E. H. Hasdeo, *Materials Research Bulletin*, 2021, **141**, 111359, DOI: 10.1016/j.materresbull.2021.111359.

[78] X. Han, Y. Hu, J. Yang, F. Cheng and J. Chen, *Chemical communications (Cambridge, England)*, 2014, **50**, 1497–1499, DOI: 10.1039/c3cc48207c.

[79] J. R. Jennings, *Catalytic Ammonia Synthesis: Fundamentals and Practice*, Springer, New York, NY, 2013.

[80] P. Majewski, L. Epple and F. Aldinger, *Journal of the American Ceramic Society*, 2000, **83**, 1513–1517, DOI: 10.1111/j.1151-2916.2000.tb01419.x.

[81] O. Chmaissem, B. Dabrowski, S. Kolesnik, J. Mais, D. E. Brown, R. Kruk, P. Prior, B. Pyles and J. D. Jorgensen, *Physical Review B*, 2001, **64**, 134412, DOI: 10.1103/PhysRevB.64.134412.

[82] L. Klaas, B. Bulfin, D. Kriechbaumer, N. Neumann, M. Roeb and C. Sattler, *Reaction Chemistry & Engineering*, 2023, **8**, 1843–1854, DOI: 10.1039/D3RE00087G.

[83] D. G. Goodwin, H. K. Moffat, I. Schoegl, R. L. Speth and B. W. Weber, *Cantera: An Object-oriented Software Toolkit for Chemical Kinetics, Thermodynamics, and Transport Processes*, 2022, DOI: 10.5281/zenodo.6387882.

[84] R. Gross and A. Marx, *Festkörperphysik*, De Gruyter, Berlin/Boston, 3rd edn., 2018, DOI: 10.1515/9783110559187.

[85] S. Ergun, *Chem. Eng. Prog.*, 1952, **48**, 89–94.

[86] *VDI-Wärmeatlas: Berechnungsunterlagen für Druckverlust, Wärme- und Stoffübertragung*, Springer, Berlin and Heidelberg, 10th edn., 2006.

[87] S. Brendelberger, H. von Storch, B. Bulfin and C. Sattler, *Solar Energy*, 2017, **141**, 91–102, DOI: 10.1016/j.solener.2016.11.023.

[88] P. Linstrom, 1997, DOI: 10.18434/T4D303.

[89] L. L. Hench and J. K. West, *Chemical reviews*, 1990, **90**, 33–72.

[90] K. C. Patil, S. T. Aruna and T. Mimani, *Current Opinion in Solid State and Materials Science*, 2002, **6**, 507–512, DOI: 10.1016/S1359-0286(02)00123-7.

[91] F. Deganello, G. Marcì and G. Deganello, *Journal of the European Ceramic Society*, 2009, **29**, 439–450, DOI: 10.1016/j.jeurceramsoc.2008.06.012.

[92] A. E. Danks, S. R. Hall and Z. Schnepp, *Materials Horizons*, 2016, **3**, 91–112, DOI: 10.1039/C5MH00260E.

[93] S. Shanmugam, *BioImpacts : BI*, 2015, **5**, 55–63, DOI: 10.15171/bi.2015.04.

[94] *Cellular ceramics: Structure, manufacturing, properties and applications*, ed. M. Scheffler, Wiley-VCH, Weinheim, 2005.

[95] M. Pein, L. Matzel, L. Oliveira, G. Alkan, A. Francke, P. Mechnich, C. Agrafiotis, M. Roeb and C. Sattler, *Advanced Energy Materials*, 2022, **12**, 2102882, DOI: 10.1002/aenm.202102882.

[96] H. M. Rietveld, *Journal of Applied Crystallography*, 1969, **2**, 65–71, DOI: 10.1107/S0021889869006558.

[97] R. E. Dinnebier, J. S. O. Evans and A. Leineweber, *Rietveld Refinement: Practical powder diffraction pattern analysis using TOPAS*, De Gruyter, Berlin and Boston, 2018, DOI: 10.1515/9783110461381.

[98] L. Klaas, B. Bulfin, D. Kriechbaumer, M. Roeb and C. Sattler, *Physical chemistry chemical physics : PCCP*, 2023, **25**, 9188–9197, DOI: 10.1039/d3cp00267e.

[99] K. R. Poeppelmeier, M. E. Leonowicz, J. C. Scanlon, J. M. Longo and W. B. Yelon, *Journal of Solid State Chemistry*, 1982, **45**, 71–79, DOI: 10.1016/0022-4596(82)90292-4.

[100] R. J. Panlener, R. N. Blumenthal and J. E. Garnier, *Journal of Physics and Chemistry of Solids*, 1975, **36**, 1213–1222, DOI: 10.1016/0022-3697(75)90192-4.

[101] J. Vieten, B. Bulfin, M. Senholdt, M. Roeb, C. Sattler and M. Schmücker, *Solid State Ionics*, 2017, **308**, 149–155, DOI: 10.1016/j.ssi.2017.06.014.

[102] P. Zhao, J. Xu, H. Wang, L. Wang, W. Kong, W. Ren, L. Bian and A. Chang, *Journal of Applied Physics*, 2014, **116**, 194901, DOI: 10.1063/1.4901636.

[103] R. P. Pawar and V. Puri, *Ceramics International*, 2014, **40**, 10423–10430, DOI: 10.1016/j.ceramint.2014.03.013.

[104] S. Capstick, *Masterthesis*, ETH, Zürich, 2021.

[105] A. R. Denton and N. W. Ashcroft, *Physical review. A, Atomic, molecular, and optical physics*, 1991, **43**, 3161–3164, DOI: 10.1103/physreva.43.3161.

[106] H. Taguchi, M. Sonoda and M. Nagao, *Journal of Solid State Chemistry*, 1998, **137**, 82–86, DOI: 10.1006/jssc.1997.7701.

[107] Materials Project, *Materials Data on Ca2MnO4 by Materials Project*, 2020, DOI: 10.17188/1193833.

[108] Materials Project, *Materials Data on CaMn2O4 by Materials Project*, 2020, DOI: 10.17188/1193549.

[109] L. Rørmark, A. B. Mørch, K. Wiik, S. Stølen and T. Grande, *Chemistry of Materials*, 2001, **13**, 4005–4013, DOI: 10.1021/cm011050l.

[110] GTT-technologies, *Privat Communications*, 6.12.2022.

[111] E. Granado, J. A. Sanjurjo, C. Rettori, J. J. Neumeier and S. B. Oseroff, *Physical Review B*, 2000, **62**, 11304–11307, DOI: 10.1103/PhysRevB.62.11304.

[112] E. Granado, N. O. Moreno, H. Martinho, A. García, J. A. Sanjurjo, I. Torriani, C. Rettori, J. J. Neumeier and S. B. Oseroff, *Physical review letters*, 2001, **86**, 5385–5388, DOI: 10.1103/PhysRevLett.86.5385.

[113] A. Sacchetti, M. Baldini, P. Postorino, C. Martin and A. Maignan, *Journal of Raman Spectroscopy*, 2006, **37**, 591–596, DOI: 10.1002/jrs.1484.

[114] E. I. Goldyreva, I. A. Leonidov, M. V. Patrakeev and V. L. Kozhevnikov, *Journal of Solid State Electrochemistry*, 2013, **17**, 3185–3190, DOI: 10.1007/s10008-013-2223-z.

[115] K. J. Albrecht, G. S. Jackson and R. J. Braun, *Applied Energy*, 2016, **165**, 285–296, DOI: 10.1016/j.apenergy.2015.11.098.

[116] M. T. Curnan and J. R. Kitchin, *The Journal of Physical Chemistry C*, 2014, **118**, 28776–28790, DOI: 10.1021/jp507957n.

[117] A. Leriche, S. Hampshire and F. Cambier, in *Encyclopedia of Materials: Technical Ceramics and Glasses*, Elsevier, 2021, pp. 349–366, DOI: 10.1016/B978-0-12-818542-1.00017-5.

[118] J. Li and F. L. Deepak, *Chemical reviews*, 2022, **122**, 16911–16982, DOI: 10.1021/acs.chemrev.1c01067.

[119] U. Holzwarth and N. Gibson, *Nature nanotechnology*, 2011, **6**, 534, DOI: 10.1038/nnano.2011.145.

[120] P. Scherrer, *Nachrichten von der Gesellschaft der Wissenschaften zu Göttingen, mathematisch-physikalische Klasse*, 1918, 98–100.

[121] A. R. Studart, U. T. Gonzenbach, E. Tervoort and L. J. Gauckler, *Journal of the American Ceramic Society*, 2006, **89**, 1771–1789, DOI: 10.1111/j.1551-2916.2006.01044.x.

[122] U. Betke, K. Schelm, A. Rodak and M. Scheffler, *Materials (Basel, Switzerland)*, 2020, **13**, 2437, DOI: 10.3390/ma13112437.

[123] H. Ferkel and R. Hellmig, *Nanostructured Materials*, 1999, **11**, 617–622, DOI: 10.1016/S0965-9773(99)00348-7.

[124] *Ceramics Science and Technology: Volume 1: Structures*, ed. R. Riedel and I.-W. Chen, Wiley-VCH, Weinheim, 1st edn., 2015.

[125] N. Kuganathan and A. Chroneos, *AIP Advances*, 2021, **11**, 055106, DOI: 10.1063/5.0048401.

[126] Q. Yang and Y. S. Lin, *Industrial & Engineering Chemistry Research*, 2006, **45**, 6302–6310, DOI: 10.1021/ie060264f.

[127] S. Kimura, Y. Takagi, S. Tone and T. Otake, *J. Chem. Eng. Japan (Journal of Chemical Engineering of Japan)*, 1983, **16**, 217–223, DOI: 10.1252/jcej.16.217.

[128] S. Kimura, *AIChE Journal*, 1989, **35**, 339–342, DOI: 10.1002/aic.690350224.

[129] W. D. Kingery, H. K. Bowen and D. R. Uhlmann, *Introduction to ceramics*, Wiley, New York, 2nd edn., 1976.

Acknowledgments

This work would not have been possible without the support of Prof. Dr. Christian Sattler. Thank you very much for being my doctoral supervisor. I would also like to express my deep gratitude to Prof. Dr. Martin Schmücker for being my second examiner. Explicitly, I thank you for the discussion and the guided tour at the Hochschule Ruhr West.

Furthermore, I want to especially thank Prof. Dr.-Ing. Robert Pitz-Paal and Prof. Dr.-Ing. Bernhard Hoffschmidt for their inspiring questions during our periodic scientific discussions at DLR.

I gratefully acknowledge funding for my work from the SesAm project (EFRE-0801808), which is co-funded by the state of North Rhine-Westphalia, Germany, and the European EFRE fund, and the IN2SOLAIR project (SURPF2101290008), which is part of the SFERA-III transnational access program.

Many thanks go to Dr. Martin Roeb, who repeatedly supported my work with scientific suggestions and took over the supervision during the absence of Dr. Dorottya Kriechbaumer.

I am very grateful for the supervision of Dr. Dorottya Kriechbaumer. She encouraged me to design my own work and has provided me with the necessary framework. She always took the time to discuss my questions and thoughts.

Special thanks go to the team of the project SesAm - Dr. Dorottya Kriechbaumer, Dr. Nicole Neumann, Dr. Asmaa Eltayeb, Bruno Lachmann and Fabio Pierno. The team inspired me for the subject of the thesis and has always motivated me along the way. Many thanks to Dr. Nicole Neumann for the many scientific discussions and the curious questions. I would especially like to thank Bruno Lachmann and Fabio Pierno for their impressive craftsmanship and commitment.

Many thanks to Mathias Pein for the countless discussions, the joint supervision of a master's thesis and the great support in the lab and with measurements. Through our joyful collaboration, my knowledge of materials science has widened and deepened.

I would like to thank Dr. Asmaa Eltayeb and Philipp Holzemer-Zerhusen, for the great atmosphere in the shared office and the many discussions. Many thanks to Dr. Asmaa Eltayeb for the production of the foams. I would also like to thank Lamark de Oliveira for his impressive support in the lab, especially when it came to making powders and granules on a kg scale.

A big thank you goes to the Institute of Materials Research for allowing me to use their devices. Many thanks to Alexander Francke for the support with the XRD measurements and the introduction to the conducting and evaluation of XRD measurements. Many thanks to Dr. Gözde Alkan for her scientific exchange and the creation of some SEM images.

My sincere thanks to Prof. Dr. Aldo Steinfeld from ETH Zürich for enabling me as a guest scientist not only to use the equipment of the research group, but also to have many further discussions with the members of the group. Special thanks to the research group for welcoming me in such an open and friendly way and for the many inspiring discussions.

A big thanks to Dr. Brendan Bulfin for his scientific input, sharing of existing resources, and co-authoring of several publications. I have taken a lot of your scientific approach to heart.

Big credit to Max, you made the trips to DLR by car in the early years not only faster, but more fun. Many thanks to Merve, Clara, Betty and Max. You have accompanied me in the adventure of studying physics, which I started curiously but respectfully and which led me to my doctorate in the end.

I thank my parents, Gaby and Friedhelm, and my brother, Lennart, for the great support. You helped me to find a suitable balance between enjoyment and dedication. From the bottom of my heart, I thank my husband, Dio, for his support, his balance and our many discussions.